Robust design of acoustic treatment for nacelle noise reduction using computational aeroacoustics and uncertainty quantification

Vincent Dangla

École doctorale 531 : Sciences, ingénierie et environnement

Doctorat UGE

THÈSE

Pour obtenir le grade de docteur délivré par

Université Gustave Eiffel

Spécialité doctorale "Sciences de l'Ingénieur"

présentée et soutenue publiquement par

Vincent Dangla

11 Septembre 2020

Robust design of acoustic treatment for nacelle noise reduction using computational aeroacoustics and uncertainty quantification

Directeur de thèse :	**Pr. Christian Soize**
Encadrant de thèse :	**Dr. Guilherme Cuelho-Cunha**
Encadrant de thèse :	**Dr. Morad Kassem**

Jury

R. Ohayon,	Professeur émérite, CNAM, Paris	Président
R. Ghanem,	Professeur, University of Southern California	Rapporteur
D. Juvé,	Professeur, Ecole Centrale de Lyon	Rapporteur
C. Desceliers,	Professeur, Université Gustave Eiffel	Examinateur
B. Van den Nieuwenhof,	Docteur, Expert Free Field Technologies	Examinateur
S. Lidoine,	Docteur, Ingénieur Airbus France	Examinateur
G. Coelho-Cunha,	Docteur, Ingénieur Airbus France	Examinateur
C. Soize,	Professeur émérite, Université Gustave Eiffel	Directeur de thèse

Thèse préparée à AIRBUS Opérations S.A.S, Département Engineering Powerplant Acoustics

Laboratoire Modélisation et Simulation Multi-Échelle (MSME)
UMR CNRS 8208 Marne la Vallée, France

Acknowledgements

First of all, I would like to thank Philippe Homsi, head of Engineering Powerplant Acoustics, Delphine Cadot-Burillet, former head of Exterior Noise Integration and Services and Louis Ratier, head of Nacelle and Acoustic treatments for giving me the opportunity to carry out this thesis work within the Nacelle and Acoustic treatments team. My sincere thanks go to Morad Kassem and Guilherme Coelho-Cunha for supervising this work and for all the precious advices they gave me during this work. They took a lot of time to answer my questions and to help me organising my life inside Airbus. I also wish to acknowledge the help of Aurélien Mosson and Jean-Yves Surrateau, head of Acoustic methods on many aspects of the present work.

I am particularly grateful to Professor Christian Soize for supervising my work, for his help and wise advices and for taking a lot of his time out to hear, guide and keep me on the correct path. I also wish to sincerely thank him for the intense reading and correction phases of the present manuscript.

My thanks are addressed to Professor Roger Ohayon for accepting to chair the jury, Professor Roger Ghanem, and Professor Daniel Juvé, for accepting to report this work. I also acknowledge the presence of Professor Christophe Desceliers in the jury, in particular the presence of Stéphane Lidoine and Benoît Van den Nieuwenhof and for their help all along those three years.

My sincere thanks go to Charles Cariou, Florent Mercat, Julien Primus, Arnulfo Carazo-Mendez, Julien Espuche and Maud Lavieille for their warm welcome and for the answers they gave me during those three years. I also wish to thank Fabien Vieuille, Jean-Paul Roméo, Grégoire Pont, Sébastien Le-Saint, Sébastien Drouilhet-Peyre, Alois Sengissen, and Philippe Sauvage, for their help on computational aspects.

I am grateful for the help I received from my former colleagues of Free Field Technologies, in particular Jonathan Caprile and Eveline Rosseel who had the misfortune to carry the developments of Actran in the framework of this thesis, for three years.

My special thanks go to Bernard Coignus and Jean-Marc Prosper for taking time on their schedules to show us Airbus facilities and for their communicative cheerfulness.

My deepest thanks go to my colleagues Quentin, Anthony, Justin, Anthony and Brian for all the time we spent together, for all the meals shared, for all the coffee, and for all the no-work we did together.

I sincerely wish to thank my best friends Valentin for leading the way towards the acoustic field since we were teenagers, as we shared the same passion for music and sciences. And Jean-Baptiste, with whom I spend a lot of time since engineering school, discussing our thesis, being retarded and slow (it's a $p(x)$ Jean-Baptiste).

I finally wish to sincerely thank all my friends that I did not mentionned (sorry guys, page limitation you know), my family, especially my father and my mother, sister and breauf for their unconditional support and the moments we spent together during those three years, that allowed me for stepping aside of this subject for a while. I particularly wish to thank my grandparents without whom I would not have reached this step.

Introduction

General context

In modern turbofan engines, fan noise is one of the main noise sources due to the constant increasing of engines bypass ratio for fuel burn reduction purposes. Since the air traffic has known a great expansion in the last decades, and especially since the recent events that negatively impacted the aeronautic industry, the environment problematic became a main focus for all protagonists. In particular, aircraft noise represent a significant interest for the aeronautic community whether it is a question of ground impact or customer comfort. Moreover, the certification of aircraft is increasingly strict in terms of noise pollution, and forces engine and aircraft manufacturers to work in early phases of the aircraft development on noise reduction solutions, way before the aircraft first flight. As fan noise is characterized by broadband and tonal components, acoustic liners (acoustic treatments) are introduced for their effectiveness in mitigating both components. The tonal component is reduced by a resonance effect, while broadband noise is tackled by dissipation effects due to viscosity effects. Both dissipation effects are tuned on specific frequencies by modifying the liner geometry or intrinsic properties.

In order to be efficient, namely to absorb the fan noise, liners have to be studied in their operating environment, for several flight conditions that consist in specific engine rotation speeds, aircraft trajectories, and thus, thermodynamic conditions. For that purpose, simulations issued from prediction numerical tools are extensively used, since experiments cannot be considered for obvious costs reasons.
From the theory of acoustic propagation in a fluid flow written by authors such as Lighthill [30, 31] who gave birth to the aeroacoustics field of research, Rienstra [20] who developed the theory of acoustic propagation in ducts, and many others which contributed to the development of fluid dynamic [27, 37] or acoustics [9, 45], these prediction numerical tools have been created and constantly improved since the last century with the work of authors such as Jones [25] on the aeroacoustic propagation, Tam [61, 64, 63, 62] on computational aeroacoustic matters such as the acoustic boundary conditions, and others [73, 16, 14, 19]. For such prediction numerical models, the flow behaviour inside and outside the nacelle is characterized using computational fluid dynamics tools ([70, 33]), and allows for knowing the thermodynamical state of the fluid in which the acoustic perturbation propagates. Some works have been devoted to acoustic noise sources generated by the flow itself such as Bailly and Juvé [5, 6] in which a stochastic noise generation process is solved using linearized Euler equation. In the present work, acoustic source terms are neglected as the fan acoustic excitation is accounted for under the form of a duct modal expansion.
In the framework of nacelle intake liners performance prediction, several working axes can be drawn.

1) Noise generation, propagation and transmission in a moving fluid In order to understand the mechanisms responsible for the noise production, some studies have been carried out such as [3, 20, 29, 16] on fan noise propagation in duct, and [14] on the transmission/radiation

of sound and vibration. This axis is of major importance since knowing the phenomena and mechanisms responsible for acoustic noise in the nacelle allows for developing solutions that are more efficient in mitigating it. The noise generation, which in our case mainly concerns the study of the interaction between a moving fluid and moving mechanical parts such as the fan or the engine internal systems, its propagation in a ducted environment for which the interaction between the flow and the wall, under the form of a boundary layer is of major importance when studying lined environments, and finally the transmission/radiation phenomenon can be studied separately and are not in the framework of this thesis.

2) Acoustic treatments as mechanical systems A second axis is related to the mechanical system that characterizes the liner itself. Such a mechanical system is an assembly of several components for which the dissipation phenomena are to be well-modeled so it can be designed to optimimal at specific frequencies (tunable to specific frequencies). The main quantity used for characterizing a liner is its acoustic impedance. The theory of impedance calculation has been introduced by Guess [18] for the mathematical formulation of perforations, or Parrott, Jones, and Watson [43, 24, 23] on the assembly of several parts and the effects of liner geometry on its acoustic impedance. In presence of a moving fluid, the dissipation phenomena are more complex and are studied by several authors, especially at NASA and ONERA, using experiments ([8, 47, 65, 74, 75, 76]), and/or simulations, such as CFD [69, 51, 36, 34, 72, 12, 48] or computational aeroacoustic codes (CAA) [13, 44, 71, 73].

3) Acoustic absorption using liners, and liner performance A final axis concerns the absorption of acoustic perturbation in lined ducts in presence of a moving fluid. This axis is devoted to the optimization of such liners in their operating environment in order to maximize their ability to absorb the noise produced by the fan. Studies have been carried out on optimization methods [50, 26, 11, 68] in order to improve their effectiveness in finding the combination of design parameters that is the most adequate to tackle a specific noise frequency range. These improvements concern the numerical tools used, the design parameters that are the most impacting, or the choice of representation for the fan acoustic excitation. In [26], the interest of an axially-segmented liner instead of a uniform one is demonstrated, using a multi-modal representation of the fan noise, as it is done in the present work.

Motivations and goals

As the design of liner systems is frozen in early stages of an aircraft development, it exists a non-negligible variability on the operating environment. This variability directly impacts the design of liners by inducing large discrepancies on the quantities used for its design. Moreover, each time these quantities are updated due to the increased maturity of the aircraft program, lined surfaces are to be reoptimized in order to correctly respond to these updates, as well as verifying that the previous optimum design is still up to date. The updating phase thus represents important costs in terms of computational time as well as workforce time. These costs could be avoided, in a certain measure, by accounting for such a variability in early phases of the liner design. This is the main problematic of the present work. As this external variability directly impacts the environment of the liner, and more generally, the acoustic response of the lined system for which the flow is highly dependant on the environment (thermodynamic quantities such as the mean pressure, velocity, density of the fluid), the computational modeling of the liner acoustic performance is uncertain.

In order to quantify and account for such an uncertain nature, a robust design of the liner is carried out, by quantifying the overall uncertainty that lies within the liner design computational process. The uncertainty quantification needs to be performed in a well-defined mathematical

framework. The state-of-the-art computational aeroacoustic model of nacelle liners performance is an industrial numerical code, Actran/TM, which has to be extensively studied so as to exhibit the main components that are subject to the overall uncertainty. This first step is fundamental in the framework of robust design and is considered as a challenge since the thesis work is articulated around such an unknown system.

Once the state-of-the-art computational model is fully defined, a stochastic modeling of uncertainties is introduced and grafted on the computational model. This stochastic modeling allows for simulating the previously mentioned external variability, by accounting for the uncertainty that lies within the model (modeling errors and model parameters errors), through parametric and nonparametric probabilistic approaches of uncertainties. For instance, the parametric probabilistic approach of uncertainties can be used for analyzing the stochastic acoustic response of the system for which some parameters, such as the aircraft flight conditions, the liner geometry, or the fan excitation definition, are modeled by random variables. Then, the propagation of uncertainties in the system is analyzed using the computational model and stochastic solver, such as the Monte Carlo method. The acoustic response is then random and the quantification of uncertainties consists in estimating statistics, such as the mean, the variance, or the confidence regions associated with a certain confidence level of quantities of interest. From these statistical information, the robustness of a given liner design towards a simulated variability on its performance model can be defined, in addition to the state-of-the-art liner acoustic performance. This information, coupled to the performance information, allows for knowing the propensity of a given liner design for maintaining its nominal performance when its environment is changing in a predefined range of variation accounted for by the level of uncertainty imposed on the stochastic model. Then, making a compromise between performance and robustness, the liner design can be chosen. The level of uncertainty is to be identified, prior to the optimization step, using experimental data for example.

The general nonparametric and parametric probabilistic approaches of uncertainties, their propagation, and their quantification solving statistical inverse problems can be found in [17]. Some works based on the use of the parametric probabilistic approach of uncertain parameters, devoted to uncertainty quantification for the liner impedance in presence of a flow have been carried out in the last decade such as Jones [23] on a two-parameter liner impedance model and Brown [8] on the test bench used at NASA for liner impedance measurements. In the same framework, other also worked on the uncertainty quantification of liner impedance eduction methods such as Nark [39] and Zhou [77] and the uncertainty on liner performance as done by Robinson [50]. Nevertheless, to our knowledge, uncertainty quantification in liner performance aeroacoustic models has never been undertaken in the past. For that, the nonparametric probabilistic approach of modeling errors [60] must also be used for taking into account model uncertainties.

The main goals of this thesis work can be summarized as follows.

1. Development of the fundamental equations for the convected acoustic propagation model in lined ducts, on which Actran/TM is based. Construction of the boundary value problem and its weak formulation in order to construct the computational aeroacoustic model. Use of the finite element and infinite element methods for constructing the computational models.

2. Formulation of a reduced-order computational model that is adapted to the implementation of model uncertainties based on the use of random matrix theory.

3. Adaptation of the code to an interface problem focused on the liner using the reduced-order model.

4. Development of an adapted probabilistic model for main uncertain operators and the fan excitation.

5. Identification of the hyperparameters that control the probabilistic models by solving statistical inverse problems with experimental measurements.

6. Robust optimization of liners in presence of the previously identified probabilistic models of uncertainties.

Thesis outline

Mathematical framework and computational model

The present work is devoted to the construction of such a robust optimization framework. A first Chapter is focused on the mathematical background on which the computational aeroacoustic model of nacelle intake liner performance (Actran/TM) is constructed. We start from the governing equations for the acoustic propagation in lined ducts in presence of a moving fluid. The discretization of such a problem in a computational framework using finite and infinite elements is performed. The degrees of freedom of the computational model are organized in order that the system matrix allows for representing the liner surface and its interaction with the flow. The fan acoustic excitation is also a crucial point that has to be investigated, because the modal expansion on duct modes is not well defined in terms of acoustic energy repartition between each mode. The model reduction method that is employed, following the matrix-system reorganization is described and allow to set a proper environment for the robust optimization, for which main components are exhibited.

Uncertainty quantification

As previously explained, the modeling errors are taken into account using the nonparametric probabilistic approach of model uncertainties induced by modeling errors [54, 57, 60] and the parametric probabilistic approach is used for uncertain parameters (see for instance [17, 60]). The use of these probabilistic approaches to structural acoustics and vibration can be found in [40, 41]. The proposed construction is extensively detailed in Chapter 2. The main components of the computational model that have been exhibited in the first chapter are adequately randomized using a proper modeling, constructed by respecting the physical and energetic properties of each component, such as the energy conservation and dissipation properties. Then, the stochastic computational model is operated and a sensitivity study of the acoustic response towards each source of uncertainty is carried out in Chapter 4. This makes it possible to understand and predict the behavior of the model subjected to variability, under the form of uncertainties. Statistical inverse problems are solved for identifying the hyperparameters of the probabilistic models using experimental measurements. The main goal is then to draw confidence regions from the stochastic acoustic responses and try to frame a maximum of experimental points inside the confidence region, and that, for each one of the sources of uncertainties. This is one of the most important steps of this work since the stochastic model physical representativeness is extensively studied, and since the identified levels of uncertainties are set at this stage, for the rest of the robust optimization process.

Optimization of liners in presence of uncertainties

Finally, the last Chapter is devoted to the robust optimization of lined surfaces in presence of the probabilistic models of uncertainties, previously identified, and constitutes the final step and objective of this work. During this optimization, two different liners are used, for which the intrinsic properties or design parameters are very different. A first step consists in choosing,

from the available design parameters, the ones that are the most impacting the liner acoustic performance. Then, a specific range for each parameters is defined by taking a proportion of the nominal value (which corresponds to the optimum found by Airbus) from each side. A map is drawn from the stochastic results computed for each liner design, and the optimum in terms of performance is deduced, as well as the optimum in terms of robustness.

Scientific interest, novelties, and engineering aspects for aeronautical industries

This work is devoted to the improvement of optimization methods for liner performance by giving, not only an insight on the performance of a given liner design, but also on its ability to keep its acoustic performance stable towards an external variability.
(i) A model reduction method has specifically been developed by Free Field Technologies in Actran in order to be able to implement the nonparametric probabilistic model of uncertainties in the aeroacoustic computational model for liner performance. Moreover, this work provides a development of a stochastic reduced-order model adapted to the interface problem between an acoustic liner and the acoustic perturbation created by the fan rotation, convected by a moving fluid. The nonparametric stochastic modeling is used to construct such a stochastic model, which is then adapted to the accounting of modeling errors within a computational model used for industrial purposes, as well as the model parameters errors that are induced by an external variability.
(ii) A parametric probabilistic model is developed to take into account uncertainties in the fan excitation, that is an important point.
(iii) A methodology for the identification of hyperparameters of the probabilistic models is proposed using experimental measurements.
(iv) A robust optimization of liners is proposed using the stochastic aeroacoustic computational model for a very complex system based on the use of high-dimensional fidelity computational model.
(v) The results obtained are completely novels in the framework of the robust design of acoustic treatment for nacelle noise reduction.

Contents

1 Computational Model and Fundamental Equations **19**

1.1 Problem to be solved . . . 20
1.2 Strategy for solving the problem . . . 20
1.3 Conventions and notations . . . 21
1.4 Fundamental equations for fluid dynamics . . . 21
1.5 Transformations of fundamental equations . . . 22
1.6 Steady flow computation . . . 23
1.7 Linearized equations for acoustic propagation in a moving fluid . . . 23
1.8 Boundary value problem for the linearized acoustic propagation . . . 27
1.9 Modeling of the liner (acoustic treatment) . . . 32
1.10 Weak formulation of the boundary value problem for the linearized acoustic propagation for the inlet case . . . 33
1.11 Finite/Infinite Elements discretization of the weak formulation of the boundary value problem related to the inlet . . . 34
1.12 Frequency by frequency static condensation with respect to the liner dofs and expression of the fan acoustic excitation . . . 37
1.13 Computational reduced-order model using a pellicular projection . . . 38
1.14 Defining quantities of interest . . . 41
1.15 Robust design optimization problem . . . 42

2 Uncertainty Quantification **45**

2.1 Brief summary of the nonparametric probabilistic approach of uncertainties . . . 46
2.2 Methodology for uncertainty quantification . . . 46
2.3 Construction of the probabilistic model of complex generalized liner impedance matrix. . . . 48
2.4 Construction of the probabilistic model of the generalized aeroacoustic matrix. . . . 51
2.5 Statistical dependence properties of random matrices. . . . 52
2.6 Parametric probabilistic modeling of the fan acoustic excitation . . . 53
2.7 Construction of the SROM by using the nonparametric probabilistic approach of uncertainties . . . 56
2.8 Stochastic solver . . . 56
2.9 Construction of a matrix representing the QoIs for a multiple loadcases . . . 57
2.10 Estimation of the robust-design objective function and convergence with respect to the number of realizations . . . 57
2.11 Implementation of the Monte Carlo solver . . . 58

3 Nominal Nacelle Intake Model **59**

3.1 Definition of the system design obtained with Computer Assisted Drawing tool (CAD) . . . 60
3.2 Fluid mesh for Computational Fluid Dynamics (CFD) . . . 60
3.3 Aeroacoustic mesh for Computational AeroAcoustics (CAA) . . . 62

3.4 Acoustic mesh for computational aeroacoustics . . . 63
3.5 Nominal liner configuration considered in the application . . . 64
3.6 Quantities of interest (output indicators) . . . 64

4 Identification of modal content and uncertainty levels 65
4.1 Definition of the general Quantities of Interest . . . 66
4.2 Definition of experimental QoIs . . . 67
4.3 Definition of simulated QoIs . . . 68
4.4 Sensitivity analysis of QoIs with respect to uncertainties . . . 70
4.5 Statistical inverse identification of uncertainty levels . . . 85
4.6 Discussion . . . 92

5 Liner optimization in presence of uncertainties 93
5.1 Identification of the most important design parameters . . . 94
5.2 Strategy for optimizing liner surfaces . . . 94
5.3 Optimization of the forward fan case liner (FFC) . . . 95
5.4 Optimization of the inlet liner . . . 98

APPENDICES 107

A Steady flow computation 107

B Fan excitation 109
B.1 Definition of hypotheses for characterizing the excitation . . . 109
B.2 Acoustic intensity in a hardwall duct in presence of a flow . . . 110

C Acoustic treatment modeling 111
C.1 Modeling of the liner . . . 112

D Algorithms 117

Nomenclature

Abbreviations

CFD	Computational Fluid Dynamics
DNS	Direct Numerical Simulations
LES	Large Eddy Simulations
NLF	NonLinear Factor
POA	Pourcentage of Open Area
QoI	Quantity of Interest

Symbols

$[\mathbf{A}_I]$	Random imaginary part of the generalized Aeroacoustic matrix
$[\mathbf{A}_R]$	Random real part of the generalized Aeroacoustic matrix
$[\mathbf{Z}^{\text{NS}}]$	Random nonsymmetric part of the generalized Liner matrix
$[\mathbf{Z}_I]$	Random imaginary part of the generalized Liner matrix
$[\mathbf{Z}_I^{\text{SS}}]$	Random skew-symmetric imaginary part of the generalized Liner matrix
$[\mathbf{Z}_I^{\text{S}}]$	Random symmetric imaginary part of the generalized Liner matrix
$[\mathbf{Z}_R]$	Random real part of the generalized Liner matrix
$[\mathcal{A}_\ell]$	Aeroacoustic matrix condensed on liner dofs
$[\mathcal{K}_L]$	Stiffness matrix of the pellicular domain
$[\mathcal{M}_L]$	Mass matrix of the pellicular domain
$[\mathcal{Z}_\ell]$	Liner matrix condensed on liner dofs
$[\mathbb{A}]$	Generalized aeroacoustic matrix
$[\mathbb{A}_I]$	Imaginary part of the generalized Aeroacoustic matrix
$[\mathbb{A}_R]$	Real part of the generalized Aeroacoustic matrix
$[\mathbb{Z}]$	Generalized Liner matrix
$[\mathbb{Z}^{\text{NS}}]$	Nonsymmetric part of the generalized Liner matrix
$[\mathbb{Z}_I]$	Imaginary part of the generalized Liner matrix

$[\mathbb{Z}_I^{\mathrm{ss}}]$	Skew-symmetric imaginary part of the generalized Liner matrix
$[\mathbb{Z}_I^{\mathrm{s}}]$	Symmetric imaginary part of the generalized Liner matrix
$[\mathbb{Z}_R]$	Real part of the generalized Liner matrix
$[\sigma]$	Second-order stress tensor
$[\tilde{\tau}]$	Second-order viscous stress tensor
$[\varepsilon_{\mathrm{if}}]$	Transfer matrix of zeros and ones selecting nonzeros dofs related to fan excitation
$[C_{\mathrm{i}}]$	Damping matrix of the inner domain finite element discretization
$[C_{\mathrm{o}}]$	Damping matrix of the outer domain infinite element discretization
$[H]$	Coupling matrix between inner and outer domain finite elment discretization
$[I]$	Second-order identity tensor
$[K_{\mathrm{i}}]$	Stiffness matrix of the inner domain finite element discretization
$[K_{\mathrm{o}}]$	Stiffness matrix of the outer domain infinite element discretization
$[M_{\mathrm{i}}]$	Mass matrix of the inner domain finite element discretization
$[M_{\mathrm{o}}]$	Mass matrix of the outer domain infinite element discretization
$[Z_{\mathrm{i}}]$	Liner impedance matrix of the inner domain finite/infinite element discretization
$\mathbf{c}^+$	Vector of incident duct modes amplitudes
$\mathbf{g}$	External acceleration vector induced by a gravity field
$\mathbf{n}$	Outward unit normal of surface Γ
$\mathbf{n}_{\mathrm{duct}}$	Outward unit normal of surface Γ_{duct}
$\mathbf{n}_{\mathrm{f}}$	Outward unit normal of surface Γ_{f}
$\mathbf{n}_{\mathrm{f}}$	Vector of the nonzeros dofs of $\mathbf{n}_{\mathrm{i}}$
$\mathbf{n}_{\mathrm{ho}}$	Outward unit normal of surface Γ_{ho}
$\mathbf{n}_{\mathrm{h}}$	Outward unit normal of surface Γ_{h}
$\mathbf{n}_{\mathrm{io}}$	Outward unit normal of surface Γ_{io}
$\mathbf{n}_{\mathrm{i}}$	Excitation vector of the discretized inner domain
$\mathbf{q}$	Generalized coordinates of the Reduced-Order Model
$\mathbf{r}$	Space three-dimensional vector
$\mathbf{v}$	Fluctuating fluid velocity
$\mathbf{v}_0$	Steady flow velocity
$\mathbf{v}_\Gamma(\mathbf{r},\omega)$	Wall acoustic velocity for the liner (Myers boundary condition)
$\mathbf{v}_\infty$	Uniform flow velocity

$\mathcal{F}_\ell$	Excitation vector condensed on liner dofs
$\mathcal{S}_{\text{duct}}$	Cross section of the duct domain Ω_{duct}
Δ_{xy}	Laplacian in the transversal plane (x, y)
Γ	Acoustic treatments surface
Γ_{duct}	Semi-infinite duct surface
Γ_{f}	Surface for acoustic sources induced by the fan
Γ_{ho}	Outer hardwall surface
Γ_{h}	Hardwall part of the model
Γ_{io}	Interface between inner and outer domains
κ	Fluid heat conductivity
$\mathbb{F}$	Generalized excitation vector
ω	Angular frequency
Ω_{duct}	Duct domain of the intake acoustic problem
Ω_{i}	Inner domain of the intake acoustic problem
Ω_{o}	Outer domain of the intake acoustic problem
$\partial\Omega_{\text{duct}}$	Duct domain boundary
$\partial\Omega_{\text{i}}$	Inner domain boundary
$\partial\Omega_{\text{o}}$	Outer domain boundary
ψ_{i}	Acoustic velocity potential in the inner domain
ψ_{o}	Acoustic velocity potential in the outer domain
QoI	Vector of the quantities of interest
ρ	Fluctuating mass density
ρ_0	Steady flow mass density
ρ_∞	Uniform flow mass density
$\tilde{\mathbf{v}}$	Fluid velocity
$\tilde{\rho}$	Fluid mass density
$\tilde{B}$	Fluid stagnation enthalpy
$\tilde{h}$	Fluid enthalpy
$\tilde{p}$	Pressure field
$\tilde{s}$	Fluid entropy
$\tilde{T}$	Fluid temperature field

$\tilde{X}$	Thermodynamic variable, function of space and time
φ	Acoustic velocity potential in the duct domain
$\varphi_\alpha(x, y)$	Eigenfunction of a duct mode α
B	Fluctuating stagnation enthalpy
B_0	Steady flow stagnation enthalpy
c	Speed of sound
c_α	Amplitude of a duct mode α
h	Fluctuating enthalpy
h_0	Steady flow enthalpy
j	Imaginary unit
k_{xy_α}	Transversal wavenumber of a duct mode α
k_{z_α}	Axial wavenumber of a duct mode α
M	Local Mach number
M_∞	Mach number at the infinite (uniform flow)
N_d	Number of cut-on modes
N_f	Number of dofs in the discretized fan surface
N_i	Number of dofs in the discretized inner domain
N_o	Number of dofs in the discretized outer domain
p	Fluctuating pressure field
p_0	Steady flow pressure field
R	Norm of the radial unitary vector $\mathbf{r}$
s	Fluctuating entropy
s_0	Steady flow entropy
$S_f(\mathbf{r}, \omega)$	Acoustic source term induced by then fan rotation
T	Fluctuating temperature field
t	Time scalar variable
T_0	Steady flow temperature field
X	Fluctuating component of a thermodynamic variable
x	Cardinal space coordinate
X_0	Static component of a thermodynamic variable
y	Cardinal space coordinate

z	Cardinal space coordinate
$Z(\mathbf{r}, \omega)$	Liner local impedance
$Z_I(\mathbf{r}, \omega)$	Liner local reactance
$Z_R(\mathbf{r}, \omega)$	Liner local resistance

Chapter 1

Fundamental equations, computational model, and robust design optimization formulation

Contents

1.1 Problem to be solved **20**
1.2 Strategy for solving the problem **20**
1.3 Conventions and notations **21**
1.4 Fundamental equations for fluid dynamics **21**
1.5 Transformations of fundamental equations **22**
1.6 Steady flow computation **23**
1.7 Linearized equations for acoustic propagation in a moving fluid . . **23**
1.8 Boundary value problem for the linearized acoustic propagation . . **27**
1.9 Modeling of the liner (acoustic treatment) **32**
1.10 Weak formulation of the boundary value problem for the linearized acoustic propagation for the inlet case **33**
1.11 Finite/Infinite Elements discretization of the weak formulation of the boundary value problem related to the inlet **34**
1.12 Frequency by frequency static condensation with respect to the liner dofs and expression of the fan acoustic excitation **37**
1.13 Computational reduced-order model using a pellicular projection . **38**
1.14 Defining quantities of interest **41**
1.15 Robust design optimization problem **42**

Abstract: *The problem to be solved is firstly introduced by describing the acoustical system that is considered. The strategy for solving the problem is then presented. The physical/mathematical framework is introduced by presenting the fundamental equations for linearized acoustic propagation in a moving fluid, related to nacelle-noise reduction. The boundary value problem, its weak formulation, and the computational model obtained by finite element and infinite element discretization are presented. A reduced-order computational model is especially constructed, which allows for exhibiting the impedance matrix of the liner and the aeroacoustics that will be randomized in order to take uncertainties into account. The fan excitation model is also presented in order to be adequately randomized as well. Finally, the formulation of the robust design optimization of nacelle noise-reduction technology is given.*

1.1 Problem to be solved

Acoustic liners in both intake and bypass sections of the engine are effective in mitigating noise generated by the fan. In order to be efficient, namely to absorb the fan noise, liners have to be studied in their operating environment. For this purpose, the acoustic problem has to be written so as to model liners acoustical behavior, exposed to the fan acoustical excitation.

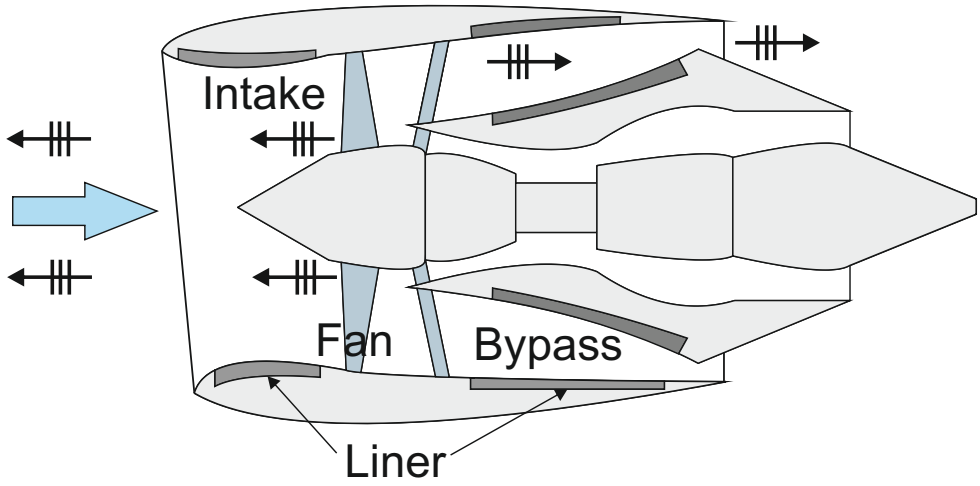

Figure 1.1: Illustration of the mechanical problem

From a physical point of view, the mechanical systems that are generally considered are the lined intake and the lined bypass represented on a schematic view of the nacelle (Fig. 1.1). These two acoustic systems are gathered into one domain called inner domain, separating the unsteady flow (deformed by the plane passage) in the near-field from the uniform flow (coming from the infinite and representing the plane movement through the air) in the far-field. Both systems are acoustically excited by the fan rotation. In the present work, only the intake acoustic system excited by the fan rotation is studied.

1.2 Strategy for solving the problem

The most general approach to aeroacoustic problems consists in solving the compressible Navier-Stokes equations [9] through a direct numerical simulation (DNS) or Large Eddy Simulation (LES) techniques. In this approach, the largest scales are resolved, from large to small (the viscous scale for example). However, because of their numerical cost that grows exponentially when computing propagation problem over long distances, studies are limited to low Reynolds number.
Solving engineering problems thus requires an alternative approach such as the acoustic analogy proposed by Lighthill [30]. Acoustic analogy assumes that noise generation and propagation are decoupled. This implies that flow-generated noise does not impact the flow. The solution is obtained in two steps: a first one computing aerodynamic sources, according to Möhring's [37] analogy, using the Computational Fluid Dynamics (CFD); and a second one propagating the acoustic waves.

As explained above, this work is devoted to the analysis of the acoustic propagation in a moving fluid. The acoustic sources generated by the flow itself are not considered. The reason why is that the noise induced by the flow is negligible with respect to the fan-generated noise.

The inhomogeneous nature of the fluid affects the acoustic wave propagation (convection effect, refraction, etc.) It also produces aerodynamic noise that is not accounted for in this work as explained above. Möhring's comprehension and development of Lighthill's work [37] takes flow inhomogeneities such as vortices and entropy variations into account under the form of flow-induced acoustic sources. He also uses a convected wave operator to represent the propagation in a moving fluid, whereas Lighthill uses the classic Helmholtz wave operator in a steady flow [30].

Since aeroacoustic sources are not taken into account in this work, and since the walls are fixed (no wall displacement), the formulation for the acoustic propagation in a moving fluid could be obtained by using the usual convected Helmholtz equation for which the velocity field of the steady flow is computed by solving the Navier-Stokes equation. Consequently, the acoustic equation could be derived from a direct linearization of the Navier-Stokes equation keeping only the pressure mode (neglecting the entropy and the rotational modes). Nevertheless, since the software development associated with this work is done in the framework of Actran/TM (chosen for its effectiveness in solving industrial convected acoustic problems), that is the general code taking into account acoustic sources, we have used the same formulation with the stagnation enthalpy B. Obviously, the two types of formulation give the same convected Helmholtz equation formulated using the acoustic velocity potential.

1.3 Conventions and notations

Thermodynamic variable $\tilde{X}$ that is a function of space and time, is written as the sum of a static component, corresponding to the local fluid equilibrium, denoted by the subscript X_0, and the corresponding fluctuating component is noted X. Interacting fluctuating quantities can be turbulent associated with viscosity and rotational effects, entropic related to thermal conductivity, and acoustic induced by the fluid compressibility.
The system is studied in a cartesian space defined by the coordinates $(0, x, y, z)$. The space dimension is accounted for under the form of a three-dimensional vector $\mathbf{r} = (x, y, z)$ and the time dimension as a scalar t.
The operator nabla is defined in such a space as $\boldsymbol{\nabla} = \left(\frac{\partial}{\partial x}, \frac{\partial}{\partial y}, \frac{\partial}{\partial z}\right)$.

1.4 Fundamental equations for fluid dynamics

In this section, the fundamental equations for fluid dynamics are presented. From these fundamental equations, specific equations related to steady flow computation and convected acoustic propagation are derived. The fundamental equations can be found in [27] and another presentation reformulated for computational aeroacoustic can be found in [19].

1.4.1 Mass conservation equation

Considering that there is no pulsating acoustic source, which means that no mass is added to the system (right-hand side of the equation is then equal to zero), then the mass conservation equation is written as,

$$\frac{\partial \tilde{\rho}}{\partial t} + \boldsymbol{\nabla} \cdot (\tilde{\rho}\, \tilde{\mathbf{v}}) = 0\,, \tag{1.1}$$

in which $\tilde{\rho}$ is the mass density of the fluid and $\tilde{\mathbf{v}} = (\tilde{v_x}, \tilde{v_y}, \tilde{v_z})$ is the fluid velocity.

1.4.2 Momentum conservation equation

Introducing the second-order stress tensor $[\sigma] = -\tilde{p}[I] + [\tilde{\tau}]$ in which $[\tilde{\tau}]$ is the second-order viscous stress tensor, $\tilde{p}$ is the pressure field, and $[I]$ the second-order identity tensor, the Navier-Stokes equation can be written [19] as,

$$\frac{\partial \tilde{\mathbf{v}}}{\partial t} - \tilde{\mathbf{v}} \times (\boldsymbol{\nabla} \times \tilde{\mathbf{v}}) = -\frac{1}{\tilde{\rho}} \boldsymbol{\nabla} \tilde{p} - \boldsymbol{\nabla} \left(\frac{||\tilde{\mathbf{v}}||^2}{2} \right) + \frac{1}{\tilde{\rho}} \boldsymbol{\nabla} \cdot [\tilde{\tau}] + \mathbf{g} \,, \tag{1.2}$$

in which the vector $\mathbf{g}$ is the external acceleration induced by a gravity field.

1.4.3 Energy conservation equation.

Using Fourier's law, in which κ is the heat conductivity of the fluid,

$$q = -\kappa \, \boldsymbol{\nabla} \tilde{T} \,, \tag{1.3}$$

the energy equation can be written [27] as,

$$\frac{\partial}{\partial t} \left(\frac{1}{2} \tilde{\rho} \, \tilde{\mathbf{v}}^2 + \tilde{\rho} \, \tilde{h} - \tilde{p} \right) = -\boldsymbol{\nabla} \cdot \left(\tilde{\rho} \, \tilde{\mathbf{v}} \left(\frac{\tilde{\mathbf{v}}^2}{2} + \tilde{h} \right) - \tilde{\mathbf{v}} \, [\tilde{\tau}] - \kappa \, \boldsymbol{\nabla} \tilde{T} \right) + \tilde{\rho} \, \tilde{\mathbf{v}} \cdot \mathbf{g} \,, \tag{1.4}$$

where $\tilde{\rho} \, \tilde{\mathbf{v}} \cdot \mathbf{g}$ represents the power of the gravity field, $\tilde{h} = \tilde{\epsilon} + \dfrac{\tilde{p}}{\tilde{\rho}}$ is the fluid enthalpy, and $\tilde{T}$ is the temperature field.

1.5 Transformations of fundamental equations

The system of fundamental equations described in Section 1.4 is transformed in order to obtain a suitable form for solving the acoustic problem.

1.5.1 Transformation of the momentum conservation equation

By introducing the entropy thermodynamic law,

$$d\tilde{h} = \tilde{T} \, d\tilde{s} + \frac{1}{\tilde{\rho}} \, d\tilde{p} \,, \tag{1.5}$$

we can write,

$$\tilde{T} \, \boldsymbol{\nabla} \tilde{s} = \boldsymbol{\nabla} \tilde{h} - \frac{\boldsymbol{\nabla} \tilde{p}}{\tilde{\rho}} \,. \tag{1.6}$$

In addition, introducing the stagnation enthalpy,

$$\tilde{B} = \tilde{h} + \left(\frac{||\tilde{\mathbf{v}}||^2}{2} \right) \,, \tag{1.7}$$

which is the enthalpy that the fluid would reach if it were brought to zero speed by a steady, adiabatic process with no external work. The momentum conservation equation (1.2) can be rewritten as,

$$\tilde{\rho} \left(\frac{\partial \tilde{\mathbf{v}}}{\partial t} + \boldsymbol{\nabla} \tilde{B} \right) = \tilde{\rho} \, \tilde{T} \, \boldsymbol{\nabla} \tilde{s} + \tilde{\rho} \, \tilde{\mathbf{v}} \times (\boldsymbol{\nabla} \times \tilde{\mathbf{v}}) + \boldsymbol{\nabla} [\tilde{\tau}] + \tilde{\rho} \, \mathbf{g} \,. \tag{1.8}$$

1.5.2 Transformation of the energy conservation equation

Using the definition of the stagnation enthalpy $\tilde{B}$ Eq. (1.7) and its convective derivative $\frac{D\tilde{B}}{Dt} = \frac{\partial \tilde{B}}{\partial t} + \tilde{\mathbf{v}} \cdot \boldsymbol{\nabla} \tilde{B}$, such as,

$$\frac{D\tilde{B}}{Dt} = \frac{\partial}{\partial t}\left(\tilde{h} + \frac{||\tilde{\mathbf{v}}||^2}{2}\right) + \tilde{\mathbf{v}} \cdot \boldsymbol{\nabla}\left(\tilde{h} + \frac{||\tilde{\mathbf{v}}||^2}{2}\right), \tag{1.9}$$

the energy conservation equation (1.4) can be written as,

$$\tilde{\rho}\frac{D\tilde{B}}{Dt} - \frac{\partial \tilde{p}}{\partial t} = \boldsymbol{\nabla} \cdot (\tilde{\mathbf{v}}\,[\tilde{\tau}]) + \boldsymbol{\nabla} \cdot \left(\kappa\, \boldsymbol{\nabla} \tilde{T}\right) + \tilde{\rho}\, \tilde{\mathbf{v}}\, \mathbf{g}\,. \tag{1.10}$$

1.6 Steady flow computation

For a problem involving a convected fluid, steady thermodynamic values such as $p_0, \mathbf{v}_0$, and ρ_0, are needed to compute the acoustic propagation. These values are computed using Computational Fluid Dynamics (CFD) for steady flows.
The CFD solver used is based on the compressible Euler equations, which are derived from the Navier-Stokes equations [27], in which the viscous, thermal, and gravity effects are neglected. Euler equations are defined as follows.

The mass conservation equation is written as,

$$\frac{\partial \tilde{\rho}}{\partial t} + \boldsymbol{\nabla} \cdot (\tilde{\rho}\, \tilde{\mathbf{v}}) = 0\,. \tag{1.11}$$

The momentum conservation equation is written as,

$$\frac{\partial \tilde{\mathbf{v}}}{\partial t} - \tilde{\mathbf{v}} \times (\boldsymbol{\nabla} \times \tilde{\mathbf{v}}) = -\frac{1}{\tilde{\rho}}\, \boldsymbol{\nabla} \tilde{p} - \boldsymbol{\nabla}\left(\frac{||\tilde{\mathbf{v}}||^2}{2}\right). \tag{1.12}$$

The energy conservation equation is written as,

$$\frac{\partial}{\partial t}\left(\frac{1}{2}\tilde{\rho}\, \tilde{\mathbf{v}}^2 + \tilde{\rho}\, \tilde{h} - \tilde{p}\right) = -\boldsymbol{\nabla} \cdot \left(\tilde{\rho}\, \tilde{\mathbf{v}}\left(\frac{\tilde{\mathbf{v}}^2}{2} + \tilde{h}\right)\right). \tag{1.13}$$

1.7 Linearized equations for acoustic propagation in a moving fluid

This section presents the derivation of the wave equation, needed to describe the evolution of the stagnation enthalpy throughout the acoustic model. A set of hypotheses is used to describe the acoustic fluid, as it has been made for the flow. These hypotheses are defined hereinafter.

The fluid accounted for is the air assimilated to an ideal gas characterized by a specific mass ratio $\gamma = \frac{C_p}{C_v} = 1.4$. The boundary layer formed on the wall due to viscous effects is not accounted for. It should be noted that such an assumption can be made in the case where the pressure fluctuations induced by the boundary layer are small compared to the acoustic pressure fluctuations induced by the fan rotation [29].

It is known that a major problem in aeroacoustic is that the equations are nonlinear (as noted by Rienstra and Hirschberg in [20]). This implies that an exact general solution of these equations

is not available. Acoustics is a first-order approximation (linear approximation) assuming that the acoustic perturbations are small compared to the mean flow quantities. This means that $p \ll p_0$, $\rho \ll \rho_0$, $\|\mathbf{v}\| \ll \|\mathbf{v}_0\|$, $T \ll T_0$, and $s \ll s_0$, in which p_0, ρ_0, $\mathbf{v}_0$, T_0, and s_0 correspond to the steady flow values, where p, ρ, $\mathbf{v}$, T, and s are small fluctuations. This leads to neglect second-order terms and beyond (non linear effects). Nevertheless, in [29], Lidoine explains that this assumption is only valid for acoustic fields of intensity inferior to 140 dB. For higher intensity level, the nonlinear effects cannot be neglected. All sources taken into account are therefore supposed to respect this limitation.

1.7.1 Convected wave equation

In order to write the convected wave equation describing the pressure behavior using the stagnation enthalpy $\tilde{B}$ as variable, a set of hypotheses is introduced as follows.

- No aerodynamic acoustic source terms are considered in the domain. The acoustic system is only excited by the fan rotation (boundary condition).
- No heat production due to viscous dissipation occurs in the flow.
- The system is considered adiabatic, no heat transfer occurs in the flow.
- Gravity forces are neglected.
- The flow is locally isentropic (entropy can vary in space but not in time)

Following the above hypotheses (neglecting viscous stresses, heat conduction, and gravity), Eq. (1.10) yields the relation between pressure and stagnation enthalpy,

$$\frac{D\tilde{B}}{Dt} = \frac{1}{\tilde{\rho}} \frac{\partial \tilde{p}}{\partial t} \,. \tag{1.14}$$

Moreover, Eq. (1.8) is simplified as,

$$\tilde{\rho} \left(\frac{\partial \tilde{\mathbf{v}}}{\partial t} + \boldsymbol{\nabla} \tilde{B} \right) = \tilde{\rho}\, \tilde{\mathbf{v}} \times (\boldsymbol{\nabla} \times \tilde{\mathbf{v}}) + \tilde{\rho}\, \tilde{T}\, \boldsymbol{\nabla} \tilde{s} \,. \tag{1.15}$$

We introduce the time variations of the fluid density related to entropy variation,

$$\frac{\partial \tilde{\rho}}{\partial t} = \left(\frac{\partial \tilde{\rho}}{\partial \tilde{p}} \right)_{\tilde{s}} \frac{\partial \tilde{p}}{\partial t} + \left(\frac{\partial \tilde{\rho}}{\partial \tilde{s}} \right)_{\tilde{p}} \frac{\partial \tilde{s}}{\partial t} \,, \tag{1.16}$$

and the speed of sound definition c,

$$c^2 = \left(\frac{\partial \tilde{p}}{\partial \tilde{\rho}} \right)_{\tilde{s}} \,. \tag{1.17}$$

Using Eqs. (1.14) and (1.17), Eq. (1.16) yields an equation between stagnation enthalpy $\tilde{B}$ and density $\tilde{\rho}$,

$$\frac{\partial \tilde{\rho}}{\partial t} = \frac{\tilde{\rho}}{c^2} \frac{D\tilde{B}}{Dt} + \frac{\partial \tilde{\rho}}{\partial \tilde{s}} \frac{\partial \tilde{s}}{\partial t} \,. \tag{1.18}$$

Using Eq. (1.18) and using the following identity,

$$\frac{\partial (\tilde{\rho}\, \tilde{\mathbf{v}})}{\partial t} = \tilde{\rho} \frac{\partial \tilde{\mathbf{v}}}{\partial t} + \tilde{\mathbf{v}} \frac{\partial \tilde{\rho}}{\partial t} \,, \tag{1.19}$$

the term $\tilde{\rho} \dfrac{\partial \tilde{\mathbf{v}}}{\partial t}$ can be replaced by $\dfrac{\partial (\tilde{\rho}\, \tilde{\mathbf{v}})}{\partial t} - \tilde{\mathbf{v}} \dfrac{\partial \tilde{\rho}}{\partial t}$ in Eq. (1.15) as follows,

$$\frac{\partial(\tilde{\rho}\tilde{\mathbf{v}})}{\partial t} - \frac{\tilde{\rho}\,\tilde{\mathbf{v}}}{c^2}\frac{D\tilde{B}}{Dt} - \frac{\partial\tilde{\rho}}{\partial\tilde{s}}\,\tilde{\mathbf{v}}\,\frac{\partial\tilde{s}}{\partial t} = \tilde{\rho}\,\tilde{\mathbf{v}}\times(\boldsymbol{\nabla}\times\tilde{\mathbf{v}}) + \tilde{\rho}\,\tilde{T}\,\boldsymbol{\nabla}\tilde{s}\,. \tag{1.20}$$

By taking the difference between the divergence of Eq. (1.20) and the time derivative of Eq. (1.1), the wave equation can be written as,

$$\frac{\partial}{\partial t}\left(\frac{\tilde{\rho}}{c^2}\frac{D\tilde{B}}{Dt}\right) + \boldsymbol{\nabla}\cdot\left(\frac{\tilde{\rho}\,\tilde{\mathbf{v}}}{c^2}\frac{D\tilde{B}}{Dt} - \tilde{\rho}\boldsymbol{\nabla}\tilde{B}\right) = \tilde{R}\,, \tag{1.21}$$

with $\tilde{R}$ gathering all aerodynamic source terms (entropy and vorticity sources),

$$\tilde{R} = -\boldsymbol{\nabla}\cdot(\tilde{\rho}\,\tilde{\mathbf{v}}\times(\boldsymbol{\nabla}\times\tilde{\mathbf{v}})) - \boldsymbol{\nabla}\cdot\left(\frac{\partial\tilde{\rho}}{\partial\tilde{s}}\,\tilde{\mathbf{v}}\,\frac{\partial\tilde{s}}{\partial t} + \tilde{\rho}\,\tilde{T}\,\boldsymbol{\nabla}\tilde{s}\right) - \frac{\partial}{\partial t}\left(\frac{\partial\tilde{\rho}}{\partial\tilde{s}}\frac{\partial\tilde{s}}{\partial t}\right)\,, \tag{1.22}$$

Eq. (1.21) and Eq. (1.22) are then rewritten following Möhring [37], based on Howe [4, 21] for a high Reynolds and homentropic flow (the second and third terms in Eq. (1.22) are then neglected since the entropy is constant), as,

$$\frac{D}{Dt}\left(\frac{1}{c^2}\frac{D\tilde{B}}{Dt}\right) - \frac{1}{\tilde{\rho}}\boldsymbol{\nabla}\cdot(\tilde{\rho}\boldsymbol{\nabla}\tilde{B}) = \frac{1}{\tilde{\rho}}\boldsymbol{\nabla}\cdot(\tilde{\rho}\mathbf{v}\times(\boldsymbol{\nabla}\times\mathbf{v})\,, \tag{1.23}$$

in which the right-hand side is 0, assuming that vorticity terms are neglected while using a duct modal expansion for the acoustic excitation as explained in Section 1.8.2.1.

1.7.2 Linearization of the convected wave equation

The unsteady flow is linearized around the steady flow whose fields notations are indexed by 0 (as introduced in Section 1.6). Consequently, we write,

$$\begin{cases} \tilde{p}(\mathbf{r},t) = p_0(\mathbf{r}) + p(\mathbf{r},t) \text{ the pressure,} \\ \tilde{\rho}(\mathbf{r},t) = \rho_0(\mathbf{r}) + \rho(\mathbf{r},t) \text{ the density,} \\ \tilde{\mathbf{v}}(\mathbf{r},t) = \mathbf{v}_0(\mathbf{r}) + \mathbf{v}(\mathbf{r},t) \text{ the vectorial velocity,} \\ \tilde{T}(\mathbf{r},t) = T_0(\mathbf{r}) + T(\mathbf{r},t) \text{ the temperature,} \\ \tilde{s}(\mathbf{r},t) = s_0(\mathbf{r}) + s(\mathbf{r},t) \text{ the entropy,} \\ \tilde{B}(\mathbf{r},t) = B_0(\mathbf{r}) + B(\mathbf{r},t) \text{ the stagnation enthalpy.} \end{cases} \tag{1.24}$$

For writing simplicity, spatial and temporal dependencies are omitted hereafter.

Since the flow is homentropic, the gradient of B_0 is always perpendicular to $\mathbf{v}_0$ as,

$$\boldsymbol{\nabla}B_0 = \mathbf{v}_0\times(\boldsymbol{\nabla}\times\mathbf{v}_0)\,, \tag{1.25}$$

which imposes $\mathbf{v}_0\cdot\boldsymbol{\nabla}B_0 = 0$. Neglecting $\tilde{R}$, using $\mathbf{v}_0\cdot\boldsymbol{\nabla}B_0 = 0$, and $\dfrac{\partial B_0}{\partial t} = 0$, the linearization of Eq. (1.23) around ρ_0, B_0 and $\mathbf{v}_0$ yields,

$$\frac{\partial}{\partial t}\left[\frac{\rho_0}{c^2}\left(\frac{\partial B}{\partial t}+\mathbf{v}_0\cdot\boldsymbol{\nabla}B+\mathbf{v}\cdot\boldsymbol{\nabla}B_0\right)\right]+\boldsymbol{\nabla}\cdot\left[\frac{\rho_0\,\mathbf{v}_0}{c^2}\left(\frac{\partial B}{\partial t}+\mathbf{v}_0\cdot\boldsymbol{\nabla}B+\mathbf{v}\cdot\boldsymbol{\nabla}B_0\right)-\rho_0\boldsymbol{\nabla}B\right]=0\,. \tag{1.26}$$

Rearranging Eq. (1.26), the linearized convective derivative $\dfrac{D_0}{Dt}=\dfrac{\partial}{\partial t}+\mathbf{v}_0\cdot\boldsymbol{\nabla}$ appears as follows,

$$\frac{\partial}{\partial t}\left[\frac{\rho_0}{c^2}\left(\frac{\partial B}{\partial t}+\mathbf{v}_0\cdot\boldsymbol{\nabla}B\right)\right]+\boldsymbol{\nabla}\cdot\left[\frac{\rho_0\,\mathbf{v}_0}{c^2}\left(\frac{\partial B}{\partial t}+\mathbf{v}_0\cdot\boldsymbol{\nabla}B\right)-\rho_0\boldsymbol{\nabla}B\right]= -\frac{\rho_0}{c^2}\frac{\partial}{\partial t}\left(\mathbf{v}\cdot\boldsymbol{\nabla}B_0\right)-\frac{\rho_0\,\mathbf{v}_0}{c^2}\boldsymbol{\nabla}\cdot\left(\mathbf{v}\cdot\boldsymbol{\nabla}B_0\right)\,. \tag{1.27}$$

Since vorticity and entropy aeroacoustic source terms are neglected, as previously mentioned, the vorticity terms in Eq. (1.27) are neglected ($\boldsymbol{\nabla}B_0$ is then zero) such as,

$$\frac{\partial}{\partial t}\left(\frac{\rho_0}{c^2}\frac{D_0B}{Dt}\right)+\boldsymbol{\nabla}\cdot\left(\frac{\rho_0\,\mathbf{v}_0}{c^2}\frac{D_0B}{Dt}-\rho_0\boldsymbol{\nabla}B\right)=0\,, \tag{1.28}$$

which corresponds to the partial linearization explained in [28, 15], and which can be rewritten using Möhring's [37] and Howe's [4, 21] formulations as,

$$\frac{D_0}{Dt}\left(\frac{1}{c^2}\frac{D_0}{Dt}\right)B-\frac{1}{\rho_0}\boldsymbol{\nabla}\cdot(\rho_0\boldsymbol{\nabla}B)=0\,. \tag{1.29}$$

The linearization of Eq.(1.14) yields

$$\rho_0\frac{D_0B}{Dt}=\frac{\partial p}{\partial t}\,. \tag{1.30}$$

1.7.2.1 Frequency formulation of the convected wave equation

In this work, the following convention of Fourier transform with respect to time t and to space $\mathbf{r}$ is the following,

$$q(\mathbf{r},\omega)=\int_{\mathbb{R}}q(\mathbf{r},t)e^{-j\omega t}dt\quad,\quad q(\mathbf{k},\omega)=\int_{\mathbb{R}^3}\int_{\mathbb{R}}q(\mathbf{r},t)e^{-j\omega t+j\mathbf{k}\cdot\mathbf{r}}d\mathbf{r}\,dt\,, \tag{1.31}$$

in which $j=\sqrt{-1}$. For simplifying the writing, we use the same notation for q and for its Fourier transform (no confusion is possible).

The harmonic convention associated with this Fourier transform convention is thus, $q_0e^{j\omega t-j\mathbf{k}\cdot\mathbf{r}}$ with ω in rad/s.

By taking the Fourier transform of Eq. (1.28) with respect to time t yields,

$$-\frac{\omega^2\rho_0}{c^2}B+\frac{j\omega\,\rho_0}{c^2}\mathbf{v}_0\cdot\boldsymbol{\nabla}B+\boldsymbol{\nabla}\cdot\left(\frac{j\omega\rho_0\mathbf{v}_0}{c^2}B+\frac{\rho_0\,\mathbf{v}_0}{c^2}\mathbf{v}_0\cdot\boldsymbol{\nabla}B-\rho_0\boldsymbol{\nabla}B\right)=0\,. \tag{1.32}$$

Taking the Fourier transformation of Eq. (1.30) with respect to t yields the equation that allows for retrieving the pressure,

$$j\omega p=\rho_0(j\omega B+\mathbf{v}_0\cdot\boldsymbol{\nabla}B)\,. \tag{1.33}$$

1.8 Boundary value problem for the linearized acoustic propagation

The linearized convected wave equation defined by Eq. (1.32) is quite general. For a given acoustic problem, the boundary conditions associated with Eq. (1.32) must be defined in order to obtain a well-posed boundary value problem. For general geometry, this boundary value problem cannot exactly be solved, and must be solved using numerical methods. For this purpose, the weak formulation of the boundary value problem is constructed. This weak formulation allows for introducing the boundary conditions. Then, the finite element method and the boundary element method are used. The formulation of both methods lays on a specific formulation, presented in the following section.

Definition of the acoustic problem geometry .

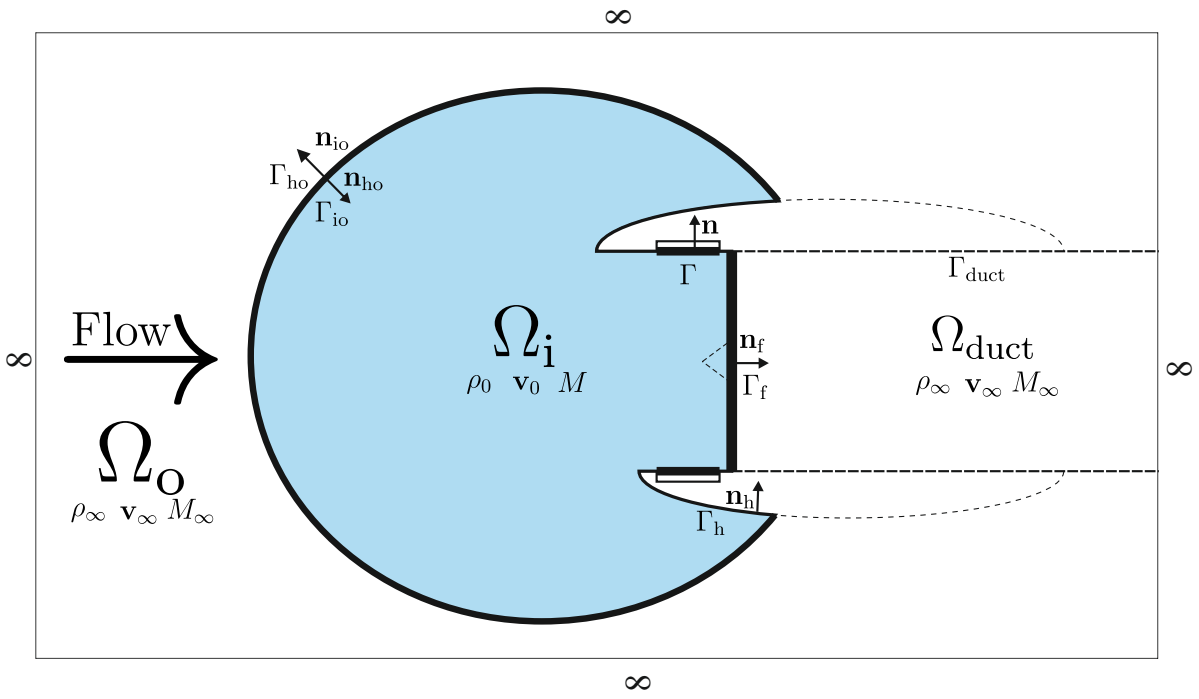

Figure 1.2: Inlet acoustic problem

Figure 1.2 presents the geometry of the inlet acoustic problem, in which $\mathbb{R}^3$ is the whole domain, Ω_i is the inner bounded open domain of $\mathbb{R}^3$ of boundary $\partial\Omega_i = \Gamma_{io} \cup \Gamma_h \cup \Gamma \cup \Gamma_f$, and $\Omega_o = \mathbb{R}^3 \backslash \overline{\Omega}_i$ is the outer unbounded open domain of $\mathbb{R}^3$, whose boundary $\partial\Omega_o$.

Definition of the geometry and boundary conditions for inner domain Ω_i. The unit normal to boundary $\partial\Omega_i$ outward of domain Ω_i is written $\mathbf{n}_{io}$ for the part Γ_{io}, $\mathbf{n}_h$ for the part Γ_h, $\mathbf{n}$ for the part Γ, and $\mathbf{n}_f$ for the part Γ_f. Part Γ of the boundary $\partial\Omega_o = \partial\Omega_i$ is the coupling interface between the acoustic part Ω_i and the liner, while Γ_f is the part on which the fan excitation is applied. The inner problem implies the use of the following boundary conditions,

- Γ_{io} (inner outer) represents a nonphysical interface between inner and outer domains, on which the continuity condition is written for the acoustic velocity potential and for its gradient.
- Γ_h (hardwall) corresponds to rigid or "hardwall" part characterized by a zero normal acoustic velocity.

- Γ (liner) corresponds to acoustic treatments characterized by their impedance.
- Γ_f (fan) corresponds to the part of the boundary on which act acoustic sources induced by the fan.

Definition of the geometry and boundary conditions for outer domain Ω_o. The boundary $\partial\Omega_o$ of Ω_o is written as $\Gamma_{io} \cup \Gamma_{ho}$ in which $\Gamma_{ho} = \Gamma_h \cup \Gamma \cup \Gamma_f$ (this means that $\partial\Omega_o = \partial\Omega_i$). The unit normal to boundary $\partial\Omega_o$ outward of domain Ω_o is written as, $\mathbf{n}_{oi} = -\mathbf{n}_{io}$ for the part Γ_{io} and $\mathbf{n}_{ho}$ for the part Γ_{ho}. For the acoustic wave propagation in the outer domain, Γ_{ho} corresponds to a rigid wall on which the normal acoustic velocity will be equal to zero.
The outer problem implies the use of the following boundary conditions,

- Γ_{io} (inner outer) is a nonphysical coupling interface between inner and outer domains, on which the continuity is written for the acoustic velocity potential and for its gradient (note that infinite boundary elements will be used on Γ_{io} for accounting for the effects of Ω_o on Ω_i through the coupling interface Γ_{io})).
- Γ_{ho} (hardwall outer) corresponds to a rigid wall characterized by a zero normal acoustic velocity.

Definition of the geometry and boundary conditions for the semi-infinite duct Ω_{duct}. A semi-infinite cylindrical duct Ω_{duct} is connected to the inner domain Ω_i (the subscript i refers to the inner domain) for which the coupling interface is the fan plane Γ_f. The boundary $\partial\Omega_{duct}$ of semi-infinite domain Ω_{duct} is written as $\partial\Omega_{duct} = \Gamma_f \cup \Gamma_{duct}$ in which Γ_{duct} is the cylindrical-surface part of the boundary of Ω_{duct}. It should be noted that this domain is only introduced for generating the acoustic excitation induced by the fan and consequently, has to be viewed as a "fictional domain" with respect to the formulation of the boundary value problem related to $\overline{\Omega_i \cup \Omega_o}$. This is the reason why $\Omega_o = \mathbb{R}^3 \backslash \overline{\Omega}_i$. In this semi-infinite duct, the sound field is the sum of a given incident sound field (represented by symbol +) and an unknown reflected sound field (represented by symbol -), which will be represented (projected) on the duct modes (see Section 1.8.1.3). The wall of the boundary of Ω_{duct} is rigid on which a zero normal acoustic velocity is applied.

1.8.1 Boundary value problem in the inner domain for the inlet case

1.8.1.1 Convected Helmhlotz equation in Ω_i

Introducing the function $\psi_i = \dfrac{-B}{j\omega}$, the linearized frequency formulation of the convected wave equation defined by Eq. (1.32) can be written in Ω_i as,

$$-\frac{\omega^2\rho_0}{c^2}\psi_i + \frac{j\omega\rho_0}{c^2}\mathbf{v}_0\cdot\boldsymbol{\nabla}\psi_i + \boldsymbol{\nabla}\cdot\left(\frac{j\omega\rho_0\mathbf{v}_0}{c^2}\psi_i + \frac{\rho_0\mathbf{v}_0}{c^2}\mathbf{v}_0\cdot\boldsymbol{\nabla}\psi_i - \rho_0\boldsymbol{\nabla}\psi_i\right) = 0\,. \tag{1.34}$$

1.8.1.2 Pressure and acoustic velocity in Ω_i

The pressure is given by Eq. (1.33) that is written as,

$$p = -j\omega\rho_0\,\psi_i - \rho_0\mathbf{v}_0\cdot\boldsymbol{\nabla}\psi_i\,. \tag{1.35}$$

The acoustic velocity in Ω_i is derived as follows. For the linearized acoustic problem, Eq. (1.8) yields ($\boldsymbol{\nabla}B_0 = 0$ neglecting vorticity forces as in Eq. (1.27)),

$$\frac{\partial \mathbf{v}}{\partial t} + \boldsymbol{\nabla} B = 0\,. \tag{1.36}$$

Taking the Fourier transformation and taking $B = -j\omega\psi_\mathrm{i}$, we obtain,

$$\mathbf{v} = \boldsymbol{\nabla}\psi_\mathrm{i}\,. \tag{1.37}$$

1.8.1.3 Boundary conditions on $\partial\Omega_\mathbf{i} = \Gamma_\mathbf{io} \cup \Gamma_\mathbf{h} \cup \Gamma \cup \Gamma_\mathbf{f}$

Boundary condition on $\Gamma_\mathbf{io}$. The continuity of the acoustic velocity potential and of its gradient is written on Γ_io,

$$\psi_\mathrm{i} = \psi_\mathrm{o} \quad , \quad \boldsymbol{\nabla}\psi_\mathrm{i} = \boldsymbol{\nabla}\psi_\mathrm{o}\,, \tag{1.38}$$

in which ψ_o is the acoustic velocity potential in the outer domain Ω_o (see section 1.8.3).

Boundary condition on $\Gamma_\mathbf{h}$. Boundary Γ_h is a rigid wall, called "hardwall", and consequently, the boundary condition on Γ_h is written as,

$$\frac{\partial \psi_\mathrm{i}}{\partial \mathbf{n}_\mathrm{h}} = 0\,. \tag{1.39}$$

Boundary condition on Γ. Acoustic treatment or liner is characterized by its acoustic absorption. The absorption value of a liner depends on the material properties, which is modeled by its local impedance. A continuity of the normal acoustic velocity $\mathbf{v}_\Gamma \cdot \mathbf{n}$ of the wall and the acoustic fluid is implied. The impedance characterizes the liner, which relates the acoustic pressure p to the normal acoustic velocity $\mathbf{v}_\Gamma \cdot \mathbf{n}$ by the following equation (see Section 1.9),

$$p(\mathbf{r},\omega) = Z(\mathbf{r},\omega)\,\mathbf{v}_\Gamma(\mathbf{r},\omega)\cdot\mathbf{n}(\mathbf{r})\,. \tag{1.40}$$

In presence of a flow, the behavior of a liner is given by the Myers boundary condition [38]. At the interface between the liner and the acoustic moving fluid (assumed inviscid and isentropic), which is assimilated to an acoustic diopter, Myers considers in his paper the continuity of normal Eulerian displacements. In [29], Lidoine starts from the continuity of Lagrangian normal displacements, citing Poirée's work, which gives a better physical representation of the problem than the Eulerian representation. Using a mixed representation that allows for writing the Lagrangian displacements as a function of the Eulerian coordinates linked to the flow, the equation between $\mathbf{v}\cdot\mathbf{n}$ and $\mathbf{v}_\Gamma\cdot\mathbf{n}$ is written as,

$$\mathbf{v}\cdot\mathbf{n} = \left(-1 + \frac{1}{j\omega}\mathbf{v}_0\cdot\boldsymbol{\nabla} - \frac{1}{j\omega}\mathbf{n}\cdot(\mathbf{n}\cdot\boldsymbol{\nabla})\mathbf{v}_0\right)(\mathbf{v}_\Gamma\cdot\mathbf{n})\,, \tag{1.41}$$

in which $\mathbf{v}_\Gamma\cdot\mathbf{n}$ represents the normal acoustic velocity of the surface Γ assimilated to the liner. From Eqs. (1.35), (1.37), (1.40), and (1.41), it can be deduced that

$$\frac{\partial \psi_i}{\partial \mathbf{n}} = \left(1 - \frac{1}{j\omega}\mathbf{v}_0\cdot\boldsymbol{\nabla} + \frac{1}{j\omega}\mathbf{n}\cdot(\mathbf{n}\cdot\boldsymbol{\nabla})\mathbf{v}_0\right)\frac{1}{Z}(j\omega\rho_0\psi_\mathrm{i} + \rho_0\mathbf{v}_0\cdot\boldsymbol{\nabla}\psi_\mathrm{i})\,, \tag{1.42}$$

in which $\dfrac{1}{Z}$ denotes the local admittance at point $\mathbf{r}$ and at frequency ω of the liner.
The local impedance $Z(\mathbf{r},\omega)$ can be written as

$$Z(\mathbf{r},\omega) = Z_R(\mathbf{r},\omega) + jZ_I(\mathbf{r},\omega)\,, \tag{1.43}$$

in which the real part $Z_R(\mathbf{r},\omega)$ is a resistance that is positive and where $Z_I(\mathbf{r},\omega)$ can have any sign.

Boundary condition on $\Gamma_{\mathbf{f}}$ expressed in terms of the acoustic velocity potential in $\Omega_{\mathbf{duct}}$. The boundary condition on Γ_{f} will be taken into account in the weak formulation of the boundary value problem in the inner domain Ω_{i} (see Eq. (1.62) and Eq. (1.63)) by specifying the value of ψ_{i} and $\boldsymbol{\nabla}\psi_{\mathrm{i}}$ such that,

$$\psi_{\mathrm{i}} = \varphi \quad , \quad \boldsymbol{\nabla}\psi_{\mathrm{i}} = \boldsymbol{\nabla}\varphi \, , \tag{1.44}$$

in which φ is the acoustic velocity potential in the semi-infinite duct represented by the "fictional" domain Ω_{duct}, which will have to satisfy the boundary value problem in Ω_{duct}, which is detailed in Section 1.8.2. This acoustic velocity field will be represented on duct modes.

1.8.2 Boundary value problem in the semi-infinite duct for the inlet case and duct modes

The fan excitation and the coupling condition on Γ_f will be represented on a family of acoustic duct modes (see for instance [45] and [20]). The acoustic velocity field in Ω_{duct} will be projected on the family of acoustic duct modes and will allow (i) for ensuring the coupling between the semi-infinite duct Ω_{duct} (see Fig. 1.2) and the inner domain Ω_{i} on boundary Γ_f, and (ii) for representing the acoustic excitation produced by the fan. It should be noted that the duct modes are explicitly known for a simple cross-section of the duct such as a circle, an annular cross-section or a rectangle, and can be computed for a nonsimple geometry of the cross-section.

In this work, it is assumed that Ω_{duct} is a straight cylinder with z-axis, for which its cross-section is constant and consequently, independent of z.

1.8.2.1 Boundary value problem in $\Omega_{\mathbf{duct}}$

In cartesian coordinates (x, y, z), the acoustic velocity field $\varphi(x, y, z)$ for the acoustic propagation in z-direction of the semi-infinite straight duct Ω_{duct} of axis z with a constant cross-section, in which the steady flow is assumed to be subsonic and uniform along the z-direction, verifies the following convected Helmholtz equation,

$$\Delta_{xy}\varphi + (1 - M^2)\frac{\partial^2 \varphi}{\partial z^2} - 2jkM\frac{\partial \varphi}{\partial z} + k^2\varphi = 0 \quad \text{in} \quad \Omega_{\mathrm{duct}} \, , \tag{1.45}$$

where Δ_{xy} is the Laplacian in the transversal plane (x, y), $M = ||\mathbf{v}_\infty||/c$ is the Mach number associated to the steady flow, $k = \omega/c$ is the wave number, and φ is the potential of the acoustic velocity field. The boundary condition on Γ_{duct} consists in writing that the normal derivative of the acoustic velocity potential is zero, that is to say,

$$\frac{\partial \varphi}{\partial \mathbf{n}_{\mathrm{duct}}} = 0 \quad \text{on} \quad \Gamma_{\mathrm{duct}} \, , \tag{1.46}$$

where $\mathbf{n}_{\mathrm{duct}}$ is the external unit normal to $\partial\Omega_{\mathrm{duct}}$. In addition, the continuity of the acoustic velocity potential φ with the acoustic velocity potential ψ_{i} is written on the interface Γ_f,

$$\varphi = \psi_{\mathrm{i}} \quad \text{on} \quad \Gamma_f \, . \tag{1.47}$$

1.8.2.2 Duct modes and modal representation of the acoustic velocity field.

Let $\mathcal{S}_{\mathrm{duct}} \in \mathbb{R}^2$ be the constant cross-section (independent of z) of the straight cylindrical duct Ω_{duct}. The solution of the boundary value problem defined in Section 1.8.2.1 can be written as,

$$\varphi(x, y, z) = \sum_{\alpha=1}^{\infty} c_\alpha \varphi_\alpha(x, y) \, e^{jk_{z_\alpha} z} \, , \tag{1.48}$$

in which $(x, y) \mapsto \varphi_\alpha(x, y)$ is defined in $\mathcal{S}_{\text{duct}}$, where k_{z_α} is the axial wavenumber of the duct mode α (note that we have used the opposite of the harmonic wave convention previously introduced, it is $+jk_{z_\alpha}z$ and not $-jk_{z_\alpha}z$). Substituting Eq. (1.48) into Eq. (1.45), it can be seen that φ_α has to verify the following wave equation in cross-section, which is written as [49],

$$\Delta_{xy}\,\varphi_\alpha(x,y) + k_{xy_\alpha}^2\,\varphi_\alpha(x,y) = 0 \quad \text{in} \quad \mathcal{S}_{\text{duct}}\,. \tag{1.49}$$

The family of real-valued eigenfunctions $\{\varphi_\alpha\}_\alpha$ that is obtained by solving the above eigenvalue problem in cross-section are orthonormal and are normalized such that,

$$\int_{\mathcal{S}_{\text{duct}}} \varphi_\alpha\,\varphi_\beta\,d\mathcal{S}_{\text{duct}} = \delta_{\alpha\beta}\,, \tag{1.50}$$

for α and β in $\{1, 2, \ldots\}$ and where $\delta_{\alpha\beta}$ is the Kronecker symbol. The transversal wavenumber k_{xy_α} of a given duct mode α is related to the axial wavenumber k_{z_α} by the two following equations,

$$k_{z_\alpha} = \frac{kM \pm \sqrt{k^2 - B^2 k_{xy_\alpha}^2}}{B^2}\,, \tag{1.51}$$

in which $B = \sqrt{1 - M^2}$ and where $k = \omega/c_0$ is the acoustic wavenumber. The axial wavenumber k_{z_α} of a given mode α can be real (propagative mode) or imaginary (evanescent mode).

1.8.2.3 Modal representation for the acoustic excitation by the fan and the reflected sound field

The acoustic velocity field φ defined by Eq. (1.48) is rewritten by keeping only a finite number N_d of duct modes and by showing the contribution of the given incident sound field (represented by symbol + and representing the acoustic excitation induced by the fan) and the contribution of the unknown associated reflected sound field (represented by symbol -). From Eqs. (1.48) and (1.51), function $\varphi(x, y, z)$ can be written as,

$$\varphi(x,y,z) = \sum_{\alpha=1}^{N_d} \varphi_\alpha(x,y)\left[c_\alpha^+ e^{jk_{z_\alpha}^+ z} + c_\alpha^- e^{jk_{z_\alpha}^- z}\right]\,, \tag{1.52}$$

in which $k_{z_\alpha}^+$ is the axial wavenumber of the wave propagating in the upstream direction and $k_{z_\alpha}^-$ is the axial wavenumber of the wave propagating in the downstream direction, which are expressed using Eq. (1.51) as,

$$k_{z_\alpha}^\pm = \frac{kM \pm \gamma_\alpha}{B^2}\,, \tag{1.53}$$

where $\gamma_\alpha = \sqrt{k^2 - B^2 k_{xy_\alpha}^2}$ can be expressed in terms of $k_{z_\alpha}^-$ and $k_{z_\alpha}^+$ as,

$$\gamma_\alpha = \pm(k_{z_\alpha}^\pm B^2 - kM)\,, \tag{1.54}$$

For more details, see Appendix B.

It should be noted that the acoustic excitation by the fan, which is associated with the incident sound field, will be defined by giving the vector $\mathbf{c}^+ = (c_1^+, \ldots, c_{N_d}^+)$, while the unknown reflected sound field depends on the vector $\mathbf{c}^- = (c_1^-, \ldots, c_{N_d}^-)$ should be included with all the unknown fields of the acoustic problem. Note that it is not a requirement to have as many constrained modes as reflected modes. Also, the connection with the acoustic domain may induce reflected modes in the duct that have wavelengths different from the injected modes.

1.8.3 Boundary value problem in the outer domain for the inlet case

1.8.3.1 Convected Helmholtz equation in Ω_o

Similarly to Eq. (1.34), the convected Helmholtz equation in Ω_o (the subscript o refers to the outer domain) is written as,

$$-\frac{\omega^2\rho_\infty}{c^2}\psi_o+\frac{j\omega\rho_\infty}{c^2}\mathbf{v}_\infty\cdot\boldsymbol{\nabla}\psi_o+\boldsymbol{\nabla}\cdot\left(\frac{j\omega\rho_\infty\mathbf{v}_\infty}{c^2}\psi_o+\frac{\rho_\infty\mathbf{v}_\infty}{c^2}\mathbf{v}_\infty\cdot\boldsymbol{\nabla}\psi_o-\rho_\infty\boldsymbol{\nabla}\psi_o\right)=0\,, \quad (1.55)$$

in which ρ_∞ and $\mathbf{v}_\infty$ are the constant density and the constant velocity field corresponding to the uniform inflow condition for the steady flow.

1.8.3.2 Boundary conditions on $\partial\Omega_o = \Gamma_{io}$

Boundary condition on Γ_{io}. On Γ_{io}, the boundary condition writes,

$$\psi_o=\psi_i \quad , \quad \boldsymbol{\nabla}\psi_o=\boldsymbol{\nabla}\psi_i\,, \quad (1.56)$$

in which ψ_i is calculated by solving the boundary value problem in the inner domain Ω_i (see section 1.8.1) and where $\dfrac{\partial\psi_o}{\partial\mathbf{n}_{oi}}=\boldsymbol{\nabla}\psi_i\cdot\mathbf{n}_{oi}$ with $\mathbf{n}_{oi}=-\mathbf{n}_{io}$ in which $\mathbf{n}_{oi}$ is the unit normal to boundary $\partial\Omega_o$ outward of domain Ω_o.

Boundary condition on Γ_{ho}. For the acoustic propagation in the outer domain, Γ_{ho} is considered as a rigid wall, and consequently, the boundary condition is written as,

$$\frac{\partial\psi_o}{\partial\mathbf{n}_{oi}}=0\,. \quad (1.57)$$

Boundary condition at infinity. On this boundary there is the outward Sommerfeld radiation condition at infinity, which is written as,

$$\lim_{R\to+\infty}\left[\frac{\partial\psi_o}{\partial R}+j\frac{\omega}{c}\psi_o+M_\infty\frac{\partial\psi_o}{\partial R}\right]=0\,, \quad (1.58)$$

with $R=||\mathbf{r}||$, where $\dfrac{\partial}{\partial R}$ denotes the derivative in the radial direction from the origin, and $M_\infty=\dfrac{||\mathbf{v}_\infty||}{c}$.

1.9 Modeling of the liner (acoustic treatment)

As explained in Section 1.8.1.3, the effects of the liner on the acoustic propagation are modeled by a local impedance. This local impedance is a complex number defined at a given point $\mathbf{r}=(x,y,z)$ belonging to surface Γ, and at a given frequency ω, by a relation linking acoustic pressure $p(\mathbf{r},\omega)$ and the acoustic normal velocity of surface Γ $\mathbf{v}_\Gamma(\mathbf{r},\omega)\cdot\mathbf{n}(\mathbf{r})$, such that,

$$p(\mathbf{r},\omega)=Z(\mathbf{r},\omega)\,\mathbf{v}_\Gamma(\mathbf{r},\omega)\cdot\mathbf{n}_\Gamma(\mathbf{r})\,. \quad (1.59)$$

The modeling of the liner and the associated design parameters are presented and detailed in Appendix C.

1.10 Weak formulation of the boundary value problem for the linearized acoustic propagation for the inlet case

1.10.1 Weak formulation of the boundary value problem in the inner domain

The weak formulation of the boundary value problem defined by Eqs. (1.34), (1.38), (1.39), (1.42), and (1.44), relative to the inner domain for the inlet case, is written, for all $\delta\psi_{\rm i}$ in the admissible space of sufficiently regular real-valued functions defined on $\Omega_{\rm i}$, as,

$$\int_{\Omega_{\rm i}} \delta\psi_{\rm i} \left(\frac{-\omega^2\rho_0}{c^2}\psi_{\rm i} + \frac{j\omega\rho_0}{c^2}\mathbf{v}_0\cdot\boldsymbol{\nabla}\psi_{\rm i} \right) d\mathbf{r} + \int_{\Omega_{\rm i}} \delta\psi_{\rm i}\boldsymbol{\nabla}\cdot\left(\frac{j\omega\rho_0\mathbf{v}_0}{c^2}\psi_{\rm i} + \frac{\rho_0\mathbf{v}_0}{c^2}\mathbf{v}_0\cdot\boldsymbol{\nabla}\psi_{\rm i} - \rho_0\boldsymbol{\nabla}\psi_{\rm i} \right) d\mathbf{r} = 0\,. \tag{1.60}$$

The second term of (1.60) is transformed by using the Green formula,

$$\int_{\Omega_{\rm i}} \delta\psi_{\rm i}\,\boldsymbol{\nabla}\cdot\mathbf{F}\,d\mathbf{r} = \int_{\partial\Omega_{\rm i}} \delta\psi_{\rm i}\,\mathbf{F}\cdot\mathbf{n}_{\rm i}\,ds - \int_{\Omega_{\rm i}} (\boldsymbol{\nabla}\delta\psi_{\rm i})\cdot\mathbf{F}\,ds\,, \tag{1.61}$$

where $\partial\Omega_{\rm i}$ is the boundary of the inner acoustic domain $\Omega_{\rm i}$, $\mathbf{n}_{\rm i}$ its outward unit normal, and where ds is a surface measure on $\partial\Omega_{\rm i}$. Taking into account the boundary conditions on the parts $\Gamma_{\rm io}$, Γ, $\Gamma_{\rm f}$, and $\Gamma_{\rm h}$ of $\partial\Omega_{\rm i}$, and the notations for the associated unit normals previously defined, taking into account that $\mathbf{v}_0\cdot\mathbf{n} = 0$ on Γ and $\mathbf{v}_0\cdot\mathbf{n}_{\rm h} = 0$ on $\Gamma_{\rm h}$ (boundary conditions induced by the Euler steady flow, which imposes the noslip condition by neglecting viscous effects), and taking into account Eq. (1.44) for the acoustic source induced by the fan, Eq.(1.60) yields,

$$\begin{aligned}
&-\omega^2\int_{\Omega_{\rm i}} \frac{\rho_0}{c^2}\,\delta\psi_{\rm i}\,\psi_{\rm i}d\mathbf{r} \\
&+ j\omega\int_{\Omega_{\rm i}} \frac{\rho_0}{c}\left\{ \delta\psi_{\rm i}\frac{\mathbf{v}_0}{c}\cdot\boldsymbol{\nabla}\psi_{\rm i} - \boldsymbol{\nabla}\delta\psi_{\rm i}\cdot\frac{\mathbf{v}_0}{c}\psi_{\rm i} \right\} d\mathbf{r} \\
&+ \int_{\Omega_{\rm i}} \rho_0\left\{ \boldsymbol{\nabla}\psi_{\rm i}\cdot\boldsymbol{\nabla}\delta\psi_{\rm i} - \left(\boldsymbol{\nabla}\delta\psi_{\rm i}\cdot\frac{\mathbf{v}_0}{c}\right)\left(\frac{\mathbf{v}_0}{c}\cdot\boldsymbol{\nabla}\psi_{\rm i}\right) \right\} d\mathbf{r} \\
&+ \int_{\Gamma} \frac{\rho_0^2}{j\omega Z(\mathbf{r},\omega)}\left(j\omega + \mathbf{v}_0\cdot\boldsymbol{\nabla}\right)\,\delta\psi_{\rm i}\,\left(j\omega - \mathbf{v}_0\cdot\boldsymbol{\nabla}\right)\psi_{\rm i}ds \\
&+ \int_{\Gamma_{\rm io}} \rho_\infty\delta\psi_{\rm i}\left\{ \frac{j\omega}{c^2}\mathbf{v}_\infty\cdot\mathbf{n}_{\rm io}\psi_{\rm o} + \left(\frac{\mathbf{v}_\infty}{c}\cdot\mathbf{n}_{\rm io}\right)\left(\frac{\mathbf{v}_\infty}{c}\cdot\boldsymbol{\nabla}\psi_{\rm o}\right) - \frac{\partial\psi_{\rm o}}{\partial\mathbf{n}_{\rm io}} \right\} ds \\
&= \int_{\Gamma_{\rm f}} \delta\psi_{\rm i}S_{\rm f}(\mathbf{r},\omega)ds,
\end{aligned} \tag{1.62}$$

where the second term of the integral on Γ, which results from the Green formula and which corresponds to the integral over the outline of Γ, is neglected as rotational terms are not accounted for, and with,

$$S_{\rm f}(\mathbf{r},\omega) = \rho_0\frac{\partial\varphi}{\partial\mathbf{n}_{\rm f}} - j\frac{\omega}{c}\rho_0\frac{\mathbf{v}_0}{c}\cdot\mathbf{n}_{\rm f}\,\varphi - \rho_0\left(\frac{\mathbf{v}_0}{c}\cdot\mathbf{n}_{\rm f}\right)\left(\frac{\mathbf{v}_0}{c}\cdot\boldsymbol{\nabla}\varphi\right)\,. \tag{1.63}$$

The term in the right-hand side member of Eq. (1.62) represents the acoustic source induced by the fan (incident sound field (+)) and also a coupling term due to the unknown reflected sound

field (-). The last term in the left-hand side member represents the coupling term between the inner domain and the outer domain.

1.10.2 Weak formulation of the boundary value problem in the outer domain

The weak formulation of the boundary value problem defined by Eqs. (1.55),(1.56), (1.57), and (1.58) relative to the outer domain for the inlet case is written, for all $\delta\psi_{\rm o}$ in the admissible space of sufficiently regular real-valued functions defined on $\Omega_{\rm o}$, as,

$$\int_{\Omega_{\rm o}} \delta\psi_{\rm o} \left(\frac{-\omega^2 \rho_\infty}{c^2} \psi_{\rm o} + \frac{j\omega\rho_\infty}{c^2} \mathbf{v}_\infty \cdot \boldsymbol{\nabla}\psi_{\rm o} \right) d\mathbf{r}$$
$$+ \int_{\Omega_{\rm o}} \delta\psi_{\rm o} \boldsymbol{\nabla} \cdot \left(\frac{j\omega\rho_\infty \mathbf{v}_\infty}{c^2} \psi_{\rm o} + \frac{\rho_\infty \mathbf{v}_\infty}{c^2} \mathbf{v}_\infty \cdot \boldsymbol{\nabla}\psi_{\rm o} - \rho_\infty \boldsymbol{\nabla}\psi_{\rm o} \right) d\mathbf{r} = 0\,. \tag{1.64}$$

The second term of Eq. (1.64) is transformed by using the Green formula, where $\partial\Omega_{\rm o} = \Gamma_{\rm io} \cup \Gamma_{\rm ho}$ is the boundary of the outer acoustic domain $\Omega_{\rm o}$, $\mathbf{n}_{\rm oi}$ is the outward unit normal to $\Gamma_{\rm io}$, $\mathbf{n}_{\rm ho}$ is the outward unit normal to $\Gamma_{\rm ho}$, and where ds is the surface measure on $\partial\Omega_{\rm o}$. Taking into account the boundary conditions on the part $\Gamma_{\rm io}$ and $\Gamma_{\rm ho}$ of $\partial\Omega_{\rm o}$, Eq.(1.64) yields,

$$- \omega^2 \int_{\Omega_{\rm o}} \frac{\rho_\infty}{c^2}\, \delta\psi_{\rm o}\, \psi_{\rm o} d\mathbf{r}$$
$$+ j\omega \int_{\Omega_{\rm o}} \frac{\rho_\infty}{c} \left\{ \delta\psi_{\rm o} \frac{\mathbf{v}_\infty}{c} \cdot \boldsymbol{\nabla}\psi_{\rm o} - \boldsymbol{\nabla}\delta\psi_{\rm o} \cdot \frac{\mathbf{v}_\infty}{c} \psi_{\rm o} \right\} d\mathbf{r}$$
$$+ \int_{\Omega_{\rm o}} \rho_\infty \left\{ \boldsymbol{\nabla}\psi_{\rm o} \cdot \boldsymbol{\nabla}\delta\psi_{\rm o} - \left(\boldsymbol{\nabla}\delta\psi_{\rm o} \cdot \frac{\mathbf{v}_\infty}{c} \right) \left(\frac{\mathbf{v}_\infty}{c} \cdot \boldsymbol{\nabla}\psi_{\rm o} \right) \right\} d\mathbf{r}$$
$$+ \int_{\Gamma_{\rm io}} \rho_\infty \delta\psi_{\rm o} \left\{ \frac{j\omega}{c^2} \mathbf{v}_\infty \cdot \mathbf{n}_{\rm oi} \psi_{\rm i} + \left(\frac{\mathbf{v}_\infty}{c} \cdot \mathbf{n}_{\rm oi} \right) \left(\frac{\mathbf{v}_\infty}{c} \cdot \boldsymbol{\nabla}\psi_{\rm i} \right) - \frac{\partial\psi_{\rm i}}{\partial \mathbf{n}_{\rm oi}} \right\} ds$$
$$= 0\,. \tag{1.65}$$

The last term in the left-hand side member represents the coupling term between the outer domain and the inner domain.

1.11 Finite/Infinite Elements discretization of the weak formulation of the boundary value problem related to the inlet

For all ω fixed in $\mathbb{R}$, let $\boldsymbol{\psi}_{\rm i}(\omega)$ be the complex vector in $\mathbb{C}^{N_{\rm i}}$ corresponding to the finite element discretization of field $\psi_{\rm i}(\mathbf{r},\omega)$ in which $N_{\rm i}$ is the number of degrees of freedom (dofs) for the discretization of $\boldsymbol{\psi}_{\rm i}(\omega)$. Let $\boldsymbol{\psi}_{\rm o}(\omega)$ be the complex vector in $\mathbb{C}^{N_{\rm o}}$ corresponding to the infinite element discretization of field $\psi_{\rm o}(\mathbf{r},\omega)$ in which $N_{\rm o}$ is the number of dofs for the discretization of $\boldsymbol{\psi}_{\rm o}(\omega)$. Consequently, vector $\boldsymbol{\psi}_{\rm i}(\omega)$ corresponds to all the dofs associated with the nodes of the mesh of domain $\Omega_{\rm i}$, while $\boldsymbol{\psi}_{\rm o}(\omega)$ corresponds only to the dofs associated with the nodes of the mesh of surface $\Gamma_{\rm io}$. The formulation of the infinite elements that are used is the one proposed in [15], for which there are internal nodes in the infinite domain (it is not true nodes) and primary nodes that are located on finite-infinite interface $\Gamma_{\rm io}$, which coincides with the nodes of the finite elements of the inner domain, for which the dofs are gathered in complex vector $\boldsymbol{\psi}_o(\omega)$.

1.11.1 Matrix equation for the acoustic problem

The finite element discretization of Eqs. (1.62) with (1.63) yields the following matrix equation,

$$\left\{-\omega^2[M_{\rm i}] + j\omega[C_{\rm i}] + [K_{\rm i}] + [Z_{\rm i}(\omega)]\right\} \boldsymbol{\psi}_{\rm i}(\omega) + [H(\omega)]\boldsymbol{\psi}_{\rm o}(\omega) = \mathbf{f}_{\rm i}(\omega)\,. \tag{1.66}$$

The infinite element discretization of Eq. (1.65) yields the following matrix equation,

$$\left\{-\omega^2[M_{\rm o}] + j\omega[C_{\rm o}] + [K_{\rm o}]\right\} \boldsymbol{\psi}_{\rm o}(\omega) - [H(\omega)]^T\boldsymbol{\psi}_{\rm i}(\omega) = 0\,. \tag{1.67}$$

- The symmetric $(N_{\rm i} \times N_{\rm i})$ real matrix $[M_{\rm i}]$ is positive definite and corresponds to the discretization (finite elements) of the bilinear form,

$$\int_{\Omega_{\rm i}} \frac{\rho_0}{c^2}\, \delta\psi_{\rm i}\, \psi_{\rm i} d\mathbf{r}\,.$$

- The $(N_{\rm i} \times N_{\rm i})$ real matrix $[C_{\rm i}]$ corresponds to the discretization (finite elements) of the bilinear form,

$$\int_{\Omega_{\rm i}} \frac{\rho_0}{c} \left\{\delta\psi_{\rm i} \frac{\mathbf{v}_0}{c}\cdot\boldsymbol{\nabla}\psi_{\rm i} - \boldsymbol{\nabla}\delta\psi_{\rm i}\cdot\frac{\mathbf{v}_0}{c}\psi_{\rm i}\right\} d\mathbf{r}\,.$$

- The symmetric $(N_{\rm i}\times N_{\rm i})$ real matrix $[K_{\rm i}]$ corresponds to the discretization (finite elements) of the bilinear form,

$$\int_{\Omega_{\rm i}} \rho_0 \left\{\boldsymbol{\nabla}\psi_{\rm i}\cdot\boldsymbol{\nabla}\delta\psi_{\rm i} - \left(\boldsymbol{\nabla}\delta\psi_{\rm i}\cdot\frac{\mathbf{v}_0}{c}\right)\left(\frac{\mathbf{v}_0}{c}\cdot\boldsymbol{\nabla}\psi_{\rm i}\right)\right\} d\mathbf{r}\,.$$

- The $(N_{\rm i} \times N_{\rm i})$ complex matrix $[Z_{\rm i}(\omega)]$ corresponds to the discretization (finite elements) of the bilinear form,

$$\int_{\Gamma} \frac{\rho_0^2}{j\omega Z(\mathbf{r},\omega)}\, (j\omega + \mathbf{v}_0\cdot\boldsymbol{\nabla})\, \delta\psi_{\rm i}\, (j\omega - \mathbf{v}_0\cdot\boldsymbol{\nabla})\, \psi_{\rm i} ds\,.$$

  It should be noted that matrix $[Z_{\rm i}(\omega)]$ has nonzero entries only for the block submatrix corresponding to the dofs associated with the nodes belonging to Γ (the liner).

- The $(N_{\rm i} \times N_{\rm o})$ complex matrix $[H(\omega)]$ corresponds to the discretization (finite elements for $\psi_{\rm i}$ and infinite elements for $\psi_{\rm o}$) of the bilinear form,

$$\int_{\Gamma_{\rm io}} \rho_\infty \delta\psi_{\rm i} \left\{\frac{j\omega}{c^2}\mathbf{v}_\infty\cdot\mathbf{n}_{\rm io}\psi_{\rm o} + \left(\frac{\mathbf{v}_\infty}{c}\cdot\mathbf{n}_{\rm io}\right)\left(\frac{\mathbf{v}_\infty}{c}\cdot\boldsymbol{\nabla}\psi_{\rm o}\right) - \frac{\partial\psi_{\rm o}}{\partial\mathbf{n}_{\rm io}}\right\} ds\,.$$

- The symmetric $(N_{\rm o} \times N_{\rm o})$ real matrix $[M_{\rm o}]$ is positive definite and corresponds to the discretization (infinite elements) of the bilinear form,

$$\int_{\Omega_{\rm o}} \frac{\rho_\infty}{c^2}\, \delta\psi_{\rm o}\, \psi_{\rm o} d\mathbf{r}\,.$$

- The skew-symmetric $(N_\mathrm{o} \times N_\mathrm{o})$ real matrix $[C_\mathrm{o}]$ corresponds to the discretization (infinite elements) of the bilinear form,

$$\int_{\Omega_\mathrm{o}} \frac{\rho_\infty}{c} \left\{ \delta\psi_\mathrm{o} \frac{\mathbf{v}_\infty}{c} \cdot \boldsymbol{\nabla}\psi_\mathrm{o} - \boldsymbol{\nabla}\delta\psi_\mathrm{o} \cdot \frac{\mathbf{v}_\infty}{c} \psi_\mathrm{o} \right\} d\mathbf{r} \,.$$

- The symmetric $(N_\mathrm{o} \times N_\mathrm{o})$ real matrix $[K_\mathrm{o}]$ corresponds to the discretization (infinite elements) of the bilinear form,

$$\int_{\Omega_\mathrm{o}} \rho_\infty \left\{ \boldsymbol{\nabla}\psi_\mathrm{o} \cdot \boldsymbol{\nabla}\delta\psi_\mathrm{o} - \left(\boldsymbol{\nabla}\delta\psi_\mathrm{o} \cdot \frac{\mathbf{v}_\infty}{c} \right) \left(\frac{\mathbf{v}_\infty}{c} \cdot \boldsymbol{\nabla}\psi_\mathrm{o} \right) \right\} d\mathbf{r} \,.$$

- The $\mathbb{C}^{N_\mathrm{i}}$-valued vector $\mathbf{f}_\mathrm{i}(\omega)$ corresponds to the discretization (finite elements) of the linear form,

$$\int_{\Gamma_\mathrm{f}} \delta\psi_\mathrm{i} S_\mathrm{f}(\mathbf{r}, \omega) ds \,.$$

1.11.2 Matrix representation of $\mathbf{f}_\mathrm{i}$ (fan acoustic excitation and reflected field)

Since $\mathbf{f}_\mathrm{i}(\omega)$ is related to boundary Γ_f, only the components of $\mathbf{f}_\mathrm{i}(\omega)$ related to the $N_\mathrm{f} < N_\mathrm{i}$ dofs in Γ_f are not zero. Let $\mathbf{f}_\mathrm{f}(\omega)$ be the vector in $\mathbb{C}^{N_\mathrm{f}}$ constituted of the components of $\mathbf{f}_\mathrm{i}(\omega)$ that are not equal to zero (components related to Γ_f). Consequently, vector $\mathbf{f}_\mathrm{i}(\omega)$ can be written as

$$\mathbf{f}_\mathrm{i}(\omega) = [\mathcal{E}_\mathrm{if}]\, \mathbf{f}_\mathrm{f}(\omega) \,, \tag{1.68}$$

in which the sparse $(N_i \times N_\mathrm{f})$ real matrix $[\mathcal{E}_\mathrm{if}]$ is constituted of 0 and 1. Taking into account the expression of φ defined by Eq. (1.52), which shows that φ is a linear mapping of the complex vector $(\mathbf{c}^+, \mathbf{c}^-) \in \mathbb{C}^{N_d} \times \mathbb{C}^{N_d}$, with,

$$\mathbf{c}^+ = (c_1^+, \ldots, c_{N_d}^+) \in \mathbb{C}^{N_d} \quad , \quad \mathbf{c}^- = (c_1^-, \ldots, c_{N_d}^-) \in \mathbb{C}^{N_d} \,, \tag{1.69}$$

and taking into account the expression of the N_f complex vector $\mathbf{f}_\mathrm{f}(\omega)$ deduced from $\mathbf{f}_\mathrm{i}(\omega)$ constructed at the end of Section 1.11.1, vector $\mathbf{f}_\mathrm{f}(\omega)$ belonging to $\mathbb{C}^{N_\mathrm{f}}$ can be written as,

$$\mathbf{f}_\mathrm{f}(\omega) = [F^+(\omega)]\, \mathbf{c}^+ + [F^-(\omega)]\, \mathbf{c}^- \tag{1.70}$$

1.11.3 Matrix representation of the duct modal coupling with the inner domain

For given vector $\mathbf{c}^+$ that defined the fan acoustic excitation, since vector $\mathbf{c}^-$ is an unknown of the problem, the matrix equations defined by Eqs. (1.74) and (1.70) are not algebraically closed and we have to write, in the weak form, the continuity on Γ_f of the acoustic velocity potential ψ_i with φ. It is assumed that boundary Γ_f is the end cross-section of the duct for which $z = z_f$. The weak form of the continuity of ψ_i with φ is then written as

$$\int_{\Gamma_f} \varphi_\alpha (\psi_\mathrm{i} - \varphi)\, d\Gamma_f = 0 \quad , \quad \alpha = 1, \ldots, N_d \,, \tag{1.71}$$

which can be rewritten, using the expansion of φ given by Eq. (1.52) and the orthogonality property of the duct modes defined by Eq. (1.50), as

$$\int_{\Gamma_f} \varphi_\alpha \psi_\mathrm{i}\, d\Gamma_f - (c_\alpha^+ e^{jk_{z_\alpha}^+ z_f} + c_\alpha^- e^{jk_{z_\alpha}^- z_f}) = 0 \quad , \quad \alpha = 1, \ldots, N_d \,. \tag{1.72}$$

Using the finite element discretization of the inner domain, the finite element approximation of the first term in the left-hand side of Eq. (1.72) can be written as $[E]\,\boldsymbol{\psi}_{\rm i}(\omega)$ in which $[E]$ is a constant $(N_d \times N_{\rm i})$ real matrix. Introducing the diagonal $(N_d \times N_d)$ complex matrices $[R^+(\omega)]$ and $[R^-(\omega)]$ such that $[R^\pm(\omega)]_{\alpha\beta} = \delta_{\alpha\beta} e^{j k^\pm_{z_\alpha} z_f}$, the matrix representation of Eq. (1.72) can be written as

$$[E]\,\boldsymbol{\psi}_{\rm i}(\omega) - ([R^+(\omega)]\,\mathbf{c}^+ + [R^-(\omega)]\,\mathbf{c}^-) = 0\,. \tag{1.73}$$

1.11.4 Assembling the matrix equation for the acoustic problem

Note that, even if $\mathbf{c}^+$ was chosen as independent of ω (that is not necessary, because $\mathbf{c}^+$ can depend on ω), then $\mathbf{c}^-$ would depend on ω. It will now be noted as $\mathbf{c}^-(\omega)$. The unknowns of the acoustic problem are the vectors $\boldsymbol{\psi}_{\rm i}(\omega)$, $\boldsymbol{\psi}_{\rm o}(\omega)$, and $\mathbf{c}^-(\omega)$. The assembling of the matrix equation for the acoustic problem is obtained by gathering Eqs. (1.66), (1.67), and (1.73), which yields,

$$\begin{bmatrix} [A_{\rm i}(\omega)] + [Z_{\rm i}(\omega)] & [H(\omega)] & -[\mathcal{E}_{\rm if}]\,[F^-(\omega)] \\ -[H(\omega)]^T & [A_{\rm o}(\omega)] & [0] \\ [E] & [0] & -[R^-(\omega)] \end{bmatrix} \begin{bmatrix} \boldsymbol{\psi}_{\rm i}(\omega) \\ \boldsymbol{\psi}_{\rm o}(\omega) \\ \mathbf{c}^-(\omega) \end{bmatrix} = \begin{bmatrix} [\mathcal{E}_{\rm if}]\,[F^+(\omega)] \\ [0] \\ [R^+(\omega)] \end{bmatrix} \mathbf{c}^+\,, \tag{1.74}$$

in which complex matrices $[A_{\rm i}(\omega)]$ and $[A_{\rm o}(\omega)]$ are written as

$$[A_{\rm i}(\omega)] = -\omega^2\,[M_{\rm i}] + j\omega\,[C_{\rm i}] + [K_{\rm i}]\,, \tag{1.75}$$

$$[A_{\rm o}(\omega)] = -\omega^2\,[M_{\rm o}] + j\omega\,[C_{\rm o}] + [K_{\rm o}]\,. \tag{1.76}$$

1.12 Frequency by frequency static condensation with respect to the liner dofs and expression of the fan acoustic excitation

In Chapter 2, we will present the probabilistic modeling of uncertainties in the computational model defined by Eq. (1.74). These uncertainties will be taken into account for both the parametric uncertainties and the model uncertainties induced by the modeling errors for the aeroacoustic and for the liner. Consequently, we need to reorganize the algebraic structure of the complex matrix equation Eq. (1.74) in order to exhibit the complex vector $\boldsymbol{\psi}_\ell(\omega)$ belonging to $\mathbb{C}^{N_\ell}$ of the N_ℓ dofs of the liner and the complex vector $\boldsymbol{\psi}_a$ belonging to $\mathbb{C}^{N_a}$ of the N_a other dofs of $(\boldsymbol{\psi}_{\rm i}(\omega), \boldsymbol{\psi}_{\rm o}(\omega), \mathbf{c}^-(\omega))$. This means that $N_a = N_{\rm i} + N_{\rm o} + N_d - N_\ell$ and that,

$$\begin{bmatrix} \boldsymbol{\psi}_{\rm i}(\omega) \\ \boldsymbol{\psi}_{\rm o}(\omega) \\ \mathbf{c}^-(\omega) \end{bmatrix} \quad \text{is rewritten as} \quad \begin{bmatrix} \boldsymbol{\psi}_\ell(\omega) \\ \boldsymbol{\psi}_a(\omega) \end{bmatrix} \quad , \quad N_{\rm i} + N_{\rm o} + N_d = N_\ell + N_a\,. \tag{1.77}$$

Since we have $\Gamma \cap \Gamma_{\rm f} = \{\emptyset\}$,

$$\begin{bmatrix} [\mathcal{E}_{\rm if}]\,[F^+(\omega)] \\ [0] \\ [R^+(\omega)] \end{bmatrix} \mathbf{c}^+ \quad \text{is rewritten as} \quad \begin{bmatrix} \mathbf{0} \\ \mathbf{f}_a(\omega) \end{bmatrix} \quad , \quad N_{\rm i} + N_{\rm o} + N_d = N_\ell + N_a\,, \tag{1.78}$$

in which the $\mathbb{C}^{N_a}$-vector $\mathbf{f}_a(\omega)$ can be written as

$$\mathbf{f}_a(\omega) = [\mathcal{B}_a(\omega)]\,\mathbf{c}^+\,, \tag{1.79}$$

where $[\mathcal{B}_a(\omega)]$ is a known complex $(N_a \times N_d)$ matrix.

Using Eqs. (1.77) and (1.78), the computational model defined by Eq. (1.74) can be rewritten in a block form as,

$$\begin{bmatrix} [A_{\ell\ell}(\omega)] & [A_{\ell a}(\omega)] \\ [A_{a\ell}(\omega)] & [A_{aa}(\omega)] \end{bmatrix} \begin{bmatrix} \boldsymbol{\psi}_\ell(\omega) \\ \boldsymbol{\psi}_a(\omega) \end{bmatrix} + \begin{bmatrix} [Z_\ell(\omega)] & 0 \\ 0 & 0 \end{bmatrix} \begin{bmatrix} \boldsymbol{\psi}_\ell(\omega) \\ \boldsymbol{\psi}_a(\omega) \end{bmatrix} = \begin{bmatrix} \mathbf{0} \\ \mathbf{f}_a(\omega) \end{bmatrix} . \tag{1.80}$$

The static condensation ω by ω is performed in eliminating the vector $\mathbf{x}_a$ in the following matrix equation,

$$\begin{bmatrix} [A_{\ell\ell}(\omega)] & [A_{\ell a}(\omega)] \\ [A_{a\ell}(\omega)] & [A_{aa}(\omega)] \end{bmatrix} \begin{bmatrix} \mathbf{x}_\ell \\ \mathbf{x}_a \end{bmatrix} = \begin{bmatrix} \mathbf{0} \\ \mathbf{f}_a(\omega) \end{bmatrix} , \tag{1.81}$$

which yields,

$$[\mathcal{A}_\ell(\omega)]\, \mathbf{x}_\ell = \boldsymbol{\mathcal{F}}_\ell(\omega) , \tag{1.82}$$

in which the $(N_\ell \times N_\ell)$ complex matrix $[\mathcal{A}_\ell(\omega)]$ and the N_ℓ complex vector $\boldsymbol{\mathcal{F}}_\ell(\omega)$ are written as,

$$[\mathcal{A}_\ell(\omega)] = [A_{\ell\ell}(\omega)] - [A_{\ell a}(\omega)][A_{aa}(\omega)]^{-1}[A_{a\ell}(\omega)] , \tag{1.83}$$

$$\boldsymbol{\mathcal{F}}_\ell(\omega) = -[A_{\ell a}(\omega)][A_{aa}(\omega)]^{-1}\mathbf{f}_a(\omega) . \tag{1.84}$$

Using Eq. (1.79), Eq. (1.84) can be written as

$$\boldsymbol{\mathcal{F}}_\ell(\omega) = -[A_{\ell a}(\omega)]\, [A_{aa}(\omega)]^{-1}\, [\mathcal{B}_a(\omega)]\, \mathbf{c}^+ , \tag{1.85}$$

that is to say,

$$\boldsymbol{\mathcal{F}}_\ell(\omega) = [\mathcal{B}_\ell(\omega)]\, \mathbf{c}^+ , \tag{1.86}$$

in which the $(N_\ell \times N_d)$ complex matrix $[\mathcal{B}_\ell(\omega)]$ is defined by

$$[\mathcal{B}_\ell(\omega)] = -[A_{\ell a}(\omega)]\, [A_{aa}(\omega)]^{-1}\, [\mathcal{B}_a(\omega)] . \tag{1.87}$$

The computation is performed thanks to the static condensation (Schur complement). Complex matrices $[\mathcal{A}_\ell(\omega)]$ and $[\mathcal{B}_\ell(\omega)]$ are the results of the static condensation ω by ω. It should be noted that this static condensation is performed using the classical Gauss elimination algorithm without computing the inverse of matrix $[A_{aa}(\omega)]$. The elimination of $\boldsymbol{\psi}_a(\omega)$ in Eq. (1.80) yields,

$$[\mathcal{A}_\ell(\omega)]\boldsymbol{\psi}_\ell(\omega) + [Z_\ell(\omega)]\boldsymbol{\psi}_\ell(\omega) = [\mathcal{B}_\ell(\omega)]\, \mathbf{c}^+ . \tag{1.88}$$

1.13 Computational reduced-order model using a pellicular projection

The algebraic structure of Eq. (1.88) that we have constructed, is adapted to the implementation of uncertainties in the computational model. Following the explanations given at the beginning of Section 1.12, both the parametric uncertainties and the model uncertainties induced by modeling errors for the liner will be taken into account by modeling complex matrix $[Z_\ell(\omega)]$ by a random complex matrix.

However, the number N_ℓ of dofs related to the liner can be very high, in general we can have several ten thousands dofs. Complex matrix $[Z_\ell(\omega)]$ is a sparse matrix, but using the nonparametric probabilistic approach of uncertainties [60], the associated complex random matrix would be full, that would induce a huge numerical cost. For this reason, we have to construct a reduced-order model of Eq. (1.88). For such a construction, a reduced-order basis has to be introduced. Following the method proposed in [15], we chose to use a pellicular basis whose construction is summarized hereinafter.

1.13.1 Construction of the pellicular basis

This pellicular basis is associated with the acoustic radiation of the liner delimited by its boundary Γ. There is a thin acoustic layer of fluid (the pellicular domain) on Γ, for which the characteristic length is significatively lower than the characteristic wavelength of the study. Considering that the acoustic layer thickness is infinitely thin with respect to the acoustic wavelength, a set of acoustic modes related to the pellicular domain is computed solving the eigenvalue problem derived from the computational model,

$$[\mathcal{K}_L]\boldsymbol{\phi}_\alpha = \lambda_\alpha [\mathcal{M}_L]\boldsymbol{\phi}_\alpha \,, \tag{1.89}$$

in which the symmetric $(N_\ell \times N_\ell)$ real matrices $[\mathcal{K}_L]$ and $[\mathcal{M}_L]$ are positive definite and represent, respectively, the acoustic stiffness matrix and the associated mass matrix. The eigenvector $\boldsymbol{\phi}_\alpha$ belonging to $\mathbb{R}^{N_\ell}$ is called a pellicular eigenvector and λ_α is its corresponding eigenvalue. These pellicular eigenvectors verify the following orthogonal properties,

$$\begin{cases} \boldsymbol{\phi}_\alpha^T \, [\mathcal{K}_L] \, \boldsymbol{\phi}_\beta = \lambda_\alpha \delta_{\alpha\beta} \\ \\ \boldsymbol{\phi}_\alpha^T \, [\mathcal{M}_L] \, \boldsymbol{\phi}_\beta = \delta_{\alpha\beta} \end{cases} \tag{1.90}$$

with $\delta_{\alpha\beta}$ the Kronecker symbol stating that for $\alpha \neq \beta$, $\delta_{\alpha\beta} = 0$.

Let n_ℓ be the number of pellicular eigenvectors $\boldsymbol{\phi}_1, \ldots, \boldsymbol{\phi}_{n_\ell}$ that are retained for the construction of the reduced-order model. We then introduce the $(N_\ell \times n_\ell)$ real matrix $[\Phi]$ whose columns are $\boldsymbol{\phi}_1, \ldots, \boldsymbol{\phi}_{n_\ell}$.

1.13.2 Construction of the reduced-order model

The reduced representation consists in writing,

$$\boldsymbol{\psi}_\ell(\omega) = [\Phi] \, \mathbf{q}(\omega) \,, \tag{1.91}$$

in which $\mathbf{q}(\omega)$, which belongs to $\mathbb{C}^{n_\ell}$, is a complex vector of the generalized coordinates. The reduced-order computational model consists in substituting Eq. (1.91) into Eq. (1.88), and then to left-multiplying it by $[\Phi]^T$. We obtain,

$$([\mathbb{A}(\omega)] + [\mathbb{Z}(\omega)]) \, \mathbf{q}(\omega) = \mathbb{F}(\omega) \,, \tag{1.92}$$

in which the $(n_\ell \times n_\ell)$ complex matrix $[\mathbb{A}(\omega)]$, the $(n_\ell \times n_\ell)$ complex matrix $[\mathbb{Z}(\omega)]$, and the $\mathbb{C}^{n_\ell}$-valued vector $\mathbb{F}(\omega)$ are written as,

$$[\mathbb{A}(\omega)] = [\Phi]^T [\mathcal{A}_\ell(\omega)] [\Phi] \,, \tag{1.93}$$

$$[\mathbb{Z}(\omega)] = [\Phi]^T [Z_\ell(\omega)] [\Phi] \,, \tag{1.94}$$

$$\mathbb{F}(\omega) = [\mathbb{B}(\omega)] \, \mathbf{c}^+ \,, \tag{1.95}$$

in which the $(n_\ell \times N_d)$ complex matrix $[\mathbb{B}(\omega)]$ is written as,

$$[\mathbb{B}(\omega)] = [\Phi]^T [\mathcal{B}_\ell(\omega)] \,. \tag{1.96}$$

Consequently, Eq. (1.92) can be rewritten as,

$$([\mathbb{A}(\omega)] + [\mathbb{Z}(\omega)]) \, \mathbf{q}(\omega) = [\mathbb{B}(\omega)] \, \mathbf{c}^+ \,. \tag{1.97}$$

Once $\boldsymbol{\psi}_\ell(\omega)$ has been computed with Eqs. (1.91) and (1.97), vector $\boldsymbol{\psi}_a(\omega)$ is computed with the second line of Eq. (1.80) with Eqs. (1.79) and (1.91), that is to say, solving the matrix equation,

$$[A_{aa}(\omega)]\,\boldsymbol{\psi}_a(\omega) = -[A_{a\ell}(\omega)]\,[\Phi]\,\mathbf{q}(\omega) + [\mathcal{B}_a(\omega)]\,\mathbf{c}^+\,. \tag{1.98}$$

The reduced-order model is then constituted of Eqs. (1.91), (1.97), and (1.98). In the framework of the nonparametric probabilistic approach, the uncertainties in the computational model will be implemented by substituting complex matrices $[\mathbb{A}(\omega)]$ and $[\mathbb{Z}(\omega)]$ by random complex matrices $[\mathbf{A}(\omega)]$ and $[\mathbf{Z}(\omega)]$.

1.13.3 Algebraic properties of complex matrix $[\mathbb{Z}(\omega)]$

The complex matrix $[\mathbb{Z}(\omega)]$ in Eq. (1.97) is associated with matrix $[Z_i(\omega)]$, which corresponds to the finite element discretization of the complex bilinear form of the term generated by the Myers boundary condition (see fourth term of the left-hand side of Eq. (1.62)).
The complex matrix $[\mathbb{Z}(\omega)]$ is written as

$$[\mathbb{Z}(\omega)] = [\mathbb{Z}_R(\omega)] + j\,[\mathbb{Z}_I(\omega)]\,, \tag{1.99}$$

where $[\mathbb{Z}_R(\omega)] = Re\{[\mathbb{Z}(\omega)]\}$ and $[\mathbb{Z}_I(\omega)] = Im\{[\mathbb{Z}(\omega)]\}$ are nonsymmetric real matrices (the symmetry only appears for $\mathbf{v}_0 = \mathbf{0}$).
Given Eq. (1.97) and the definition of matrix $[\mathbb{A}(\omega)]$, it appears that the dissipative term induced by complex matrix $[\mathbb{Z}(\omega)]$ in the coupled system, corresponds to the real matrix $[\mathbb{Z}_I(\omega)]$. As $[\mathbb{Z}(\omega)] \neq [\mathbb{Z}(\omega)]^T$ (matrix nonsymmetric for $\mathbf{v}_0 \neq \mathbf{0}$), the dissipative part is generated by the symmetric part $[\mathbb{Z}_I^{\mathrm{S}}(\omega)]$ of $[\mathbb{Z}_I(\omega)]$, the skew-symmetric part $[\mathbb{Z}_I^{\mathrm{SS}}(\omega)]$ of $[\mathbb{Z}_I(\omega)]$ does not dissipate energy. Consequently, the real matrix $[\mathbb{Z}_I(\omega)]$ is written as

$$[\mathbb{Z}_I(\omega)] = [\mathbb{Z}_I^{\mathrm{S}}(\omega)] + [\mathbb{Z}_I^{\mathrm{SS}}(\omega)] \tag{1.100}$$

in which

$$[\mathbb{Z}_I^{\mathrm{S}}(\omega)] = ([\mathbb{Z}_I(\omega)] + [\mathbb{Z}_I(\omega)]^T)/2 \quad , \quad [\mathbb{Z}_I^{\mathrm{SS}}(\omega)] = ([\mathbb{Z}_I(\omega)] - [\mathbb{Z}_I(\omega)]^T)/2\,, \tag{1.101}$$

where $[\mathbb{Z}_I^{\mathrm{S}}(\omega)]$ and $[\mathbb{Z}_I^{\mathrm{SS}}(\omega)]$ are symmetric and skew-symmetric matrices. It can be viewed that the positive-definite symmetric real matrix $[\mathbb{Z}_I^{\mathrm{S}}(\omega)]$ is associated with the bilinear form

$$\int_\Gamma \frac{\rho_0^2 Z_R(\mathbf{r},\omega)}{\omega\,\big(Z_R^2(\mathbf{r},\omega) + Z_I^2(\mathbf{r},\omega)\big)}\,\big(\omega^2\psi_i\,\delta\psi_i + (\mathbf{v}_0\cdot\boldsymbol{\nabla}\psi_i)(\mathbf{v}_0\cdot\boldsymbol{\nabla}\delta\psi_i)\big)\,ds(\mathbf{r})\,, \tag{1.102}$$

that is effectively a positive-definite symmetric bilinear form because $\omega > 0$ and the local resistance $Z_R(\mathbf{r},\omega)$ is positive (see Eq. (1.43)). Finally, matrix $[\mathbb{Z}(\omega)]$ defined by Eq. (1.99) can be rewritten as,

$$[\mathbb{Z}(\omega)] = [\mathbb{Z}^{\mathrm{NS}}(\omega)] + j\,[\mathbb{Z}_I^{\mathrm{S}}(\omega)]\,, \tag{1.103}$$

with

$$[\mathbb{Z}^{\mathrm{NS}}(\omega)] = [\mathbb{Z}_R(\omega)] + j\,[\mathbb{Z}_I^{\mathrm{SS}}(\omega)] \tag{1.104}$$

in which $[\mathbb{Z}^{\mathrm{NS}}(\omega)]$ is a complex matrix that is not symmetric (and not skew-symmetric) and where $[\mathbb{Z}_I^{\mathrm{S}}(\omega)]$ is a positive-definite symmetric real matrix corresponding to a dissipative term in the coupled equation defined by Eq. (1.97).

1.13.4 Algebraic properties of complex matrix $[\mathbb{A}(\omega)]$

In Eq. (1.97), the reduced complex matrix $[\mathbb{A}(\omega)]$, related to aeroacoustics, is defined by Eq. (1.93). This complex matrix $[\mathbb{A}(\omega)]$ can be written as

$$[\mathbb{A}(\omega)] = [\mathbb{A}_R(\omega)] + j\,[\mathbb{A}_I(\omega)]\,, \tag{1.105}$$

where $[\mathbb{A}_R(\omega)] = Re\{[\mathbb{A}(\omega)]\}$ and $[\mathbb{A}_I(\omega)] = Im\{[\mathbb{A}(\omega)]\}$ are nonsymmetric real matrices due to the flow ($\mathbf{v}_0 \neq \mathbf{0}$). In the aeroacoustics phenomenon related to the boundary value problem for the inlet case, there is a radiation of the outgoing acoustic fields at infinity (Sommerfeld condition in the outer domain Ω_o and in the duct domain Ω_{duct}), which induces an apparent dissipation. Unfortunately, due to the presence of the flow, the method presented in Sec 1.13.3 for extracting the dissipation part in the complex matrix $\mathbb{Z}(\omega)$ cannot be used for the complex aeroacoustic matrix $\mathbb{A}(\omega)$ in the framework of the generalized formulation available in ACTRAN/TM. Consequently, because the dissipation part cannot be extracted, the stochastic modeling of the aeroacoustic matrix will globally be carried out as presented in Chapter 2, without separating the conservative part from the dissipative part.

1.14 Defining quantities of interest

The vector-valued Quantity of Interest, $\mathbf{qoI}(\omega)$, is written as,

$$\mathbf{qoI}(\omega) = [\mathbb{O}_{\text{obs}}(\omega)]\boldsymbol{\psi}_a(\omega)\,, \tag{1.106}$$

in which $[\mathbb{O}_{\text{obs}}(\omega)]$ is an observation complex matrix giving the position of virtual microphones placed in the far-field for the inlet case. Assuming that the virtual microphones are located in the outer domain, then $\mathbf{qoI}(\omega)$ will not depend on all the dofs gathered in $\boldsymbol{\psi}_a(\omega)$ but only on the dofs corresponding to the nodes located on finite-infinite interface Γ_{io}. Using Eq. (1.98), $\mathbf{qoI}(\omega)$ is given by

$$\mathbf{qoI}(\omega) = [\mathbb{F}_{\text{qoI}}(\omega)]\,\mathbf{c}^+ - [\mathbb{A}_{\text{qoI}}(\omega)]\mathbf{q}(\omega)\,, \tag{1.107}$$

in which,

$$[\mathbb{F}_{\text{qoI}}(\omega)] = [\mathbb{O}_{\text{obs}}(\omega)]\,[A_{aa}(\omega)]^{-1}\,[\mathcal{B}_a(\omega)]\,, \tag{1.108}$$

$$[\mathbb{A}_{\text{qoI}}(\omega)] = [\mathbb{O}_{\text{obs}}(\omega)][A_{aa}(\omega)]^{-1}[A_{a\ell}(\omega)]\,[\Phi]\,, \tag{1.109}$$

where vector $\mathbf{q}(\omega)$ is the solution of the deterministic equation defined by Eq. (1.97).

Using Eq. (1.97), vector $\mathbf{q}(\omega)$ of generalized coordinates can be written as,

$$\mathbf{q}(\omega) = \left([\mathbb{A}(\omega)] + [\mathbb{Z}(\omega)]\right)^{-1}[\mathbb{B}(\omega)]\,\mathbf{c}^+\,. \tag{1.110}$$

Substituting Eq. (1.110) into Eq. (1.107) yields,

$$\mathbf{qoI}(\omega) = [\mathbb{T}(\omega)]\,\mathbf{c}^+\,, \tag{1.111}$$

in which $[\mathbb{T}(\omega)] = [\mathbb{F}_{\text{qoI}}(\omega)] - [\mathbb{A}_{\text{qoI}}(\omega)]\left([\mathbb{A}(\omega)] + [\mathbb{Z}(\omega)]\right)^{-1}[\mathbb{B}(\omega)]$.

A detailed view of the algorithms used during the present work are presented in Appendix D.

1.15 Robust design optimization problem

1.15.1 Definition of the robust design optimization problem

The objective of this work is to perform robust design optimization, that is to say solving a design optimization problem by taking into account uncertainties in the computational model. We will have then to solve an optimization problem under uncertainties (OUU) related to an objective function $J(\mathbf{w})$ that will be constructed using the random quantities of interest gathered in random vector $\mathbf{QoI}(\omega)$.

The design optimization problem is formulated with respect to vector $\mathbf{w} = (w_1, \ldots, w_{n_w})$ of the design parameters related to the liner (geometrical parameters, mechanical properties, etc, see Appendix C). Consequently, the impedance $Z(\mathbf{r}, \omega)$ depends on $\mathbf{w}$ and the complex matrix $[\mathbb{Z}(\omega)]$ in Eq. (1.97) that is rewritten as $[\mathbb{Z}(\omega; \mathbf{w})]$. Due to uncertainties, matrix $[\mathbb{Z}(\omega; \mathbf{w})]$ is modeled by a random matrix $[\mathbf{Z}(\omega; \mathbf{w})]$ whose probabilistic model is detailed in Chapter 2. Vector $\mathbf{w}$ belongs to an admissible set $\mathcal{C}_w \subset \mathbb{R}^{n_w}$. The optimization problem consists in minimizing a deterministic objective function, denoted by $J(\mathbf{w})$, which is constructed using statistics of stochastic process $\{\mathbf{QoI}(\omega)\}$, $\omega \in [\omega_{\min}, \omega_{\max}]$. The optimal value of $\mathbf{w}^{\text{opt}}$ is then obtained by solving the following optimization problem,

$$\mathbf{w}^{\text{opt}} = \min_{\mathbf{w} \in \mathcal{C}_w} J(\mathbf{w}) \,. \tag{1.112}$$

1.15.2 Example of objective function

We consider the stochastic computational model for which the complex matrix $[\mathbb{Z}(\omega; \mathbf{w})]$ in Eq. (1.97) is modeled by random complex matrix $[\mathbf{Z}(\omega; \mathbf{w})]$ and the complex matrix $[\mathbb{A}(\omega)]$ in Eq. (1.97) is modeled by a random complex matrix $[\mathbf{A}(\omega)]$. These two random complex matrices are written, taking into account Eqs. (1.103), (1.104), and (1.105), as

$$[\mathbf{Z}(\omega; \mathbf{w})] = [\mathbf{Z}^{\text{NS}}(\omega; \mathbf{w})] + j\, [\mathbf{Z}^{\text{S}}_I(\omega; \mathbf{w})] \,, \tag{1.113}$$

and

$$[\mathbf{A}(\omega)] = [\mathbf{A}_R(\omega)] + j\, [\mathbf{A}_I(\omega)] \,, \tag{1.114}$$

in which $[\mathbf{Z}^{\text{NS}}(\omega; \mathbf{w})]$ and $[\mathbf{A}(\omega)]$ are random complex matrices (not Hermitian, not symmetric, not skew-symmetric) and where random variable $[\mathbf{Z}^{\text{S}}_I(\omega; \mathbf{w})]$ is with values in the set of all the positive-definite symmetric real matrices. Consequently, at a given frequency ω, the pressure in the far-field (in the outer domain) in a given direction ξ (angle in *rad* defining the direction) is a complex-valued random variable denoted by $P(\omega, \xi)$. Let $\{\omega_1, \ldots, \omega_{n_\omega}\}$ be the set of the n_ω frequencies of interest and let $\{\xi_1, \ldots, \xi_{n_\xi}\}$ be the set of the n_ξ angles of interest for which we want to minimize the pressure. Let $\{s_{jk}, j = 1, \ldots, n_\omega,\ k = 1, \ldots, n_\xi\}$ some positive weights that allow for favoring certain frequencies and certain angles. The weights must be such that $\sum_j \sum_k = s_{jk} = 1$. The objective function will be, for instance, of the following type,

$$J(\mathbf{w}) = E\left\{ \frac{1}{n_\omega + n_\xi} \sum_{j=1}^{n_\omega} \sum_{k=1}^{n_\xi} s_{jk} \left| P(\omega_j, \xi_k; \mathbf{w}) \right|^2 \right\} , \tag{1.115}$$

in which E is the mathematical expectation.

Let $\mathbf{QoI}(\omega; \mathbf{w}) = \{\text{QoI}_1(\omega; \mathbf{w}), \ldots, \text{QoI}_{\text{n}_\xi}(\omega; \mathbf{w})\}$ be the random vector such that $\text{QoI}_{\text{k}}(\omega; \mathbf{w}) = \text{P}(\omega, \xi_{\text{k}}; \mathbf{w})$. Consequently, the set $\{P(\omega_j, \xi_k; \mathbf{w}),\ j = 1, \ldots, n_\omega,\ k = 1, \ldots, n_\xi\}$ of random quantities of interest is represented by the set of random vectors $\{\mathbf{QoI}(\omega_j; \mathbf{w}), j = 1, \ldots, n_\omega\}$.

1.15.3 Computation of the objective function

From Eq. (1.97), the random vector $\mathbf{Q}(\omega)$ is solution of the random complex matrix equation,

$$([\mathbf{A}(\omega)] + [\mathbf{Z}(\omega;\mathbf{w})])\,\mathbf{Q}(\omega;\mathbf{w}) = [\mathbb{B}(\omega)]\,\mathbf{c}^{+}\,, \tag{1.116}$$

and the random $\mathbf{QoI}(\omega;\mathbf{w})$ is given by Eq. (1.107) that is rewritten as,

$$\mathbf{QoI}(\omega;\mathbf{w}) = [\mathbb{F}_{\mathrm{qoI}}(\omega)]\,\mathbf{c}^{+} - [\mathbb{A}_{\mathrm{qoI}}(\omega)]\,\mathbf{Q}(\omega;\mathbf{w})\,, \tag{1.117}$$

in which, matrices $[\mathbb{F}_{\mathrm{qoI}}(\omega)]$ and $[\mathbb{A}_{\mathrm{qoI}}(\omega)]$ are defined by Eq. (1.108) and Eq. (1.109).

It should be noted that, in the proposed probabilistic model of uncertainties, matrix $[\mathbb{B}(\omega)]$ is kept as a deterministic matrix, although the reduced aeroacoustic matrix $[\mathbb{A}(\omega)]$ has been modeled by a random matrix for taking into account model uncertainties in the aeroacoustic part (see the explanations given in Chapter 2).

Chapter 2

Probabilistic approach for uncertainty quantification and stochastic solver

Contents

2.1 Brief summary of the nonparametric probabilistic approach of uncertainties **46**
2.2 Methodology for uncertainty quantification **46**
2.3 Construction of the probabilistic model of complex generalized liner impedance matrix. **48**
2.4 Construction of the probabilistic model of the generalized aeroacoustic matrix. **51**
2.5 Statistical dependence properties of random matrices. **52**
2.6 Parametric probabilistic modeling of the fan acoustic excitation . . **53**
2.7 Construction of the SROM by using the nonparametric probabilistic approach of uncertainties **56**
2.8 Stochastic solver **56**
2.9 Construction of a matrix representing the QoIs for a multiple load-cases **57**
2.10 Estimation of the robust-design objective function and convergence with respect to the number of realizations **57**
2.11 Implementation of the Monte Carlo solver **58**

Abstract: *In this chapter three sources of uncertainties are taken into account. The first one is related to uncertainties induced by modeling errors in the impedance matrix of the liner appearing in the reduced-order computational model. The second one corresponds to model uncertainties in the aeroacoustic part of the computational model (including the mean-flow already computed by CFD, the acoustic equations in moving fluids, and the duct acoustic related to the fan excitation). The third one is related to uncertainties in the acoustic excitation induced by the fan. The stochastic solver of the random equation is presented. For each value of the frequency, the stochastic reduced-order model (SROM) is solved by the Monte Carlo method. The convergence analysis is carried out with respect to the number of realizations.*

2.1 Brief summary of the nonparametric probabilistic approach of uncertainties

For a given flight condition and given environment, the boundary problem considered is that of aeroacoustics, the equations of which are that of the linearized convected acoustic wave equations formulated in the frequency domain. This aeroacoustic boundary problem depends on the geometry of the very complex and unbounded domain, on the boundary conditions and in particular the impedance of the liner that is an elastoacoustic system, on the physical parameters, on the velocity field of the flow, which is calculated by the CFD for the fixed flight condition, and on the acoustic excitation induced by the fan. The development of the aeroacoustic computational model for this boundary value problem requires the introduction of simplifications and approximations: simplification of the geometry and the representation describing the acoustic excitation of the fan, simplification of the internal geometry of the reactor, introduction of two vector bases for constructing the reduced-order computational model, and simplification of the elastoacoustic model to build the impedance of the liner. In this aeroacoustic problem there are many model uncertainties induced by modeling errors. It is known for a long time that model uncertainties cannot be taken into account by parametric probabilistic approaches. It is for this reason that the nonparametric probabilistic approach of model uncertainties was proposed in 2000 [54, 55, 57] and has given rise to numerous developments and validation works over the past 20 years, and has now become a standard method, which is, for example, implemented in commercial software such as MSC Nastran software.
Concepts, mathematical developments, and experimental validations can be found, for example, in [56, 60, 59], in particular in [58, 41, 60, 42] for elastoacoustic problems, and for more recent advances, for instance, in [2, 1]. Because of model uncertainties induced by modeling errors, the boundary value problem that is constructed, from which the computational model is derived, does not correspond to the physical reality that is modeled. It is therefore necessary to generate a stochastic family of boundary value problems whose solution space is large enough to contain the targets such as the experimental results. We recall that the family generated by a parametric approach does not allow the construction of such a family (see for example [60]). The so-called nonparametric probabilistic approach consists in generating this stochastic family by modeling operators of the boundary problems using random operators whose levels of statistical fluctuations, that is to say, the levels of uncertainty, are controlled by hyperparameters. The mathematical properties of the considered operators are preserved during the construction of the associated random operators. One thus generates a family of stochastic solutions, which obviously do not satisfy the initial boundary value problem by construction. If all the mathematical concepts and developments associated with the nonparametric probabilistic approach can be used for the aeroacoustic problem considered in this work, it is necessary to specify the algebraic properties of each random operator considered in order to use the appropriate subsets of random matrices and to build their probabilistic models. These are the developments that are presented in this chapter.

2.2 Methodology for uncertainty quantification

The three sources of uncertainties are involved as follows.
- The first one, which is related to modeling errors in the computational model of the impedance matrix of the liner, is taken into account by the nonparametric probabilistic approach.
- The second one, which corresponds to model uncertainties in the aeroacoustic part of the computational model including the mean velocity field generated by CFD, is also taken into account by the nonparametric approach.
- The third one, which is related to uncertainties in the fan acoustic excitation is accounted for by the parametric probabilistic approach.

Since the sources of uncertainties related to the impedance matrix of the liner are independent of the sources of uncertainties related to the aeroacoustic matrix, the two random matrices that model the impedance of the liner and the aeroacoustics are statistically independent. For the fan acoustic excitation, matrix $[\mathbb{B}(\omega)]$ is kept as a deterministic matrix in the proposed model of uncertainties, although the reduced aeroacoustic matrix $[\mathbb{A}(\omega)]$ is modeled by a random matrix for taking into account model uncertainties in the aeroacoustic part. This is a reasonable approximation that is introduced because the nonparametric probabilistic approach is implemented on the generalized coordinates (expanded on pellicular modes) and $[\mathbb{B}(\omega)]$ involves the physical coordinates.

All the random variables that are introduced in this chapter are defined on a probability space $(\Theta, \mathcal{T}, \mathcal{P})$.

(i) - Nonparametric probabilistic approach of uncertainties in the liner.

We use the nonparametric probabilistic approach introduced in [54], developed and detailed in [60], which allows for taking into account both the parametric uncertainties and the model uncertainties induced by modeling errors in the computational model of the liner impedance.

This approach is going to be used for taking into account uncertainties induced by the liner model in the nominal reduced-order computational model (ROM) of acoustic radiation of an inlet. Introducing such uncertainties allows for constructing a stochastic reduced-order computational model (SROM) that depends on the frequency.

The nonparametric probabilistic approach is based on the use of sets of random matrices that have especially been developed for that and whose mathematical constructions are summarized in [60]. For the uncertainties in the liner model, this approach requires the probabilistic construction of the complex random matrix $[\mathbf{Z}(\omega; \mathbf{w})]$, depending on the design parameter $\mathbf{w}$, which is defined (see Eq. (1.113)) by

$$[\mathbf{Z}(\omega; \mathbf{w})] = [\mathbf{Z}^{\mathrm{NS}}(\omega; \mathbf{w})] + j\, [\mathbf{Z}^{\mathrm{S}}_I(\omega; \mathbf{w})]\,. \tag{2.1}$$

The probabilistic model of $[\mathbf{Z}(\omega; \mathbf{w})]$ could be constructed by using a Hilbert transform between the real part and the imaginary part of $[\mathbf{Z}(\omega; \mathbf{w})]$ in order to take into account the causality of the dynamical system (as explained in [60]). Nevertheless, such a model is relatively difficult to implement but above all, generates a significant computational cost, which can be huge for the computational models such those used in the present work. Consequently, it is proposed to use another model for which the causality is not imposed but, which has the advantage to respect the algebraic properties of the random complex matrices, in particular the symmetry properties and the positive-definiteness of the matrix associated with a dissipation.

The proposed probabilistic model of random complex matrix $[\mathbf{Z}^{\mathrm{NS}}(\omega; \mathbf{w})]$ is thus constructed using the extension presented in [35] of the one introduced in [57] for rectangular real random matrices, while the probabilistic model of positive-definite symmetric real matrix $[\mathbf{Z}^{\mathrm{S}}_I(\omega; \mathbf{w})]$ is constructed using the set of positive-definite random matrices introduced in [54].

In this chapter, in order to simplify the notation, the design parameter $\mathbf{w}$ is removed from equations.

(ii) - Nonparametric probabilistic approach of uncertainties for the aeroacoustic part of the computational model.

As mentioned in Section 1.13.4, matrix $[\mathbb{A}(\omega)]$ cannot be splitted into conservative and dissipative parts. Consequently, the use of the nonparametric probabilistic approach for random matrix $[\mathbf{A}(\omega)]$ consists in modeling it in the subset of random matrices, that we have introduced for matrix $[\mathbf{Z}^{\text{NS}}(\omega)]$ related to the liner (see previous point *(i)*).

As for uncertainties related to the liner model, this approach is going to be used for taking into account model uncertainties induced by the mean-flow computation (CFD), the acoustic equations in moving fluids, the duct acoustic related to the fan excitation, and their approximations for constructing the computational model. These uncertainties are also integrated in the stochastic reduced-order computational model (SROM) mentionned in *(i)* as it can be viewed in Eq. (1.116).

The probabilistic model of random complex matrix $[\mathbf{A}(\omega)]$ is thus done similarly to $[\mathbf{Z}^{\text{NS}}(\omega)]$.

As previously explained, random matrix $[\mathbf{A}(\omega)]$ is assumed to be statistically independent of random matrix $[\mathbf{Z}(\omega)]$.

(iii) - Parametric probabilistic approach of uncertainties for the fan acoustic excitation.

The uncertainties for the complex vector $\mathbf{c}^+$ that has been introduced for describing the fan acoustic excitation (incident wave, see Eqs. (1.52)) and (1.69)) is modeled in the framework of parametric probabilistic approach [60] using the Maximum Entropy principle.

2.3 Construction of the probabilistic model of complex generalized liner impedance matrix.

2.3.1 Construction of the probabilistic model of random complex matrix $[\mathbf{Z}^{\text{NS}}(\omega)]$.

The positive real parameter ω represents the frequency and is assumed to be fixed.
For this construction, we first introduce the polar decomposition of deterministic complex matrix $[\mathbb{Z}^{\text{NS}}(\omega)]$ and then, we construct the complex random matrix $[\mathbf{Z}^{\text{NS}}(\omega)]$.

(i) - Polar decomposition of complex matrix $[\mathbb{Z}^{\text{NS}}(\omega)]$.

It is assumed that the $(n_\ell \times n_\ell)$ complex matrix $[\mathbb{Z}^{\text{NS}}(\omega)]$ is invertible. Therefore, it is proven below that $[\mathbb{Z}^{\text{NS}}(\omega)]$ can be written (polar decomposition) as,

$$[\mathbb{Z}^{\text{NS}}(\omega)] = [U_{\mathbb{Z}}(\omega)]\,[T_{\mathbb{Z}}(\omega)]\,, \tag{2.2}$$

in which $[U_{\mathbb{Z}}(\omega)]$ is a complex unitary matrix in $\mathbb{M}_{n_\ell}(\mathbb{C})$, which is such that,

$$[U_{\mathbb{Z}}(\omega)]^*\,[U_{\mathbb{Z}}(\omega)] = [I_{n_\ell}]\,, \tag{2.3}$$

in which $[U_{\mathbb{Z}}(\omega)]^* = \overline{[U_{\mathbb{Z}}(\omega)]}^T$, which belongs to $\mathbb{M}_{n_\ell}(\mathbb{C})$, is the transpose conjugate of matrix $[U_{\mathbb{Z}}(\omega)]$ and where $[I_{n_\ell}]$ is the $(n_\ell \times n_\ell)$ identity matrix. The matrix $[T_{\mathbb{Z}}(\omega)]$ belongs to the set $\mathbb{M}^+_{n_\ell}(\mathbb{C})$ of all the positive-definite Hermitian $(n_\ell \times n_\ell)$ complex matrices,

$$[T_{\mathbb{Z}}(\omega)] \in \mathbb{M}^+_{n_\ell}(\mathbb{C})\,. \tag{2.4}$$

This means that $[T_{\mathbb{Z}}(\omega)]$ is invertible, is such that $[T_{\mathbb{Z}}(\omega)]^* = [T_{\mathbb{Z}}(\omega)]$ (Hermitian symmetry), and is such that $\mathbf{z}^* [T_{\mathbb{Z}}(\omega)] \mathbf{z} > 0$ for all $\mathbf{z}$ in $\mathbb{C}^{n_\ell}$ such that $\|\mathbf{z}\| \neq 0$ where $\|\mathbf{z}\|$ is the Hermitian norm in $\mathbb{C}^{n_\ell}$.

The construction of the representation defined by Eq. (2.2) can be done as follows. As $[\mathbb{Z}^{\text{NS}}(\omega)]$ is assumed to be invertible, then the matrix $[H_{\mathbb{Z}}(\omega)]$ can be written as,

$$[H_{\mathbb{Z}}(\omega)] = [\mathbb{Z}^{\text{NS}}(\omega)]^* [\mathbb{Z}^{\text{NS}}(\omega)] , \tag{2.5}$$

which belongs to $\mathbb{M}^+_{n_\ell}(\mathbb{C})$ and consequently, its spectral decomposition can be written as

$$[H_{\mathbb{Z}}(\omega)] = [\Phi_{\mathbb{Z}}(\omega)] [S_{\mathbb{Z}}(\omega)] [\Phi_{\mathbb{Z}}(\omega)]^* , \tag{2.6}$$

in which $[S_{\mathbb{Z}}(\omega)]$ is the diagonal $(n_\ell \times n_\ell)$ real matrix of the positive eigenvalues of $[H(\omega)]$ and where $[\Phi_{\mathbb{Z}}(\omega)]$ is the $(n_\ell \times n_\ell)$ complex matrix of the eigenvectors such that $[\Phi_{\mathbb{Z}}(\omega)]^* [\Phi(\omega)] = [\Phi_{\mathbb{Z}}(\omega)] [\Phi_{\mathbb{Z}}(\omega)]^* = [I_{n_\ell}]$. Note that diagonal matrix $[S_{\mathbb{Z}}(\omega)]$ can also be viewed as the diagonal matrix of the singular values of complex matrix $[\mathbb{Z}^{\text{NS}}(\omega)]$. Let us define the matrix $[T_{\mathbb{Z}}(\omega)]$ by

$$[T_{\mathbb{Z}}(\omega)] = [\Phi_{\mathbb{Z}}(\omega)] [S_{\mathbb{Z}}(\omega)]^{1/2} [\Phi_{\mathbb{Z}}(\omega)]^* . \tag{2.7}$$

It can be seen that $[T_{\mathbb{Z}}(\omega)]$ belongs to $\mathbb{M}^+_{n_\ell}(\mathbb{C})$. Let $[U_{\mathbb{Z}}(\omega)]$ be the complex matrix in $\mathbb{M}_{n_\ell}(\mathbb{C})$ defined (see Eq. (2.2)) by,

$$[U_{\mathbb{Z}}(\omega)] = [\mathbb{Z}^{\text{NS}}(\omega)] [T_{\mathbb{Z}}(\omega)]^{-1} . \tag{2.8}$$

Therefore, it can be verified that $[U_{\mathbb{Z}}(\omega)]^* [U_{\mathbb{Z}}(\omega)] = [I_{n_\ell}]$.

(ii) - Probabilistic model of random complex matrix $[\boldsymbol{Z}^{\text{NS}}(\omega)]$.

Let $[\mathbb{Z}^{\text{NS}}(\omega)]$ be the invertible complex matrix for which its polar decomposition, $[\mathbb{Z}^{\text{NS}}(\omega)] = [U_{\mathbb{Z}}(\omega)] [T_{\mathbb{Z}}(\omega)]$, is defined in paragraph 2.3.1. In this section, we perform the construction of the complex random matrix $[\mathbf{Z}^{\text{NS}}(\omega)]$, defined on a probability space $(\Theta, \mathcal{T}, \mathcal{P})$, with values in $\mathbb{M}_{n_\ell}(\mathbb{C})$, associated with $[\mathbb{Z}^{\text{NS}}(\omega)]$, which is written as,

$$[\mathbf{Z}^{\text{NS}}(\omega)] = [U_{\mathbb{Z}}(\omega)] [\mathbf{T}_{\mathbb{Z}}(\omega)] , \tag{2.9}$$

in which $[\mathbf{T}_{\mathbb{Z}}(\omega)]$ is a complex random matrix, defined on $(\Theta, \mathcal{T}, \mathcal{P})$, with values in $\mathbb{M}^+_{n_\ell}(\mathbb{C})$, and of second-order, that is to say,

$$E\{\|[\mathbf{T}_{\mathbb{Z}}(\omega)]\|_F^2\} = \int_\Theta \|[\mathbf{T}_{\mathbb{Z}}(\omega;\theta)]\|_F^2 \, d\mathcal{P}(\theta) < +\infty , \tag{2.10}$$

in which E is the mathematical expectation, where the Frobenius norm $\|[a]\|_F$ of a complex matrix $[a]$ in $\mathbb{M}_{n_\ell}(\mathbb{C})$ is such that $\|[a]\|_F^2 = \text{tr}\{[a]^* [a]\}$ where tr is the trace of a matrix.

The probabilistic construction of random matrix $[\mathbf{T}_{\mathbb{Z}}(\omega)]$ is performed as follows. As the deterministic complex matrix $[T_{\mathbb{Z}}(\omega)]$ belongs to $\mathbb{M}^+_{n_\ell}(\mathbb{C})$, its Cholesky factorization is written as,

$$[T_{\mathbb{Z}}(\omega)] = [L^{\mathbb{Z}}_T(\omega)]^* [L^{\mathbb{Z}}_T(\omega)] , \tag{2.11}$$

in which $[L^{\mathbb{Z}}_T(\omega)]$ is an upper triangular $(n_\ell \times n_\ell)$ complex matrix with positive diagonal. Let $\varepsilon > 0$ be a fixed positive small parameter ($\varepsilon \ll 1$). The random complex matrix $[\mathbf{T}_{\mathbb{Z}}(\omega)]$ with values in $\mathbb{M}^+_{n_\ell}(\mathbb{C})$, is then constructed as,

$$[\mathbf{T}_{\mathbb{Z}}(\omega)] = [L^{\mathbb{Z}}_T(\omega)]^* [\mathbf{G}^{\text{NS}}_{\mathbb{Z}}] [L^{\mathbb{Z}}_T(\omega)] , \tag{2.12}$$

in which the random $(n_\ell \times n_\ell)$ real matrix $[\mathbf{G}_{\mathbb{Z}}^{\text{NS}}]$ belongs to the set SG_ε^+ of random matrices defined below.

Definition and construction of the set SG_ε^+ of random matrices [60]. A random $(n_\ell \times n_\ell)$ real matrix $[\mathbf{G}_{\mathbb{Z}}^{\text{NS}}]$ belonging to SG_ε^+ is a random matrix with values in $\mathbb{M}_{n_\ell}^+(\mathbb{R})$, which is independent of parameter ω, and which is written as,

$$[\mathbf{G}_{\mathbb{Z}}^{\text{NS}}] = \frac{1}{1+\varepsilon}\{[\mathbf{G}_{0,\mathbb{Z}}^{\text{NS}}] + \varepsilon[I_{n_\ell}]\}\,, \tag{2.13}$$

in which $[\mathbf{G}_{0,\mathbb{Z}}^{\text{NS}}]$ is a random $(n_\ell \times n_\ell)$ real matrix with values in $\mathbb{M}_{n_\ell}^+(\mathbb{R})$, defined on $(\Theta, \mathcal{T}, \mathcal{P})$, independent of parameter ω, and which belongs to the set SG_0^+ of random matrices defined in [60]. Random matrix $[\mathbf{G}_{0,\mathbb{Z}}^{\text{NS}}]$ has been constructed using the Maximum Entropy principle under the constraints defined by the following available information,

$$E\{[\mathbf{G}_{0,\mathbb{Z}}^{\text{NS}}]\} = [I_{n_\ell}] \quad , \quad E\{\log(\det[\mathbf{G}_{0,\mathbb{Z}}^{\text{NS}}])\} = \nu_{G_{0,\mathbb{Z}}} \quad , \quad |\nu_{G_{0,\mathbb{Z}}} < +\infty|\,. \tag{2.14}$$

in which $\nu_{G_{0,\mathbb{Z}}}$ is any constant such that $|\nu_{G_{0,\mathbb{Z}}}| < +\infty$. The probability distribution obtained for $[\mathbf{G}_{0,\mathbb{Z}}^{\text{NS}}]$ is not Gaussian and depends on constant $\nu_{G_{0,\mathbb{Z}}}$. This probability distribution is reparameterized with the dispersion parameter $\delta_{\text{G},\mathbb{Z}}^{\text{NS}}$, which is assumed to be independent of parameter ω, defined by,

$$\delta_{\mathbb{Z}}^{\text{NS}} = \left\{ \frac{E\{||\,[\mathbf{G}_{0,\mathbb{Z}}^{\text{NS}}] - E\{[\mathbf{G}_{0,\mathbb{Z}}^{\text{NS}}]\}\,||_F^2\}}{||E\{[\mathbf{G}_{0,\mathbb{Z}}^{\text{NS}}]\}||_F^2} \right\}^{1/2} = \left\{ \frac{1}{n_\ell} E\{||\,[\mathbf{G}_{0,\mathbb{Z}}^{\text{NS}}] - [I_{n_\ell}]\,||_F^2\} \right\}^{1/2}. \tag{2.15}$$

Consequently, the probability distribution of the non-Gaussian random matrix $[\mathbf{G}_{0,\mathbb{Z}}^{\text{NS}}]$ depends only on one hyperparameter that is $\delta_{\mathbb{Z}}^{\text{NS}}$. This hyperparameter allows for controlling the level of statistical fluctuations, that is to say, for controlling the level of uncertainties.

Using $E\{[\mathbf{G}_{0,\mathbb{Z}}^{\text{NS}}]\} = [I_{n_\ell}]$, Eq. (2.13) yields $E\{[\mathbf{G}_{\mathbb{Z}}^{\text{NS}}]\} = [I_{n_\ell}]$. From Eqs. (2.11) and (2.12), it can then be deduced that $E\{[\mathbf{T}_{\mathbb{Z}}(\omega)]\} = [T_{\mathbb{Z}}(\omega)]$. Therefore, Eqs. (2.2) and (2.9) show that

$$E\{[\mathbf{Z}^{\text{NS}}(\omega)]\} = [\mathbb{Z}^{\text{NS}}(\omega)]\,. \tag{2.16}$$

Using the previous equations, it can be seen that any realization $[\mathbf{Z}^{\text{NS}}(\omega;\theta)]$ of random matrix $[\mathbf{Z}^{\text{NS}}(\omega)]$, with θ in Θ, is computed by using the following formulas,

$$[\mathbf{Z}^{\text{NS}}(\omega,\theta)] = [U_{\mathbb{Z}}(\omega)]\,[\mathbf{T}_{\mathbb{Z}}(\omega;\theta)]\,, \tag{2.17}$$

$$[\mathbf{T}_{\mathbb{Z}}(\omega;\theta)] = [L_T^{\mathbb{Z}}(\omega)]^*\,[\mathbf{G}_{\mathbb{Z}}^{\text{NS}}(\theta)]\,[L_T^{\mathbb{Z}}(\omega)]\,, \tag{2.18}$$

$$[\mathbf{G}_{\mathbb{Z}}^{\text{NS}}(\theta)] = \frac{1}{1+\varepsilon}\{[\mathbf{G}_{0,\mathbb{Z}}^{\text{NS}}(\theta)] + \varepsilon[I_{n_\ell}]\}\,, \tag{2.19}$$

in which $\varepsilon = 1e^{-13}$ and in which the realization $[\mathbf{G}_{0,\mathbb{Z}}^{\text{NS}}(\theta)]$ is computed by using the following representation of random matrix $[\mathbf{G}_{0,\mathbb{Z}}^{\text{NS}}]$,

$$[\mathbf{G}_{0,\mathbb{Z}}^{\text{NS}}] = [\mathbf{L}_{\mathbb{Z}}^{\text{NS}}]^T\,[\mathbf{L}_{\mathbb{Z}}^{\text{NS}}]\,, \tag{2.20}$$

in which $[\mathbf{L}_{\mathbb{Z}}^{\text{NS}}]$ is an upper triangular random matrix with values in $\mathbb{M}_{n_\ell}(\mathbb{R})$ such that,

1. the random variables $\{[\mathbf{L}_{\mathbb{Z}}^{\text{NS}}]_{jj'}, j \le j'\}$ are mutually independent.
2. for $j < j'$, we have $[\mathbf{L}_{\mathbb{Z}}^{\text{NS}}]_{jj'} = \sigma_{\text{G},\mathbb{Z}}^{\text{NS}}\mathcal{G}_{\text{G},\mathbb{Z}_{jj'}}^{\text{NS}}$ in which $\sigma_{\text{G},\mathbb{Z}}^{\text{NS}} = \delta_{\text{G},\mathbb{Z}}^{\text{NS}}\,(n_\ell+1)^{-1/2}$ and where $\mathcal{G}_{\text{G},\mathbb{Z}_{jj'}}^{\text{NS}}$ is a real-valued Gaussian random variable with zero mean and with a variance that is equal to 1.

3. for $j = j'$, we have $[\mathbf{L}^{\text{NS}}_{\text{G},\mathbb{Z}}]_{jj} = \sigma^{\text{NS}}_{\text{G},\mathbb{Z}}\sqrt{2\mathcal{V}^{\text{NS}}_{\text{G},\mathbb{Z}_j}}$ where $\mathcal{V}^{\text{NS}}_{\text{G},\mathbb{Z}_j}$ is a positive-valued Gamma random variable whose probability density function with respect to dv is written as

$$p_{\mathcal{V}^{\text{NS}}_{\text{G},\mathbb{Z}_j}}(v) = \mathbb{1}_{\mathbb{R}^+}(v)\frac{1}{\Gamma\left(\frac{n_\ell+1}{2(\delta^{\text{NS}}_{\text{G},\mathbb{Z}})^2}+\frac{1-j}{2}\right)}\, v^{\frac{n_\ell+1}{2(\delta^{\text{NS}}_{\text{G},\mathbb{Z}})^2}-\frac{1+j}{2}}\; e^{-v}\,. \tag{2.21}$$

The random variable $\nu^{\text{NS}}_{\mathbb{Z}\,j}$ can be rewritten as the nonlinear transformation $h(\mathcal{G}^{\text{NS}}_{\text{G},\mathbb{Z}_{jj}}; n_\ell; \delta^{\text{NS}}_{\text{G},\mathbb{Z}})$ of a real-valued Gaussian random variable $\mathcal{G}^{\text{NS}}_{\text{G},\mathbb{Z}_{jj}}$ with zero mean and with a variance that is equal to 1.

4. The Gaussian random variables $\{\mathcal{G}^{\text{NS}}_{\text{G},\mathbb{Z}_{jj'}}, 1 \le j \le j' \le n_\ell\}$ are statistically independent.

Remarks.

1. The algebraic representation defined by Eq. (2.20) shows that although the entries $\{[\mathbf{L}^{\text{NS}}_{\mathbb{Z}}]_{jj'}, j \le j'\}$ of $[\mathbf{L}^{\text{NS}}_{\mathbb{Z}}]$ are mutually independent, the entries $\{[\mathbf{G}^{\text{NS}}_{0,\mathbb{Z}}]_{jj'}, j \le j'\}$ of $[\mathbf{G}^{\text{NS}}_{0,\mathbb{Z}}]$ are mutually dependent.

2. The diagonal entries $[\mathbf{L}^{\text{NS}}_{\mathbb{Z}}]_{jj}, j = 1, \ldots, n_\ell$ of random matrix $[\mathbf{L}^{\text{NS}}_{\mathbb{Z}}]$ depend on j.

2.3.2 Construction of the probabilistic model of positive-definite symmetric real random matrix $[\mathbf{Z}^{\text{S}}_I(\omega)]$.

The construction of the positive-definite symmetric real $(n_\ell \times n_\ell)$ matrix $[\mathbb{Z}^{\text{S}}_I(\omega)]$ is written as

$$[\mathbb{Z}^{\text{S}}_I(\omega)] = [L^{\text{S}}_{\mathbb{Z}}(\omega)]^*\,[L^{\text{S}}_{\mathbb{Z}}(\omega)]\,, \tag{2.22}$$

in which $[L^{\text{S}}_{\mathbb{Z}}(\omega)]$ is an upper triangular $(n_\ell \times n_\ell)$ complex matrix with positive diagonal. Let $\varepsilon > 0$ be a fixed positive small parameter ($\varepsilon \ll 1$). The random complex matrix $[\mathbf{Z}^{\text{S}}_I(\omega)]$ with values in $\mathbb{M}^+_{n_\ell}(\mathbb{C})$, is then constructed as,

$$[\mathbf{Z}^{\text{S}}_I(\omega)] = [L^{\text{S}}_{\mathbb{Z}}(\omega)]^*\,[\mathbf{G}^{\text{S}}_{\mathbb{Z}}]\,[L^{\text{S}}_{\mathbb{Z}}(\omega)]\,, \tag{2.23}$$

in which $[\mathbf{G}^{\text{S}}_{\mathbb{Z}}]$ is a random matrix belonging to the set SG^+_ε defined and constructed in Section 2.3, for which the hyperparameter is $\delta^{\text{S}}_{\text{G},\mathbb{Z}}$ and allows for controling the level of uncertainties.

2.4 Construction of the probabilistic model of the generalized aeroacoustic matrix.

2.4.1 Construction of the probabilistic model of random complex matrix $[\mathbf{A}(\omega)]$.

For this construction, we use the polar decomposition of deterministic complex matrix $[\mathbb{A}(\omega)]$ presented in Section 2.3.1-(i) and then, we construct the complex random matrix $[\mathbf{A}(\omega)]$, using the nonparametric probabilistic approach described in Section 2.3.1-(ii).

(i) - Polar decomposition of complex matrix $[\mathbb{A}(\omega)]$.

As explained in Section 2.3.1-*(i)*, the $(n_\ell \times n_\ell)$ complex matrix $[\mathbb{A}(\omega)]$ can be written (polar decomposition) as,

$$[\mathbb{A}(\omega)] = [U_{\mathbb{A}}(\omega)]\,[T_{\mathbb{A}}(\omega)]\,, \tag{2.24}$$

in which $[U_{\mathbb{A}}(\omega)]$ is a complex unitary matrix in $\mathbb{M}_{n_\ell}(\mathbb{C})$, which is such that,

$$[U_{\mathbb{A}}(\omega)]^* [U_{\mathbb{A}}(\omega)] = [I_{n_\ell}] , \tag{2.25}$$

and where $[T_{\mathbb{A}}(\omega)]$ is a positive-definite Hermitian matrix that belongs to the set $\mathbb{M}^+_{n_\ell}(\mathbb{C})$,

$$[T_{\mathbb{A}}(\omega)] \in \mathbb{M}^+_{n_\ell}(\mathbb{C}) . \tag{2.26}$$

(ii) - Probabilistic model of random complex matrix $[\boldsymbol{A}(\omega)]$.

Matrix $[\mathbb{A}(\omega)]$ is modeled by the random matrix $[\mathbf{A}(\omega)]$ using the representation defined by Eq. (2.24), in which matrix $[T_{\mathbb{A}}(\omega)]$ is modeled by a random matrix $[\mathbf{T}_{\mathbb{A}}(\omega)]$ as performed in Section 2.3.1.
The probabilistic construction of random matrix $[\mathbf{T}_{\mathbb{A}}(\omega)]$ is performed in a similar way as it is done for the randomization of $[\mathbf{T}_{\mathbb{Z}}(\omega)]$ in Section 2.3.1-*(ii)*. As the deterministic complex matrix $[T_{\mathbb{A}}(\omega)]$ belongs to $\mathbb{M}^+_{n_\ell}(\mathbb{C})$, its Cholesky factorization is written as,

$$[T_{\mathbb{A}}(\omega)] = [L^{\mathbb{A}}_T(\omega)]^* [L^{\mathbb{A}}_T(\omega)] , \tag{2.27}$$

in which $[L^{\mathbb{A}}_T(\omega)]$ is an upper triangular $(n_\ell \times n_\ell)$ complex matrix with positive diagonal. Let $\varepsilon > 0$ be a fixed positive small parameter ($\varepsilon \ll 1$). The random complex matrix $[\mathbf{T}_{\mathbb{A}}(\omega)]$ with values in $\mathbb{M}^+_{n_\ell}(\mathbb{C})$, is then constructed as,

$$[\mathbf{T}_{\mathbb{A}}(\omega)] = [L^{\mathbb{A}}_T(\omega)]^* [\mathbf{G}_{\mathbb{A}}] [L^{\mathbb{A}}_T(\omega)] , \tag{2.28}$$

in which the random $(n_\ell \times n_\ell)$ real matrix $[\mathbf{G}_{\mathbb{A}}]$ belongs to the set $\mathrm{SG}^+_\varepsilon$ of random matrices defined in Section 2.3.1-(ii), for which the hyperparameter is $\delta_{\mathrm{G},\mathbb{A}}$ and allows for controling the level of uncertainties.

2.5 Statistical dependence properties of random matrices.

2.5.1 Statistical dependence properties of random matrices $[\mathbf{Z}^{\mathrm{NS}}(\omega)]$ and $[\mathbf{Z}^{\mathrm{S}}_I(\omega)]$

As explained in Sections 2.3 and 2.4, the level of uncertainties of random matrices $[\mathbf{Z}^{\mathrm{NS}}(\omega)]$ and $[\mathbf{Z}^{\mathrm{S}}_I(\omega)]$ is controled by hyperparameters $\delta^{\mathrm{NS}}_{\mathrm{G},\mathbb{Z}}$ and $\delta^{\mathrm{S}}_{\mathrm{G},\mathbb{Z}}$ that are used in the construction of random matrices $[\mathbf{G}^{\mathrm{NS}}_{\mathbb{Z}}]$ and $[\mathbf{G}^{\mathrm{S}}_{\mathbb{Z}}]$. The introduction of statistical dependencies between $[\mathbf{Z}^{\mathrm{NS}}(\omega)]$ and $[\mathbf{Z}^{\mathrm{S}}_I(\omega)]$ can only be done by the introduction of statistical dependencies between $[\mathbf{G}^{\mathrm{NS}}_{\mathbb{Z}}]$ and $[\mathbf{G}^{\mathrm{S}}_{\mathbb{Z}}]$. Two stochastic models related to the description of dependencies are proposed below.

(i) There is no available information concerning the dependencies and the Maximum Entropy principle is used. Therefore, the result of the Maximum Entropy principle is that the two random matrices are independent, which means that random matrices $[\mathbf{G}^{\mathrm{NS}}_{\mathbb{Z}}]$ and $[\mathbf{G}^{\mathrm{S}}_{\mathbb{Z}}]$ are taken as independent random matrices.

(ii) It is assumed that the sources of uncertainties are the same for the two random matrices. Consequently, these matrices are perfectly statistically dependent, but their level of uncertainties can be different ($\delta^{\mathrm{NS}}_{\mathrm{G},\mathbb{Z}}$ not equal to $\delta^{\mathrm{S}}_{\mathrm{G},\mathbb{Z}}$). In this case, the proposed stochastic model consists in choosing the same family of independent Gaussian random variables $\{\mathcal{G}^{\mathrm{NS}}_{\mathbb{Z}\,jj'}, 1 \leq j \leq j' \leq n_\ell\}$ for the constuction of $[G^{\mathrm{NS}}_{\mathbb{Z}}]$ and $\{\mathcal{G}^{\mathrm{S}}_{\mathbb{Z}jj'}, 1 \leq j \leq j' \leq n_\ell\}$ for $[G^{\mathrm{S}}_{\mathbb{Z}}]$, that is to say, $\mathcal{G}^{\mathrm{NS}}_{\mathbb{Z}\,jj'} = \mathcal{G}^{\mathrm{S}}_{\mathbb{Z}jj'}$ for all j and j'.

2.5.2 Statistical dependence properties of stochastic processes $\{[\mathbf{Z}(\omega)],\ \omega \in [\omega_{\min}, \omega_{\max}]\}$, $\{[\mathbf{A}(\omega)], \omega \in [\omega_{\min}, \omega_{\max}]\}$, and $\{\mathbf{C}^+(\omega),\ \omega \in [\omega_{\min}, \omega_{\max}]\}$

(i) - For all ω fixed in $[\omega_{\min}, \omega_{\max}]$, the random matrices $[\mathbf{A}(\omega)]$ and $[\mathbf{Z}(\omega)]$, and the random vector $\mathbf{C}^+(\omega)$, are statistically independent (see the explanations given at the begining of Section 2.2).

(ii) - Since the random matrices $[\mathbf{G}_{\mathbb{Z}}^{\mathrm{NS}}]$ and $[\mathbf{G}_{\mathbb{Z}}^{\mathrm{S}}]$ are independent of ω, for any finite partition $\omega_1, \ldots, \omega_{n_\omega}$, the random matrices $[\mathbf{Z}(\omega_1)], \ldots, [\mathbf{Z}(\omega_{n_\omega})]$ are statistically dependent.

(iii) - Similarly, since the random matrix $[\mathbf{G}_{\mathbb{A}}]$ is independent of ω, for any finite partition $\omega_1, \ldots, \omega_{n_\omega}$, the random matrices $[\mathbf{A}(\omega_1)], \ldots, [\mathbf{A}(\omega_{n_\omega})]$ are statistically dependent.

(iv) - The random vectors $[\mathbf{C}^+(\omega_1), \ldots, \mathbf{C}^+(\omega_{n_\omega})]$, are dependent or independent following the probabilistic model that is used.

2.6 Parametric probabilistic modeling of the fan acoustic excitation

There are two possible approaches, described in Sections 2.6.1 and 2.6.2 for constructing the parametric probabilistic model of the fan excitation. The first one consists in using the modal components $\{c_\alpha^+, \alpha = 1, \ldots, N_d\}$, while the second one uses the modal intensity $\{I_\alpha^+, \alpha = 1, \ldots, N_d\}$ of the duct modes. The choice is oriented by the available information in the result file (output) of Actran/TM.

2.6.1 Probabilistic modeling of complex vector c^+

In order to take into account the uncertainties on the complex vector $\mathbf{c}^+$ that has been introduced for describing the fan acoustic excitation (incident wave, see Eqs. (1.52) and (1.69)), vector $\mathbf{c}^+$ is modeled by a random vector $\mathbf{C}^+$ with values in $\mathbb{C}^{N_d}$. This random vector $\mathbf{C}^+(\omega)$ depends on frequency ω. Nevertheless, in order to simplify the notation, this frequency dependence will be removed in Section 2.6. The methodology used for performing the probabilistic construction is based on the use of the Maximum Entropy principle. The first step consists in defining the nominal value of $\mathbf{c}^+$, the second one in defining the available information, and the third one in applying the Maximum Entropy principle under the constraints defined by the available information.

(i) Nominal value. For α fixed in $\{1, \ldots, N_d\}$, the component c_α^+ of vector $\mathbf{c}^+ = (c_1^+, \ldots, c_{N_d}^+)$ is written as,

$$c_\alpha^+ = \underline{a}_\alpha \, e^{j\underline{\varphi}_\alpha} \,, \tag{2.29}$$

in which $\underline{a}_\alpha$ is the amplitude and $\underline{\varphi}_\alpha$ is the phase. The nominal value of vector $\mathbf{c}^+$ is then represented by the vector $\underline{\mathbf{a}} = (\underline{a}_1, \ldots, \underline{a}_{N_d})$ of the nominal values of the amplitudes and the vector $\underline{\boldsymbol{\varphi}} = (\underline{\varphi}_1, \ldots, \underline{\varphi}_{N_d})$ of the nominal values of the phases. The nominal values are assumed to be given and consequently, the deterministic vectors $\underline{\mathbf{a}}$ and $\underline{\boldsymbol{\varphi}}$ are given.

(ii) Available information. The component α of random vector $\mathbf{C}^+ = (C_1^+, \ldots, C_{N_d}^+)$ is written as,

$$C_\alpha^+ = A_\alpha^+ \, e^{j\Phi_\alpha^+} \,. \tag{2.30}$$

We then introduce the random vector $\mathbf{A}^+ = (A_1^+, \ldots, A_{N_d}^+)$ of the amplitudes, and the random vector $\mathbf{\Phi}^+ = (\Phi_1^+, \ldots, \Phi_{N_d}^+)$ of the phase. We then have to construct the probability distribution of the random variable $(\mathbf{A}^+, \mathbf{\Phi}^+)$ using the Maximum Entropy principle for which the available information is defined as follows.

For α in $\{1, \ldots, N_d\}$,

1. A_α^+ is a second-order random variable with values in $\mathbb{R}^+$.
2. The mean value of A_α^+ is $\underline{a}_\alpha$, that is to say, $E\{A_\alpha^+\} = \underline{a}_\alpha$.
3. For $a \to 0_+$ (0_+ denotes 0 by upper values), the probability density function $a \mapsto p_{A_\alpha^+}(a)$ must go to zero (if not, the value of $p_{A_\alpha^+}(0)$ should be given and we have no information about this). The weak constraint that allows for imposing this condition is $E\{\log(A_\alpha^+)\} = b_\alpha^+$ in which $|b_\alpha^+| < +\infty$ and where log is a Neperian logarithm. This unknown constant b_α^+ will be reexpressed in terms of the coefficient of variation $\delta_\alpha = \sigma_\alpha / \underline{a}_\alpha$ of random variable A_α^+ in which σ_α is the standard deviation of A_α^+. This coefficient of variation is unknown and is, either used as a sensitivity parameter with respect to the level of uncertaities, or identified if experimental results are available.
4. Φ_α^+ is a second-order random variable that is centered in the nominal value $\underline{\varphi}_\alpha$ that is to say, $E\{\Phi_\alpha^+\} = \underline{\varphi}_\alpha$.
5. The random variable Φ_α^+ is with values in $[\underline{\varphi}_\alpha - \pi\,, \underline{\varphi}_\alpha + \pi]$.

(iii) Maximum Entropy principle. We have to construct the probability density function $(\mathbf{a}, \boldsymbol{\varphi}) \mapsto p_{\mathbf{A}^+, \mathbf{\Phi}^+}(\mathbf{a}, \boldsymbol{\varphi})$ of random variable $(\mathbf{A}^+, \mathbf{\Phi}^+)$, which is defined on $\{\prod_{\alpha=1}^{N_d} \mathbb{R}^+\} \times \{\prod_{\alpha=1}^{N_d} [\underline{\varphi}_\alpha - \pi\,, \underline{\varphi}_\alpha + \pi]\}$. Applying the Maximum Entropy principle under the constraints defined by *(ii)*-1 to *(ii)*-5 yields the following results ([60]):

1. The random variables $A_1^+, \ldots, A_{N_d}^+, \Phi_1^+, \ldots, \Phi_{N_d}^+$ are statistically independent, which means that

$$p_{\mathbf{A}^+, \mathbf{\Phi}^+}(\mathbf{a}, \boldsymbol{\varphi}) = \prod_{\alpha=1}^{N_d} \{p_{A_\alpha^+}(a_\alpha) p_{\Phi_\alpha^+}(\varphi_\alpha)\}\,, \tag{2.31}$$

   in which $\mathbf{a} = (a_1, \ldots, a_{N_d})$ and $\boldsymbol{\varphi} = (\varphi_1, \ldots, \varphi_{N_d})$. It should be noted that this result is due to the fact that no information is given concerning the dependencies of the components of random variables $\mathbf{A}^+$ and $\mathbf{\Phi}^+$.

2. For α in $\{1, \ldots, N_d\}$, the probability density function $p_{A_\alpha^+}$ of random variable A_α^+ is a gamma pdf that is written as

$$p_{A_\alpha^+}(a_\alpha) = \mathbb{1}_{]0\,, +\infty[}(a_\alpha) \frac{(\delta_\alpha^{-2})^{\delta_\alpha^{-2}}}{\Gamma(\delta_\alpha^{-2})\, \underline{a}_\alpha} \left(\frac{a_\alpha}{\underline{a}_\alpha}\right)^{\delta_\alpha^{-2}-1} \exp\{-\frac{a_\alpha}{\delta_\alpha^2 \underline{a}_\alpha}\}\,, \tag{2.32}$$

   in which $0 \leq \delta_\alpha < 1/\sqrt{(2)}$ and where $\Gamma(\beta)$ is a Gamma function.
   The probability density function $p_{\Phi_\alpha^+}$ of random variable Φ_α^+ is a uniform pdf that is written as

$$p_{\Phi_\alpha^+}(\varphi_\alpha) = \frac{1}{2\pi} \mathbb{1}_{[\underline{\varphi}_\alpha - \pi\,, \underline{\varphi}_\alpha + \pi]}(\varphi_\alpha)\,. \tag{2.33}$$

Taking into account Eq. (2.33), random variable Φ_α^+ can be written as

$$\Phi_\alpha^+ = \underline{\varphi}_\alpha + \varepsilon_\alpha \pi \left(2U_\alpha^+ - 1\right), \tag{2.34}$$

in which U_α^+ is a uniform random variable on $[0\,,1]$ and where we have introduced the indicator ε_α whose value is zero or one. This parameter allows for killing the statistical fluctuations of the phase taking $\varepsilon_\alpha = 0$; if not $\varepsilon_\alpha = 1$.

(iv) Remarks concerning the use of the probabilistic model. For α fixed in $\{1, \ldots, N_d\}$,

1. if $\delta_\alpha = 0$, then the amplitude $A_\alpha^+ = \underline{a}_\alpha$ is deterministic and equal to the nominal value. In this case, $C_\alpha^+ = \underline{a}_\alpha\, e^{j\Phi_\alpha^+}$ is a random complex coefficient with deterministic modulus and random phase. In addition, if $\varepsilon_\alpha = 0$, then $C_\alpha^+ = c_\alpha^+$ is a complex deterministic coefficient equal to the nominal value.

2. if $\underline{a}_\alpha = 0$, then $A_\alpha^+ = 0$ because a gamma random variable with zero mean is equal to zero. In this case, the complex random coefficient C_α^+ is zero.

3. if $\underline{a}_\alpha > 0$, if $\delta_\alpha > 0$, and if $\varepsilon_\alpha = 0$, then the random complex coefficient C_α^+ is written as $C_\alpha^+ = A_\alpha^+\, e^{j\underline{\varphi}_\alpha}$. That is to say, the amplitude is random and the phase is deterministic.

2.6.2 Probabilistic modeling of the modal intensity of the fan excitation duct modes

Definition of the modal intensity I_α^+ In the present paragraph, the frequency ω is fixed and is removed for simplifying the writing. The acoustic pressure p is related to the velocity potential φ by Eq. (1.35), in which the velocity potential φ, given by Eq. (1.48), can be rewritten as

$$\varphi = \varphi^+ + \varphi^-\,, \tag{2.35}$$

where

$$\varphi^+(x,y,z) = \sum_\alpha c_\alpha^+ \varphi_\alpha(x,y) e^{jk_{z_\alpha} z}\,. \tag{2.36}$$

We then define p_α^+, using Eq. (1.35), by

$$p_\alpha^+ = -j\omega\rho_0 \varphi_\alpha^+ - \rho_0 \mathbf{v}_0 \cdot \boldsymbol{\nabla}\varphi_\alpha^+\,. \tag{2.37}$$

in which φ_α^+ is the contribution of mode α in φ^+. The modal intensity I_α^+, related to pressure p_α^+, is defined by

$$I_\alpha^+ = 10 \log_{10}\left(\frac{|p_\alpha^+|^2}{p_{\mathrm{ref}}^2}\right), \tag{2.38}$$

in which p_{ref} is a reference pressure.

Probabilistic model of I_α^+ The probabilistic model I_α^+ of the random modal intensity could be derived from the one used for C_α^+. Nevertheless, for civil aircraft applications, a deterministic model $\underline{I}_\alpha^+$ is often used by the manufacturers and this model has to be accounted for in the construction of the probabilistic model. This probabilistic model is thus constructed using $\underline{I}_\alpha^+$, which is chosen as the mean value of I_α^+. The available information concerning the positive random variable I_α^+ is its mean value $\underline{I}_\alpha^+$ and the amplitude of variations defined by a positive interval $\mathcal{I}_\alpha \subset \mathbb{R}^+$ depending on α and containing the mean value. In addition, there is no available information concerning the statistical dependence of the random variables $I_1^+, \ldots, I_{N_d}^+$.

Using the MaxEnt principle of Information Theory, it is concluded that the random variables $I_1^+, \ldots, I_{N_d}^+$ are statistically independent, and the probability distribution of each I_α^+ is uniform with support $\mathcal{I}_\alpha$ and with mean value $\underline{I}_\alpha^+$. Interval $\mathcal{I}_\alpha$ is parameterized using a positive hyperparameter $\sigma_\alpha > 0$ such that $\mathcal{I}_\alpha = [\underline{I}_\alpha^+(1-\sigma_\alpha)\,, \underline{I}_\alpha^+(1+\sigma_\alpha)]$. Therefore, the random variable I_α^+ can be written as

$$I_\alpha^+ = \underline{I}_\alpha^+(1+\sigma_\alpha U_\alpha) \quad , \quad 0 < \sigma_\alpha < 1\,, \tag{2.39}$$

in which U_α is a centered uniform random variable on the interval $[-1\,, 1]$.

2.7 Construction of the SROM by using the nonparametric probabilistic approach of uncertainties

From Eq. (1.106), the vector-valued random quantity of interest $\mathbf{QoI}(\omega)$ at frequency ω is written as,

$$\mathbf{QoI}(\omega) = [\mathbb{O}_{\rm obs}(\omega)]\boldsymbol{\Psi}_a(\omega)\,, \tag{2.40}$$

in which $[\mathbb{O}_{\rm obs}(\omega)]$ is the observation matrix introduced in Section 1.14.

As previously explained, the nonparametric probabilistic approach of both the parametric uncertainties and the model uncertainties induced by modeling errors in the computational model of the acoustic radiation of an inlet consists in modeling matrix $[\mathbb{Z}(\omega)]$ of the ROM by the random complex matrix $[\mathbf{Z}(\omega)]$ constructed in Section 2.3 and $[\mathbb{A}(\omega)]$ of the ROM by the random complex matrix $[\mathbf{A}(\omega)]$ constructed in Section 2.4. The uncertainties on the fan acoustic excitation consist in modeling $\mathbf{c}^+(\omega)$ by the random complex vector $\mathbf{C}^+(\omega)$ as constructed in Section 2.6. From Eqs. (1.117) and (1.116), it can be deduced that the SROM can be rewritten as,

$$\mathbf{QoI}(\omega) = [\mathbb{F}_{\rm QoI}(\omega)]\,\mathbf{C}^+(\omega) - [\mathbb{A}_{\rm QoI}(\omega)]\mathbf{Q}(\omega)\,, \tag{2.41}$$

in which the random vector $\mathbf{Q}(\omega)$ of the generalized coordinates verifies the stochastic equation,

$$([\mathbf{A}(\omega)] + [\mathbf{Z}(\omega)])\,\mathbf{Q}(\omega) = [\mathbb{B}(\omega)]\,\mathbf{C}^+(\omega)\,. \tag{2.42}$$

The random complex vector $\mathbf{Q}(\omega_j;\theta_\ell)$ of stochastic generalized coordinates is then written as,

$$\mathbf{Q}(\omega_j;\theta_\ell) = ([\mathbf{A}(\omega_j;\theta_\ell)] + [\mathbf{Z}(\omega_j;\theta_\ell)])^{-1}\,[\mathbb{B}(\omega_j)]\,\mathbf{C}^+(\omega_j;\theta_\ell)\,, \tag{2.43}$$

2.8 Stochastic solver

The Monte Carlo method is used for solving the SROM. It consists in computing a set of ν_s independent realizations, with ν_s sufficiently large, of the random quantities of interest by using Eqs. (2.41) and (2.42). From this set of independent realizations, estimates of the statistics for the quantities of interest are computed, such as probability density functions, moments (means, standard deviations), confidence intervals. The convergence of the estimates are analyzed with respect to ν_s.

The frequency band of analysis $[\omega_{\min}, \omega_{\max}]$ is sampled in n_ω points $\{\omega_1, \ldots \omega_{n_\omega}\}$. For given ω_j, ν_s realizations $\mathbf{QoI}(\omega_j;\theta_\ell)$ for $\ell = 1, \ldots, \nu_s$ are given by

$$\mathbf{QoI}(\omega_j;\theta_\ell) = [\mathbb{F}_{\rm qoI}(\omega_j)]\,\mathbf{C}^+(\omega_j;\theta_\ell) - [\mathbb{A}_{\rm qoI}(\omega_j)]\,\mathbf{Q}(\omega_j;\theta_\ell)\,, \tag{2.44}$$

in which the realization $\mathbf{Q}(\omega_j;\theta_\ell)$ of random vector $\mathbf{Q}(\omega_j)$ is given by solving the deterministic linear matrix equation,

$$([\mathbf{A}(\omega_j;\theta_\ell)] + [\mathbf{Z}(\omega_j;\theta_\ell)])\,\mathbf{Q}(\omega_j;\theta_\ell) = [\mathbb{B}(\omega_j)]\,\mathbf{C}^+(\omega_j;\theta_\ell)\,, \tag{2.45}$$

in which $\{[\mathbf{A}(\omega_j;\theta_\ell)], [\mathbf{Z}(\omega_j;\theta_\ell)], \mathbf{C}^+(\omega_j;\theta_\ell), \ell = 1,\ldots,\nu_s\}$ are ν_s independent realizations of random complex matrix $[\mathbf{A}(\omega_j)]$, $[\mathbf{Z}(\omega_j)]$ and of random complex vector $\mathbf{C}^+(\omega_j)$.

Substituting $\mathbf{Q}(\omega_j;\theta_\ell)$ given by Eq. (2.45) in Eq. (2.44) yields,

$$\mathbf{QoI}(\omega_j;\theta_\ell) = [\mathbf{P}(\omega_j;\theta_\ell)]\,\mathbf{C}^+(\omega_j;\theta_\ell)\,, \tag{2.46}$$

in which,

$$[\mathbf{P}(\omega_j;\theta_\ell)] = [\mathbb{F}_{\text{qoI}}(\omega_j)] - [\mathbb{A}_{\text{qoI}}(\omega_j)]\,([\mathbb{A}(\omega_j)] + [\mathbf{Z}(\omega_j;\theta_\ell)])^{-1}\,[\mathbb{B}(\omega_j)] \tag{2.47}$$

is a complex matrix.

2.9 Construction of a matrix representing the QoIs for a multiple loadcases

Let us consider a multiple loadcases made up of N_d elementary loadcases $\mathbf{c}^{+,\alpha}$ for $\alpha = 1,\ldots,N_d$, in which $\mathbf{c}^{+,\alpha} = (0,\ldots,1,\ldots,0)$ is a real vector of length N_d with zero components except component α, which is equal to 1. Let $[c^+] = [\mathbf{c}^{+,1}\ldots\mathbf{c}^{+,N_d}]$ be the $(N_d \times N_d)$ real matrix of the multiple loadcase for which the columns are the elementary loadcases. With such a definition of $\mathbf{c}^{+,\alpha}$, it can be seen that $[c^+] = [I_{N_d}]$. Denoting by $[QoI(\omega_j,\theta_\ell)]$ the rectangular complex matrix obtained with a computational code for this multiple loadcase, shows that

$$[\mathbf{P}(\omega_j;\theta_\ell)] = [\mathbf{QoI}(\omega_j,\theta_\ell)]\,. \tag{2.48}$$

2.10 Estimation of the robust-design objective function and convergence with respect to the number of realizations

In the framework of the robust optimization problem, the random stochastic process $\{\mathbf{QoI}(\omega),\ \omega \in [\omega_{\min},\omega_{\max}]\}$ is considered as a function of the desgin parameter $\mathbf{w}$ that belongs to the admissible set $\mathcal{C}_w$. This stochastic process is then rewritten as $\{\mathbf{QoI}(\omega;\mathbf{w}), \omega \in [\omega_{\min},\omega_{\max}]\}$ (as explained in Section 1.15.2, the random far-field pressure $P(\omega;\xi;\mathbf{w})$ depends on $\mathbf{w}$).

For all $\mathbf{w}$ fixed in $\mathcal{C}_\mathbf{w}$, from Section 1.15.2, it can be deduced that the estimate $J^{(\nu_s)}(\mathbf{w})$ of objective function $J(\mathbf{w})$ is written as,

$$J^{(\nu_s)}(\mathbf{w}) = \frac{1}{\nu_s}\sum_{\ell=1}^{\nu_s}\left\{\frac{1}{n_\omega+n_\xi}\sum_{j=1}^{n_\omega}\sum_{k=1}^{n_\xi} s_{jk}\,|P(\omega_j,\xi_k;\theta_\ell;\mathbf{w})|^2\right\}, \tag{2.49}$$

For all $\mathbf{w}$ fixed in $\mathcal{C}_\mathbf{w}$, the mean-square convergence of statistics (see for instance [60]) related to stochastic process $\{\mathbf{QoI}(\omega;\mathbf{w}), \omega \in [\omega_{\min},\omega_{\max}]\}$, with respect to ν_s, could be analyzed without difficulties. Nevertheless, we are interested in the convergence of estimate $J^{(\nu_s)}(\mathbf{w})$ with respect to ν_s.

The convergence analysis of the objective function with respect to ν_s will be carried out as follows. For any given $\varepsilon > 0$ sufficiently small with respect to 1, for all $\mathbf{w}$ fixed in $\mathcal{C}_w$, for a given integer ν_s sufficiently large, the convergence of $J^{(\nu_s)}(\mathbf{w})$ will be reached if, for all ν and for all ν' greater than or equal to ν_s, $|J^{(\nu)}(\mathbf{w}) - J^{(\nu')}(\mathbf{w})| \leq \varepsilon$.

2.11 Implementation of the Monte Carlo solver

The computational implementation of the Monte Carlo method can be written under the form of an algorithm. It is recalled that random real matrices $[\mathbf{G}_{\mathbb{Z}}^{\mathrm{NS}}]$, $[\mathbf{G}_{\mathbb{Z}}^{\mathrm{S}}]$, and $[\mathbf{G}_{\mathbb{A}}]$ are independent of ω and statistically independent. Let us assume that the deterministic upper triangular matrices $[L_{\mathbb{Z}}^{\mathrm{S}}(\omega_1)], \ldots, [L_{\mathbb{Z}}^{\mathrm{S}}(\omega_{n_\omega})]$, $[L_T^{\mathbb{Z}}(\omega_1)], \ldots, [L_T^{\mathbb{Z}}(\omega_{n_\omega})]$, and $[L_T^{\mathbb{A}}(\omega_1)], \ldots, [L_T^{\mathbb{A}}(\omega_{n_\omega})]$ and the deterministic square matrices $[U_{\mathbb{Z}}(\omega_1)], \ldots, [U_{\mathbb{Z}}(\omega_{n_\omega})]$ and $[U_{\mathbb{A}}(\omega_1)], \ldots, [U_{\mathbb{A}}(\omega_{n_\omega})]$, can be stored in memory. Under this condition, the algorithm, which minimizes CPU time, is as follows (it should be noted, that the loops that appear in algorithm 1 can be parallelized). An important notice to be made is that, in the algorithm exposed below, the randomization of the excitation vector $\mathbf{c}^+$ is not done at this stage, but is operated in post-processing, as the linear acoustics approximation is used. Such a randomization process is detailed in Chapter 4, using the probabilist approach detailed in Section 2.6.

Algorithm 1 Monte Carlo method algorithm for the randomization of the aeroacoustic and liner matrices

Fixing a value $\mathbf{w}$ in $\mathcal{C}_w$ of the design parameter.
Fixing a multiple load case.
for $j = 1$ to n_ω (loop ACTRAN) **do**
Calculation of the deterministic upper triangular complex matrices $[L_{\mathbb{Z}}^{\mathrm{S}}(\omega_j; \mathbf{w})]$, $[L_T^{\mathbb{Z}}(\omega_j; \mathbf{w})]$, $[L_T^{\mathbb{A}}(\omega_j; \mathbf{w})]$, and the deterministic square complex matrix $[U_{\mathbb{Z}}(\omega_j; \mathbf{w})]$ and $[U_{\mathbb{A}}(\omega_j; \mathbf{w})]$

Initialization of the random number generator (same sequence for all the values of $\mathbf{w}$ and ω)
for $\ell = 1$ to ν_s **do**
Calculation of the full square real matrices $[\mathbf{G}_{\mathbb{Z}}^{\mathrm{S}}(\theta_\ell)]$ $[\mathbf{G}_{\mathbb{Z}}^{\mathrm{NS}}(\theta_\ell)]$, and $[\mathbf{G}_{\mathbb{A}}(\theta_\ell)]$.

Final assembly of the matrices in Eq. (2.45)
Solving the assembled linear system Eq. (2.45)
Calculation and storing $\mathbf{QoI}(\omega_j; \theta_\ell; \mathbf{w})$ by Eq. (2.44)
end for
end for

A detailed view of the algorithms used during the present work are presented in Appendix D.

Chapter 3

Nominal computational model for the nacelle intake used for the application

Contents

3.1 **Definition of the system design obtained with Computer Assisted Drawing tool (CAD)** **60**
3.2 **Fluid mesh for Computational Fluid Dynamics (CFD)** **60**
3.3 **Aeroacoustic mesh for Computational AeroAcoustics (CAA)** **62**
3.4 **Acoustic mesh for computational aeroacoustics** **63**
3.5 **Nominal liner configuration considered in the application** **64**
3.6 **Quantities of interest (output indicators)** **64**

Abstract: *This chapter describes the application devoted to a nacelle intake and presents the construction of the nominal computational model for the aeroacoustics computation. We present the methodology adopted to obtain the steady flow and the final intake acoustic mesh for computational aeroacoustics. Note that all figures shown in this chapter use a 2D view.*

The aeroacoustic model presented here is used throughout the whole thesis. It corresponds to the nacelle used during noise development static test (NDST) performed by the engine manufacturer. Its geometry is slightly different from the one used for flight configuration. A static test lip called "minibell" is used, which allows for ensuring a flow-field in the fan region, that is equivalent to the one obtained in flight.

3.1 Definition of the system design obtained with Computer Assisted Drawing tool (CAD)

The starting point of every numerical study is the design of the actual system. Its complexity depends on the degree of approximation needed for the study. The design is obtained by using the aerolines of the nacelle given by the aerodynamics team at Airbus. The CAD obtained can also be adapted for liner studies. It should be noted that the evaluation of the impact of the liner design on the aerodynamic performances of the nacelle is of major importance. The CAD of the application presented in this work is depicted in Fig. 3.1.

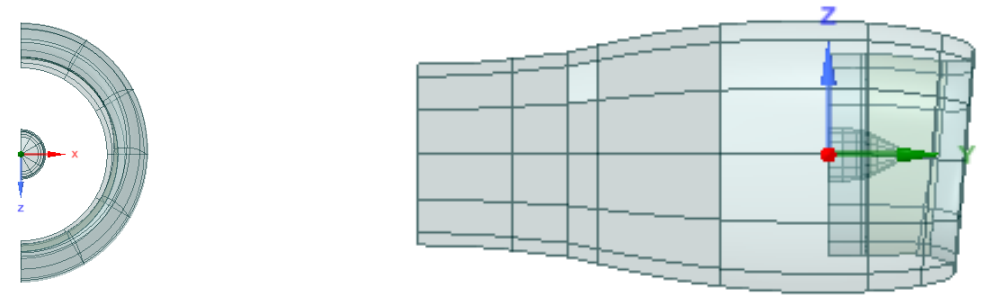

(a) Front view

(b) Side view

Figure 3.1: Intake model CAD.

3.2 Fluid mesh for Computational Fluid Dynamics (CFD)

3.2.1 Thermodynamic data associated with flight conditions

Once the system is designed, a set of thermodynamic values associated with flight conditions at each certification point are needed in order to represent the uniform upstream flow. The engine rotation speed (rpm), the mass flow rate of the fan (kg/s) are directly retrieved from the flight conditions and the engine manufacturers data. Inside the duct, the specific thermodynamic parameters are the in-duct static temperature T_{duct}, the in-duct static pressure p_{duct}, and the in-duct Mach number M_{duct}. Outside, the specific thermodynamic values for the upstream flow are the static temperature at infinity T_∞, the static pressure at infinity p_∞, and the Mach number at infinity M_∞, which are generally retrieved at the plane altitude from the 1976 U.S Standard Atmosphere [67] (relative humidity of 70% at ISA+10°C). The following work is based on static tests performed on ground, in which the engine regime is the only varying parameter, not the altitude of the plane. Consequently, infinite thermodynamic values are the same for all conditions.

The CFD computation (see Fig. 3.3) is carried out for aerodynamic conditions, not presented here for confidentiality reasons, for each certification flight conditions (engine regime), by solving the set of equations described in section 1.6. For the application presented, the effects of the incidence are not accounted for.

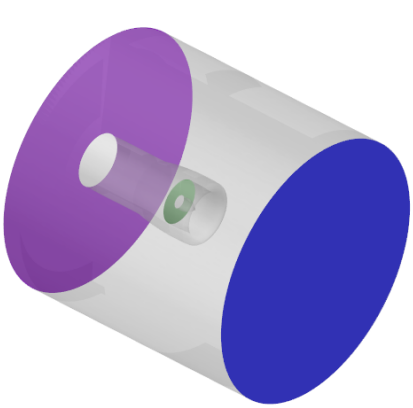

(a) CFD 3D mesh

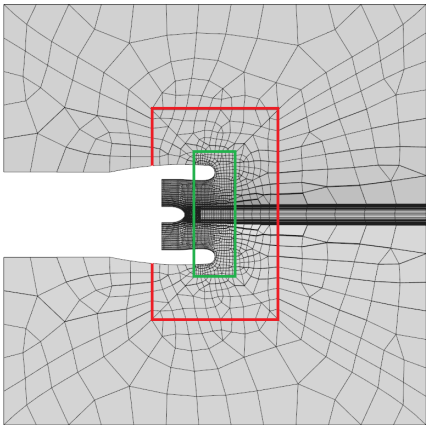

(b) 2D view of the 3D mesh (center cutplane)

Figure 3.2:
Left: Illustration of the 3D CFD mesh in which the purple surface in the background imposes a zero velocity potential (full absorption), the blue surface in the first plane imposes a zero velocity, and the green plane in the center of the figure imposes a non-zero velocity.
Right: Illustration of the center cutplane of the 3D CFD mesh (left figure) in which a red rectangle and a smaller green rectangle illustrate the different mesh sizes.

3.2.2 Rules for the fluid domain construction

The fluid domain is constructed following rules that only depend on a scalar parameter R related to the duct radius. The fan plane is located where the flow can be considered as uniform, while the other rules allow to take a sufficiently large zone to account for both heterogeneous and uniform flows.

3.2.3 Fluid mesh

The mesh refinement is also constrained by specific criteria, which allow for giving sufficiently small elements to correctly represent the flow in critical regions, and conversely, to keep acceptable memory and time consumptions by giving large elements where the flow is considered as uniform. These criteria are function of the acoustic convected wavelength $\lambda = \dfrac{c - ||\tilde{\mathbf{v}}||}{f}$, where c is the local speed of sound that can be approximated by the equation (see [9] p.531 Eq. (10.63)), $c = c_\infty \pm \dfrac{\gamma - 1}{2}||\tilde{\mathbf{v}}||$, in which c_∞ is the speed of sound in the fluid, in the upstream flow. The mean mesh size L_e is defined by $L_e = \dfrac{\lambda}{4}$ and where $||\tilde{\mathbf{v}}||$ is taken at the fan plane, and some refinements are applied in the fluid domain.

3.2.4 Steady flow computation (CFD)

The steady flow is computed with the ACTRAN Flow utility, for which the formulation used is summarized in Appendix A.
Figure 3.3 shows the steady flow results for the mass density and the velocity fields of the intake model at the approach condition, for a mesh dimensioned at $f = 1\,000$ Hz. These figures show the existence of critical regions that require a mesh refinement. For example, one can observe in Fig. 3.3b that the flow velocity is significantly higher in the duct, and even higher close to the interior lip.

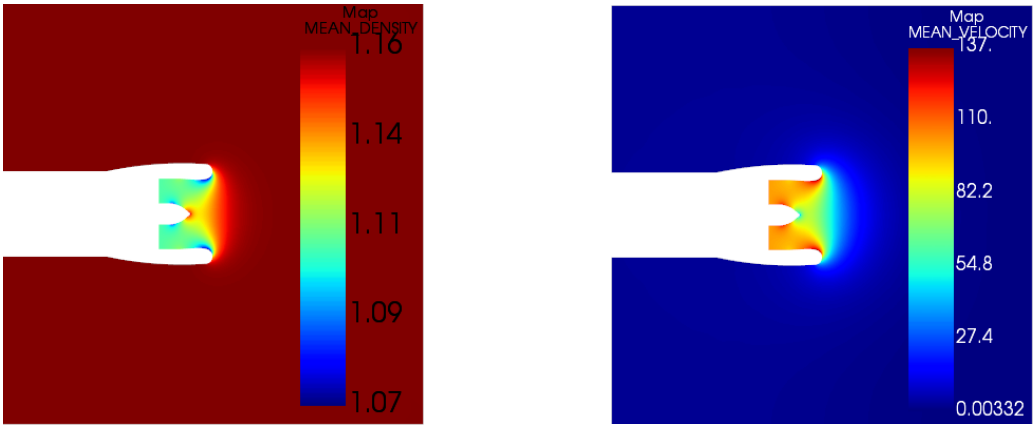

(a) Steady flow mass density field

(b) Steady flow velocity field

Figure 3.3: Illustration of steady flow results obtained by CFD for the nacelle intake model at approach condition

3.3 Aeroacoustic mesh for Computational AeroAcoustics (CAA)

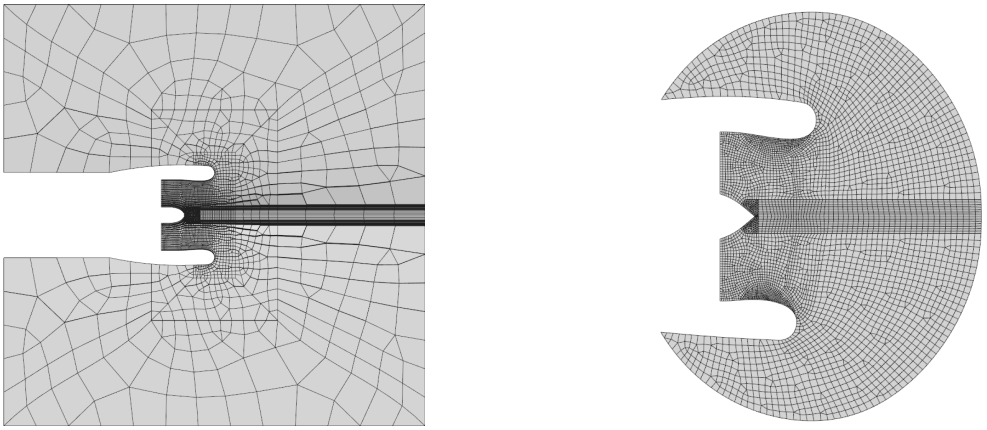

(a) CFD domain selection to CAA mesh (2D view)

(b) CAA mesh (2D view)

Figure 3.4: 2D view of the 3D CFD mesh and 2D view of the 3D CAA mesh, for a maximum frequency $f = 1\,000$ Hz.

The aeroacoustic mesh, which is as well issued from the CAD, corresponds to a selection of the CFD mesh elements. An ellipse is drawn on the CFD mesh following certain criteria on the convected acoustic wavelength and the velocity field, as depicted in Fig. 3.4a, which decomposes the whole domain in two subdomains whose meshes are differently refined. The inner domain gathers the duct and the near-field, and the outer domain is the rest of the domain. The different meshes are built following aeroacoustic meshing criteria. Finite elements are used to represent the inner domain, while infinite elements represent the outer pseudo-infinite domain.

The meshing criteria of the CAA mesh depend on the acoustic convected wavelength, which depend on the studied frequencies. The computational frequency chosen for this study is the blade passing frequency (BPF). The studied frequency is assessed by using a specific mesh, dimensioned by the highest frequency (one mesh at 1 000 Hz), that is around 500 kdofs.

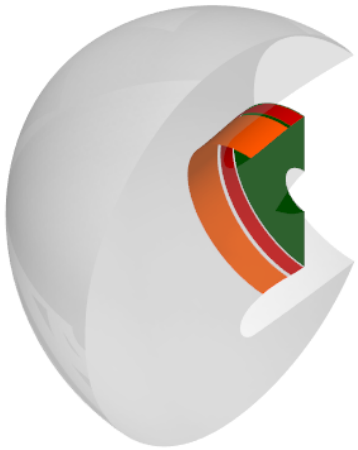

Figure 3.5: 3D view of the intake CAA mesh, which depicts the Inlet surface (orange part in the center of the figure), the Forward Fan Case surface (red part in the center of the figure close to the fan plane), and the excitation plane (green part at the background of the figure)

3.4 Acoustic mesh for computational aeroacoustics

The steady flow velocity field computed by CFD is interpolated on the acoustic mesh shown in Fig. 3.5. We then obtained the steady flow thermodynamic values at each node of the CAA mesh. The acoustic solution is computed with this acoustic mesh.

Figure 3.6 shows the mass density, pressure, and velocity fields of the steady flow, interpolated on the acoustic mesh for the three aircraft noise certification configurations. Since the results are close for the three conditions, only the "approach" condition is presented for the low-frequency mesh (1 000 Hz).

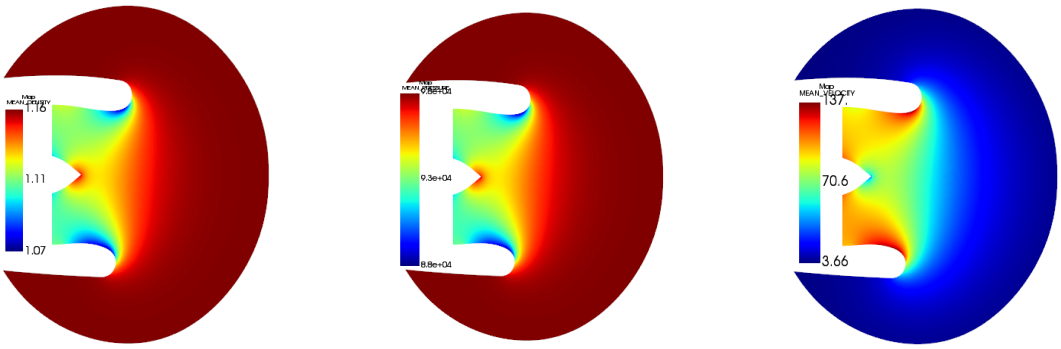

(a) Steady flow density field (b) Steady flow pressure field (c) Steady flow velocity field

Figure 3.6: 2D view of the 3D steady flow fields interpolated on the acoustic mesh for the approach condition at $f = 1\,000$ Hz.

Nodes repartition. Once the acoustic mesh is built, it can be decomposed in several subdomains, needed to impose boundary conditions. For example, a subdomain is created for the liner, on which its impedance will be calculated at each node of the subdomain. The nodes repartition is given in Table 3.1.

Mesh	FEM	IEM	Inlet	FFC	Excitation	Sym plane	Total
$f = 1\,000$ Hz	423 498	9 182	4 821	981	3 285	16 559	458 521
$f = 2\,000$ Hz	2 939 198	24 805	8 665	1 875	8 277	73 189	3 056 476

Table 3.1: Intake CAA mesh nodes repartition for the application

3.5 Nominal liner configuration considered in the application

In the application presented, the nominal liners considered are SDOF (see Appendix C), whose physical properties are not presented here for confidentiality reasons.
From these physical properties, the impedance of the liner is calculated for each frequency, for the whole discretized liner surface (by finite elements, whose mesh is presented in Fig. 3.5). These calculations are performed using an Airbus internal iterative code whose models are presented in Appendix C. This Airbus code computes the values of the impedance by iterating until a tolerance value defined by the user is reached. A model uncertainty is then introduced in this impedance model, which is taken into account using the nonparametric probabilistic approach of uncertainties presented in Chapter 2.

3.6 Quantities of interest (output indicators)

The acoustic solution can be obtained for each node of the acoustic mesh. For obvious computational cost reasons, the acoustic field is generally not computed on the whole mesh. Virtual points are placed in the 3D inner or outer domain, on which the acoustic pressure is observed (quantities of interest). In the present work, a noise development static test (experiments) is used. The two microphones configurations used are presented hereinafter.

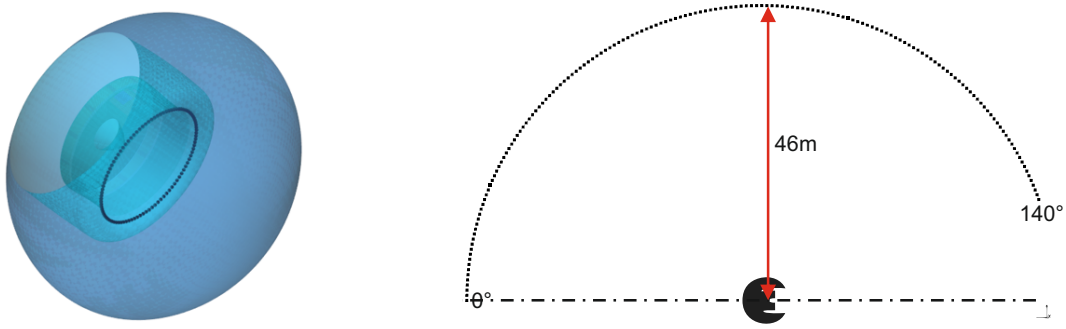

(a) Intake lip ring of microphones

(b) Far-field arc of microphones

Figure 3.7: Microphones configurations during noise development static test

a) Modal detection ring: The experimental modal detection ring consists of $N_{\text{mics}} = 100$ flush-mounted microphones distributed on the intake lip (see Figure 3.7a). For the simulations, the microphone ring is located inside the inner domain (finite elements)

b) Far-field array: During static ground tests (NDST) microphones are located on an arc placed on the ground. This arc is characterized by a radius of 46 m from the center of the nacelle axis taken at the vertical of the lip leading edge, as depicted by Fig. 3.7b. For the far-field simulations, the microphones (points) are located every degree from 0 to 140° in the outer domain (infinite elements).

Chapter 4

Identification of the fan excitation modal content, aeroacoustic, liner and modal content uncertainties using experiments

Contents

4.1	**Definition of the general Quantities of Interest**	**66**
4.2	**Definition of experimental QoIs**	**67**
4.3	**Definition of simulated QoIs**	**68**
4.4	**Sensitivity analysis of QoIs with respect to uncertainties**	**70**
4.5	**Statistical inverse identification of uncertainty levels**	**85**
4.6	**Discussion**	**92**

Abstract: *This chapter is devoted to the uncertainty quantification for 3D acoustic performance model of nacelle liners (acoustic treatments). Uncertainties are taken into account in order to increase the robustness of the predictions. A full computational acoustic propagation model based on the convected Helmholtz equation in presence of a non-homogeneous flow velocity field computed by solving the potential Euler Equations is used. A reduced-order computational model is deduced in order to implement the probabilistic model of uncertainties. The model uncertainties induced by modeling errors have been taken into account for the acoustic propagation model and the liner model, using the nonparametric probabilistic approach. In addition, the uncertainties on the acoustic excitation induced by the fan have been introduced using the parametric probabilistic approach. The developed methodology is applied to a 3D nacelle intake and allows for computing the confidence regions of the random far-field radiated pressure in terms of random SPL (Sound Pressure Level), which are compared to experiments for several flight conditions and frequencies.*

The lack of knowledge related to the acoustic excitation induced by the fan rotation is a major contribution to the overall uncertainty of the computational model. As explained in Section 1.8.2, the acoustic excitation is represented by a finite sum of N_d duct modes imposed to the acoustic system. In Section 2.6.2, the deterministic modal intensity $\underline{I}_\alpha^+$ and its random counterpart I_α^+ of the duct modes have been defined. Concerning the construction of $\underline{I}_\alpha^+$, an empirical model based on civil-aircraft-manufacturer expertise is used. The current section aims to present the identification of the level of uncertainty associated with the acoustic excitation modal content. For that purpose, experimental data are used, corresponding to acoustic pressures measured at points located on a ring at the intake lip, and also on a far-field microphones array. The ring pressures are also simulated with the stochastic computational aeroacoustic model defined in Chapter 3. The identification of the level of the mean value $\underline{I}_\alpha^+$ and the hyperparameter σ_α of the random variable I_α^+ is then performed minimizing the distance between experimental and simulated data.

In a similar way, aeroacoustic and liner uncertainties are identified by comparing experimental data and simulated data for which the modal content has already been identified. A first step consists in introducing aeroacoustic uncertainties in the stochastic reduced-order model, using the hardwall case. The SROM is then operated several times for which the level of aeroacoustic uncertainties varies, following a trial method. Then, a confidence region corresponding to a 95% level of confidence is drawn from each stochastic computation (resulting from the Monte Carlo stochastic solver), and compared to experimental data. The main objective is therefore to frame a maximum of experimental points inside the calculated confidence region, while keeping it the thinnest possible. The same study is carried out by introducing liner uncertainties, using the lined case. And finally, as aeroacoustic and liner uncertainties are fixed following the previously mentioned constraints, uncertainties on the multi-modal (broadband) and emergences acoustic levels are identified.

4.1 Definition of the general Quantities of Interest

4.1.1 Quantities of Interest on the ring

Acoustic pressure on the ring

$$p_{\text{ring,i}}(\omega) = \sum_{m=-N_{\text{azi}}}^{N_{\text{azi}}} a_m(\omega) e^{jm\varphi_i}\,, \tag{4.1}$$

in which ω is the angular frequency, m is the azimuthal order, $a_m(\omega)$ is the complex amplitude of the azimuthal order m, and $\varphi_i = 2\pi(i-1)/N_{\text{mics}}$ is the angle in rad of the i^{th} microphone (which is thus different from the phase operator introduced in Eq. (2.29)), in which N_{mics} is the number of microphones on the ring. Equation (4.1) can be rewritten, in a matrix form, as

$$\mathbf{p}_{\text{ring}}(\omega) = [\Phi]\,\mathbf{a}(\omega)\,, \tag{4.2}$$

in which $\mathbf{p}_{\text{ring}}(\omega) = (p_{\text{ring},1}(\omega), \ldots, p_{\text{ring,N}_{\text{mics}}})$ is the complex vector in $\mathbb{C}^{N_{\text{mics}}}$, $\mathbf{a}(\omega) = (a_{-N_{\text{azi}}}(\omega), \ldots, a_0(\omega), \ldots, a_{N_{\text{azi}}}(\omega))$ is the complex amplitude vector in $\mathbb{C}^{2N_{\text{azi}}+1}$, and $[\Phi]$ is the complex matrix in $\mathbb{M}_{N_{\text{mics}},2N_{\text{azi}}+1}(\mathbb{C})$ such that $[\Phi]_{im} = e^{jm\varphi_i}$.

Azimuthal amplitude for the ring acoustic pressure Assuming that $2N_{\text{azi}} + 1 \leq N_{\text{mics}}$, the complex amplitude vector $\mathbf{a}(\omega)$ is obtained by using the left pseudo-inversion, as

$$\mathbf{a}(\omega) = \left(([\Phi]^*[\Phi])^{-1}\,[\Phi]^* \right)\,\mathbf{p}_{\text{ring}}(\omega)\,. \tag{4.3}$$

Azimuthal Sound Pressure Level for the ring acoustic pressure The azimuthal amplitude of azimuthal order m of the acoustic pressure on the ring, expressed in dB, is defined, for $m \in \{-N_{\text{azi}}, \ldots, 0, \ldots, N_{\text{azi}}\}$, by

$$\text{SPL}_{\text{ring},m}(\omega) = 10 \log_{10} \left(\frac{|a_m(\omega)|^2}{p_{\text{ref}}^2} \right) . \tag{4.4}$$

4.1.2 Quantities of Interest for the far-field

Acoustic pressure in the far-field For the i^{th} microphone on the far-field arc defined in Fig. 3.7b, for which there are N_{mics} microphones, the acoustic pressure is denoted by $p_{\text{ff},i}(\omega)$. The complex vector in $\mathbb{C}^{N_{\text{mics}}}$ of the acoustic far-field pressures are then defined by

$$\mathbf{p}_{\text{ff}}(\omega) = (p_{\text{ff},1}(\omega), \ldots, p_{\text{ff},N_{\text{mics}}}(\omega)) . \tag{4.5}$$

Sound Pressure Level in the far-field The sound pressure level of the i^{th} microphone is defined by

$$\text{SPL}_{\text{ff,i}}(\omega) = 10 \log_{10} \left(\frac{|p_{\text{ff,i}}(\omega)|^2}{p_{\text{ref}}^2} \right) , \tag{4.6}$$

in which $p_{\text{ff,i}}(\omega)$ is defined by Eq. (4.5).

4.2 Definition of experimental QoIs

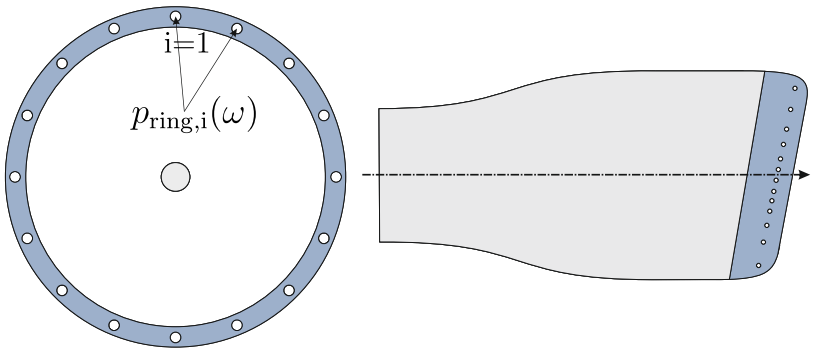

Figure 4.1: Experimental set-up: pressure measurements on the ring mounted on the nacelle inlet.

Experimental QoI on the ring The experimental data are acquired on the ring that consists of $N_{\text{mics}} = 100$ flush-mounted microphones distributed on the intake lip (see Figure 4.1). The azimuthal sound pressure level on the ring is written as

$$\text{SPL}^{\text{exp}}_{\text{ring},m}(\omega) = 10 \log_{10} \left(\frac{|a_m^{\text{exp}}(\omega)|^2}{p_{\text{ref}}^2} \right) , \tag{4.7}$$

in which $a_m^{\text{exp}}(\omega)$ is given by Eq. (4.3) for experimental data.

Experimental QoI in the far-field The sound pressure level in the far-field is written as

$$\mathrm{SPL}_{\mathrm{ff,i}}^{\mathrm{exp}}(\omega) = 10\log_{10}\left(\frac{|p_{\mathrm{ff,i}}^{\mathrm{exp}}(\omega)|^2}{p_{\mathrm{ref}}^2}\right). \tag{4.8}$$

4.3 Definition of simulated QoIs

The stochastic computational aeroacoustic model used for representing the experimental set-up depicted in Figure **??**, is the one defined in Chapter 3. Since the aeroacoustic computational model is linear, in order to avoid the call to the computational model a large number of times during the identification algorithm, the acoustic pressures on the ring and in the far-field, are firstly computed for a given reference modal intensity $I_\alpha^{+,\mathrm{ref}}(\omega)$. For instance, such a reference $I_\alpha^{+,\mathrm{ref}}(\omega)$ is chosen as 100 dB for all ω and for all α. Then, these results are used for computing the acoustic pressures on the ring and in the far-field for a given modal intensity $I_\alpha^{+}(\omega)$. This is the reason why we need to rewrite the different QoIs in function of the modal intensity I_α^{+} through the use of the reference modal intensity $I_\alpha^{+,\mathrm{ref}}(\omega)$.

4.3.1 Expression of the different Quantities of Interest as a function of the modal intensity I_α^+

The acoustic pressure $p_i(\omega)$ for each microphone i (ring or far-field) and for mode α is computed using the computational aeroacoustic model. This acoustic pressure corresponds to an injected acoustic modal intensity $I_\alpha^{+,\mathrm{ref}}$ for each duct mode α (see Section 2.6.2). From Eq. (2.38), the square of the acoustic pressure modulus corresponding to each duct mode α corresponding to $I_\alpha^{+,\mathrm{ref}}(\omega)$, is defined by

$$|p_\alpha^{\mathrm{ref}}(\omega)|^2 = p_{\mathrm{ref}}^2\, 10^{(I_\alpha^{+,\mathrm{ref}}(\omega)/10)}, \tag{4.9}$$

in which $p_{\mathrm{ref}} = 2e^{-6}$ is the acoustic pressure of reference. For the modal intensity $I_\alpha^+(\omega)$, the square of the acoustic pressure modulus is then written as

$$|p_\alpha(\omega)|^2 = p_{\mathrm{ref}}^2\, 10^{(I_\alpha^{+}(\omega)/10)}, \tag{4.10}$$

which can be rewritten using the reference modal intensity $I_\alpha^{+,\mathrm{ref}}$ as

$$|p_\alpha(\omega)|^2 = p_{\mathrm{ref}}^2\, 10^{(I_\alpha^{+}(\omega) - I_\alpha^{+,\mathrm{ref}}(\omega))/10}, \tag{4.11}$$

Expression of the simulated QoIs on the ring Let $\mathbf{a}^\alpha(\omega) \in \mathbb{C}^{2N_{\mathrm{azi}}+1}$ be the complex amplitude vector of mode α such that

$$\mathbf{a}^{\alpha,\mathrm{ref}}(\omega) = \left(([\Phi]^*[\Phi])^{-1}[\Phi]^*\right)\mathbf{p}_{\mathrm{ring}}^{\alpha,\mathrm{ref}}(\omega), \tag{4.12}$$

in which $\mathbf{p}_{\mathrm{ring}}^{\alpha,\mathrm{ref}}(\omega)$ is the vector in $\mathbb{C}^{N_{\mathrm{mics}}}$ of the acoustic pressures on the ring computed for the reference modal intensity $I_\alpha^{+,\mathrm{ref}}$. The azimuthal sound pressure level $\mathrm{SPL}_{\mathrm{ring},m}^{\mathrm{sim}}(\omega)$ on the ring for the modal intensity $I_\alpha^+(\omega)$ is then given, for $m \in \{-N_{\mathrm{azi}}, \ldots, 0, \ldots, N_{\mathrm{azi}}\}$, by

$$\mathrm{SPL}_{\mathrm{ring},m}^{\mathrm{sim}}(\omega) = 10\log_{10}\left(\frac{1}{N_d}\sum_{\alpha=1}^{N_d}\frac{|a_m^{\alpha,\mathrm{ref}}(\omega)|^2}{p_{\mathrm{ref}}^2}\times 10^{(I_\alpha^{+}(\omega) - I_\alpha^{+,\mathrm{ref}}(\omega))/10}\right). \tag{4.13}$$

Expression of the simulated far-field QoIs The sound pressure level in the far-field for the modal intensity $I_\alpha^+(\omega)$ is given by

$$\mathrm{SPL}_{\mathrm{ff}}^{\mathrm{sim}}(\omega) = 10\log_{10}\left(\frac{1}{N_d}\sum_{\alpha=1}^{N_d}\frac{|p_{\mathrm{ff}}^{\alpha,\mathrm{ref}}(\omega)|^2}{p_{\mathrm{ref}}^2}\times 10^{(I_\alpha^+(\omega)-I_\alpha^{+,\mathrm{ref}}(\omega))/10}\right), \tag{4.14}$$

in which $\mathbf{p}_{\mathrm{ff}}^{\alpha,\mathrm{ref}}(\omega)$ is the vector in $\mathbb{C}^{N_{\mathrm{mics}}}$ of the acoustic pressures on the far-field arc computed for the reference modal intensity $I_\alpha^{+,\mathrm{ref}}$.

4.3.2 Notation for the random variable and the mean value of the QoIs

For the hardwall case (no liner), in the stochastic computational aeroacoustic model, the random quantities are (1) the modal intensity $I_\alpha^+(\omega)$, whose hyperparameters of the probabilistic model are $\underline{I}_\alpha^+(\omega)$ and σ_α (see Section 4.3.1), which are identified separately, and (2) the generalized aeroacoustic matrix for which the hyperparameter is δ_A. In this condition, the sound pressure level becomes random and denotes these random variables and their mean values as follows.

- The random azimuthal sound pressure level on the ring, defined by Eq. (4.13), is denoted $\mathrm{SPL}_{\mathrm{ring},m}^{\mathrm{sim}}(\omega)$ (notation unchanged). A realization of this random variable is $\mathrm{SPL}_{\mathrm{ring},m}^{\mathrm{sim}}(\omega;\theta)$. Its mean value is denoted $\underline{\mathrm{SPL}}_{\mathrm{ring},m}^{\mathrm{sim}}(\omega)$.

- The random sound pressure level in the far-field, defined by Eq. (4.14), is denoted $\mathrm{SPL}_{\mathrm{ff}}^{\mathrm{sim}}(\omega)$ (notation unchanged). A realization of this random variable is $\mathrm{SPL}_{\mathrm{ff}}^{\mathrm{sim}}(\omega;\theta)$. Its mean value is denoted $\underline{\mathrm{SPL}}_{\mathrm{ff}}^{\mathrm{sim}}(\omega)$.

4.3.3 Modeling of the deterministic modal intensity $\underline{I}_\alpha^+$

Simulated data are computed following hypotheses on the modal content that concern broadband and emergence levels, and energy repartition between the different modes. For that purpose, a state-of-the-art modal content used by Airbus is introduced. A broadband level is set for all azimuthal and radial orders. An emergence level corresponding to the engine order is set. Then, a number of azimuthal orders from each side of the engine order mode is set, for which the acoustic energy decays as a function of the azimuthal order. For the azimuthal order that corresponds to the engine order, at the blade passing frequency that is studied here, we make the hypothesis that the energy is only carried by the first radial order.

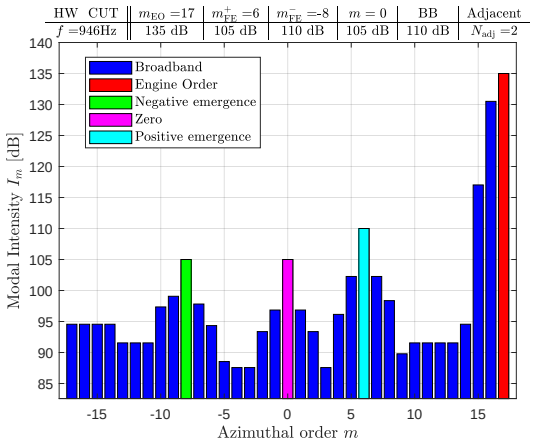

- I_{EO} is the modal intensity of the engine order of azimuthal order $m = m_{\mathrm{EO}}$ (red bar),

- I_{FE^-} is the modal intensity of the negative flexible emergence of azimuthal order $m = m_{\mathrm{FE}^-}$ (green bar),

- I_{Zero} is the modal intensity of the azimuthal order $m = 0$ emergence (purple bar),

- I_{FE^+} is the modal intensity of the positive flexible emergence of azimuthal order $m = m_{\mathrm{FE}^+}$ (cyan bar),

- I_{BB} is the modal intensity of the broadband (blue bar),

Algebraically, the modal content can be described as follows,

$$
\begin{cases}
\text{if } m = m_{\mathrm{EO}}, \quad I_\alpha^{+,\mathrm{mod}} = I_{\mathrm{EO}}, \\
\\
\text{if } m = m_{\mathrm{FE}^+}, \quad I_\alpha^{+,\mathrm{mod}} = I_{\mathrm{FE}^+}, \\
\\
\text{if } m = 0, \quad I_\alpha^{+,\mathrm{mod}} = I_{\mathrm{Zero}}, \\
\\
\text{if } m = m_{\mathrm{FE}^-}, \quad I_\alpha^{+,\mathrm{mod}} = I_{\mathrm{FE}^-}, \\
\\
\text{if } (|m - m_{\mathrm{EO}}| \leq N_{\mathrm{adj}}), \\
\quad I_\alpha^{+,\mathrm{mod}} = I_{\mathrm{EO}} \left(1 - \left(\frac{m - m_{\mathrm{EO}}}{N_{\mathrm{adj}} + 1}\right)^2\right) + (I_{\mathrm{BB}} - 10\log_{10}(N_{\mathrm{azi}})) \left(\frac{m - m_{\mathrm{EO}}}{N_{\mathrm{adj}} + 1}\right)^2 - 10\log_{10}(N_{\mathrm{rad}}(m)), \\
\\
\text{if } (|m - m_{\mathrm{FE}^+}| \leq N_{\mathrm{adj}}), \\
\quad I_\alpha^{+,\mathrm{mod}} = I_{\mathrm{FE}^+} \left(1 - \left(\frac{m - m_{\mathrm{FE}^+}}{N_{\mathrm{adj}} + 1}\right)^2\right) + (I_{\mathrm{BB}} - 10\log_{10}(N_{\mathrm{azi}})) \left(\frac{m - m_{\mathrm{FE}^+}}{N_{\mathrm{adj}} + 1}\right)^2 - 10\log_{10}(N_{\mathrm{rad}}(m)), \\
\\
\text{if } (|m - 0| \leq N_{\mathrm{adj}}), \\
\quad I_\alpha^{+,\mathrm{mod}} = I_{\mathrm{Zero}} \left(1 - \left(\frac{m}{N_{\mathrm{adj}} + 1}\right)^2\right) + (I_{\mathrm{BB}} - 10\log_{10}(N_{\mathrm{azi}})) \left(\frac{m}{N_{\mathrm{adj}} + 1}\right)^2 - 10\log_{10}(N_{\mathrm{rad}}(m)), \\
\\
\text{if } (|m - m_{\mathrm{FE}^-}| \leq N_{\mathrm{adj}}), \\
\quad I_\alpha^{+,\mathrm{mod}} = I_{\mathrm{FE}^-} \left(1 - \left(\frac{m - m_{\mathrm{FE}}^-}{N_{\mathrm{adj}} + 1}\right)^2\right) + (I_{\mathrm{BB}} - 10\log_{10}(N_{\mathrm{azi}})) \left(\frac{m - m_{\mathrm{FE}}^-}{N_{\mathrm{adj}} + 1}\right)^2 - 10\log_{10}(N_{\mathrm{rad}}(m)), \\
\\
\text{else}, \quad I_\alpha^{+,\mathrm{mod}} = I_{\mathrm{BB}} - 10\log_{10}(N_{\mathrm{azi}} N_{\mathrm{rad}}(m)).
\end{cases}
\tag{4.15}
$$

in which, I_{mn} is the modal intensity of azimuthal order m and radial order n, I_{EO} is the modal intensity of the engine order of azimuthal order $m = m_{\mathrm{EO}}$, I_{FE^-} is the modal intensity of the negative flexible emergence of azimuthal order $m = m_{\mathrm{FE}^-}$, I_{Zero} is the modal intensity of the azimuthal order $m = 0$, I_{FE^+} is the modal intensity of the positive flexible emergence of azimuthal order $m = m_{\mathrm{FE}^+}$, I_{BB} is the modal intensity of the broadband, N_{adj} is the number of adjacent modes on which the engine order acoustic energy is reverberated, N_{azi} is the number of azimuthal orders, and N_{rad} is the number of radial orders per azimuthal order.

4.4 Sensitivity analysis of QoIs with respect to uncertainties

This section aims to present some results of the sensitivity analysis with respect to uncertainties in order to assess their impact on both far-field and ring modal pressure responses, for both approach and cutback flight conditions. At the blade passing frequency (BPF), the excitation modal content is different for the two flight conditions. It is then interesting to study both of them in order to understand how the stochastic acoustic response will be impacted by higher order emergences such as the engine order, which is cut-off for the approach condition, and cut-on for the cutback condition.

4.4.1 Approach condition

4.4.1.1 Sensitivity study of modal Sound Pressure Levels towards uncertainties

In this subsection, the sensitivity of modal QoIs towards aeroacoustic and liner uncertainties on specific modes is undertaken. The main objective is to observe the raw impact of uncertainties on those modes, by avoiding unwanted effects such as the smoothing due to the averaging over all modes accounted for in the calculation of global SPLs. A comparison between hardwall configuration with aeroacoustic uncertainties only and lined configuration with liner uncertainties only is done as well as a comparison between far-field and ring datasets. This preliminary study is done for the same flight condition (approach) and frequency (1 BPF), and allows for controlling the validity of the problem physical representativeness. For this specific configuration, fan noise signature contains multimodal (broadband) noise and tonal noise. Tonal noise is generally carried by modes for which the azimuthal order corresponds to the engine order, and/or the rotor-stator interaction mode (Tyler and Sofrin [66]). As these specific modes are cut-off in this specific configuration, the same sensitivity analysis should be done on another configuration, for which the excitation modal content contains these modes. The present preliminary study is carried out for a relatively simple configuration that allows for computational costs to remain low (and thus allow for more analyses).

First mode $(m, n) = (0, 1)$ The first mode generally radiates in the nacelle axis direction and is not impacted by lined surfaces since its acoustic energy is concentrated at the center. This mode is then interesting to be investigated in order to confirm that liner uncertainties will have low to zero impact on the acoustic response in this configuration.

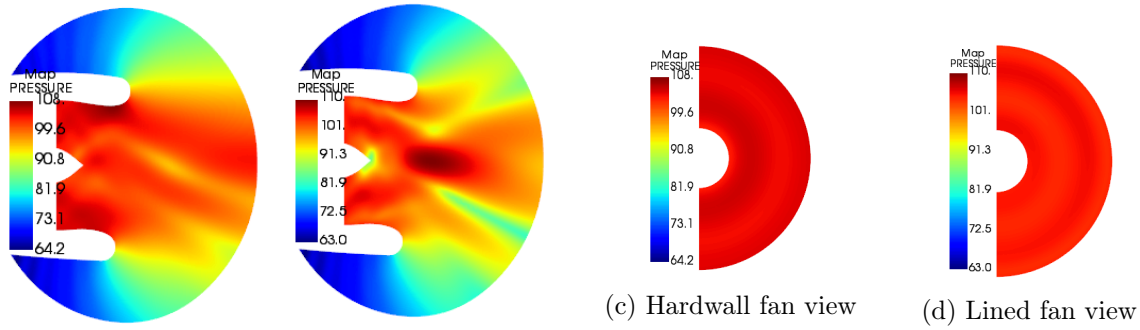

(a) Hardwall duct view (b) Lined duct view (c) Hardwall fan view (d) Lined fan view

Figure 4.2: Visualization of the acoustic pressure (dB) for the first mode $(m, n) = (0, 1)$ and for the approach condition, inside the duct from two perspectives: side and front. Hardwall and lined configuration are depicted.

In Fig. 4.2, the acoustic pressure (dB) for the first mode $(m, n) = (0, 1)$ is shown from two perspectives. Inside the duct (Fig. 4.2a and Fig. 4.2b), the acoustic pressure is quite heterogeneous along the nacelle axis, depicting a zone where it is higher (at the top, close to the lip for the hardwall configuration, and outside along the nacelle axis for the lined configuration). In a cross section of the nacelle where the fan is located (Fig. 4.2c and Fig. 4.2d), the difference between hardwall and lined configuration is not important (only the global amplitude of the swelling mode is different).

Before observing the differences of sensitivity between hardwall and lined configurations, it is firstly important to have in mind how these differences behave using the nominal model.
In Fig. 4.3, the difference of hardwall and lined datasets are shown for the mode $(m, n) = (0, 1)$. On the ring, the difference is clear and not surprising. Lined data are less energetic since the

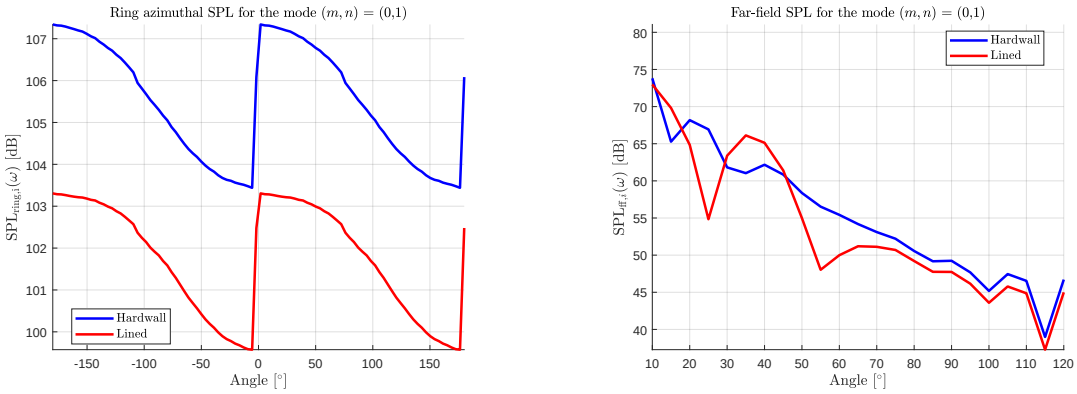

(a) Ring azimuthal SPL. (b) Far-field SPL.

Figure 4.3: Difference between Hardwall and Lined configurations for the ring nominal dataset (left) and the far-field nominal dataset (right) for the approach condition at the blade passing frequency $f = 654$ Hz (1 BPF) for the mode $(m, n) = (0, 1)$. One graduation equals 1 dB on left plot and 5 dB on right plot.

acoustic energy is absorbed by the liners. Nevertheless, for this mode, in the far-field, the difference is not clear. There is apparently an odd creation of energy in the angle region 25° to 55°. This is probably a numerical artefact, or less probably, a diffraction effect due to the presence of the liner, which creates surface modes that cannot be accounted for since no boundary layer is accounted for in this modeling of the liner in presence of a grazing flow. This can be also related to the odd overpressure zone that is shown in Fig. 4.2b.

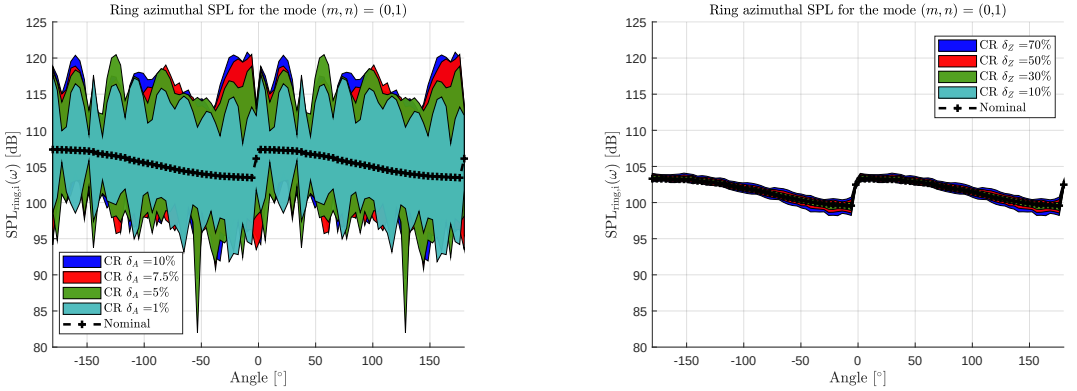

(a) Hardwall with aeroacoustic uncertainties only (b) Lined with liner uncertainties only

Figure 4.4: Sensitivity of modal ring SPL data towards aeroacoustic uncertainty level δ_A (left) and liner uncertainty level δ_Z (right) for the approach condition at the blade passing frequency $f = 654$ Hz (1 BPF) for the mode $(m, n) = (0, 1)$ by comparison between nominal data (black line) and simulation data for different values of parameters δ_A and δ_Z. One graduation equals 5 dB.

In Fig. 4.4, the sensitivity of the mode $(m, n) = (0, 1)$ towards aeroacoustic and liner uncertainties is presented, observed on the ring microphone array. For the hardwall condition (Fig. 4.4a), one can notice that the confidence region associated with each one of the uncertainty level values (from 1 to 10%) thicken then quickly stabilize. This is a saturation phenomenon that occurs for $\delta_A = 7.5\%$, and means that by adding more uncertainties, the width of the confidence region would not increase much. This cannot be observed on the lined dataset for which uncertainties have a low impact on ring acoustic pressure (Fig. 4.4b), which is not surprising as the acoustic

energy in the duct is located at the center.

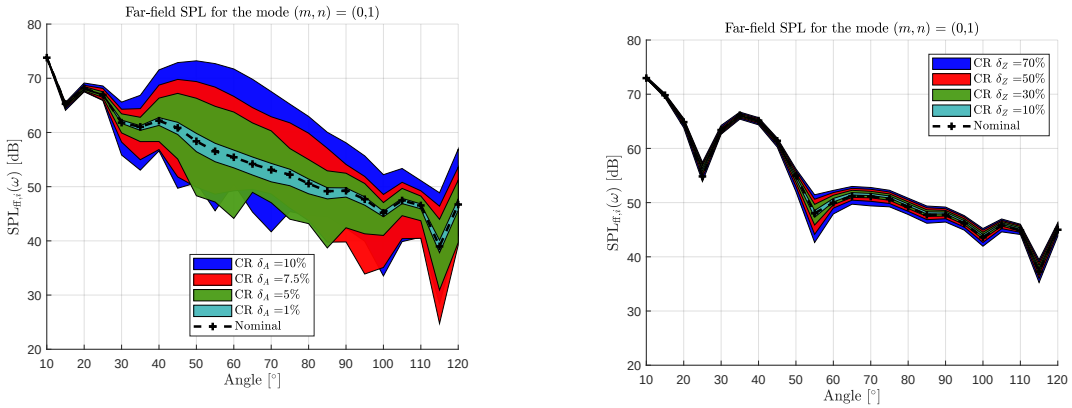

(a) Hardwall configuration with aeroacoustic uncertainties only

(b) Lined configuration with liner uncertainties only

Figure 4.5: Sensitivity of far-field modal SPL data towards aeroacoustic uncertainty level δ_{A} (left) and liner uncertainty level δ_{Z} (right) for the approach condition at the blade passing frequency $f = 654$ Hz (1 BPF) for the mode $(m, n) = (0, 1)$ by comparison between nominal data (black line) and simulation data for different values of parameters δ_{A} and δ_{Z}. One graduation equals 10 dB.

In Fig. 4.5a, the impact of aeroacoustic uncertainties over the hardwall far-field dataset is assessed for different levels. One can notice that the confidence regions increase linearly as δ_{A} increases. The saturation effect observed in Fig. 4.4a might appear for a greater value of δ_{A} on the far-field dataset. Giving the presence of a rather heterogeneous repartition of energy inside the duct, and especially close to the lip (see Fig. 4.2b), the impact of aeroacoustic uncertainties seems legitimate. For the lined configuration (Fig. 4.5b), the impact of liner uncertainties is far less important than aeroacoustic uncertainties on the hardwall case. Nevertheless, the impact is much more visible on the far-field array than on the ring array for this configuration (see Fig. 4.4b) simply because the dynamic is different in both figures, the confidence region being approximately 2dB thick for both ring and far-field datasets.

Last mode $(m, n) = (10, 1)$ The second mode to be investigated correspond to the last cut-on mode of the excitation modal content. This mode is interesting because of its energy repartition inside the duct, which is mainly concentrated close to the duct wall. As this mode is supposed to be strongly attenuated by lined surfaces, liner uncertainties should have a higher impact on the acoustic response.
Fig. 4.6 shows the acoustic pressure (dB) for the last mode $(m, n) = (10, 1)$. Inside the duct (Fig. 4.6a), the acoustic pressure is mainly concentrated close to the duct wall. This is conform with what can be seen in Fig. 4.6c, on which one can observe the alternation between pressure zeros and nonzeros. Since this mode has a high cut-off ratio and a short wavelength, and since its energy is concentrated on the wall, this mode is highly absorbed by liner surfaces. This is verified by a simple comparison between hardwall and lined duct views for which there is a clear impact of the liner on the acoustic pressure (Fig. 4.6a).

As done for the first mode, we first observe the difference between hardwall and lined cases in terms of modal SPL.
In Fig. 4.7, the difference between Hardwall and Lined configurations for the ring nominal dataset (Fig. 4.7a) and the far-field nominal dataset Fig. 4.7b is presented. Contrarily to the first mode (Fig. 4.3b), far-field hardwall and lined cases do not show an odd acoustic response. Nevertheless, on the ring, one can observe a pattern in the acoustic response, which could be

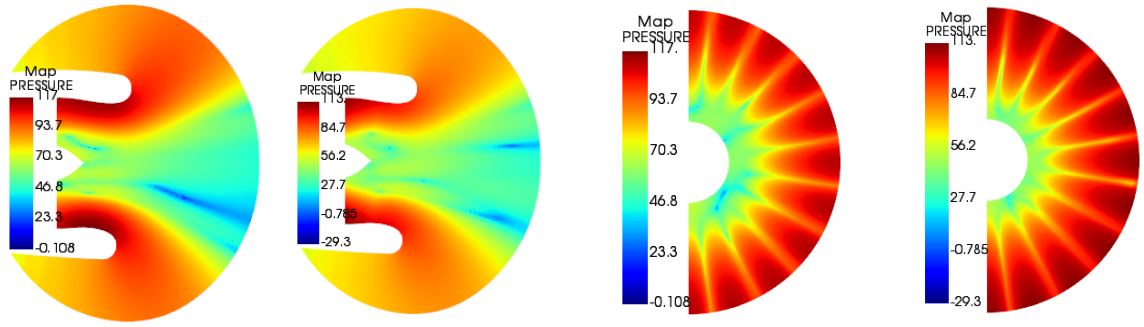

(a) Hardwall duct view (b) Lined duct view (c) Hardwall fan view (d) Lined fan view

Figure 4.6: Visualization of the acoustic pressure (dB) for the mode $(m, n) = (10, 1)$ and for the approach condition, inside the duct from two perspectives: side and front. Hardwall and lined configuration are depicted.

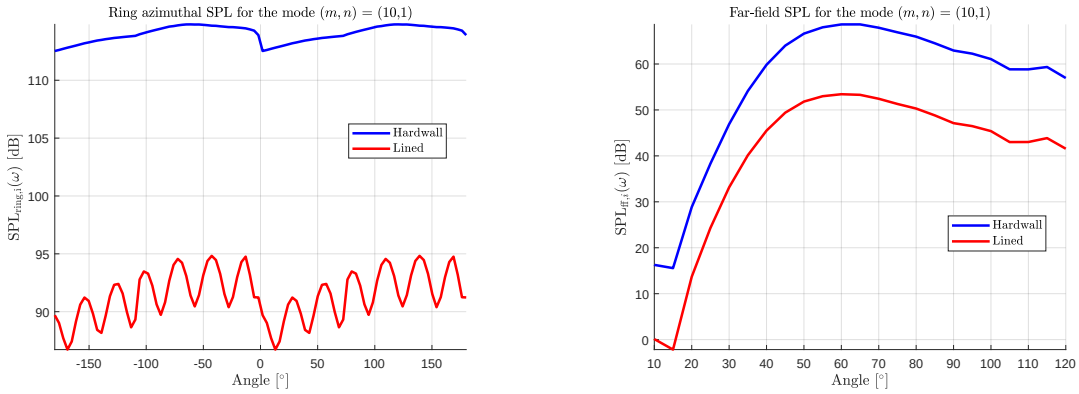

(a) Ring azimuthal SPL. (b) Far-field SPL.

Figure 4.7: Difference between Hardwall and Lined configurations for the ring nominal dataset (left) and the far-field nominal dataset (right) for the approach condition at the blade passing frequency $f = 654$ Hz (1 BPF) for the mode $(m, n) = (10, 1)$. One graduation equals 5 dB on left plot and 10 dB on right plot.

related to the alternance of pressure zeros and nonzeros that can be observed in Fig. 4.6d for the lined case. In the far-field, this phenomenon seems to be erased due to the far-field propagation effects.

In Fig. 4.8a, the saturation phenomenon is still present and even more important than previously presented (Fig. 4.4a) for the first mode. For $\delta_A = 5\%$, ring data are saturated by aeroacoustic uncertainties. This is not the case for the lined configuration for which liner uncertainties have a little impact on ring data. They have still more impact on this mode than for the mode $(m, n) = (0, 1)$ (see Fig. 4.4b). Since this mode has a high cut-off ratio (in comparison with the mode $(m, n) = (0, 1)$), and consequently a short wavelength, this mode is more impacted by the presence of the liner and so by liner uncertainties.

Fig. 4.9a depicts the impact of aeroacoustic uncertainties on the ring dataset corresponding to the hardwall configuration. The mode $(m, n) = (10, 1)$ seems very sensitive towards aeroacoustic uncertainties as confidence regions tend to thicken and stochastic means increase as δ_A increases. But contrarily to the first mode (see Fig. 4.5a), there is not a clear angle range for which uncertainties have no impact. The same observation can be made for the lined case (Fig. 4.9b).

This study results are not ground breaking but allow for verifying the validity of the method.

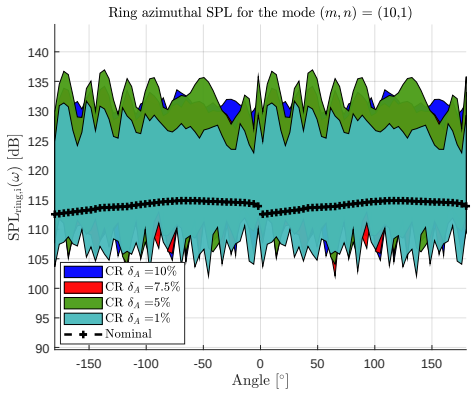

(a) Hardwall case/aeroacoustic uncertainties only

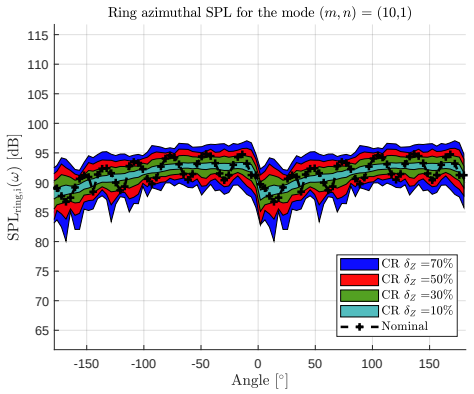

(b) Lined case/liner uncertainties only

Figure 4.8: Sensitivity of modal SPL data towards aeroacoustic uncertainty level δ_A for the approach condition at the blade passing frequency $f = 654$ Hz (1 BPF) for the mode $(m,n) = (10,1)$ by comparison between nominal data (black line) and simulation data with aeroacoustic uncertainties for different values of parameters δ_A and δ_Z. One graduation equals 5 dB.

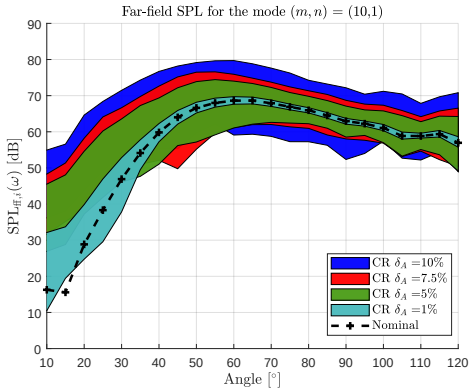

(a) Sensitivity of azimuthal ring modal SPL towards aeroacoustic uncertainties

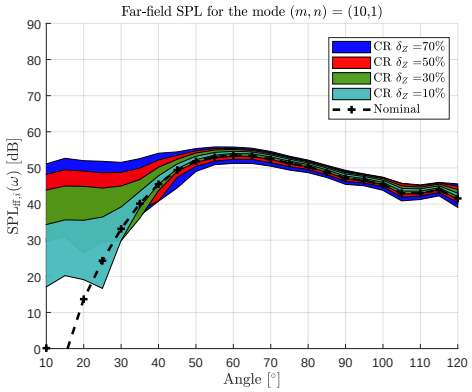

(b) Sensitivity of broadband far-field modal SPL towards aeroacoustic uncertainties

Figure 4.9: Sensitivity of modal SPL data towards aeroacoustic uncertainty level δ_A and liner uncertainty level δ_Z for the approach condition at the blade passing frequency $f = 654$ Hz (1 BPF) for the mode $(m,n) = (10,1)$ by comparison between nominal data (black line) and simulation data for different values of parameters δ_A and δ_Z. One graduation equals 10 dB.

The objective was to observe the impact of uncertainties over the ring dataset for two different modes whose energy repartition is opposite: one mode whose energy is concentrated around the nacelle axis, and another mode whose energy is located close to the wall. Aeroacoustic uncertainties have a strong impact on both modes, whereas liner uncertainties have impact only on the last mode, which is logical as it is strongly attenuated by liner surfaces.

4.4.1.2 Sensitivity of global Sound Pressure Levels towards uncertainties

In this subsection, global SPLs are used, as calculated using Eq. (4.13) for ring datasets, and Eq. (4.14) for far-field datasets.
As it has been done for the modal sensitivity study, we observe the difference between hardwall and lined datasets on global SPLs.
In Fig. 4.10, there are no odd differences between both datasets. The differences that have been observed on the first mode are "erased" by the averaging on all cut-on modes.

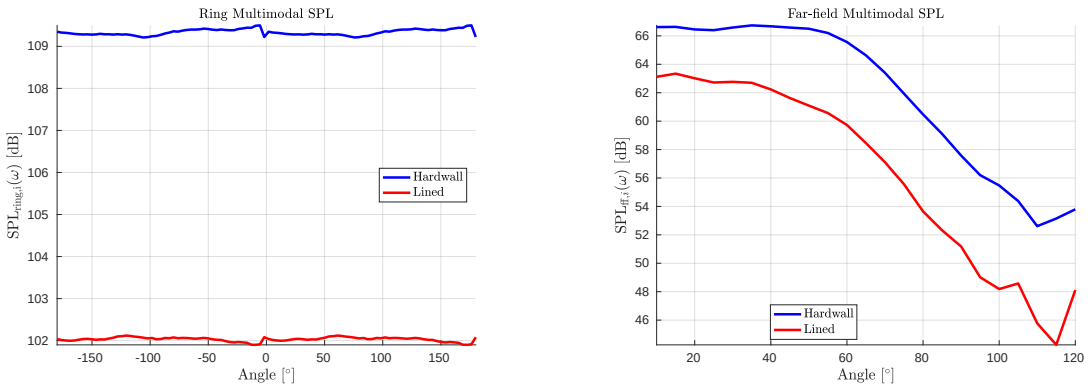

(a) Ring azimuthal SPL (b) Far-field SPL

Figure 4.10: Difference between Hardwall and Lined configurations for the ring nominal dataset (left) and the far-field nominal dataset (right) for the approach condition at the blade passing frequency $f = 654$ Hz (1 BPF). One graduation equals 1 dB on left plot and 2 dB on right plot.

Aeroacoustic uncertainties A first step consists in observing the impact of several aeroacoustic uncertainty levels (δ_A values) towards global SPLs (for both ring and far-field data). The range of δ_A ranges from minimum to maximum intuitive values such as the problem physical meaning would be respected (for example 90% of aeroacoustic uncertainties would not be a reasonable value).

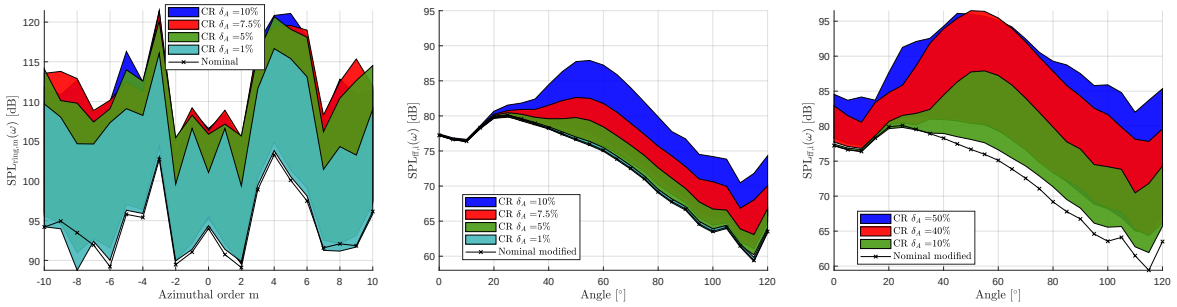

(a) Ring azimuthal SPL (b) Far-field SPL (c) Far-field SPL (saturation)

Figure 4.11: Sensitivity of global SPL data towards aeroacoustic uncertainty level δ_A for the approach condition at the blade passing frequency $f = 654$ Hz (1 BPF) by comparison between experimental data (black line) and simulation data with modified modal content and aeroacoustic uncertainties for several values. One graduation equals 5 dB.

In Fig. 4.11, the sensitivity study of global SPL towards aeroacoustic uncertainty level is presented for the approach condition at the BPF. δ_A varies from 1% to 10%. On the left figure (Fig. 4.11a), the impact of aeroacoustic uncertainties on the ring modal SPL is observed. One can notice that the sensitivity of $SPL_{ring,m}$ is a logarithm function of δ_A. While, it seems that the sensitivity of the far-field SPL (broadband) is a linear function of δ_A, as it can be seen in Fig. 4.11b. This phenomenon has been encountered during the modal SPL sensitivity study (subsection 4.4.1.1).
As explained, aeroacoustic uncertainties have a logarithmic impact on ring data, whereas a linear impact is observed on far-field data. This difference can be explained by several factors. As the aeroacoustic uncertainties increase, a saturation effect is quickly observed on ring data. While this saturation might eventually be obtained for a much higher value of δ_A on far-field data (this is the case for $\delta_A = 50\%$, see Fig. 4.11c).

If we take the example of $\delta_A = 1\%$, ring data are much more impacted than far-field data. The difference of the impact force between ring and far-field data is actually closely linked to the nature of the modes that are captured by the different microphones. This can be explained by the relative distance of the observer (ring or far-field) to the acoustic source (the fan). When duct modes exit the nacelle intake, they are captured by the ring, then propagate to be later captured by the far-field microphones. Indeed, one can notice that the ring, from its relatively close distance to the emission source (fan), is more likely to capture high cut-off ratio modes for which the acoustic wavelength is small. Whereas, as the far-field arc of microphone is far from the source, low cut-off ratio modes (which are directive in a small angle region, e.g. a small angle of emission) will mainly be captured, while high cut-off ratio modes will already be attenuated. Also, because high cut-off ratio modes have less energy than low cut-off ratio modes, the impact of uncertainties is more likely to have a stronger impact on the former. This explains the difference observed for a low level of uncertainties.

Also, as the value of δ_A increases, we observe an increasing of the stochastic mean. This is explained by the fact that uncertainties are imposed to matrix $[(\omega)]$ which is inverted during the resolution of the stochastic system. Consequently, fluctuations of the acoustic response of such a system are not linear, that is why we observe this kind of behaviour.

Liner uncertainties A sensitivity study of global sound pressure levels for both ring and far-field stochastic data towards liner uncertainties is needed to observe how the uncertainty will impact the model. For this study, a variation of liner uncertainties is undertaken ($\delta_Z = [10\%, 30\%, 50\%, 70\%]$), keeping aeroacoustic uncertainties to zero. As it has been seen in subsection 4.4.1.1, liner uncertainties have a small impact towards modal SPL, for the ring as well as the far-field data. This could be explained by the fact that the liner studied is already optimized for this flight condition/frequency. In order to confirm or infirm this hypothesis, the global stochastic SPLs are also computed using a lined surface for which the admittance has been manually altered by a factor 200%. Results can be seen in Fig. 4.12b.

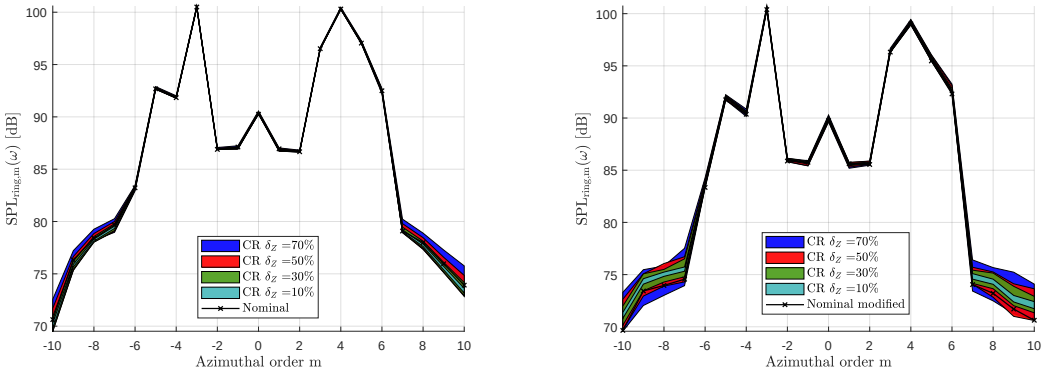

(a) Nominal impedance

(b) Altered impedance

Figure 4.12: Sensitivity of global Azimuthal SPL data towards liner uncertainty level δ_Z for the approach condition at the blade passing frequency $f = 654$ Hz (1 BPF) by comparison between experimental data (black line) and simulation data with modified modal content and aeroacoustic uncertainties for several values: $\delta_A = 10\%$ (cyan confidence region), $\delta_A = 30\%$ (green confidence region), $\delta_A = 50\%$ (red confidence region), and $\delta_A = 70\%$ (blue confidence region). Left: optimized admittance; Right: altered admittance by a factor 200%. One graduation equals 5 dB. One graduation equals 5 dB for both plots.

In Fig. 4.12 (both left and right figures), one can observe that lined uncertainties have a low impact on global ring data, especially for azimuthal orders in the range $[-6; 6]$. Whereas outside

this range, the azimuthal SPL is slightly affected by liner uncertainties. As it has been extensively explained in the previous subsection, high cut-off ratio modes are more inclined to be affected by uncertainties since they are poorly energetic. The alteration of the admittance nevertheless implies a more important effectiveness of uncertainties, which is a good result in the framework of the liner optimization for which an optimum in terms of acoustic absorbtion as well as robustness is expected.
One can observe that in Fig. 4.12, the sensitivities towards liner uncertainties are slightly different when the liner admittance is not optimal. Although this result is reassuring, it cannot be considered as conclusive. Liner uncertainties should have a more important impact on the detuned liner. Another study would consist in doing this analysis for a different flight condition and frequency for which the fan noise signature is more exhaustive, for example, a flight condition for which the mode carrying the engine order is cut-on.

4.4.2 Cutback condition

In this subsection, we reproduce the study carried out in 4.4.1.1 and 4.4.1.2.

4.4.2.1 Sensitivity study of modal Sound Pressure Levels towards uncertainties

Unlike the approach condition, the mode carrying the engine order is cut-on in cutback. The Tyler and Sofrin interaction mode is still cut-on in this configuration. The present preliminary study is carried out for a more complex configuration than presented in Subsection 4.4.1.1 and allows for studying a richer modal content.

First mode $(m, n) = (0, 1)$ The first mode generally radiates in the nacelle axis direction and is not impacted by lined surfaces since its acoustic energy is concentrated at the center. Since the cutback flight condition implies a higher engine regime, the acoustic levels should be different than the approach, and thus, the impact of uncertainties too.

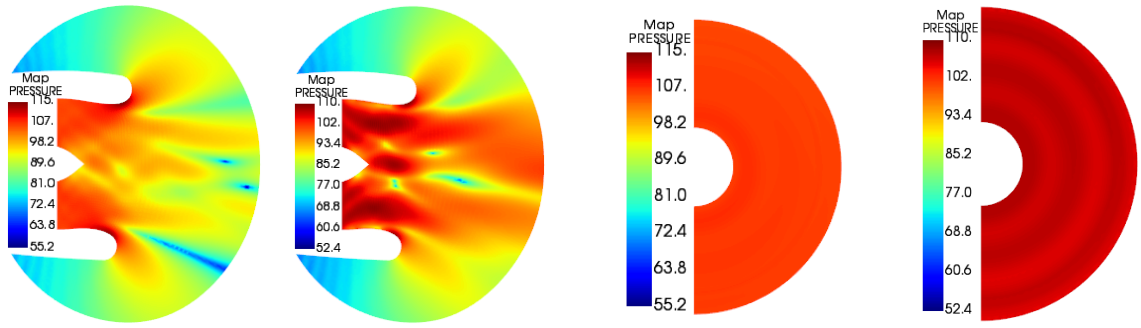

(a) Hardwall duct view (b) Lined duct view (c) Hardwall fan view (d) Lined fan view

Figure 4.13: Visualization of the acoustic pressure (dB) for the first mode $(m, n) = (0, 1)$ and for the cutback condition, inside the duct from two perspectives: side and front, for the cutback flight condition. Hardwall and lined configuration are depicted.

In Fig. 4.13, the acoustic pressure (dB) for the first mode $(m, n) = (0, 1)$ is shown from two perspectives. Inside the duct (Fig. 4.13a) for the hardwall case, the acoustic pressure is quite homogeneous except for two overpressure zones located at the nacelle lip. Whereas, for the lined case (Fig. 4.13b), it exists overpressure zones in the nacelle axis, over the liner in addition to the overpressure zones found on the hardwall case. This maybe corresponds to refraction effects due to the presence of the liners. In a cross section of the nacelle where the fan is located (Fig. 4.13c and Fig. 4.13d), the difference between hardwall and lined configuration is not important (only

the global amplitude of the swelling mode is different).

Before observing the differences of sensitivity between hardwall and lined configurations, it is firstly important to have in mind how these differences behave using the nominal model.

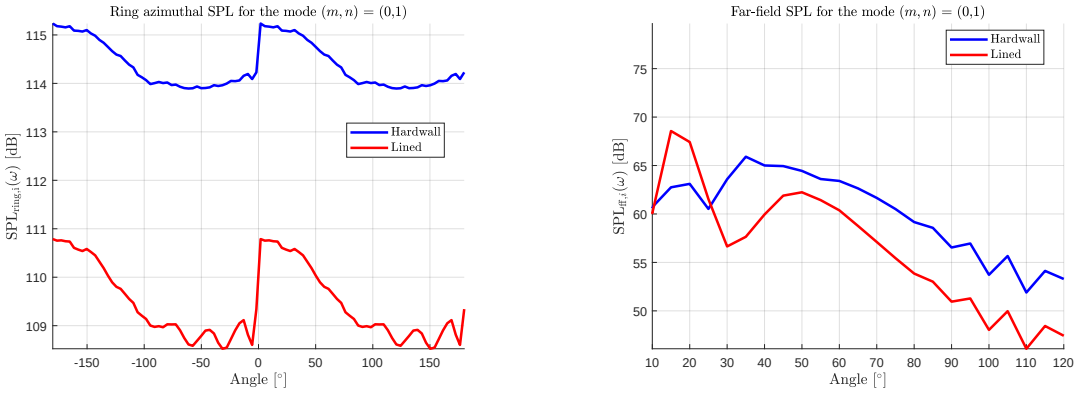

(a) Ring azimuthal SPL

(b) Far-field SPL

Figure 4.14: Difference between Hardwall and Lined configurations for the ring nominal dataset (left) and the far-field nominal dataset (right) for the cutback condition at the blade passing frequency $f = 946$ Hz (1 BPF) for the mode $(m, n) = (0, 1)$. One graduation equals 1 dB on left plot and 5 dB on right plot.

In Fig. 4.14, the difference between Hardwall and Lined configurations for the ring nominal dataset (Fig. 4.14a) and the far-field nominal dataset (Fig. 4.14b) is observed. As for the first mode at the approach condition (Fig. 4.3b), it exists an angle region in the far-field for which the acoustic energy of the lined case is greater than the hardwall case. This can also be explained by refraction effects, as it can be seen in Fig. 4.13b on which overpressures are visible in the center of the nacelle, that probably radiate in the nacelle axis. Also, as it has been observed for the last mode of the approach condition (Fig. 4.7a), it exists some rebounds on the ring acoustic response that could correspond to the number of lobes visible in Fig. 4.13b (we count 6 overpressure zones and 6 rebounds).

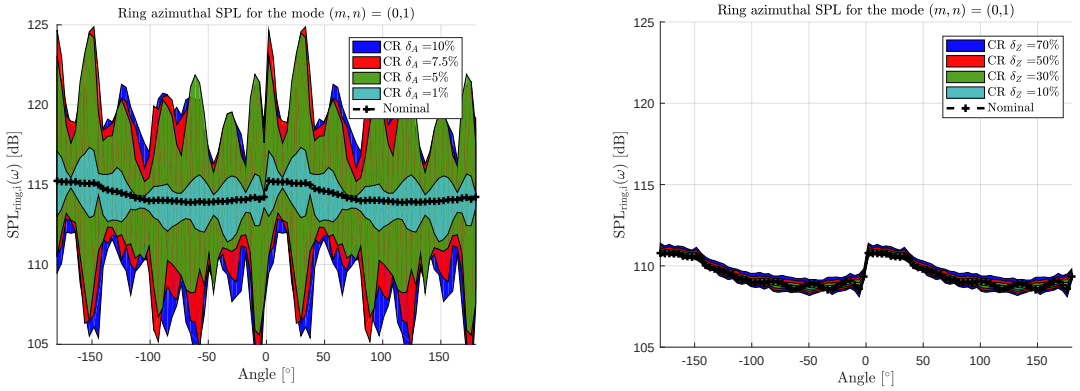

(a) Hardwall with aeroacoustic uncertainties only

(b) Lined with liner uncertainties only

Figure 4.15: Sensitivity of modal ring SPL data towards aeroacoustic uncertainty level δ_A (left) and liner uncertainty level δ_Z (right) for the approach condition at the blade passing frequency $f = 654$ Hz (1 BPF) for the mode $(m, n) = (0, 1)$ by comparison between nominal data (black line) and simulation data for different values of parameters δ_A and δ_Z. One graduation equals 5 dB.

In Fig. 4.15, the sensitivity of the mode $(m, n) = (0, 1)$ towards aeroacoustic and liner uncertainties is presented, observed on the ring microphone array. For the hardwall condition (Fig. 4.15a), the saturation phenomenon as observed in Fig. 4.4a for the approach condition, still occurs for $\delta_A = 7.5\%$, and means that by adding more uncertainties, the width of the confidence region would not increase much. This is still not observed on the lined dataset for which uncertainties have less impact on ring acoustic pressure (Fig. 4.15b). This is not surprising since this mode is not really attenuated by lined surfaces. Liner uncertainties thus have a relatively low impact.

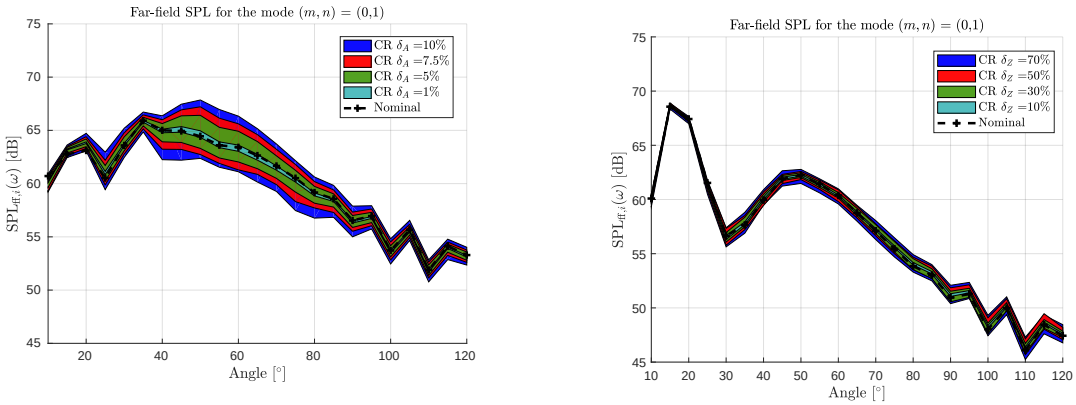

(a) Hardwall configuration with aeroacoustic uncertainties only

(b) Lined configuration with liner uncertainties only

Figure 4.16: Sensitivity of far-field modal SPL data towards aeroacoustic uncertainty level δ_A (left) and liner uncertainty level δ_Z (right) for the cutback condition at the blade passing frequency $f = 946$ Hz (1 BPF) for the mode $(m, n) = (0, 1)$ by comparison between nominal data (black line) and simulation data for different values of parameters δ_A and δ_Z. One graduation equals 5 dB.

In Fig. 4.16a, the impact of aeroacoustic uncertainties over the hardwall far-field dataset is assessed for different levels. One can notice that the confidence regions increase linearly as δ_A increases. The saturation effect observed on ring data (Fig. 4.15a) might appear for a greater value of δ_A on the far-field dataset. Giving the presence of a rather heterogeneous repartition of energy inside the duct, and especially close to the lip (see Fig. 4.13b), the impact of aeroacoustic uncertainties seems legitimate. For the lined configuration (Fig. 4.16b), the impact of liner uncertainties is far less important than aeroacoustic uncertainties on the hardwall case.

Last mode $(m, n) = (17, 1)$ The second mode to be investigated correspond to the last cut-on mode of the excitation modal content. This mode is interesting because of its energy repartition inside the duct, which is mainly concentrated close to the duct wall. As this mode is supposed to be strongly attenuated by lined surfaces, liner uncertainties should have an impact on the acoustic response.
Fig. 4.17 shows the acoustic pressure (dB) for the last mode $(m, n) = (17, 1)$. Inside the duct (Fig. 4.17a), the acoustic pressure is mainly concentrated close to the duct wall. This is conform with what can be seen in Fig. 4.17c, on which one can observe the alternation between pressure zeros and nonzeros. Since this mode has a high cut-off ratio and a short wavelength, and since its energy is concentrated on the wall, this mode is highly absorbed by liner surfaces. This is verified by a simple comparison between hardwall and lined duct views for which there is a clear impact of the liner on the acoustic pressure (Fig. 4.17a).
In Fig. 4.14, the difference between Hardwall and Lined configurations for the ring nominal dataset (Fig. 4.18a) and the far-field nominal dataset (Fig. 4.18b) are presented. As observed for the last mode of the approach condition, we also observe rebounds in the acoustic response of the lined case on the ring. These rebounds apparently correspond to alternating zeros and

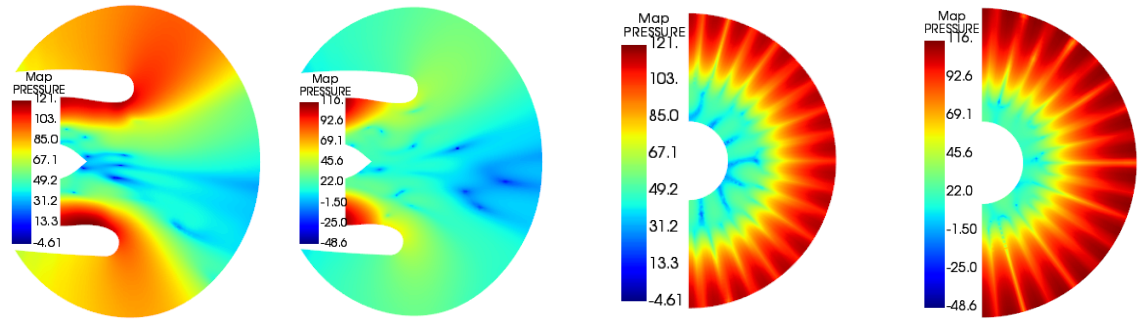

(a) Hardwall duct view (b) Lined duct view (c) Hardwall fan view (d) Lined fan view

Figure 4.17: Visualization of the acoustic pressure (dB) for the mode $(m, n) = (17, 1)$ and for the cutback condition, inside the duct from two perspectives: side and front. Hardwall and lined configuration are depicted.

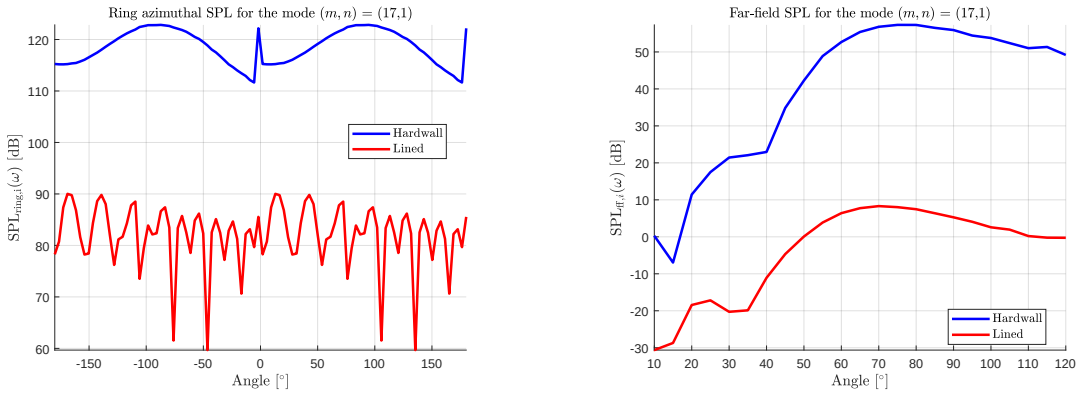

(a) Hardwall with aeroacoustic uncertainties only (b) Lined with liner uncertainties only

Figure 4.18: Difference between Hardwall and Lined configurations for the ring nominal dataset (left) and the far-field nominal dataset (right) for the approach condition at the blade passing frequency $f = 946$ Hz (1 BPF) for the mode $(m, n) = (17, 1)$. One graduation equals 5 dB on left plot and 10 dB on right plot.

nonzeros visible in Fig. 4.17d. This phenomenon is still not observable on the hardwall case, and in the far-field. Nevertheless, the peak observable at 0° for the hardwall case on the ring corresponds to the overpressure zone visible on the bottom lip of the nacelle (Fig. 4.17a), that is less important for the lined case.
In Fig. 4.19a, the saturation phenomenon is still present and even more important than previously presented (Fig. 4.15a) for the first mode. For $\delta_A = 5\%$, ring data are saturated by aeroacoustic uncertainties. This is not the case for the lined configuration for which liner uncertainties have a little impact on ring data. They have still more impact on this mode than for the mode $(m, n) = (0, 1)$ (see Fig. 4.15b). Since this mode has a high cut-off ratio (in comparison with the mode $(m, n) = (0, 1)$), and consequently a short wavelength, this mode is more impacted by the presence of the liner and so by liner uncertainties.
Fig. 4.20a depicts the impact of aeroacoustic uncertainties on the ring dataset corresponding to the hardwall configuration. The mode $(m, n) = (17, 1)$ seems very sensitive towards aeroacoustic uncertainties as confidence regions tend to thicken and stochastic means increase as δ_A increase. But contrarily to the first mode (see Fig. 4.16a), there is not a clear angle range for which uncertainties have no impact. The same observation can be made for the lined case (Fig. 4.20b).

These study results are not ground breaking but allow for verifying the validity of the method.

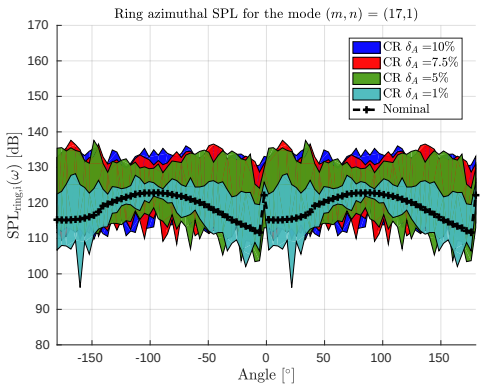

(a) Hardwall case/aeroacoustic uncertainties only

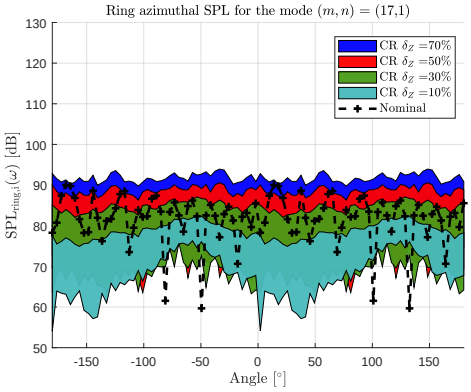

(b) Lined case/liner uncertainties only

Figure 4.19: Sensitivity of modal SPL data towards aeroacoustic uncertainty level δ_A for the approach condition at the blade passing frequency $f = 946$ Hz (1 BPF) for the mode $(m,n) = (17,1)$ by comparison between nominal data (black line) and simulation data with aeroacoustic uncertainties for different values of parameters δ_A and δ_Z. One graduation equals 5 dB.

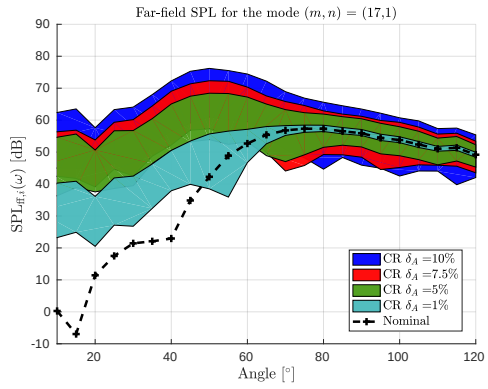

(a) Sensitivity of azimuthal ring modal SPL towards aeroacoustic uncertainties

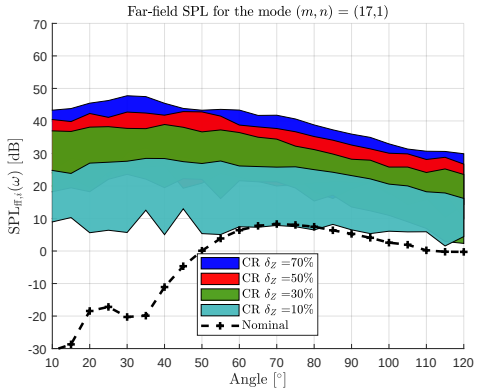

(b) Sensitivity of broadband far-field modal SPL towards aeroacoustic uncertainties

Figure 4.20: Sensitivity of modal SPL data towards aeroacoustic uncertainty level δ_A and liner uncertainty level δ_Z for the cutback condition at the blade passing frequency $f = 946$ Hz (1 BPF) for the mode $(m,n) = (17,1)$ by comparison between nominal data (black line) and simulation data for different values of parameters δ_A and δ_Z. One graduation equals 10 dB.

The objective was to observe the impact of uncertainties over the ring dataset for two different modes whose energy repartition is opposite: one mode whose energy is concentrated around the nacelle axis, and another mode whose energy is located close to the wall. Aeroacoustic uncertainties have a strong impact on both modes, whereas liner uncertainties have impact only on the last mode, which is logical as it is strongly attenuated by liner surfaces.

4.4.2.2 Sensitivity of global Sound Pressure Levels towards uncertainties

In this subsection, global SPLs are used, as calculated using Eq. (4.13) for ring datasets, and Eq. (4.14) for far-field datasets, as it has been done in subsection 4.4.1.2.
In Fig. 4.21, the difference between Hardwall and Lined configurations for the ring nominal dataset (Fig. 4.21a) and the far-field nominal dataset (Fig. 4.21b) is observed. As previously explained, on the hardwall ring dataset, it exists a larger dynamic mainly due to the existence of an overpressure region on the nacelle bottom lip (Fig. 4.17a).

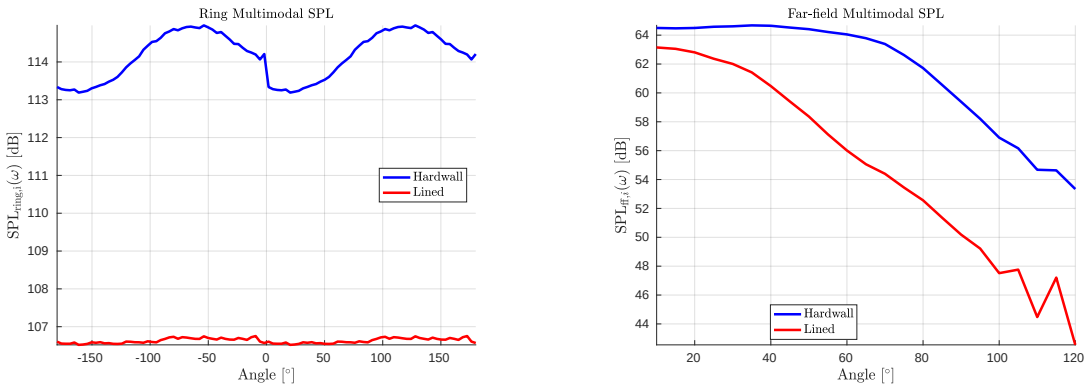

(a) Hardwall with aeroacoustic uncertainties only

(b) Lined with liner uncertainties only

Figure 4.21: Difference between Hardwall and Lined configurations for the ring nominal dataset (left) and the far-field nominal dataset (right) for the cutback condition at the blade passing frequency $f = 946$ Hz (1 BPF). One graduation equals 1 dB on left plot and 2 dB on right plot.

Aeroacoustic uncertainties A first step consists in observing the impact of several aeroacoustic uncertainty levels (δ_A values) towards global SPLs (for both ring and far-field data). The range of δ_A ranges from minimum to maximum intuitive values such as the problem physical meaning would be respected (for example, as previously, 90% of aeroacoustic uncertainties would not be a reasonable value).

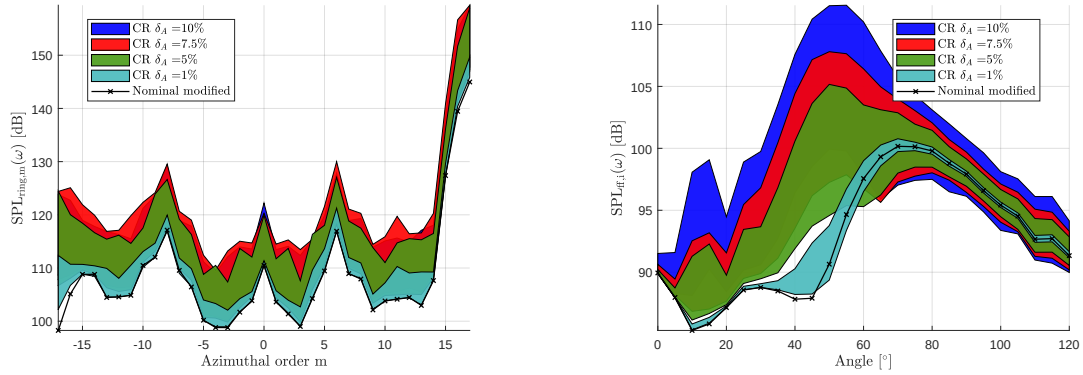

(a) Ring azimuthal SPL

(b) Far-field global SPL

Figure 4.22: Sensitivity of global SPL data towards aeroacoustic uncertainty level δ_A for the cutback condition at the blade passing frequency $f = 946$ Hz (1 BPF) by comparison between experimental data (black line) and simulation data with modified modal content and aeroacoustic uncertainties for several values. One graduation equals 10 dB on left plot and 5 dB on right plot.

In Fig. 4.22, the sensitivity study of global SPL towards aeroacoustic uncertainty level is presented for the cutback condition at the BPF. δ_A varies from 1% to 10%. On the left figure (Fig. 4.22a), the impact of aeroacoustic uncertainties on the ring modal SPL is observed. One can notice that the sensitivity of $SPL_{ring,m}$ is a logarithm function of δ_A. While, it seems that the sensitivity of the far-field SPL (broadband) is a linear function of δ_A, as it can be seen in Fig. 4.22b. This phenomenon has been encountered during the modal SPL sensitivity studies (subsections 4.4.1.1 and 4.4.2.1), and the same was observed in the sensitivity study of global SPL for the approach condition (subsection 4.4.1.2).
Nevertheless, what is more important here is that in Fig. 4.22b, we observe a great increase of

the acoustic energy due to uncertainties in the angle region [40°70°]. This is to be accounted for during the identification of all uncertainty levels.

Liner uncertainties For this study, a variation of liner uncertainties is undertaken (δ_Z = [10%,30%, 50%, 70%]), keeping aeroacoustic uncertainties to zero. As it has been seen in subsection 4.4.2.1, liner uncertainties have a small impact towards modal SPL, for the ring as well as the far-field data. This could be explained by the fact that the liner studied is already optimized for this flight condition/frequency. In order to confirm or infirm this hypothesis, the global stochastic SPLs are also computed using a lined surface for which the admittance has manually been altered by a factor 200%. Results can be seen in Fig. 4.12b for the approach condition.

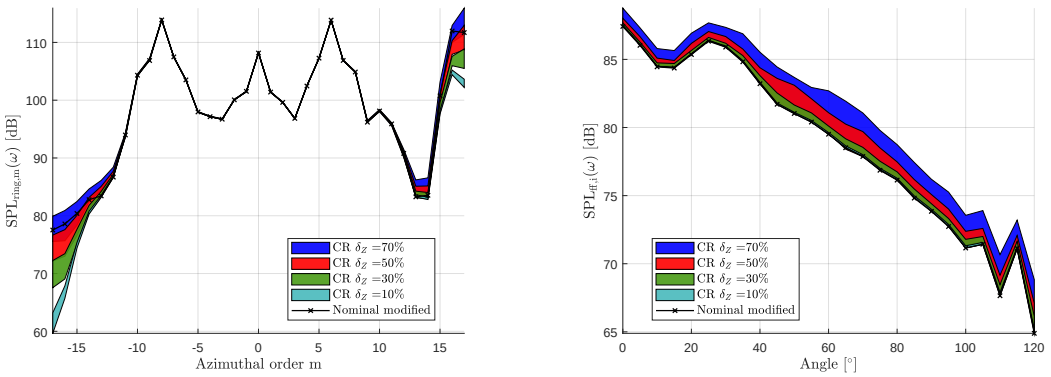

(a) Ring azimuthal SPL

(b) Far-field global SPL

Figure 4.23: Sensitivity of global SPL data towards liner uncertainty level δ_Z for the cutback condition at the blade passing frequency f = 946 Hz (1 BPF) by comparison between experimental data (black line) and simulation data with modified modal content and aeroacoustic uncertainties for several values: $\delta_A = 10\%$ (cyan confidence region), $\delta_A = 30\%$ (green confidence region), $\delta_A = 50\%$ (red confidence region), and $\delta_A = 70\%$ (blue confidence region). Left: Ring dataset; Right: Far-field dataset. One graduation equals 5 dB.

In Fig. 4.23 (both left and right figures), one can observe that lined uncertainties have a low impact on global ring data, especially for azimuthal orders in the range $[-12; 12]$. Whereas outside this range, the azimuthal SPL is slightly affected by liner uncertainties. As it has extensively been explained in the previous subsection, high cut-off ratio modes are more inclined to be affected by uncertainties since they are poorly energetic. On the right figure Fig. 4.23b (far-field dataset), one can observe a higher impact of liner uncertainties than previously observed for the approach condition (Fig. 4.12). This can be explained by the fact that there are more modes attenuated by the liner than for the approach, and thus, the uncertainties are more present.

4.5 Statistical inverse identification of uncertainty levels

In this section, we present the results of the statistical inverse identification of aeroacoustic, liner, and modal content uncertainty levels. This study is divided into 4 main steps that are (1) the identification of the deterministic modal content $\underline{I}_\alpha$ using the hardwall configuration, (2) the identification of aeroacoustic uncertainties using the hardwall configuration, (3) the identification of liner uncertainties using the lined configuration and the previously identified aeroacoustic uncertainties, and (4) the identification of modal content uncertainty levels in presence of the previously identified aeroacoustic and liner uncertainty levels. For this purpose, the underneath objective is to try to frame experimental data with the 95% confidence region associated with the stochastic response on both ring and far-field arrays. We use global SPLs (see (4.14) and (4.13)), that have different sensitivities towards uncertainties. The identification could be simply done by using only far-field data but, as the modal content of experimental data is not known, we expect to reduce the error on the modal content by identifying one using different datasets.

4.5.1 Approach condition

1) Identification of the mean modal content The lack of knowledge related to the acoustic excitation induced by the fan rotation is a major contribution to the overall uncertainty of the computational model. As explained in Section 1.8.2.1, the acoustic excitation is represented by a finite sum of N_d duct modes imposed to the acoustic system. In subsection 2.6.1, the deterministic modal intensity $\underline{I}_\alpha^+$ and its random counterpart I_α^+ of the duct modes have been defined. Concerning the construction of $\underline{I}_\alpha^+$, an empirical model based on civil-aircraft-manufacturer expertise is used. The current section aims to present the identification of the mean acoustic excitation modal content, for which the uncertainty levels associated, defined by the hyperparameter σ_α, are identified later. For that purpose, experimental data are used, corresponding to acoustic pressures measured at points located on a ring at the intake lip, and also on a far-field microphones array. The ring pressures are also simulated with the stochastic computational aeroacoustic model defined in Chapter 2. The identification of the mean value $\underline{I}_\alpha^+$ of the random variable I_α^+ is then performed by minimizing the distance between experimental and simulated data.

In this subsection, the deterministic modal content is identified by comparing experimental data and simulation data for which the modal content is modified, as explained in subsection 4.3.3. The method consists in amplifying specific modes in order to lower the difference between simulation and experimental SPL quantities. For that purpose, the hardwall configuration is used (no liners).
Fig. 4.24 shows the results of the modal content optimization using the custom modal content specified in Section 4.3.3 for which a broadband level, one positive azimuthal and one negative azimuthal emergence, and one emergence for the first mode are determined. The left figure (Fig. 4.24a) shows the azimuthal modified content associated with this optimization, in which emergences are shown. The right figure (Fig. 4.24b) shows the modification of the global sound pressure levels for both ring and far-field data (red line). The black line refers to the nominal calculation, without any modification of the modal content (all modes sent with a level of 100 dB). The main goal here is to try to tune the modal content so as to reduce the difference between experimental data and simulated data to a minimum, for both ring and far-field data.

2) Identification of the aeroacoustic uncertainty level Once the modal content is coarsely defined, the aeroacoustic uncertainties are identified by varying the parameter δ_A from 0 to 1. The main goal is to try to frame a maximum number of experimental points within the 95% confidence region plotted using superior and inferior quantiles.
As it has been showed in the previous paragraph 4.4.1.2, an aeroacoustic uncertainty level

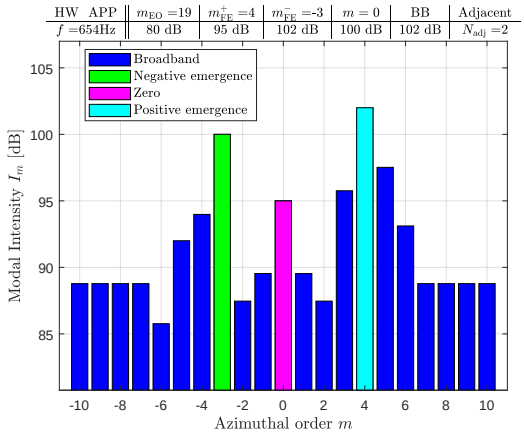

(a) Visualization of the excitation azimuthal content

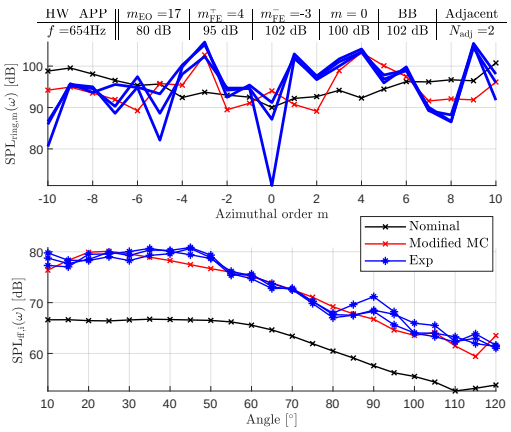

(b) Top: Ring data. Bottom: Far-field data

Figure 4.24: Identification of the deterministic modified modal content for the approach condition at the blade passing frequency $f = 654$ Hz (1 BPF) by comparison between experimental data (blue line), nominal data (black line), and simulation data with modified modal content (red line). One graduation equals 5dB on the left figure and 10 dB for both plots of the right figure.

$\delta_A = 7.5\%$ is sufficient to represent aeroacoustic uncertainties. In this paragraph, the associated results are shown for both ring and far-field global SPLs.

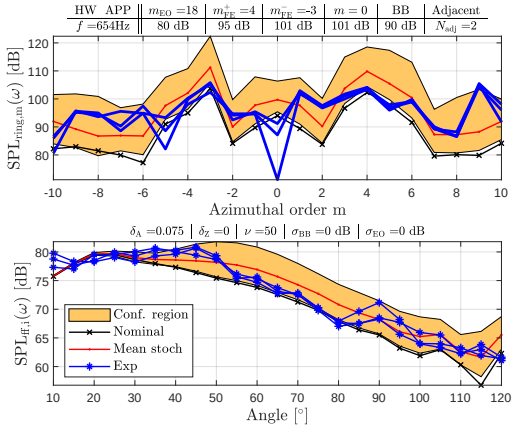

(a) Hardwall/Aeroacoustic uncertainties

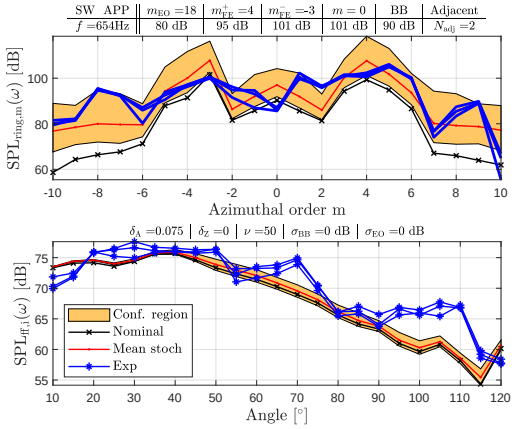

(b) Lined/Aeroacoustic uncertainties

Figure 4.25: Left: Identification of the aeroacoustic uncertainty level δ_A (one graduation equals 10dB for top and 5dB for bottom figure). Right: Observation of the aeroacoustic uncertainty level δ_A impact on the lined case (one graduation equals 20dB for top and 5dB for bottom figure). Approach condition at the blade passing frequency $f = 654$ Hz (1 BPF). Comparison between experimental data (blue line) and simulation data with modified modal content and aeroacoustic uncertainties (with the red line being the statistical mean, and the yellow patch the confidence region at 95%). Top: Azimuthal SPL of ring data. Bottom: Broadband SPL of far-field data

In Fig. 4.25a, global SPL for both ring and far-field data are computed for an aeroacoustic uncertainty level $\delta_A = 7.5\%$. One can observe that for both configurations of microphones, the confidence region frames a satisfying number of experimental points, with the far-field being the most important target. Now that aeroacoustic uncertainties are coarsely identified, liner

uncertainties can be added to the computational model in order to identify their level.

3) Identification of the liner uncertainty level As liner uncertainties are introduced, the computational model changes from hardwall to lined. Liner uncertainties are identified by varying the parameter δ_Z from 0 to 1. The main goal is to try and frame a maximum number of experimental points within the 95% confidence region plotted using superior and inferior quantiles. As it has been seen in the paragraph 4.4.1.2, liner uncertainties have a relatively small impact on global SPL. The choice of their level is then difficult to make. We then intuitively decide to apply a reasonable level of liner uncertainty $\delta_Z = 30\%$.

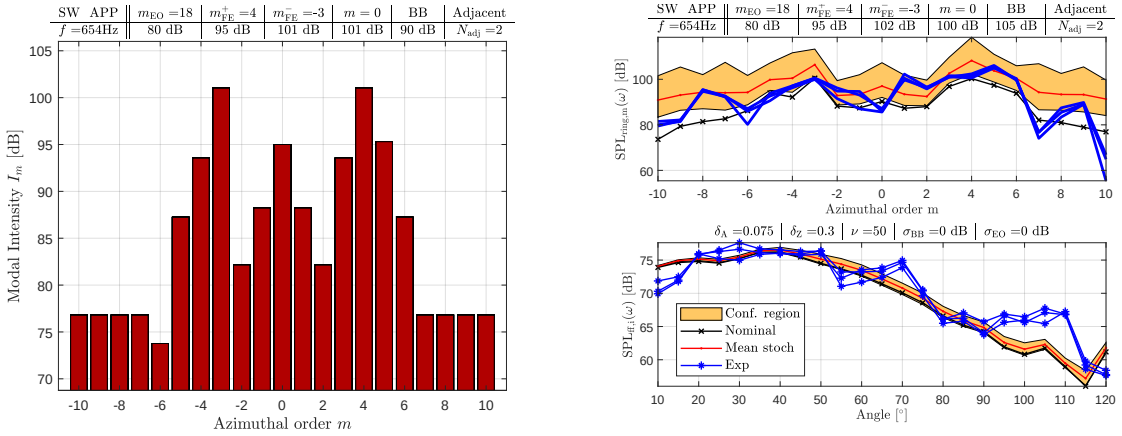

(a) Modal content

(b) Lined/Aeroacoustic uncertainties

Figure 4.26: Left: Visualization of the modal content used for the identification (one graduation equals 5dB for the bottom plot and 10 dB for the top plot). Right: Identification of the liner uncertainty level δ_Z (one graduation equals 5dB for the bottom plot and 20 dB for the top plot). Approach condition at the blade passing frequency $f = 654$ Hz (1 BPF). Comparison between experimental data (blue line) and simulation data with modified modal content and aeroacoustic uncertainties (with the red line being the statistical mean, and the yellow patch the confidence region at 95%. Top: Azimuthal SPL of ring data. Bottom: Broadband SPL of far-field data

In Fig. 4.26b, one can notice that the confidence region calculated using both aeroacoustic and liner uncertainties is not sufficiently large. This can first be explained by the lack of coherence of the modal content for both hardwall and lined cases. Indeed, as we identify the modal content on the hardwall case, in a perfect world, we could expect this modal content to be also appropriate for the lined case. By adding modal content uncertainties, the confidence region should thicken, while "explaining" the other phenomena that are responsible for the difference of modal content between hardwall and lined cases, that are not accounted for in the modeling.

4) Identification of the modal content uncertainty level As aeroacoustic and liner uncertainties has been fixed, the last parameters that allow for thickening the confidence region and frame a maximum of experimental points are the modal content uncertainties. Those are identified by varying the parameters σ_{EO} and σ_{BB} from 0 to 10 dB, keeping a confidence region as thin as possible.
In Fig. 4.27a, the azimuthal stochastic content is depicted, on which the variability on each azimuthal order is observed (±2.5dB for broadband modes and ±2.5dB for emergences). In Fig. 4.27b, the global ring and far-field SPL are plotted, taking into account the modified modal content (Subsection 4.5.1), aeroacoustic uncertainties, liner uncertainties, and modal content uncertainties. A finer optimization is then needed to obtain a better identification, by varying all parameters on small ranges around their previously identified values.

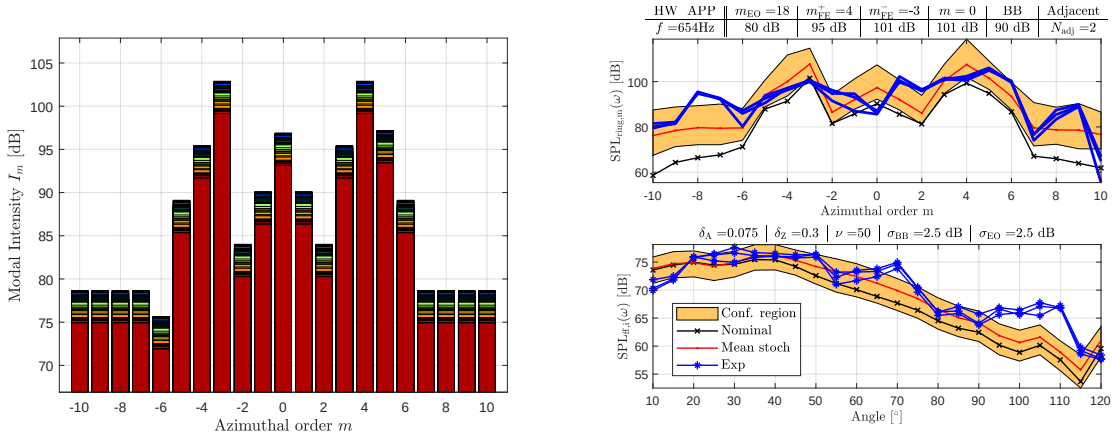

(a) Visualization of the excitation stochastic azimuthal content

(b) Top: Azimuthal SPL of ring data. Bottom: Broadband SPL of far-field data

Figure 4.27: Left: Visualization of the modal content with acoustic excitation uncertainties (one graduation equals 5dB). Right: Identification of the modal content uncertainty levels σ_{EO} and σ_{BB} for the approach condition at the blade passing frequency $f = 654$ Hz (1 BPF) by comparison between experimental data (blue line) and simulation data with modified modal content and aeroacoustic uncertainties (the red line being the statistical mean, and the yellow patch the confidence region) at 95%. One graduation equals 20dB for top and 5dB for bottom figure.

4.5.2 Cutback condition

As the liner is to be optimized for several engine regimes (e.g flight conditions), it is important to validate the identification method for at least one other engine regime. Moreover, since the optimization of liners is presented only for the cutback condition, the identification of uncertainties is of primary order.

1) Identification of the mean modal content The lack of knowledge related to the acoustic excitation induced by the fan rotation is a major contribution to the overall uncertainty of the computational model. As explained in Section 1.8.2.1, the acoustic excitation is represented by a finite sum of N_d duct modes imposed to the acoustic system. In Section 2.6.1, the deterministic modal intensity $\underline{I}_\alpha^+$ and its random counterpart I_α^+ of the duct modes have been defined. Concerning the construction of $\underline{I}_\alpha^+$, an empirical model based on civil-aircraft-manufacturer expertise is used. The current section aims to present the identification of the level of uncertainty associated with the acoustic excitation modal content. For that purpose, experimental data are used, corresponding to acoustic pressures measured at points located on a ring at the intake lip, and also on a far-field microphones array. The ring pressures are also simulated with the stochastic computational aeroacoustic model defined in Chapter 2. The identification of the mean value $\underline{I}_\alpha^+$ and the hyperparameter σ_α of the random variable I_α^+ is then performed by minimizing the distance between experimental and simulated data.

In this subsection, the deterministic modal content is identified by comparing experimental data and simulation data for which the modal content is modified, as explained in section 4.3.3. The method consists in amplifying specific modes in order to lower the difference between simulation and experimental SPL quantities. For that purpose, the hardwall configuration is used (no liners).
Fig. 4.28 shows the results of the modal content optimization using the custom modal content specified in Section 4.3.3 for which a broadband level (blue), one positive azimuthal (cyan) and

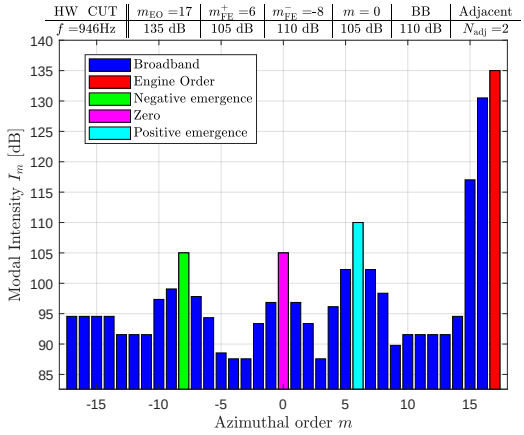

(a) Visualization of the excitation azimuthal content

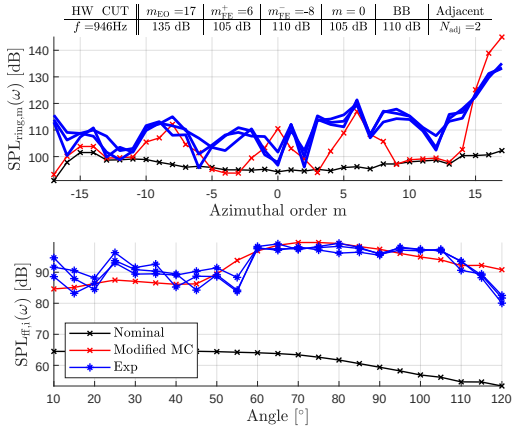

(b) Top: Ring data. Bottom: Far-field data

Figure 4.28: Identification of the deterministic modified modal content for the cutback condition at the blade passing frequency $f = 946$ Hz (1 BPF) by comparison between experimental data (blue line), nominal data (black line), and simulation data with modified modal content (red line). One graduation equals 5 dB for left plots and 10 dB for right plots.

one negative azimuthal emergence (green), one emergence for the first mode (magenta), and one emergence corresponding to the mode carrying the engine order (red), are determined. The left figure (Fig. 4.28a) shows the azimuthal modified content associated with this optimization, in which emergences are shown. The right figure (Fig. 4.28b) shows the modification of the global sound pressure levels for both ring and far-field data (red line). The black line refers to the nominal calculation, without any modification of the modal content (all modes sent with a level of 100 dB). The main goal here is to try to tune the modal content so as to reduce the difference between experimental data and simulated data to a minimum, for both ring and far-field data.

2) Identification of the aeroacoustic uncertainty level Once the modal content is coarsely defined, the aeroacoustic uncertainties are identified by varying the parameter δ_A from 0 to 1. The main goal is to try to frame a maximum number of experimental points within the 95% confidence region plotted using superior and inferior quantiles.
As it has been showed in the previous paragraph 4.4.1.2, an aeroacoustic uncertainty level $\delta_A = 7.5\%$ is sufficient to represent aeroacoustic uncertainties. In this paragraph, the associated results are shown for both ring and far-field global SPLs.
In Fig. 4.29a, global SPL for both ring and far-field data are computed for an aeroacoustic uncertainty level $\delta_A = 7.5\%$. One can observe that for both configurations of microphones, the confidence region frames a low amount of experimental points, with the far-field being the most important target. It exists an angle region between 40° and 60° for which aeroacoustic uncertainties have a strong impact. This is a difficulty that induces a conflict with the identification of the modal content. There is certainly a set of modes that radiate in this specific angle region and are very sensitive towards aeroacoustic uncertainties.
Aeroacoustic uncertainties are also imposed to the lined case (Fig. 4.29b) in order to understand their impact before adding liner uncertainties. What is observed is that on the ring dataset, for azimuthal orders in the range $[-12; 12]$, uncertainties have low impact, as it has already been observed in subsection 4.4.2.2. Modal content uncertainties will then be needed to frame experimental points in this specific azimuthal order range.

3) Identification of the liner uncertainty level As liner uncertainties are introduced, the computational model changes from hardwall to lined. Liner uncertainties are identified by

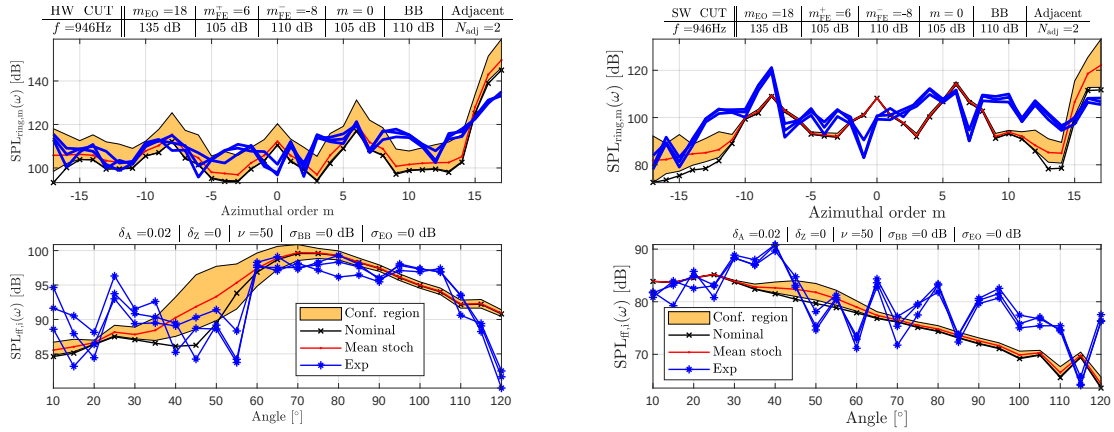

(a) Hardwall/Aeroacoustic uncertainties

(b) Lined/Aeroacoustic uncertainties

Figure 4.29: Left: Identification of the aeroacoustic uncertainty level δ_A (one graduation equals 20dB for top and 5dB for bottom figure). Right: Observation of the aeroacoustic uncertainty level δ_A on the lined (one graduation equals 20dB for top and 10dB for bottom figure). Cutback condition at the blade passing frequency $f = 954$ Hz (1 BPF). Comparison between experimental data (blue line) and simulation data with modified modal content and aeroacoustic uncertainties (with the red line being the statistical mean, and the yellow patch the confidence region at 95%. Top: Azimuthal SPL of ring data. Bottom: Broadband SPL of far-field data

varying the parameter δ_Z from 0 to 1. The main goal is to try and frame a maximum number of experimental points within the 95% confidence region plotted using superior and inferior quantiles. As it has been seen in the paragraph 4.4.1.2, liner uncertainties have a relatively small impact on global SPL. The choice of their level is then difficult to make. We then intuitively decide to apply a reasonable level of liner uncertainty $\delta_Z = 30\%$.

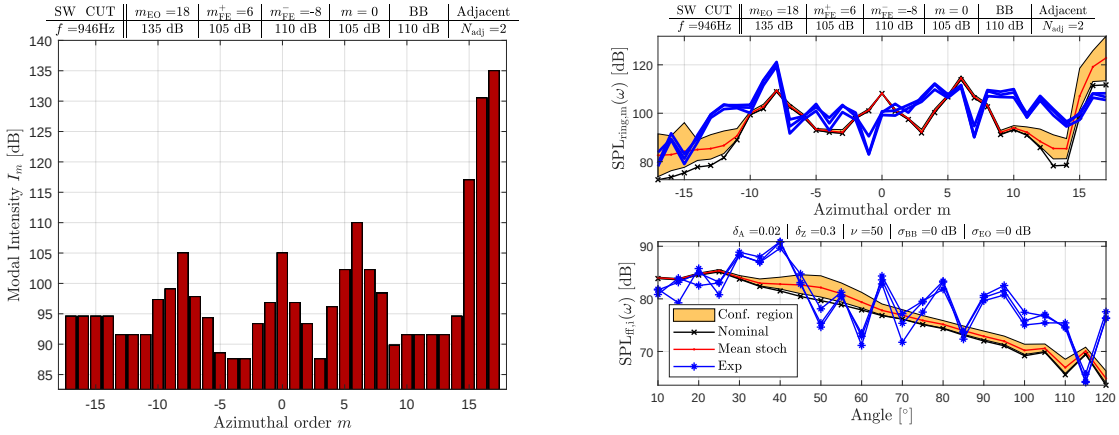

(a) Modal content

(b) Lined/Aeroacoustic uncertainties

Figure 4.30: Left: Visualization of the modal content used (one graduation equals 5dB). Right: Identification of the liner uncertainty level δ_Z. Approach condition at the blade passing frequency $f = 946$ Hz (1 BPF). Comparison between experimental data (blue line) and simulation data with modified modal content and aeroacoustic uncertainties (with the red line being the statistical mean, and the yellow patch the confidence region at 95% (one graduation equals 20dB for top and 10dB for bottom figure). Top: Azimuthal SPL of ring data. Bottom: Broadband SPL of far-field data

In Fig. 4.30b, one can notice that the confidence region calculated using both aeroacoustic and

liner uncertainties is not sufficiently large. The adding of liner uncertainties does not impact the confidence region width at all, which is not surprising regarding what has been observed during the sensitivity study (see Section 4.4). By adding modal content uncertainties, the confidence region should thicken. While Fig. 4.30a depicts the modal content without any uncertainties, which would induce some great error during the identification of liner uncertainties.

4) Identification of the modal content uncertainty level As aeroacoustic and liner uncertainties have been fixed, the last parameters that allow for thickening the confidence region and frame a maximum of experimental points are the modal content uncertainties. Those are identified by varying the parameters σ_{EO} and σ_{BB} from 0 to 10 dB, keeping a confidence region as thin as possible.

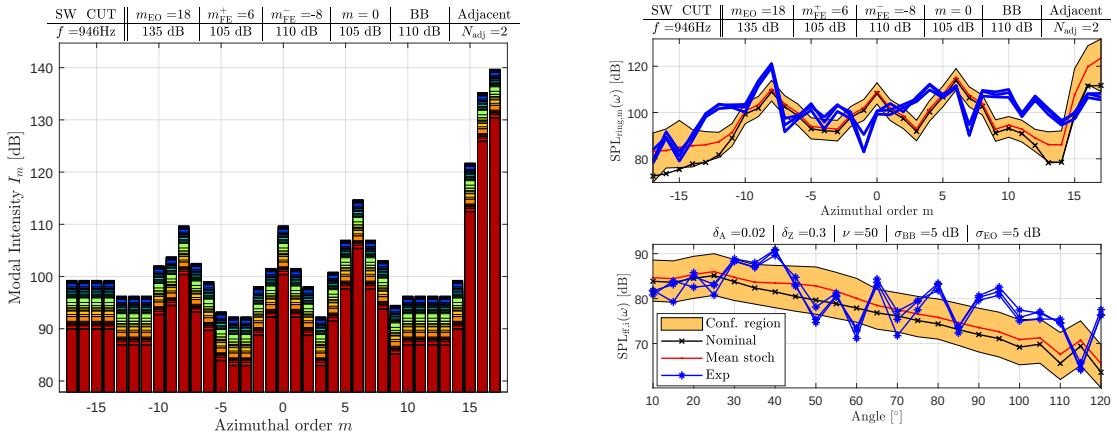

(a) Visualization of the excitation stochastic azimuthal content

(b) Top: Azimuthal SPL of ring data. Bottom: Broadband SPL of far-field data

Figure 4.31: Left: Visualization of the final modal content with excitation uncertainties (one graduation equals 10dB). Right: Identification of the modal content uncertainty levels σ_{EO} and σ_{BB} for the cutback condition at the blade passing frequency $f = 946$ Hz (1 BPF) by comparison between experimental data (blue line) and simulation data with modified modal content and aeroacoustic uncertainties (the red line being the statistical mean, and the yellow patch the confidence region) at 95%. One graduation equals 20dB for top and 10dB for bottom figure.

In Fig. 4.31a, the azimuthal stochastic content is depicted, on which the variability on each azimuthal order is observed (±5dB for broadband modes and ±5dB for emergences). In Fig. 4.27b, the global ring and far-field SPL are plotted, taking into account the modified modal content (Subsection 4.5.2), aeroacoustic uncertainties (Subsection 4.5.2), liner uncertainties (Subsection 4.5.2), and modal content uncertainties.

Qualitatively, the statistical inverse identification can be considered as correctly done. There is a sufficient number of experimental points inside the confidence region for both far-field and ring datasets. An important thing to notice is that the far-field 40 to 60° angle region is very sensitive towards aeroacoustic uncertainties and grows accordingly. This phenomenon is difficult to compensate with the modified modal content (which is logarithmic by essence). Therefore, aeroacoustic uncertainties have to be kept relatively low to avoid the growing of energy in this specific angle range. That is why, for this example, modal content uncertainties are set to a high value, in order to increase the confidence region width and frame a maximum number of experimental points.

4.6 Discussion

The main objective of the present study is the robust design of nacelle liners. As liner design is frozen in early phases of the aircraft development, the maturity of data is still very low. The idea is to anticipate changes in aircraft data that would impact the liner optimum design. For that purpose, uncertainties related to modeling errors and parameters errors in the computational model for liner performance have to be accounted for. In the computational model, the main sources of uncertainties correspond to the accounting of the flow (computed using potential Euler equations), the liner impedance calculation, and the fan acoustic excitation.
In this chapter, we have presented the inverse identification of the deterministic modal content, the aeroacoustic, and liner uncertainty levels by using experimental data issued from a static ground test for different configurations, one fully hardwall and one fully treated. Also, representative flight conditions (engine regimes corresponding to approach and cutback) and one frequency (1 BPF) are studied. From these configurations, two datasets are used, one close to the fan (on the nacelle intake lip) and one in the far-field. The main idea is to try to tune the modal content, its uncertainty levels as well as aeroacoustic and liner uncertainty levels by decreasing the distance between experimental and simulated ring data. Because ring microphones are evenly distributed in the circumferential direction, the azimuthal content should be easy to determine, whereas the radial content remains unknown. Then, the previously identified modal content and uncertainty levels (using ring data) are supposed to be coherent with far-field data. This means that, identifying the aforementioned parameters using only ring data should be sufficiently precise to also frame far-field experimental points.
As it has been observed for several applications presented here, the identification is not that simple. If the inverse identification of each parameter was a convex optimization problem with only one possible optimum, then, identifying parameters using ring data would be sufficient. But, this is not the case here, as there is a consequent number of parameters to optimize simultaneously. For example, there are several modal content definitions that can be used, each one giving different results when used on far-field data. The azimuthal "location" of emergences can wether have a strong impact on the far-field representation, or simply none, and the same is observed for the impact of uncertainty levels. This usually leads to severe differences between a tuning that is well-adapted to ring data, and a tuning that is well-adapted to far-field data, which are more important in the end. A compromise between the two is then to be made. In simpler terms, the precision of the identification of uncertainty levels strongly depends on the modal content knowledge.
The present study is preliminary and is mainly dedicated to the validation of the methodology, in addition to the identification of uncertainty levels. The respect of simple physical phenomena such as the impact of uncertainties over duct modes whose energy repartition is well defined is of major importance here. Then, the sensitivity of global sound pressure levels towards uncertainties is also assessed and allows for understanding the behavior of the stochastic modeling in an optimization framework. Above all, the synergy between the modal content and the sources of uncertainties is studied and allows for identifying the levels of uncertainties and the nominal modal content, as they are needed for the robust optimization of liners.
Nevertheless, considering the lack of knowledge related to the fan excitation modal content, which is of major importance, the identification of uncertainty levels, which has been presented here, can now be used for the robust optimization, in which for each set of design parameters, a Monte Carlo analysis is done (for which the uncertainty levels identified in this chapter are fixed). The robust optimization then gives access to the optimum of the liner in terms of acoustic performance (absorption) and also in terms of robustness, which is related to the level of deviation of stochastic acoustic pressures.

Chapter 5

Optimization of liners using the identified level of uncertainties

Contents

5.1 Identification of the most important design parameters 94
5.2 Strategy for optimizing liner surfaces 94
5.3 Optimization of the forward fan case liner (FFC) 95
5.4 Optimization of the inlet liner 98

Abstract: *In this final chapter, the main objective of the Thesis is tackled. Lined surfaces inside the intake are optimized in presence of the previously identified aeroacoustic, liner, and modal content uncertainties. Two types of liners are optimized, for which two main design parameters are chosen. For that purpose, the stochastic reduced order model introduced in Chapter 2 is extensively used so as to browse the design space built for each one of the two parameters per liner. Lined surfaces are optimized by taking into account their acoustic performance and also the robustness of the design, which is given by statistical estimates of the acoustic responses issued from the Monte Carlo stochastic solver.*

5.1 Identification of the most important design parameters

In order to identify the most important parameters that intervene in the design of the liner, one study could be done by varying each parameter on a defined range. Then, a principle component analysis (PCA) could be carried out in order to determine the relative impact of each parameter on the liner performance. This is not done here by lack of time and is not a crucial point of this part. We use the expertise of Airbus to choose the most important design parameters from the available design parameters of the computational model (see Chapter 3).

5.2 Strategy for optimizing liner surfaces

The objective of this final Chapter is to validate the methodology that has been constructed. For that purpose, the main principle of this study is to carry out an optimization study of two liners that have already been optimized by Airbus using their usual process. In a certain measure, considering that the two optimization processes are difficult to compare, the objective here is to take different values of design parameters around their optimized value (nominal) and try to determine a "new" optimum based on a slightly different performance indicator and a robustness indicator.

The first step is to compute the absorption of a given liner design. For that purpose we subtract lined data to hardwall data, as it is done during a state-of-the-art optimization study. Since both datasets are issued from the same experimental setup for which the lined surfaces are taped for hardwall measurements and untapped for lined measurements, the approximation that consists in subtracting the lined SPL from the hardwall SPL without using pressure quantities is valid. This hypothesis is valid if we suppose that both modal contents are the same. The absorption at a frequency ω, for the Monte Carlo sample θ_k, the microphone i, and a given liner design $\mathbf{w}$, is then written as,

$$\Delta\mathrm{SPL}_{\mathrm{ff}}^{\mathrm{sim}}(\omega, i; \theta_k; \mathbf{w}) = \mathrm{SPL}_{\mathrm{ff}}^{\mathrm{HW}}(\omega, i; \theta_k; \mathbf{w}) - \mathrm{SPL}_{\mathrm{ff}}^{\mathrm{SW}}(\omega, i; \theta_k; \mathbf{w})\,, \tag{5.1}$$

in which $\mathrm{SPL}_{\mathrm{ff}}^{\mathrm{sim}}(\omega)$ is given by Eq. (4.14), $\mathrm{SPL}_{\mathrm{ff}}^{\mathrm{HW}}(\omega, i; \theta_k; \mathbf{w})$ is the far-field simulated data of the hardwall case, and $\mathrm{SPL}_{\mathrm{ff}}^{\mathrm{SW}}(\omega, i; \theta_k; \mathbf{w})$ is the far-field simulated data of the lined case.
Using Eq. (5.1), the objective function associated with the mean of the stochastic acoustic response is given by,

$$J_{\mathbf{mean}}^{(\nu_s)}(\mathbf{w}) = \frac{1}{\nu_s}\sum_{k=1}^{\nu_s}\frac{1}{N_{\mathbf{mics}}}\sum_{i=1}^{N_{\mathbf{mics}}}\Delta\mathrm{SPL}_{\mathrm{ff}}^{\mathrm{sim}}(\omega, i; \theta_k; \mathbf{w}) \tag{5.2}$$

The objective function associated with the standard deviation of the stochastic acoustic response, using Eq. (5.1) and Eq. (5.2) is given by,

$$J_{\mathbf{std}}^{(\nu_s)}(\mathbf{w}) = \sqrt{\frac{1}{\nu_s - 1}\sum_{k=1}^{\nu_s}\left(\frac{1}{N_{\mathbf{mics}}}\sum_{i=1}^{N_{\mathbf{mics}}}\Delta\mathrm{SPL}_{\mathrm{ff}}^{\mathrm{sim}}(\omega, i; \theta_k; \mathbf{w}) - J_{\mathbf{mean}}^{(\nu_s)}(\mathbf{w})\right)^2} \tag{5.3}$$

Then the cost function, associated with each one of the target functions Eqs (5.2) and (5.3), has been introduced in Chapter 1, Eq. (1.112). The optimal value $\mathbf{w}^{\mathrm{opt}}$ is obtained, as a reminder, by solving the following optimization problem,

$$\mathbf{w}^{\mathrm{opt}} = \min_{\mathbf{w}\in\mathcal{C}_w} J(\mathbf{w})\,. \tag{5.4}$$

In the present framework, we try to make a compromise between liner performance and robustness towards an external variability. For that purpose, a cost function that allies both cost

functions (Eqs (5.2) and (5.3)) could be written by assigning different weights to each one of the cost functions. Considering the lack of time and maturity of this part, we prefer to use our judgement before trying to automatize the optimization problem.

5.3 Optimization of the forward fan case liner (FFC)

The FFC is characterized by a perforated resistive sheet (see Appendix C for more information) whose principal parameters are the percentage of Open Area (POA) and the diameter (DIA) of the face sheet perforations. The FFC is then, in the present study, optimized in function of these two parameters. For that purpose, we use the already optimized values of the liner to construct a design space that revolves around these nominal values. We take a percentage of the nominal values from each side to create a response surface on which the optimum is searched. The first coarse design space is constructed by taking percentages of the nominal values for each parameter, as,

$$\mathbf{w} = (1 + \mathbf{p_w})\mathbf{w}_{\text{Nom}} \tag{5.5}$$

in which $\mathbf{p_w}$ is the vector of all percentages and $\mathbf{w}_{\text{Nom}}$ is the nominal value of parameter $\mathbf{w} = (w_1, \ldots, w_N)$, where w_N is the N^{th} design parameter. For the present study, we define w_1 as POA and $\mathbf{p}_{\text{POA}} = [-90\%, -50\%, -30\%, 0\%, 30\%, 50\%, 90\%]$, 0% being the nominal value of parameter POA.
The parameter w_2 is defined as DIA for which $\mathbf{p}_{\text{DIA}} = [-90\%, -50\%, -30\%, 0\%, 30\%, 50\%, 90\%]$ also.

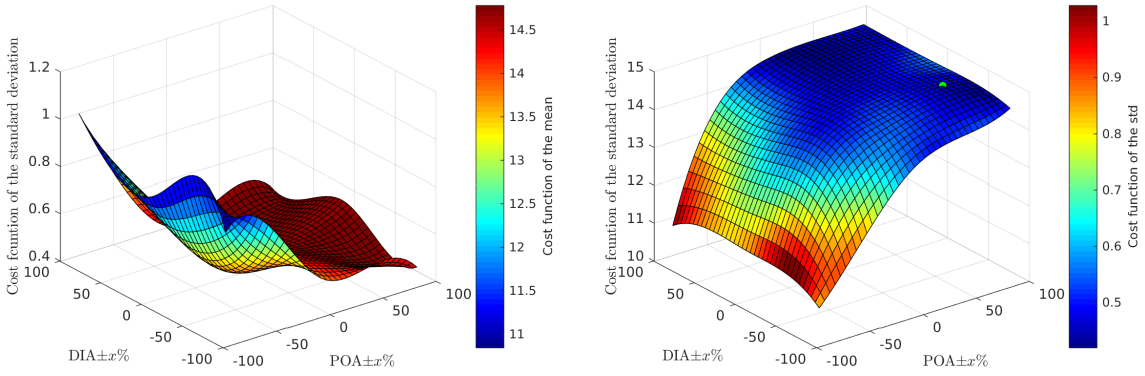

(a) Mean over standard deviation

(b) Standard deviation over mean

Figure 5.1: Cross projections of each cost function related to the FFC liner, on one another. Coarse design space.

In Fig 5.1, a visualization of the 2D performance cost function plotted on the 3D robustness cost function (Fig 5.1a) and a visualization of the 2D robustness cost function plotted on the 3D performance cost function (Fig 5.1a), are presented in order to have an idea of the indicators behavior as a function of a variation of the design parameters.

In Fig. 5.2, the impact of design changes on both POA and DIA parameters is observed in terms of stochastic mean and standard deviation. The interest of such a visualization is to confirm that this impact is real and not purely numerical. One can observe non-negligible discrepancies between each liner configuration, which is reassuring. Also, as observed during the identification of uncertainty levels, in the angle region 40° to 70°, the standard deviation admits a maximum, which indicates that uncertainties have a strong impact in this specific region. Moreover, one

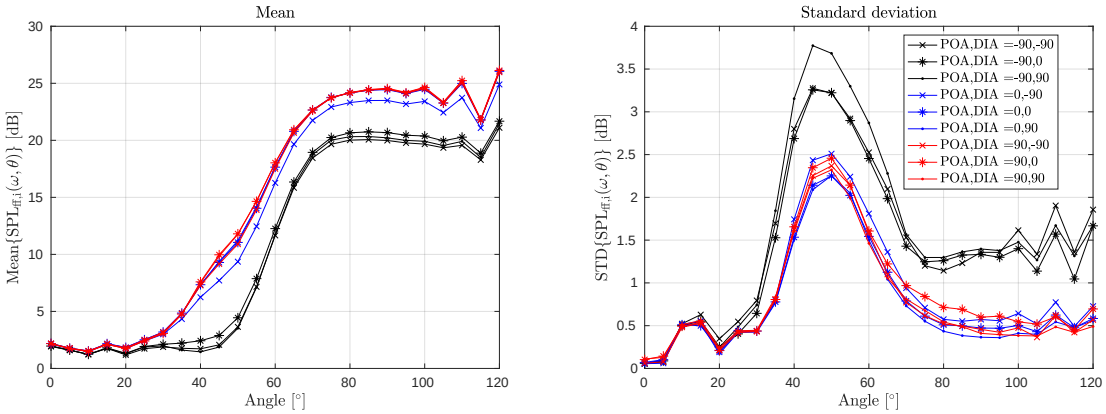

(a) Mean over std (b) Std over mean

Figure 5.2: Visualization of the impact of liner parameters on the stochastic mean and standard deviation for the FFC liner.

can observe that the liner design changes, in this specific configuration, have an impact on the acoustic response from 60° and not much before. This indicates that liner designs are quite robust in the first half of the angle range and more sensitive towards design changes in the second half. Finally, curves are grouped by colors (at iso diameter), and not by symbols (at iso POA), which means that diameter of perforations has less impact than the POA. This observation is in line with Airbus knowledge as there is a clear ranking in terms of impact between geometrical parameters, the most impacting being the POA, then the resistive sheet thickness (not tested here) and the diameter of perforation.
Another view is presented on Fig. 5.3, on which both cost functions are presented separately.

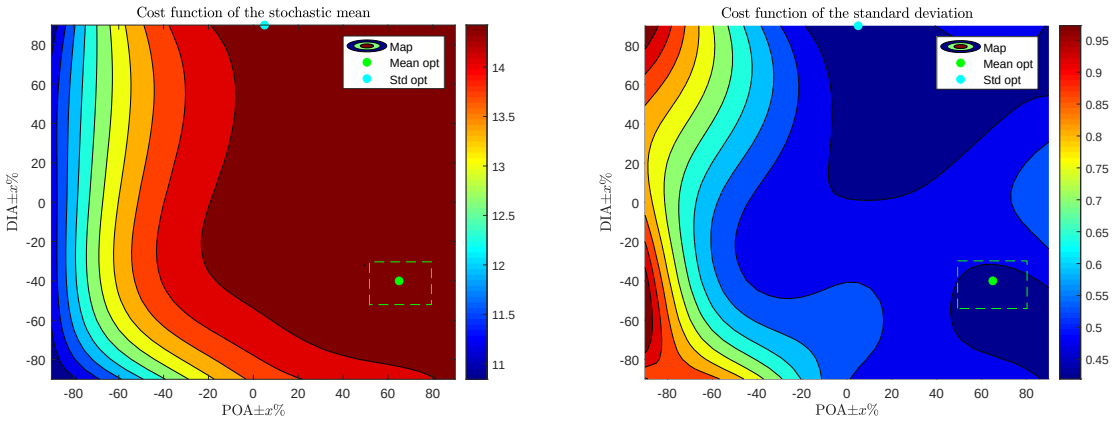

(a) Cost function of the mean (b) Cost function of the std

Figure 5.3: 2D visualization of each cost function related to the FFC optimization for the coarse design space.

In Fig. 5.3a, the cost function of the mean absorption Eq. (5.2) is presented and exhibits a dynamic of 3 dB. The green point in the region $\{\text{DIA} \in [-90\%, -30\%]; \text{POA} \in [50\%, 90\%]\}$ represents the optimum in terms of acoustic performance. The blue point at the top represents the optimum in terms of standard deviation (robustness) found and depicted in Fig. 5.3b, which exhibits a dynamic of 0.5 dB. As it can be seen on the latter, there are two zones in which the standard deviation is minimum. One in the region $\{\text{DIA} \in [60\%, 90\%]; \text{POA} \in [0\%, 30\%]\}$, and another in the region $\{\text{DIA} \in [-90\%, -30\%]; \text{POA} \in [50\%, 90\%]\}$. A compromise has

then to be made between robustness and performance. By chance, the performance in terms of acoustic performance is localized in the latter region. This allows for selecting a thinner region for the optimization, in which both optima are gathered. This region is given by the range $\mathbf{p}_{\mathrm{DIA}} = [-55\%, -45\%, -35\%, -25\%]$ for the Perforations diameter and the range $\mathbf{p}_{\mathrm{POA}} = [50\%, 60\%, 70\%, 80\%]$ for the POA.

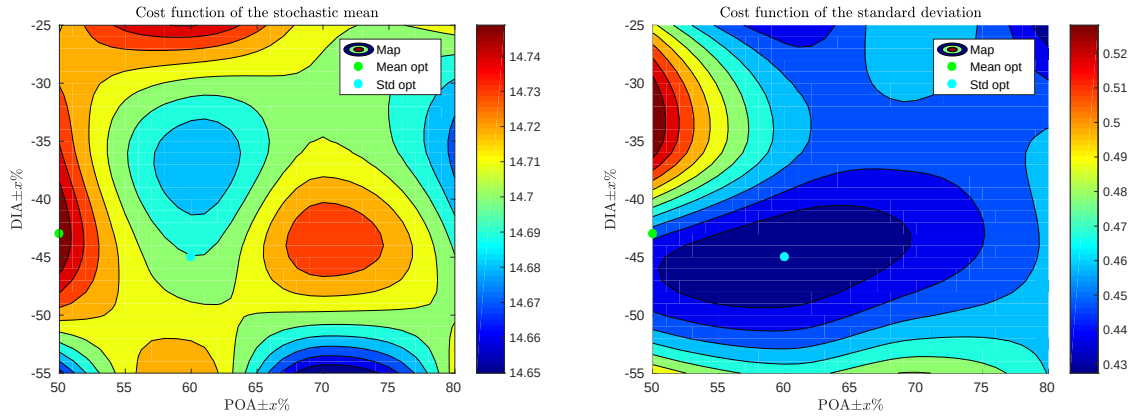

(a) Cost function of the mean

(b) Cost function of the std

Figure 5.4: 2D visualization of each cost function related to the FFC optimization for the thin design space.

In Fig. 5.4, the optimization results on a thinner range of design parameters, as defined in Fig. 5.3 by the green dashed rectangles, are shown in terms of acoustic performance (5.4a) and robustness (5.4b). The final optimum is again, a compromise between performance and robustness. Taking into account the relatively low dynamic of the performance cost function (all configurations have a approximately the same absorption), we chose to favor the robustness of the design. The final optimum for this liner in terms of perforation diameter and percentage of open area is then $\mathrm{DIA} = \mathrm{DIA}_{\mathrm{Nom}} - 45\%$) and $\mathrm{POA} = \mathrm{POA}_{\mathrm{Nom}} + 60\%$.
It is nevertheless really important to notice that, as explained earlier, the optima found in the present study do not represent absolute optima and cannot replace Airbus optima in any case. The optima given in the present study only allows for validating coarsely the method developed during the thesis.

5.4 Optimization of the inlet liner

The same study is done for the Inlet liner whose characteristics are acoustical, whereas they are geometric for the FFC. For this specific face sheet (wire mesh), acoustic properties characterize the liner and not geometrical ones. The two parameters that are chosen are the resistance at an acoustic velocity $v = 0.2$ m/s (R_{20}) and the Non-Linear Factor (NLF), which are briefly described in Appendix C. For the Inlet liner, we define w_1 as R_{20} and $\mathbf{p}_{\mathrm{R}_{20}} = [-90\%, -50\%, -30\%, 0\%, 30\%, 50\%, 90\%, 150\%]$. w_2 is defined as NLF for which $\mathbf{p}_{\mathrm{NLF}} = [-90\%, -50\%, -30\%, 0\%, 30\%, 50\%, 90\%, 150\%]$ also.

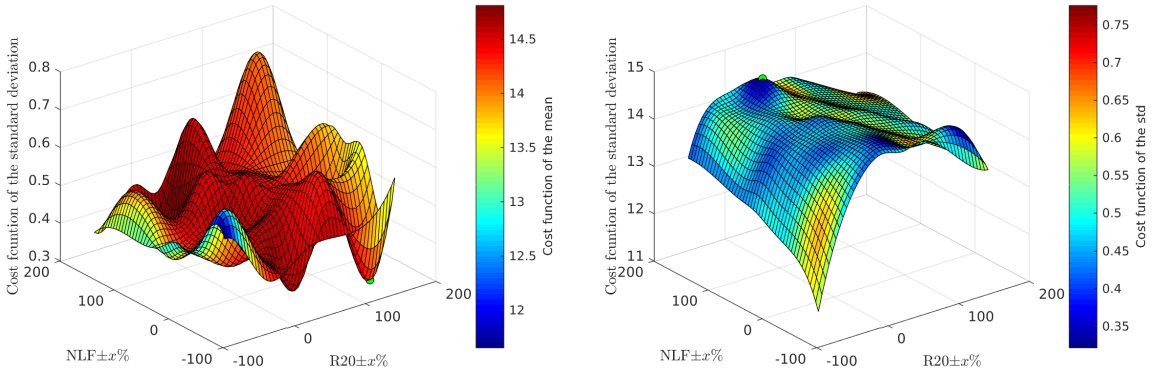

(a) Mean over std

(b) Std over mean

Figure 5.5: Cross projections of each cost function related to the Inlet liner, on one another.

In Fig. 5.5, we present again the 3D visualizations of each one of the two cost functions for which the color maps are given by the other cost function. What is clearly visible is that the performance cost function is way smoother than the robustness cost function. In both visualizations, the green point represents the optimum in terms of standard deviation.

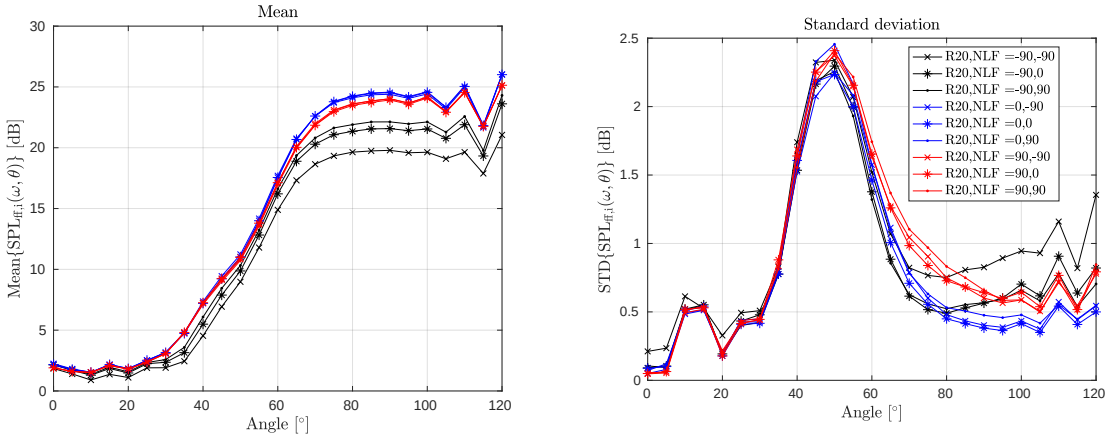

(a) Mean over std

(b) Std over mean

Figure 5.6: Visualization of the impact of liner parameters on the stochastic mean and standard deviation for the Inlet liner.

In Fig. 5.6, the impact of design changes on both R_{20} and NLF parameters is observed in terms of stochastic mean and standard deviation. The interest of such a visualization is to confirm that this impact is real and not purely numerical. One can observe non-negligible discrepancies

between each liner configuration, which is reassuring. Also, as observed during the identification of uncertainty levels, in the angle region 40° to 70°, the standard deviation admits a maximum, which indicates that uncertainties have a strong impact in this specific region. For the cutback, this phenomenon is known by Airbus, which indicates that the stochastic modeling correctly responds and do not create odd results. Moreover, one can observe that the liner design changes, in this specific configuration, have an impact on the acoustic response from 60° and not much before. This indicates that liner designs are quite robust in the first half of the angle range and more sensitive towards design changes in the second half. Finally, curves are grouped by colors (at iso NLF), and not by symbols (at iso R_{20}), which means that NLF has less impact than the R_{20}. This is a known result for wiremeshes.

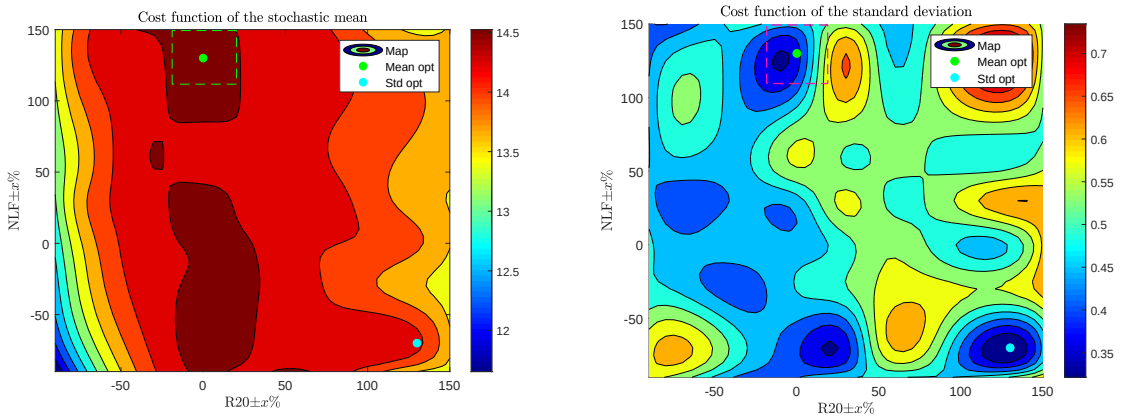

(a) Cost function of the mean

(b) Cost function of the standard deviation

Figure 5.7: 2D visualization of each cost function related to the Inlet optimization for the coarse design space.

In Fig. 5.7a, the optimum in terms of acoustic performance is presented. There is a dynamic of 2.5 dB on the acoustic performance, which is slightly inferior than the dynamic found for the FFC. Nevertheless, we observe a better sensitivity towards both parameters, even if the model is more sensitive towards the R_{20} than the NLF. Its optimum corresponds to the couple $\{R_{20}, \text{NLF}\} = \{\text{R}_{20}^{\text{Nom}} + 5\%, \text{NLF}_{\text{Nom}} + 140\%\}$ In Fig. 5.7b, the optimum in terms of robustness is presented and exhibits a dynamic of 0.35 dB on the standard deviation.

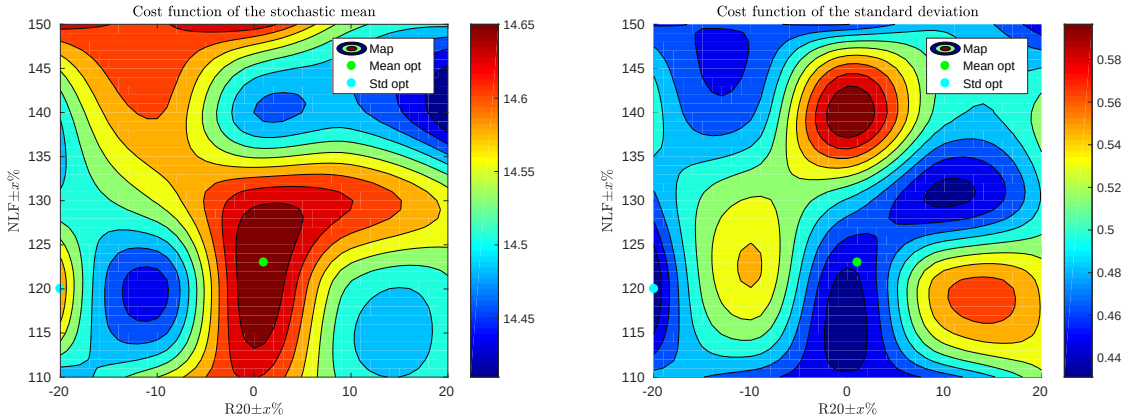

(a) Cost function of the mean

(b) Cost function of the std

Figure 5.8: 2D visualization of each cost function related to the Inlet optimization for the thin design space.

In Fig. 5.8, the thinner grid is presented (green and pruple dashed rectangles in Fig. 5.7) for which $\mathbf{p}_{R_{20}} = [-20\%, -10\%, 0\%, 10\%, 20\%]$, and $\mathbf{p}_{\text{NLF}} = [110\%, 120\%, 130\%, 140\%, 150\%]$. This allows for framing the previous optima found on the coarse grid. There is a 0.2 dB dynamic on the acoustic performance indicator, and 0.14 dB on the robustness indicator. What we observe is that, in the region $\{\mathbf{p}_{R_{20}} \in [-2\%, 2\%]; \mathbf{p}_{\text{NLF}} \in [112\%, 130\%]\}$, a compromise can be made between performance and robustness, as the performance in this region is constant (and optimum), and the robustness is maximum in the subregion $\{\mathbf{p}_{R_{20}} \in [-2\%, 2\%]; \mathbf{p}_{\text{NLF}} \in [115\%, 120\%]\}$, which is included in the acoustic performance optimum region. The final optimum for this liner in terms of Resistance at $v = 0.2$m/s and Non-Linear Factor is then $\text{R}_{20} = \text{R}_{20}^{\text{Nom}}$) and $\text{NLF} = \text{NLF}_{\text{Nom}} + 120\%$). This result is quite reassuring since the R_{20} is the most important parameter and the updated optimum is really not far from what Airbus has already optimized. For the NLF, since this parameter is less important, the great difference proposed by the new optimum is the relatively low impact of the NLF on the acoustic response of the liner.

Discussion

In this Chapter, the results of the two liners optimization in presence of the uncertainties for which the level has been identified in Chapter 4 are presented. This first optimization is done for one flight condition (cutback) and one frequency (1 BPF) only. The objective here is to compare the optimum obtained by Airbus on a full state-of-the-art optimization study, with the one found in the simplified process presented in this work. For obvious reasons, it is not possible to compare both optima in the same conditions, as Airbus includes calculations for several frequencies, flight conditions, and other refinements such as static to flight transformation, etc. Nevertheless, this comparison gives an idea of what can be obtained with the stochastic model, and more importantly, verify that the optimum found with this new method is not far away from the industrial optimum. In order to optimize the liners, two quantities are computed based on the stochastic acoustic absorption (which is the difference between hardwall and lined datasets) and allow one for knowing the performance in terms of absorption of a given design, and two for knowing the robustness the design.

A first optimization is done on the Forward Fan Case liner, which is the closest to the fan, and also the smallest in terms of acoustic surface. Two parameters are chosen in order to be optimized, the Percentage of Open Area (POA) and the diameter of the face sheet perforations (DIA). The starting point of the optimization design is the definition of Airbus optima for each parameter. A design space is then drawn from these values, by taking several percentages of these nominal values from each side. From a first coarse design space, a thinner region is cut from it, and the optimum for both parameters is drawn. For this specific study, the POA is clearly more impacting on the acoustic performance than the diameter. This leads to a one sided optimization study in terms of acoustic performance. For the robustness, the diameter has a slightly better impact, enough to allow for finding an optimum.
A second optimization is done on the Inlet liner, which has a higher acoustic surface and also a different face sheet definition (wire mesh instead of a perforated plate for the FFC). Two parameters are chosen in order to be optimized, the resistance at a velocity v =0.2 m/s (R_{20}) and the NonLinear Factor (NLF). For this study, even if the R_{20} has a significantly better impact on the acoustic absorption, the NLF impacts allows also to have a clear optimal zone for the acoustic performance, and even better for the design robustness.
For both studies, a compromise had to be made between acoustic performance in terms of absorption and robustness of the design. Even if we managed to find, by chance, both optima in similar regions each time, it will not be that easy in further studies when adding several frequencies, several flight conditions, and more design parameters. The blade passing frequency being a crucial design frequency for liner design, results are quite promising.

The important point of this study is that the stochastic model seems to correctly work, and gives, in this specific configuration, results that are not far away from the real optimum found previously by Airbus. Nevertheless, as it has been explained in the previous chapter (4), the results could be better if we managed to find a better modal content that would allow for reducing the amount of excitation levels uncertainties, and thus give a better dynamic of results and a more precise identification of aeroacoustic and liner uncertainties. This work could be done in a separate thesis and would allow for a lot of progress in that specific domain.

Conclusion

This work is devoted to the implementation of a robust design process allowing for associating to the acoustic performance of a given liner design, its propensity to keep its optimum performance stable towards an external variability. From an industrial point of view, this variability is closely linked to the lack of maturity of an aircraft program in its early development phase for which the acoustic treatments are designed. The industrial problematic is then to account for such a variability in early phases of liner design in order to anticipate small changes that would impact its design and therefore, its performance. A first goal is then to track and quantify the main sources of uncertainties that lie within the numerical tool used for the dimensioning of a liner following its acoustic performance. In such a tool, the liner design is characterized by its acoustic impedance. The variability is accounted for under the form of uncertainties within the computational model that can be induced by modeling errors such as the hypotheses and approximations that are made, and also by model parameters errors, such as variations of thermodynamic quantities that impact the calculation of the flow and the acoustic propagation.

Uncertainty quantification

In order to account for such a variability, a quantification of the overall uncertainty is carried out. A first step consisted in detailing and understanding the physics on which the computational model is constructed on. For that purpose, the fundamental equations of the convected acoustic propagation in lined ducts have been reestablished as well as the weak formulation of the associated boundary value problem. The spatial discretization of the weak formulation is made by using finite/infinite elements. In addition, an adapted reduced-order computational model has been introduced in order to allow the implementation of random matrices related to the nonparametric probabilistic approach of uncertainties on the aeroacoustic operator condensed on the liner interface and on the impedance operator of the liner. In a second step, we have analyzed the algebraic mathematical properties of the three main operators that concern the liner impedance, an operator responsible for the aeroacoustic effects of the liner in presence of the flow, and the operator responsible for the excitation induced by the fan rotation, that is assimilated to a duct modal representation.
In a third step, we have developed an appropriate probabilistic model of uncertainties for each one of the uncertain operators of the computational model, based on their algebraic properties. We have used the nonparametric probabilistic approach of uncertainties that allows to take into account both modeling errors and uncertainties on the model parameters. This approach allows for introducing random variations so as to imitate an external variability such as those induced by small changes of flow-related properties, by engine regimes, by small changes in the liner geometry such as a reduction of the perforation effective diameter and the thickness of the face sheet, which can impact the calculation of its impedance, and thus, its acoustic performance. Finally, a probabilistic model of the excitation induced by the fan has been proposed using the parametric approach of uncertainties.
Such a variability on aeroacoustic and liner operators is controlled by two hyperparameters δ_A and δ_Z that allow the level of uncertainties to be imposed. These hyperparameters have then

been identified by solving a statistical inverse problem that consists in minimizing a distance between the experimental measurements and the stochastic acoustic response simulated with the stochastic computational model. For that purpose, confidence regions are drawn from the acoustic stochastic response, and the underneath objective is then to frame a maximum of experimental points inside those confidence regions, while keeping them as thin as possible. At this stage, trying to compare experimental and simulated data is quickly impossible. Indeed, as the modal content of the fan is neither defined nor perfectly understood, and as modes are simulated with a basic level of 100 dB, the acoustic responses of both experimental and simulated setups can not be compared because of great differences of levels and modal content. An important turning point of the present work then was to investigate the excitation modal content. A customizable one was then introduced inspired by Airbus expertise. For the excitation, two hyperparameters σ_{EO} and σ_{BB} allow for imposing a variability level in dB to, respectively, the multi-modal basic acoustic level, and to each emergence level.

Sensitivity study towards uncertainties

We have extensively operated the stochastic reduced-order model in order to undertake a sensitivity analysis of the acoustic response towards aeroacoustic and liner uncertainties. In order to do so, the acoustic contribution of each excitation duct mode as well as global quantities of interest, averaged on all excitation modes, have been observed on two different microphone arrays. One is located in the nacelle intake lip, and one is located in the far-field. The interest of using the former has been to determine, through the phase of each microphone, the azimuthal response of each cylindrical duct mode. This has allowed for measuring (experimental setup) the azimuthal modal content of each mode. While the latter microphone array (far-field) is specifically used for aircraft noise certification, as imposed by the authorities, and is thus a quantity of interest for liner performance studies. During this work, two thermodynamic conditions have been used and correspond to the approach and take-off phases. Hardwall and lined results have been analyzed in order to determine the sensitivity of the model towards aeroacoustic uncertainties and liner uncertainties separately.

The results of the sensitivity analysis towards aeroacoustic uncertainties, using the hardwall case, show great differences between the two microphones arrays. Indeed, it exists some phenomena as saturation effects that can be visible on the ring for a certain amount of aeroacoustic uncertainties, and a different one in the far-field. This can be explained by several factors such as the relative distance of each microphone array to the acoustic source, which induces a better captation of high cut-off modes by the ring than the far-field array. As a matter of fact, highly cut-off modes are more impacted by uncertainties. The saturation effect is thus much more visible on the ring since the ring is more likely to capture highly ut-off modes than the far-field array. It also exists strong differences of impact between aeroacoustic and liner uncertainties on global sound pressure levels, which can be explained by the fact that aeroacoustic uncertainties have a non-negligible impact on every mode, whereas liner uncertainties only have a significant impact on the modes that are the most attenuated by liners.

A first objective of this work was to verify that the stochastic reduced-order model correctly responded to the application of uncertainties. The idea has been to observe the impact of such uncertainties on well-known excitation duct modes, for which the acoustic response is expected. For examples, the first cut-off excitation mode is not impacted by liner whereas the last one is. From this statement, an observation of the impact of uncertainties on both should follow this trend: liner uncertainties then should have a significant, or slightly better, impact on the former, whereas aeroacoustic uncertainties should impact both modes. This has been observed and has allowed us to obtain a preliminary validation.

A second objective was to understand on which specific cut-off modes aeroacoustic and liner uncertainties have an impact. We have observed that it can exist strong discrepancies in certain

angular regions, where modes are very directive. This had to be accounted for in the identification of uncertainty levels as well as the excitation modal content, because of strong conflicts between the two.

Identification of excitation modal content and uncertainty levels

The identification study has been one of the most important step of the present work. The setting of uncertainty levels and the modal content of the fan excitation representation have to be used throughout the liner optimization process. The principle has been to compare experimental data with the simulated data acquired with the stochastic computational model for which the level of uncertainties is controlled for the aeroacoustic and liner operators. The results of such a system are a set of pressure responses from which statistical information are drawn. A confidence region corresponding to a 95% degree of confidence has been calculated from it and compared to the experimental results. The method has allowed us to frame a maximum of experimental points inside the confidence region, while keeping it the thinnest possible.
The first step of the identification has consisted in determining a modal content that allows for comparing simulated and experimental data. Initially, the idea was to identify such an energy repartition between excitation modes, only by using the ring dataset, as they have been specifically acquired for that purpose. Once this would have been done, a transposition of the identified modal content would have also been appropriate to the comparison of both experimental and simulated far-field datasets. Unfortunately, we have observed important differences between ring and far-field applications of the same modal content on the acoustic response. A compromise between ring and far-field datasets has then been made, as far-field quantities of interest are of primary importance in the liner optimization process. It probably exists a difference between the post-processing of raw measured ring data and raw simulated data that explains the lack of coherence between both datasets. This needs to be furtherly investigated.
Secondly, aeroacoustic uncertainties have been identified, as mentioned earlier, by thickening a confidence region, related to an increase of the uncertainty level. For the two flight conditions tested, the statistical inverse identification of aeroacoustic uncertainties was a convex optimization problem for which there was a clear level to not overtake. Indeed, overtaking this specific level would induce an increase of the stochastic mean and thus interfere with the tuning of the modal content, previously fixed.
Then, the same analysis has been carried out for liner uncertainties, for which the hardwall case has been replaced by liners (obviously). As it has been seen during the sensitivity analysis, liner uncertainties have a significantly low impact on the acoustic quantity of interest that is the global (or multi-modal) sound pressure level, as liner uncertainties have an impact on a few excitation modes, for which the impact is flooded during the averaging on all cut-off modes. We then chose to take a reasonable value of $\delta_Z = 30\%$ for the rest of the analysis.
Finally, modal content uncertainties on the imposed acoustic levels (multi-modal and emergence levels) have been identified, in presence of the fixed modal content, aeroacoustic uncertainties and liner uncertainties. This final step has allowed for significantly improving the framing of experimental points inside the confidence region, as modal content uncertainties are the most impacting.
An important note to be made is to emphasize the need of a better modal content representation, which could drastically help with the identification of the two other uncertainty levels. Also, as we have observed, the lack of impact of liner uncertainties compared to aeroacoustic uncertainties is a difficulty for its identification. Moreover, the aeroacoustic uncertainties have a significant impact on all modes, and especially on certain modes that are strongly directive in one angular region in the far-field, and that can conflict with the previously fixed modal content.

Optimization of liners in presence of uncertainties

Once uncertainty levels and modal content are fixed, the last and main goal of the thesis has been the optimization of the two liner surfaces in presence of such uncertainties. For that purpose, the two most impacting design parameters have been selected for each one of the liners. Then, a coarse design space has been drawn by taking proportions of the nominal (optimum value found by Airbus) from each side of each design parameters. In addition, a refined design space has been derived from a first optimum, resulting from the coarse design space. It should be noted that the optimization process used by Airbus consists in giving an information about the acoustic performance of a given design (set of design parameters). What this work provides is an information, in addition to the performance information, about the propensity of a given liner design to keep its acoustic performance stable towards small changes that impacts its design parameters. Namely, an information about the robustness of a given design. This information, allied to the performance, allows for choosing a design in early phases of an aircraft development, for which the acoustic performance would not be impacted by small changes induced by the increasing maturity of the aircraft. Such a maturity increasing would then be anticipated in early phases and would save some re-optimization activities that are time consuming, and therefore give more flexibility to Airbus nacelle team, responsible for the liner acoustic performance. Moreover, this thesis work allows for a preliminary study of the uncertainty that lies within the computational model, that has never been done, to our knowledge.
The statistical inverse identification and the optimization have only been carried out for one flight condition and one frequency in order to validate the developed methods. The Airbus optimization process is more richer in terms of flight conditions and frequencies. Consequently, the optimization results presented in this work cannot directly be compared to the Airbus results, even if they are quite equivalent.

Perspectives and way forward

The work that we have presented is quite promising as the stochastic model implemented seems to correctly respond to the application of uncertainty levels, even if liner uncertainties are weak for the case that has been analyzed. This conclusion could be modified for other flight conditions or other aircrafts. The optimization in presence of uncertainties gives interesting results for two parameters. There is now an effort to be made, on one hand, on the industrialization of such a reduced-order model by grafting it to the actual optimization process used by Airbus. On the other hand, once the stochastic computational model is fully functional and linked, an optimization study done on several frequencies and several flight conditions would allow us to give a better evaluation of the pertinence of the probabilistic approach proposed from an industrial point of view. This implies the use of 2D-axisymmetric nacelle intake models that induces more model uncertainties due to the degradation of the model. The inverse identification of uncertainty levels are then to be re-done in order to account for such a model degradation. Last but not least, additional work should be undertaken concerning the representation of the fan acoustic excitation that remains an important source of errors in this specific aeroacoustic modeling. As this feature is developed in post processing, the modal content can be changed and improved at will, without questioning the stochastic modeling of aeroacoustic and liner uncertainties.

Appendix A

Steady flow computation

In this appendix, we briefly summarize the steady flow computation that is carried out with the ACTRAN flow utility.

1. Steady flow equation. The flow, which is assumed to be irrotational and compressible, is modeled by the Euler compressible potential equation,

$$\boldsymbol{\nabla} \cdot (\rho \mathbf{v}_f) = 0\,, \tag{A.1}$$

where $\mathbf{v}_f = \boldsymbol{\nabla}\psi$ is a velocity field that derives from the velocity potential ψ and where ρ is the mass density that is written as,

$$\rho = \left(1 - \frac{(\gamma-1)}{2}\frac{||\boldsymbol{\nabla}\psi||^2}{c^2}\right)^{\dfrac{1}{\gamma-1}}\,. \tag{A.2}$$

in which γ is a specific mass ratio and where c is the sound celerity.

2. Boundary conditions. The geometry of the boundaries of the fluid domain for the steady flow computation (Eq. (A.1)) are shown in Fig. A.1. The upstream boundary condition consists in imposing the value of the normal velocity for the flow condition at infinity (obtained from the Mach number M_∞ and the speed of sound c for a given atmospheric condition) as,

$$\frac{\partial\psi}{\partial\mathbf{n}} = \boldsymbol{\nabla}\psi \cdot \mathbf{n} = v_\infty = M_\infty c. \tag{A.3}$$

The downstream boundary condition consists in imposing a constant velocity potential as,

$$\psi = \psi_{\text{imposed}}. \tag{A.4}$$

On the excitation plane, a normal velocity of the flow is imposed such as,

$$\frac{\partial\psi}{\partial\mathbf{n}} = \boldsymbol{\nabla}\psi = \mathbf{q}_m\frac{1}{\rho S} = \mathbf{v}_{fan}. \tag{A.5}$$

where $\mathbf{q}_m$ is the mass flow rate and S is the section of the duct in the fan plane.

3. Computational model for the steady flow computation. The computational model is derived from the finite element discretization of the weak formulation of the boundary value problem, which is written as,

$$[A(\boldsymbol{\Psi})]\boldsymbol{\Psi} = \mathbf{f}\,, \tag{A.6}$$

in which matrix $[A(\mathbf{\Psi})]$ depends on $\mathbf{\Psi}$.

4. CFD solver. The CFD solver is based on the use of the following iterative algorithm,

$$[A(\mathbf{\Psi}_{N-1})]\mathbf{\Psi}_N = \mathbf{f}\,, \tag{A.7}$$

where $\mathbf{\Psi}_{N-1}$ and $\mathbf{\Psi}_N$ corresponds respectively to $\mathbf{\Psi}$ at iteration $N-1$ and N. The solver iterates $N = N_{\max}$ times to reach a defined tolerance τ for the mass density as,

$$|\rho_N - \rho_{N-1}| < \tau\,, \tag{A.8}$$

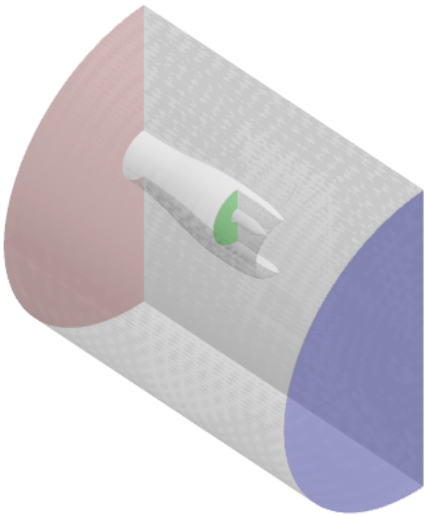

Figure A.1: Intake model CFD mesh with the upstream plane (red plane located in the figure background), the downstream plane (blue plane in the figure front), and the excitation plane (green plane in the middle of the figure)

Appendix B

Fan excitation

In Chapter 1, the excitation is represented using a modal basis, which is solution of a semi-infinite hard-walled duct eigenvalue problem, as

$$\varphi(x,y,z) = \sum_{\alpha=1}^{N_d} \varphi_\alpha(x,y) \left[c_\alpha^+ e^{jk_{z_\alpha}^+ z} + c_\alpha^- e^{jk_{z_\alpha}^- z} \right] , \tag{B.1}$$

in which $k_{z_\alpha}^+$ is the axial wavenumber of the wave propagating in the upstream direction and $k_{z_\alpha}^-$ is the axial wavenumber of the wave propagating in the downstream direction, which have been written as,

$$k_{z_\alpha}^\pm = \frac{kM \pm \gamma_\alpha}{\beta^2} , \tag{B.2}$$

where $\gamma_\alpha = \sqrt{k^2 - \beta^2 k_{xy_\alpha}^2}$ is expressed in terms of k_{xy_α} which is known from the shape of the duct.
This appendix aims to fully characterize the solution $\varphi(x,y,z)$ by defining the unknowns $c_\alpha^\pm = |c_\alpha^\pm| e^{\phi_\alpha^\pm}$ for upstream and downstream directions.

B.1 Definition of hypotheses for characterizing the excitation

The excitation plane is composed of an incident sound field and a reflected sound field. The incident sound field is represented by propagative modes in the upstream direction whose modal intensities are known and are imposed, following the different types listed in Table B.1. The corresponding reflected sound field in the downstream direction is deduced from the incident sound field.

N°	Type	Amplitude		Phase	Associated Equation
1	Mode/mode	Imposed / mode :	$a_\alpha^+ = \underline{a}_\alpha$	$\varphi_\alpha^+ = \underline{\varphi}_\alpha$	$c_\alpha^+ = \underline{a}_\alpha e^{\underline{\varphi}_\alpha}$
2	Linear combination	Equidistribution :	$\sum_\alpha a_\alpha^+ = I$	$\varphi_\alpha^+ = 0$	$c_\alpha^+ = \underline{a}_\alpha$
3	Linear combination	Equidistribution :	$\sum_\alpha a_\alpha^+ = I$	$\varphi_\alpha^+ = \varphi_\alpha^+$	$c_\alpha^+ = \underline{a}_\alpha e^{\varphi_\alpha^+}$
4	Linear combination	Equidistribution :	$\sum_\alpha A_\alpha^+ = I$	$\varphi_\alpha^+ = \Phi_\alpha^+$	$c_\alpha^+ = A_\alpha^+ e^{\Phi_\alpha^+}$

Table B.1: Excitation hypotheses on the amplitude and the phase of each duct mode

In Table B.1,

- the first three types are deterministic. The term "Equidistribution" refers to a commonly used hypothesis, which states that the amplitudes are equally distributed on all incident duct modes. We then have, $|c_\alpha^+| = I/N_d$ in which the positive amplitude I is given.

- the last type is random. As in the first three types, the amplitudes are deterministic and equally distributed on all incident duct modes, which yields $|c_\alpha^{+,rand}| = I/N_d$. The random variables $\phi_1^{+,rand}, \ldots, \phi_{N_d}^{+,rand}$ are independent copies of a uniform random variable ϕ^{rand} on $[0, 2\pi]$.

It should be noted that the intensity I is related to the modal amplitudes $|c_\alpha^+|$ and $|c_\alpha^-|$ by an equation that is developed in Section B.2. In practice, the acoustic excitation is defined by giving the coefficients $c_1^+, \ldots, c_{N_d}^+$. The coefficients $c_1^-, \ldots, c_{N_d}^-$ are calculated by solving the boundary value problem. and consequently, cannot be chosen arbitrarily.

B.2 Acoustic intensity in a hardwall duct in presence of a flow

In order to calculate the coefficients c_α associated to Eq. (B.1), the acoustic intensity in a semi-infinite hardwall duct in presence of an uniform mean-flow along the axial axis z (which implies that $\mathbf{v} \cdot \mathbf{e}_z = v_z$, $\mathbf{v}_0 \cdot \mathbf{e}_z = v_0$, in which $e_\mathbf{z}$, $\mathbf{M} \cdot \mathbf{e}_z = M$, and $M = v_0/c$) is written as [20],

$$I = \frac{P}{S} = \int_S \frac{1}{2\rho_0 c S} \mathcal{R}e\left[(p + M\rho_0 c v_z)(\rho_0 c v_z + Mp)^*\right] ds\,, \tag{B.3}$$

which can be rewritten using the velocity potential φ and $p = -j\omega\,\rho_0\,\varphi - \rho_0 v_0 \dfrac{\partial \varphi}{\partial z}$ as,

$$I = \frac{\omega \rho_0}{2cS} \int_S \mathcal{R}e\left[\varphi \left(jc\beta^2 \frac{\partial \varphi}{\partial z} + \omega M \varphi\right)^*\right] ds\,. \tag{B.4}$$

Substituting Eq. (1.52) into Eq. (B.4), the acoustic intensity writes,

$$I = \frac{\omega \rho_0}{2cS} \int_S \mathcal{R}e\left[\sum_{\alpha=1}^{N_d} \varphi_\alpha(x,y) \left\{c_\alpha^+ e^{jk_{z_\alpha}^+ z} + c_\alpha^- e^{jk_{z_\alpha}^- z}\right\} \sum_{\beta=1}^{N_d} \varphi_\beta(x,y)^* \left(\omega M \left[c_\beta^+ e^{jk_{z_\beta}^+ z} + c_\beta^- e^{jk_{z_\beta}^- z}\right] + j\beta^2 c \left[jk_{z_\beta}^+ c_\beta^+ e^{jk_{z_\beta}^+ z} + jk_{z_\beta}^- c_\beta^- e^{jk_{z_\beta}^- z}\right]\right)^*\right] ds\,. \tag{B.5}$$

Using the orthonormality of the transversal modes φ_α as,

$$\frac{1}{S} \int_S \varphi_\alpha \varphi_\beta^* ds = \delta_{\alpha\beta}\,, \tag{B.6}$$

and taking $z = 0$ (position of Γ_f), Eq. (B.5) yields,

$$I = \frac{\rho_0\,\omega}{2c} \sum_{\alpha=1}^{N_d} \mathcal{R}e\left[\left(c_\alpha^+ + c_\alpha^-\right)\left(c_\alpha^- - c_\alpha^+\right)^* c\gamma_\alpha^*\right]\,. \tag{B.7}$$

which is developed as,

$$I = \frac{\rho_0\,\omega}{2} \sum_{\alpha=1}^{N_d} \mathcal{R}e\left[\gamma_\alpha^* \left(-|c_\alpha^+|^2 + |c_\alpha^-|^2 + c_\alpha^+ c_\alpha^{-^*} - c_\alpha^- c_\alpha^{+^*}\right)\right]\,. \tag{B.8}$$

Appendix C

Acoustic treatment modeling

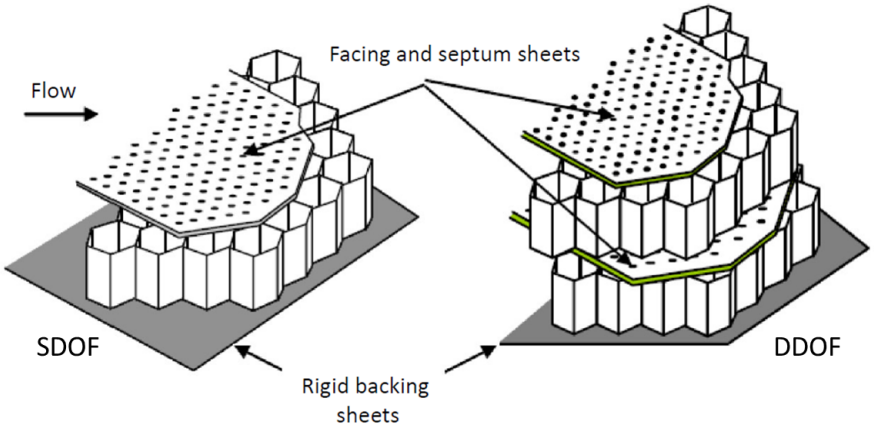

Figure C.1: Schemes of Single and Double liners

The noise produced by the turbofan is partially absorbed by acoustic treatments called liners. Giving the extreme environmental conditions (temperatures varying from $-50°$ C to $+120°$ C, and flow velocities reaching 240 m/s) inside the nacelle, these treatments are subjected to stringent requirements. From an aerodynamic point of view, the implementation of those technologies must not interfere with aerodynamic performance (in practice, recent studies quantify a 20% drag due to the implementation of liners). Moreover, acoustic liners must be of negligible mass, in a sector where every kilogram counts. Security conditions must obviously be respected as well as ruggedness and serviceability. The anti-ice system must be integrated into the nacelle, its implementation must not be complicated by the presence of the liner.
State-of-the-art liners mainly used for their respect of the above cited requirements are constituted of a resistive sheet attached to a honeycomb core, fixed on a rigid backing skin (figure C.1). This core assembly, called "Single Degree Of Freedom" (SDOF) can be superposed, creating MDOF systems. A "Double Degree Of Freedom" (DDOF) liner is constituted of two SDOF liners separated by an intermediate resistive sheet called septum, which confers a wider attenuation spectra.

The honeycomb core structure imposes locally-reacting behavior such as resonance effects, by guiding the incident wave and only allowing its transversal propagation. It acts as a quarter wave resonator, which induces a maximum attenuation of the wave at a given frequency, driven by its depth. Honeycomb core thus attenuates tonal noise, for example the one produced by the fan.
The resistive sheet is a porous sheet, which allows energy dissipation through porosities: vis-

cothermic dissipation by the holes, and calorific dissipation linked to swirl effects due to high SPL, thus is nonlinear. Energy dissipation due to the presence of resistive sheet is not frequency dependent and consequently, is used to attenuate broadband noise. The resistive sheet determines the attenuation level achieved by the liner where the honeycomb core drives the frequency band to be attenuated.

A closer view of the liner is presented in figure C.2. Geometric parameters (defined for perforated sheet) are depicted in order to introduce the different models used to represent the acoustic behavior of such liners.

C.1 Modeling of the liner

In this section, the impedance of each part of the SDOF liner (resistive sheet, honeycomb core, and rigid backing skin) is defined as a function of physical and acoustical parameters. Moreover, the calculation of the total impedance of the stacking is described.

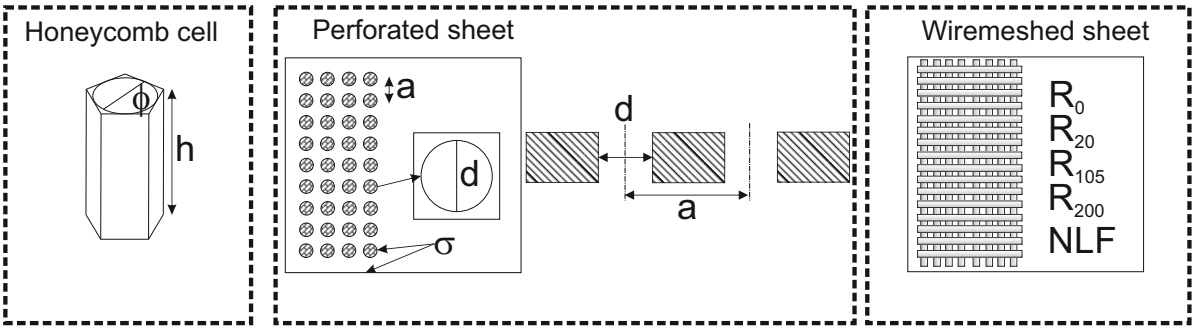

Figure C.2: Liner geometric and acoustic parameters: ϕ is the honeycomb cell diameter and h its depth; σ the percentage of open area (POA), which is the ratio between the surface of all perforations and the total surface of the sheet, d the perforation diameter, and t the resistive sheet thickness; R_0 is the wiremesh resistance at acoustic velocity $v = 0$, R_{20} at v =0.2 m/s, R_{105} at v =1.05 m/s, R_{200} at v =2.0 m/s, and $NLF = R_{200}/R_{20}$ its non-linearity factor.

Acoustic liners are characterized by their surface impedance also called local impedance. This impedance is a complex-valued function $(\mathbf{r}, \omega) \mapsto Z(\mathbf{r}, \omega)$, with $\mathbf{r} = (x, y, z)$. For ω fixed and for $\mathbf{r}$ belonging to the facing sheet, $Z(\mathbf{r}, \omega)$ is defined by,

$$Z(\mathbf{r}, \omega) = \frac{p(\mathbf{r}, \omega)}{\mathbf{v}_\Gamma(\mathbf{r}, \omega) \cdot \mathbf{n}(\mathbf{r})}, \tag{C.1}$$

in which $p(\mathbf{r}, \omega)$ is the acoustic pressure, and $\mathbf{v}_\Gamma(\mathbf{r}, \omega) \cdot \mathbf{n}(\mathbf{r})$ is the acoustic normal velocity.

C.1.1 Resistive sheet

As depicted in Fig. C.2, two kinds of resistive sheets can be used: a perforated resistive sheet or a wiremeshed resistive sheet. The models of these impedances are described hereinafter.

C.1.1.1 Perforated resistive sheet [18]

This subsection is issued from the reading of the Guess work [18] on perforated resistive sheet liners assembly, which is used in the computer code developed by Airbus.
The impedance $Z(\mathbf{r}, \omega)$ of the acoustic liner composed of an air cavity and of a perforated resistive sheet, as depicted in figure C.1, can be decomposed in three parts. A linear part,

Z_{linear}, describing the viscous and mass effects, a nonlinear part Z_{NL} describing the grazing flow effect and the high SPL effects, and a radiation part Z_{rad}. The modeling of the liner is a function of geometrical parameters, defined in figure C.2. It is assumed that these parameters (sheet thickness t, hole diameter d, and spacing between holes a) are small compared to the acoustic wavelength $\lambda = c/f = 2\pi c/\omega$. The skin thickness t and the Percentage of Open Area (POA), denoted by σ, are key parameters of the absorption achieved by such liner. The POA drives the resistance and participates, as well as the skin thickness and the hole diameter, in the mass reactance, denoted by, $\frac{\chi}{f}$.
Below, the spatial dependence in $\mathbf{r}$ of impedance Z is removed and only the dependence in frequency ω is kept.
The total impedance $Z(\omega)$ of such a liner is written as,

$$Z(\omega) = Z_{\text{linear}}(\omega) + Z_{\text{NL}}(\omega) + Z_{\text{rad}}(\omega). \tag{C.2}$$

Linear part Z_{linear}. The linear part $Z_{\text{linear}}(\omega)$ depends on ω and corresponds to the impedance of a short tube. Let ν be the kinetic viscosity of the fluid. The modeling of this impedance (see [18]) is a function of the value of the dimensionless parameter $\frac{d}{2}\sqrt{\frac{\omega}{\nu}}$ and of frequency ω that must belong to $[\omega_{\min}, \omega_{\max}]$ such that $4\pi d \leq \omega_{\min}$ and $\omega_{\max} \ll min\{\frac{2\pi c}{t}, \frac{2\pi c}{d}, \frac{2\pi c}{a}\}$. These equations are

$$\begin{cases} Z_{\text{linear}}(\omega) &= \dfrac{32\nu}{\sigma c d}\left(1+\dfrac{t}{d}\right) + j\dfrac{4\omega t}{3\sigma c} & \text{if} \quad \dfrac{d}{2}\sqrt{\dfrac{\omega}{\nu}} < 1, \\ Z_{\text{linear}}(\omega) &= \dfrac{\sqrt{8\nu\omega}}{\sigma c}\left(1+\dfrac{t}{d}\right) + j\left(\dfrac{\sqrt{8\nu\omega}}{\sigma c}\left(1+\dfrac{t}{d}\right) + \dfrac{\omega t}{\sigma c}\right) & \text{if} \quad \dfrac{d}{2}\sqrt{\dfrac{\omega}{\nu}} > 10. \end{cases} \tag{C.3}$$

In equation (C.3), the term $\left(1+\frac{t}{d}\right)$ is a corrected length (thickness) to account for viscous effects outside the entrance to the orifice (as explained in [18]).

Nonlinear part Z_{NL}. The nonlinear part Z_{NL} represents the effect of high-amplitude sound waves and steady airflow through the orifice (tangential to the plate) [18]. It mainly depends on the fluid velocity at the orifice denoted $v_{orif}(\omega) = v_{\text{surf}}^{\text{rms}}(\omega)/\sigma$, in which $v_{\text{surf}}^{\text{rms}}(\omega)$ is the root mean-square acoustic velocity at the surface of the material (taking into account all frequencies). This velocity at the orifice allows to chose between the two following equations, depending on the flow Mach number M,

$$\begin{cases} Z_{\text{NL}}(\omega) &= \dfrac{(1-\sigma^2)}{\sigma}\dfrac{|v_{orif}(\omega)|}{c} & \text{if} \quad v_{orif}(\omega) \geq 0.6M, \\ Z_{\text{NL}}(\omega) &= 0.3M\dfrac{(1-\sigma^2)}{\sigma} + \dfrac{(1-\sigma^2)}{1.2\sigma M}\left(\dfrac{|v_{orif}(\omega)|}{c}\right)^2 & \text{if} \quad v_{orif}(\omega) < 0.6M. \end{cases} \tag{C.4}$$

Radiation part Z_{rad}. The radiation part $Z_{\text{rad}}(\omega)$ represents the mass inertance effects outside the tubes, the interaction between adjacent holes and a combination of airflow and sound amplitude effects. It is given by the equation,

$$Z_{\text{rad}}(\omega) = \frac{\pi^2}{2\sigma}\left(\frac{d}{\lambda}\right)^2 + j\frac{\omega\delta}{\sigma c}, \tag{C.5}$$

in which δ is given by the equation ([18]),

$$\delta = \frac{8d}{3\pi}\frac{(1-0.7\sqrt{\sigma})}{(1+305M^3)}\frac{(1+5000M_{orif}^2)}{(1+10000M_{orif}^2)}, \tag{C.6}$$

with $M_{orif} = \dfrac{v_{orif}}{c}$. Parameter δ can be compared to the Rayleigh correction term at the end of a tube $\dfrac{8d}{3\pi}$. The term $(1-0.7\sqrt{\sigma})$ describes the interaction between adjacent holes of the perforated sheet. The factor $\left(\dfrac{1}{1+305M^3}\right)$ represents the effect of the mean flow on the liner, while the factor $\left(\dfrac{1+5000M_{orif}^2}{1+10000M_{orif}^2}\right)$ describes the effect of high-SPL.

Transfer matrix of the perforated sheet. Once the impedance $Z_{ps}(\omega)$ of such a perforated resistive sheet is obtained, its transfer matrix $[M_{ps}(\omega)]$ between the lower surface and the upper surface of the perforated resistive sheet, is such that,

$$\begin{bmatrix} p_2 \\ v_2 \end{bmatrix} = [M_{ps}(\omega)] \begin{bmatrix} p_1 \\ v_1 \end{bmatrix} \quad , \quad [M_{ps}(\omega)] = \begin{bmatrix} 1 & Z_{ps}(\omega) \\ 0 & 1 \end{bmatrix}, \tag{C.7}$$

with $Z_{ps}(\omega)$ the impedance of the resistive sheet.

C.1.1.2 Wiremeshed resistive sheet

We briefly summarize the wiremeshed resistive sheet model that is proposed in [46]. This type of resistive sheet, described in figure C.2, is represented by its resistance (real part of $Z(\omega)$) at different acoustic velocities, assuming that the resistance of the metallic mesh is a linear function of the acoustic velocity. The impedance of such a resistive sheet is given by,

$$Z_{wm}(\omega) = R_{wm}(\omega) + j\chi_{wm}(\omega). \tag{C.8}$$

To represent the impedance of such a restive sheet, empirical formulas are used, depending on the available parameters: $R_0, R_{20}, R_{105}, NLF$ (see caption of figure C.2). These parameters are function of the acoustic velocity $v = ||\mathbf{v}||$ and the porosity σ if the wiremesh is coupled to a perforated sheet. These formulas are not presented here. In the general case, only R_0 and NLF are used to characterized the impedance of linear resistive sheets. The resistance $R_{wm}(\omega)$, function of these two parameters is given by,

$$R_{wm}(\omega) = \frac{R_0}{\sigma} + \frac{R_0(NLF-1)}{(2-0.2NLF)\sigma^2}v_{ac}. \tag{C.9}$$

The reactance of a wiremesh χ_{wm} is given by,

$$\chi_{wm} = \left(\frac{\chi_{wm}}{f}\right) f, \tag{C.10}$$

with f the frequency, and $\dfrac{\chi_{wm}}{f}$ the mass reactance of the wiremeshed sheet.

Transfer matrix of the perforated sheet. Once the impedance $Z_{\mathrm{wm}}(\omega)$ of such a perforated resistive sheet is obtained, its transfer matrix $[M_{wm}(\omega)]$ between the lower surface and the upper surface of the wiremeshed resistive sheet, is such that,

$$\begin{bmatrix} p_2 \\ v_2 \end{bmatrix} = [M_{wm}(\omega)] \begin{bmatrix} p_1 \\ v_1 \end{bmatrix} \quad , \quad [M_{wm}] = \begin{bmatrix} 1 & Z_{\mathrm{wm}}(\omega) \\ 0 & 1 \end{bmatrix}, \tag{C.11}$$

with $Z_{wm}(\omega)$ the impedance of the wiremeshed resistive sheet.

C.1.2 Honeycomb core

A honeycomb cell cavity is modelled by a tube filled with air for which the transfer matrix between the lower surface and the upper surface of the honeycomb cell, $[M_{hc}(\omega)]$, is such that,

$$\begin{bmatrix} p_1 \\ v_1 \end{bmatrix} = [M_{hc}(\omega)] \begin{bmatrix} p_0 \\ v_0 \end{bmatrix} \quad , \quad [M_{hc}(\omega)] = \begin{bmatrix} \cos(kh) & j\sin(kh) \\ j\sin(kh) & \cos(kh) \end{bmatrix}, \tag{C.12}$$

from which the impedance of the cell cavity is written [43] as,

$$Z_{hc}(\omega) = \frac{-j}{\tan(kh)}\,, \tag{C.13}$$

with $k = \dfrac{\omega}{c}$ and h is the cell depth.

C.1.3 Rigid backing skin

The back end of the stacking is made of a rigid backing skin, which imposes the nullity of the acoustic velocity (rigid condition) following the transfer vector,

$$\begin{bmatrix} p_0 \\ v_0 \end{bmatrix} \quad , \quad v_0 = 0. \tag{C.14}$$

C.1.4 Assembly of a resistive sheet, a honeycomb core, and a backing skin

In the present work, SDOF liners are solely employed (assembly of a resistive sheet, a honeycomb core, and a backing skin). From Eq. (C.7) or Eq. (C.11), Eq. (C.12), and Eq. (C.14), it can be deduced that,

$$\begin{bmatrix} p_2 \\ v_2 \end{bmatrix} = [M_{rs}][M_{hc}] \begin{bmatrix} p_0 \\ v_0 \end{bmatrix} \quad , \quad v_0 = 0\,. \tag{C.15}$$

The impedance of the liner depends on the local Mach number that, consequently, depends on point $\mathbf{r}$.

C.1.5 General remarks

The liner parameters such as the POA, the geometry of the perforations, and their diameter d, have an influence on the flow through the boundary layer formed over the liner. As explained in Chapter 1, the boundary layer is not accounted for in the boundary condition related to the liner.

This influence of the liner on the flow is assumed to be small, which allows for not recomputing the CFD at each optimization step of the liner.

This approximation will be taken into account in the uncertainties model that is introduced in Chapter 2.

Appendix D

Algorithms

In this appendix, we present the different algorithms used in the present work:

1. ACTRAN/TM half 3D deterministic run with model reduction methods
2. ACTRAN/TM half 3D deterministic run with model reduction methods and modified modal content
3. ACTRAN/TM half 3D stochastic run
4. ACTRAN/TM half 3D stochastic run with modified stochastic modal content
5. Inverse identifications

   Mean modal content

   Aeroacoustic and liner uncertainty levels using experiments

   Modal content uncertainty levels using experiments
6. Robust optimization in presence of the previously identified uncertainty levels

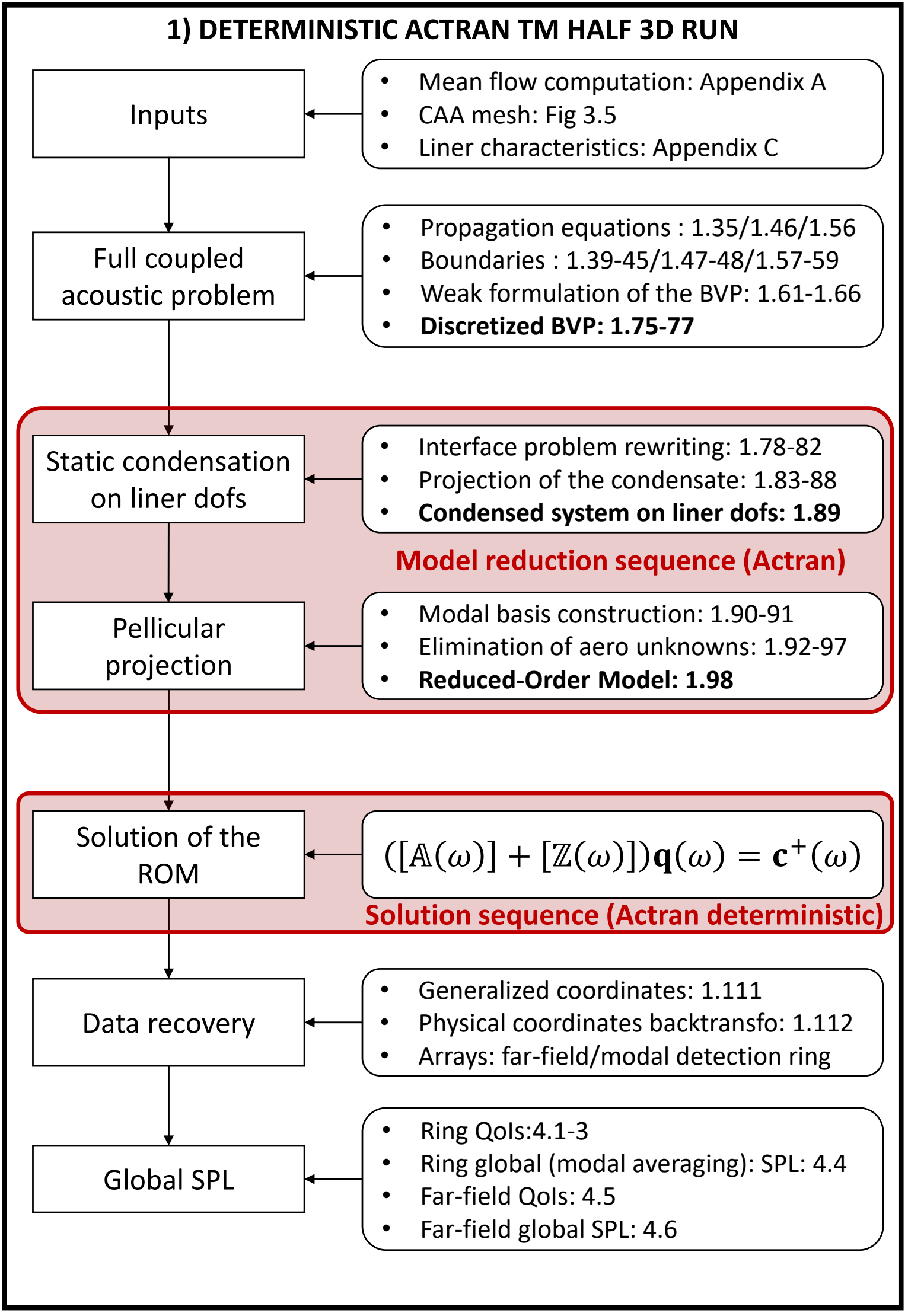
1) DETERMINISTIC ACTRAN TM HALF 3D RUN
Inputs
Mean flow computation: Appendix A
CAA mesh: Fig 3.5
Liner characteristics: Appendix C
Full coupled acoustic problem
Propagation equations : 1.35/1.46/1.56
Boundaries : 1.39-45/1.47-48/1.57-59
Weak formulation of the BVP: 1.61-1.66
Discretized BVP: 1.75-77
Static condensation on liner dofs
Interface problem rewriting: 1.78-82
Projection of the condensate: 1.83-88
Condensed system on liner dofs: 1.89
Model reduction sequence (Actran)
Pellicular projection
Modal basis construction: 1.90-91
Elimination of aero unknowns: 1.92-97
Reduced-Order Model: 1.98
Solution of the ROM
$([\mathbb{A}(\omega)] + [\mathbb{Z}(\omega)])\mathbf{q}(\omega) = \mathbf{c}^{+}(\omega)$
Solution sequence (Actran deterministic)
Data recovery
Generalized coordinates: 1.111
Physical coordinates backtransfo: 1.112
Arrays: far-field/modal detection ring
Global SPL
Ring QoIs:4.1-3
Ring global (modal averaging): SPL: 4.4
Far-field QoIs: 4.5
Far-field global SPL: 4.6

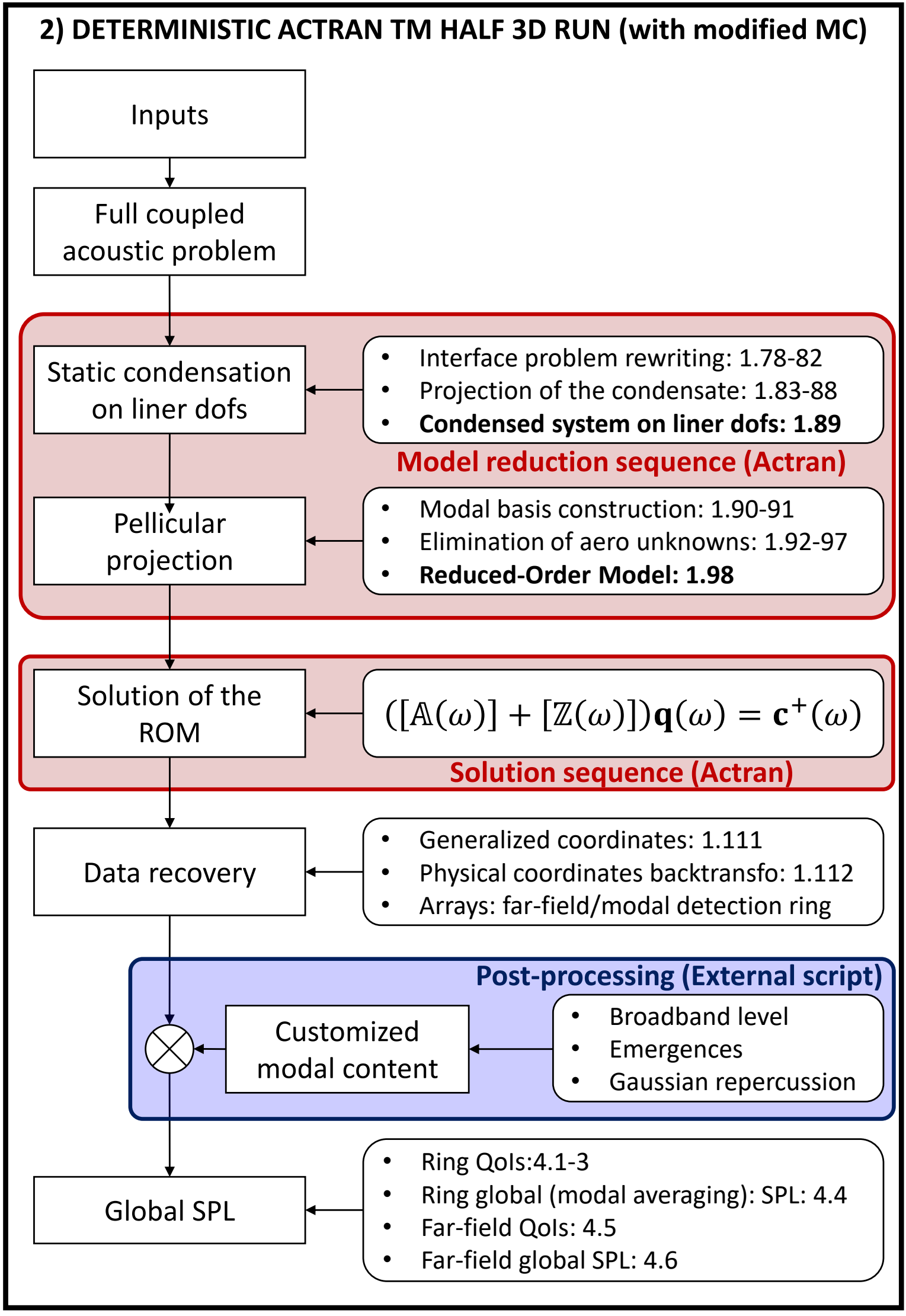
2) DETERMINISTIC ACTRAN TM HALF 3D RUN (with modified MC)
Inputs
Full coupled acoustic problem
Static condensation on liner dofs
Interface problem rewriting: 1.78-82
Projection of the condensate: 1.83-88
Condensed system on liner dofs: 1.89
Model reduction sequence (Actran)
Pellicular projection
Modal basis construction: 1.90-91
Elimination of aero unknowns: 1.92-97
Reduced-Order Model: 1.98
Solution of the ROM
$([\mathbb{A}(\omega)] + [\mathbb{Z}(\omega)])\mathbf{q}(\omega) = \mathbf{c}^{+}(\omega)$
Solution sequence (Actran)
Data recovery
Generalized coordinates: 1.111
Physical coordinates backtransfo: 1.112
Arrays: far-field/modal detection ring
Post-processing (External script)
Customized modal content
Broadband level
Emergences
Gaussian repercussion
Global SPL
Ring QoIs:4.1-3
Ring global (modal averaging): SPL: 4.4
Far-field QoIs: 4.5
Far-field global SPL: 4.6

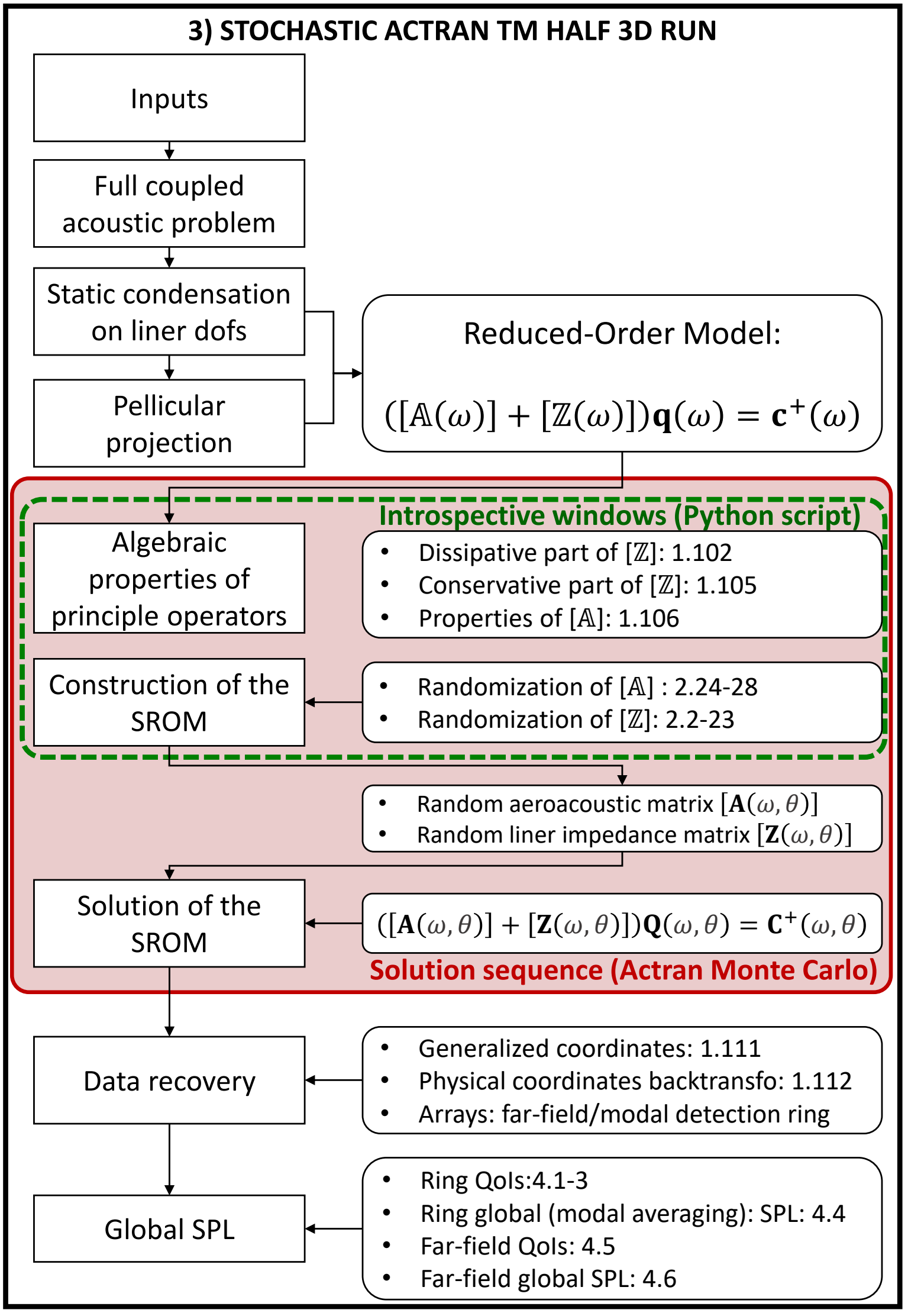
3) STOCHASTIC ACTRAN TM HALF 3D RUN
Inputs
Full coupled acoustic problem
Static condensation on liner dofs
Pellicular projection
Reduced-Order Model:
$([\mathbb{A}(\omega)] + [\mathbb{Z}(\omega)])\mathbf{q}(\omega) = \mathbf{c}^{+}(\omega)$
Introspective windows (Python script)
Algebraic properties of principle operators
Dissipative part of [ℤ]: 1.102
Conservative part of [ℤ]: 1.105
Properties of [𝔸]: 1.106
Construction of the SROM
Randomization of [𝔸] : 2.24-28
Randomization of [ℤ]: 2.2-23
Random aeroacoustic matrix $[\mathbf{A}(\omega,\theta)]$
Random liner impedance matrix $[\mathbf{Z}(\omega,\theta)]$
Solution of the SROM
$([\mathbf{A}(\omega,\theta)] + [\mathbf{Z}(\omega,\theta)])\mathbf{Q}(\omega,\theta) = \mathbf{C}^{+}(\omega,\theta)$
Solution sequence (Actran Monte Carlo)
Data recovery
Generalized coordinates: 1.111
Physical coordinates backtransfo: 1.112
Arrays: far-field/modal detection ring
Global SPL
Ring QoIs:4.1-3
Ring global (modal averaging): SPL: 4.4
Far-field QoIs: 4.5
Far-field global SPL: 4.6

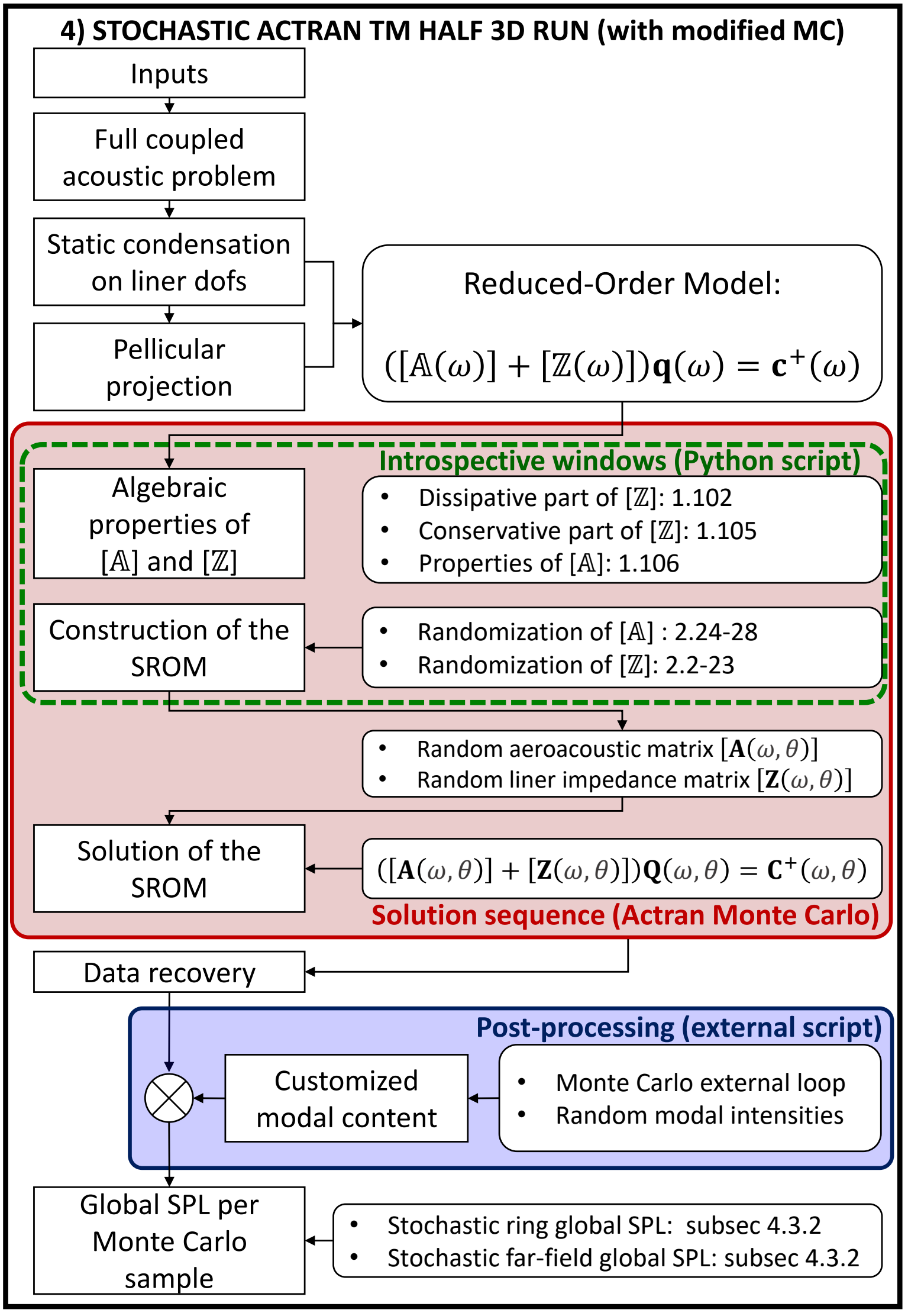
4) STOCHASTIC ACTRAN TM HALF 3D RUN (with modified MC)
Inputs
Full coupled acoustic problem
Static condensation on liner dofs
Pellicular projection
Reduced-Order Model:
$([\mathbb{A}(\omega)] + [\mathbb{Z}(\omega)])\mathbf{q}(\omega) = \mathbf{c}^{+}(\omega)$
Introspective windows (Python script)
Algebraic properties of [𝔸] and [ℤ]
• Dissipative part of [ℤ]: 1.102
• Conservative part of [ℤ]: 1.105
• Properties of [𝔸]: 1.106
Construction of the SROM
• Randomization of [𝔸] : 2.24-28
• Randomization of [ℤ]: 2.2-23
• Random aeroacoustic matrix $[\mathbf{A}(\omega,\theta)]$
• Random liner impedance matrix $[\mathbf{Z}(\omega,\theta)]$
Solution of the SROM
$([\mathbf{A}(\omega,\theta)] + [\mathbf{Z}(\omega,\theta)])\mathbf{Q}(\omega,\theta) = \mathbf{C}^{+}(\omega,\theta)$
Solution sequence (Actran Monte Carlo)
Data recovery
Post-processing (external script)
Customized modal content
• Monte Carlo external loop
• Random modal intensities
Global SPL per Monte Carlo sample
• Stochastic ring global SPL: subsec 4.3.2
• Stochastic far-field global SPL: subsec 4.3.2

5) INVERSE IDENTIFICATION OF THE MODAL CONTENT

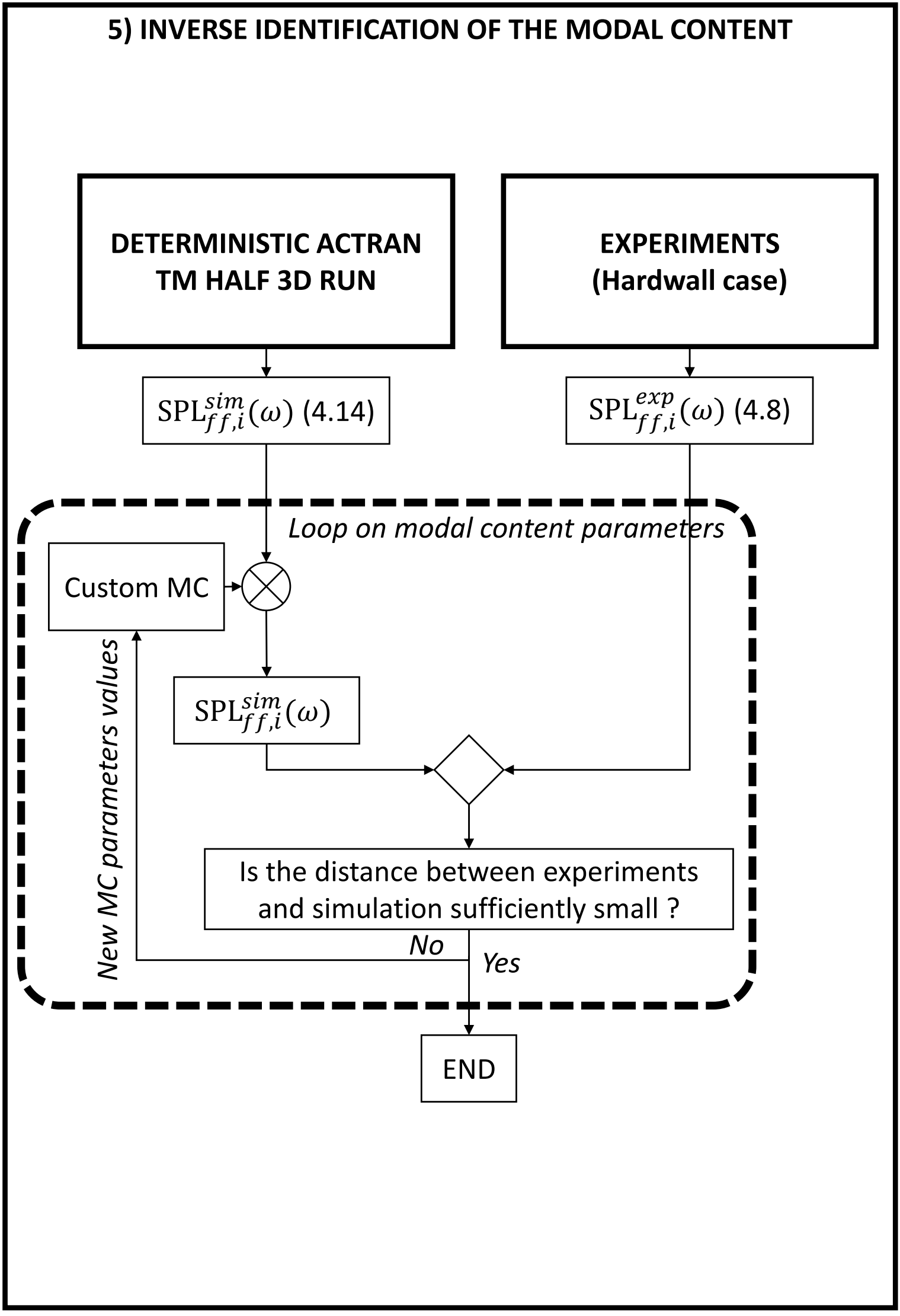

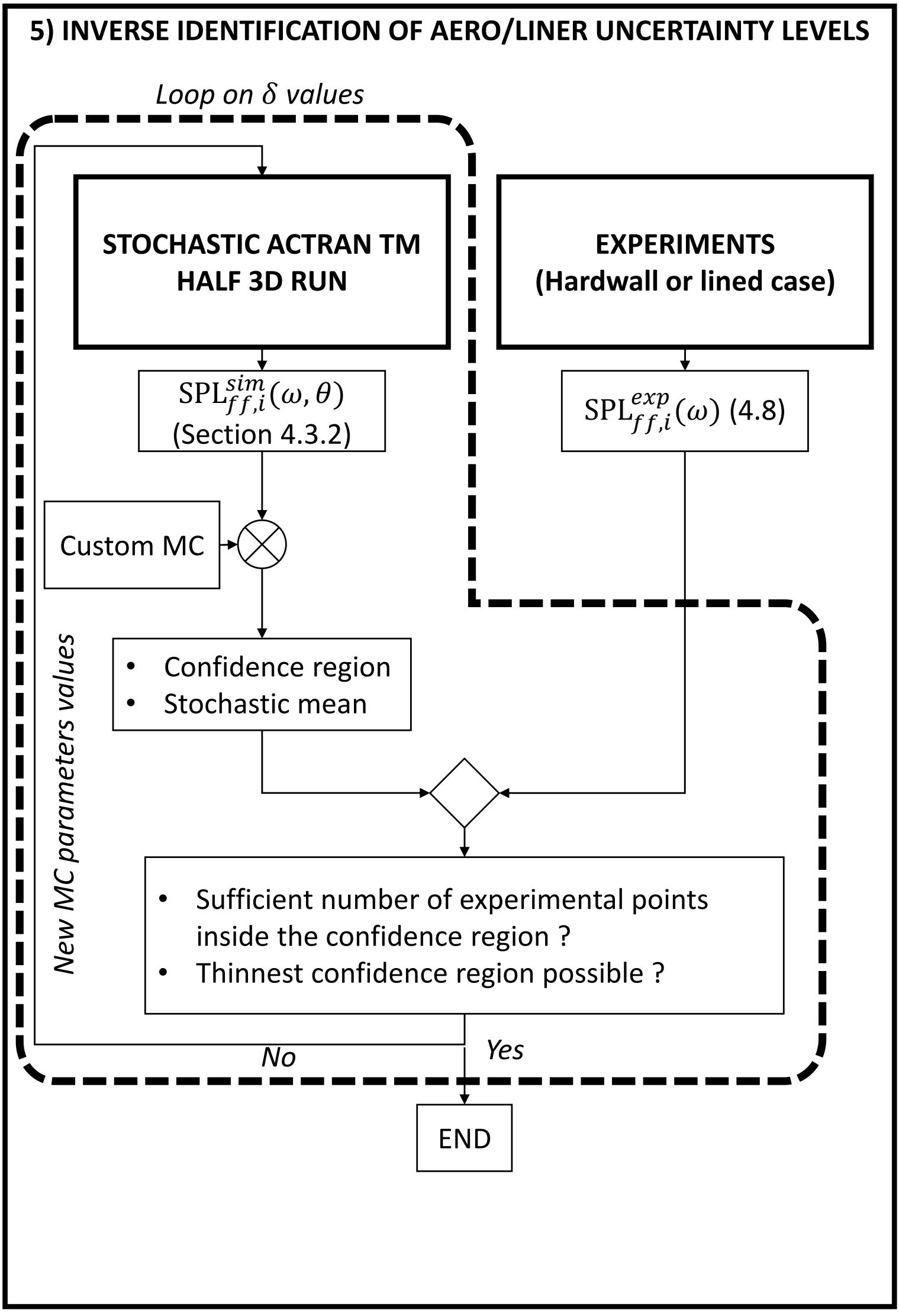
5) INVERSE IDENTIFICATION OF AERO/LINER UNCERTAINTY LEVELS
Loop on δ values
STOCHASTIC ACTRAN TM HALF 3D RUN
EXPERIMENTS (Hardwall or lined case)
$\mathrm{SPL}_{ff,i}^{sim}(\omega,\theta)$ (Section 4.3.2)
$\mathrm{SPL}_{ff,i}^{exp}(\omega)$ (4.8)
Custom MC
• Confidence region
• Stochastic mean
New MC parameters values
• Sufficient number of experimental points inside the confidence region ?
• Thinnest confidence region possible ?
No
Yes
END

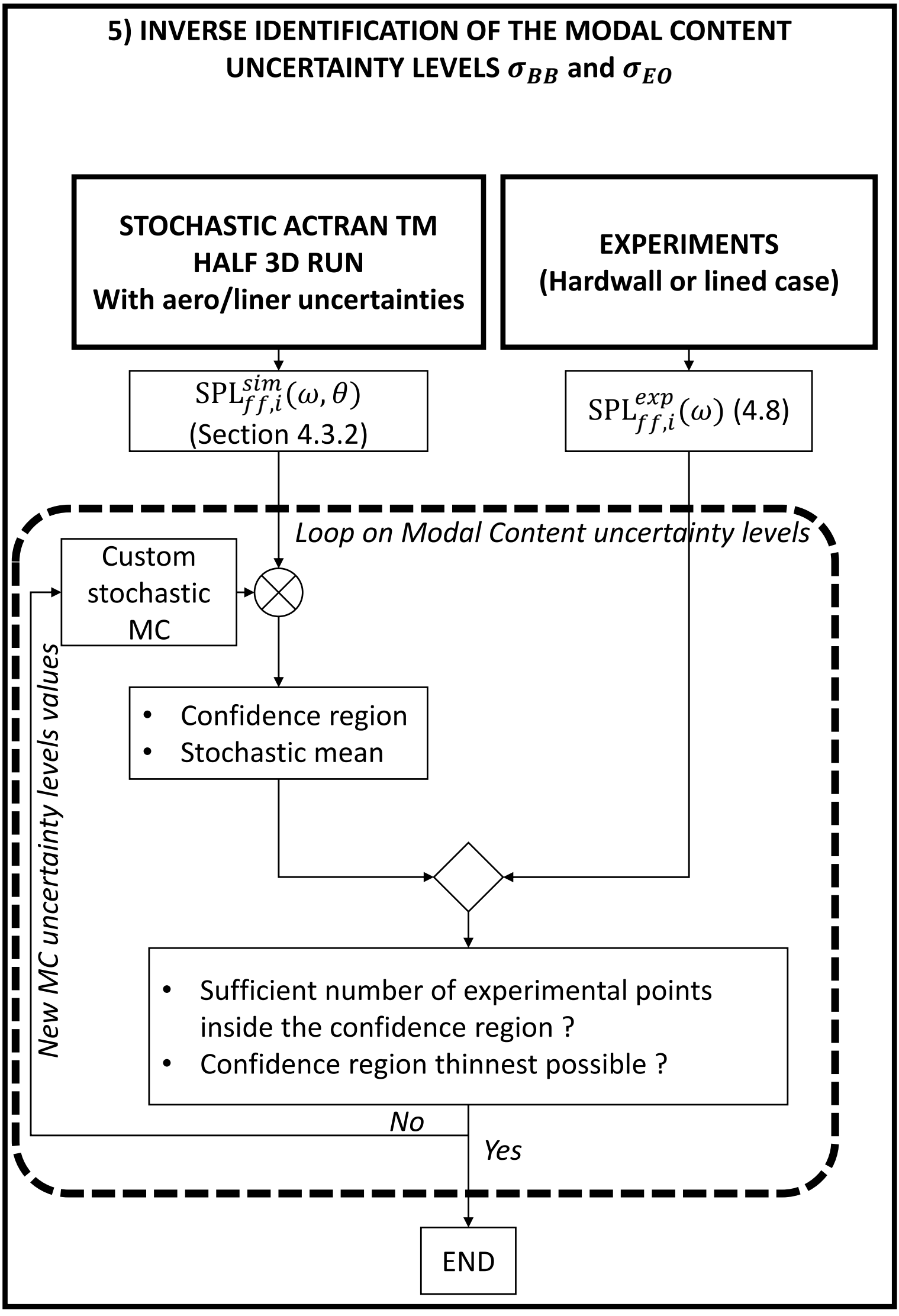
5) INVERSE IDENTIFICATION OF THE MODAL CONTENT UNCERTAINTY LEVELS σ_{BB} and σ_{EO}
STOCHASTIC ACTRAN TM HALF 3D RUN With aero/liner uncertainties
EXPERIMENTS (Hardwall or lined case)
$\mathrm{SPL}_{ff,i}^{sim}(\omega,\theta)$ (Section 4.3.2)
$\mathrm{SPL}_{ff,i}^{exp}(\omega)$ (4.8)
Loop on Modal Content uncertainty levels
Custom stochastic MC
Confidence region
Stochastic mean
Sufficient number of experimental points inside the confidence region ?
Confidence region thinnest possible ?
New MC uncertainty levels values
No
Yes
END

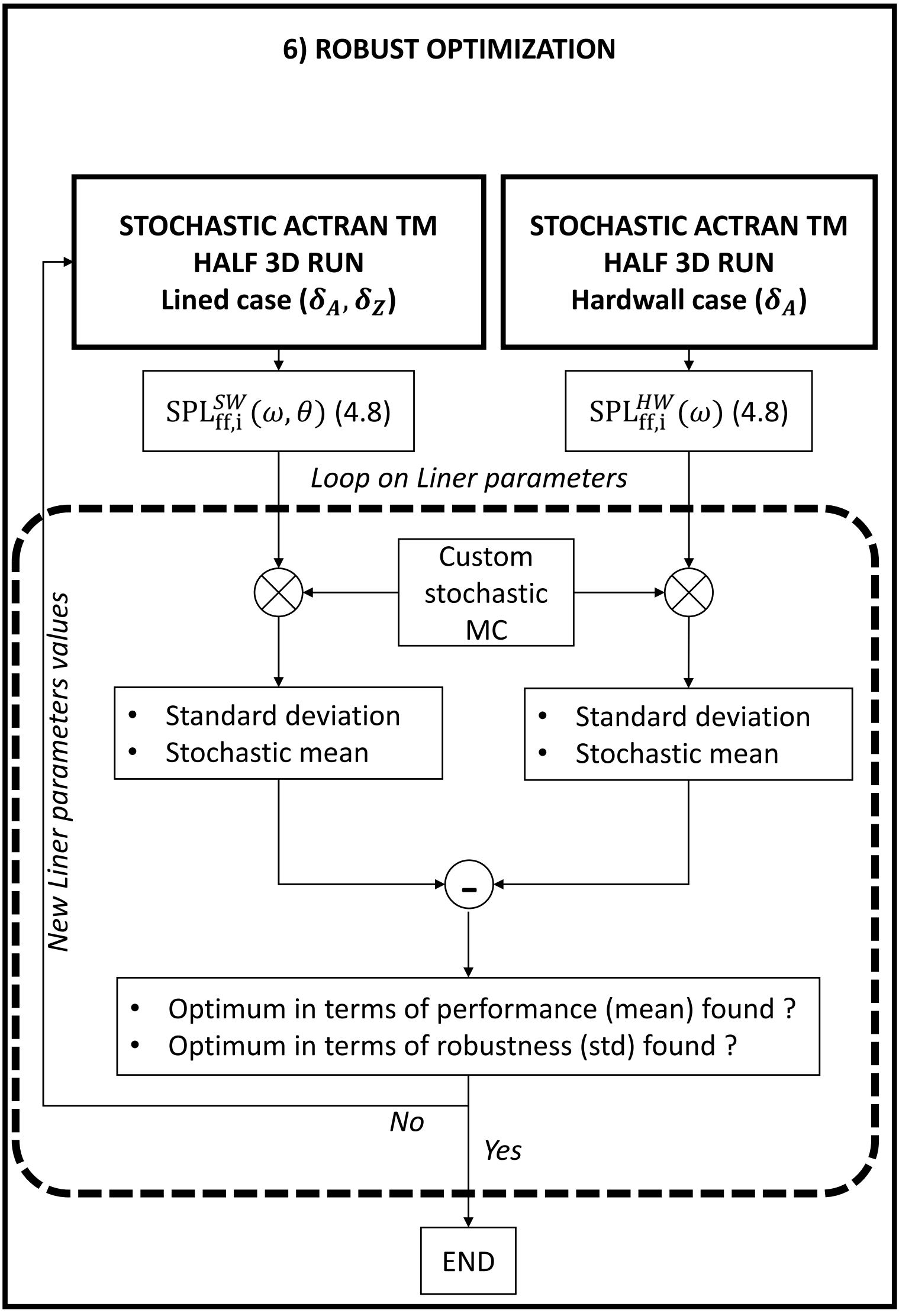
6) ROBUST OPTIMIZATION
STOCHASTIC ACTRAN TM
HALF 3D RUN
Lined case (δ_A, δ_Z)
STOCHASTIC ACTRAN TM
HALF 3D RUN
Hardwall case (δ_A)
$\mathrm{SPL}_{\mathrm{ff,i}}^{SW}(\omega,\theta)$ (4.8)
$\mathrm{SPL}_{\mathrm{ff,i}}^{HW}(\omega)$ (4.8)
Loop on Liner parameters
Custom
stochastic
MC
New Liner parameters values
• Standard deviation
• Stochastic mean
• Standard deviation
• Stochastic mean
−
• Optimum in terms of performance (mean) found ?
• Optimum in terms of robustness (std) found ?
No
Yes
END

Bibliography

[1] Akkaoui, Q., Capiez-Lernout, E., Soize, C., and Ohayon, R. Uncertainty quantification for dynamics of geometrically nonlinear structures coupled with internal acoustic fluids in presence of sloshing and capillarity. *Journal of Fluids and Structures 94* (2020), 102966.

[2] Arnst, M., and Soize, C. Identification and sampling of bayesian posteriors of high-dimensional symmetric positive-definite matrices for data-driven updating of computational models. *Computer Methods in Applied Mechanics and Engineering 352* (2019), 300–323.

[3] Astley, R., Sugimoto, R., and Mustafi, P. Computational aero-acoustics for fan duct propagation and radiation. current status and application to turbofan liner optimisation. *Journal of Sound and Vibration 330*, 16 (2011), 3832–3845.

[4] Aurégan, Y., Maurel, A., Pagneux, V., and Pinton, J.-F. *Sound-flow interactions*, vol. 586. Springer, 2008.

[5] Bailly, C., and Juvé, D. Aeroacoustic simulations and stochastic approach using linearized euler's equations. *The Journal of the Acoustical Society of America 105*, 2 (1999), 1066–1066.

[6] Bailly, C., and Juve, D. Numerical solution of acoustic propagation problems using linearized euler equations. *AIAA journal 38*, 1 (2000), 22–29.

[7] Brambley, E. J. Well-posed boundary condition for acoustic liners in straight ducts with flow. *AIAA journal 49*, 6 (2011), 1272–1282.

[8] Brown, M., Jones, M., and Watson, W. Uncertainty analysis of the grazing flow impedance tube. In *18th AIAA/CEAS Aeroacoustics Conference (33rd AIAA Aeroacoustics Conference)* (2012), p. 2296.

[9] Bruneau, M., and Scelo, T. *Fundamentals of Acoustics*. ISTE. Wiley, 2010.

[10] Cover, T. M., and Thomas, J. A. *Elements of information theory 2nd edition (wiley series in telecommunications and signal processing)*. Wiley-Interscience, 2006.

[11] Di Francescantonio, P., Casalino, D., and De Mercato, L. Aeroacoustic design of aero-engine intake liners. In *11th AIAA/CEAS Aeroacoustics Conference* (2005), p. 2942.

[12] Duchaine, F. Sensitivity analysis of heat transfer in a honeycomb acoustic liner to inlet conditions with large eddy simulation. In *ASME Turbo Expo 2017: Turbomachinery Technical Conference and Exposition* (2017), American Society of Mechanical Engineers, pp. V05BT22A002–V05BT22A002.

[13] Eldredge, J., Bodony, D., and Shoeybi, M. Numerical investigation of the acoustic behavior of a multi-perforated liner. In *13th AIAA/CEAS Aeroacoustics Conference (28th AIAA Aeroacoustics Conference)* (2007), p. 3683.

[14] Fahy, F. J., and Gardonio, P. *Sound and structural vibration: radiation, transmission and response*. Academic press, 2007.

[15] Free Field Technologies. Actran 12 user's guide, 2011.

[16] Freund, J. B. Proposed inflow/outflow boundary condition for direct computation of aerodynamic sound. *AIAA journal 35*, 4 (1997), 740–742.

[17] Ghanem, R., Higdon, D., and Owhadi, H. *Handbook of Uncertainty Quantification*, vol. 1 to 3. Springer, Cham, Switzerland, 2017.

[18] Guess, A. Calculation of perforated plate liner parameters from specified acoustic resistance and reactance. *Journal of Sound and Vibration 40*, 1 (1975), 119–137.

[19] Hirsch, C. *Numerical Computation of Internal and External Flows, Fundamentals of Numerical Discretization*. Numerical Computation of Internal and External Flows. Wiley, 1991.

[20] Hirschberg, A., and Rienstra, S. W. An introduction to aeroacoustics. *Eindhoven university of technology* (2004).

[21] Howe, M. S. *Theory of vortex sound*, vol. 33. Cambridge university press, 2003.

[22] Jaynes, E. T. Information theory and statistical mechanics. *Physical review 106*, 4 (1957), 620.

[23] Jones, M., Parrott, T., and Watson, W. Uncertainty and sensitivity analyses of a two-parameter impedance prediction model. In *14th AIAA/CEAS Aeroacoustics Conference (29th AIAA Aeroacoustics Conference)* (2008), p. 2928.

[24] Jones, M., Tracy, M., Watson, W., and Parrott, T. Effects of liner geometry on acoustic impedance. In *8th AIAA/CEAS Aeroacoustics Conference & Exhibit* (2002), p. 2446.

[25] Jones, M., Watson, W., and Parrott, T. Benchmark data for evaluation of aeroacoustic propagation codes with grazing flow. In *11th AIAA/CEAS Aeroacoustics Conference* (2005), p. 2853.

[26] Lafronza, L., McAlpine, A., Keane, A., and Astley, J. Response surface method optimization of uniform and axially segmented duct acoustics liners. *Journal of Aircraft 43*, 4 (2006), 1089–1102.

[27] Landau, L. D., and Lifshitz, E. *Fluid Mechanics: Vol 6*. Elsevier, 2013.

[28] Legendre, C. *On the interactions of sound waves and vortices*. Lulu. com, 2015.

[29] Lidoine, S. *Approches théoriques du problème du rayonnement acoustique par une entrée d'air de turboréacteur: Comparaisons entre différentes méthodes analytiques et numériques*. PhD thesis, Ecully, Ecole centrale de Lyon, 2002.

[30] Lighthill, M. J. On sound generated aerodynamically. i. general theory. In *Proceedings of the Royal Society of London A: Mathematical, Physical and Engineering Sciences* (1952), vol. 211, The Royal Society, pp. 564–587.

[31] Lighthill, M. J. *Waves in fluids*. Cambridge university press, 2001.

[32] Ma, Z., and Zhang, X. Numerical investigation of broadband slat noise attenuation with acoustic liner treatment. *AIAA journal 47*, 12 (2009), 2812–2820.

[33] Manoha, E., Troff, B., and Sagaut, P. Trailing-edge noise prediction using large-eddy simulation and acoustic analogy. *AIAA journal 38*, 4 (2000), 575–583.

[34] Marx, D., and Aurégan, Y. Effect of turbulent eddy viscosity on the unstable surface mode above an acoustic liner. *Journal of Sound and Vibration 332*, 15 (2013), 3803–3820.

[35] Mbaye, M., Soize, C., Ousty, J.-P., and Capiez-Lernout, E. Robust analysis of design in vibration of turbomachines. *Journal of Turbomachinery 135*, 2 (2013), 021008.

[36] Mendez, S., and Eldredge, J. D. Acoustic modeling of perforated plates with bias flow for large-eddy simulations. *Journal of Computational Physics 228*, 13 (2009), 4757–4772.

[37] Mohring, W. A well posed acoustic analogy based on a moving acoustic medium. *arXiv preprint arXiv:1009.3766* (2010).

[38] Myers, M. On the acoustic boundary condition in the presence of flow. *Journal of Sound and Vibration 71*, 3 (1980), 429–434.

[39] Nark, D. M., Jones, M. G., and Piot, E. Assessment of axial wave number and mean flow uncertainty on acoustic liner impedance eduction. In *2018 AIAA/CEAS Aeroacoustics Conference* (2018), p. 3444.

[40] Ohayon, R., and Soize, C. *Structural Acoustics and Vibration.* Academic Press, 1998.

[41] Ohayon, R., and Soize, C. *Advanced computational vibroacoustics: reduced-order models and uncertainty quantification.* Cambridge University Press, 2014.

[42] Ohayon, R., and Soize, C. Computational vibroacoustics in low-and medium-frequency bands: damping, rom, and uq modeling. *Applied Sciences 7*, 6 (2017), 586.

[43] Parrott, T. L., and Jones, M. G. Parallel-element liner impedances for improved absorption of broadband sound in ducts. *Noise Control Engineering Journal 43*, 6 (1995), 183–195.

[44] Pascal, L., Piot, E., and Casalis, G. A new implementation of the extended helmholtz resonator acoustic liner impedance model in time domain caa. *Journal of Computational Acoustics 24*, 01 (2016), 1550015.

[45] Pierce, A. D., and Beyer, R. T. Acoustics: An introduction to its physical principles and applications. 1989 edition, 1990.

[46] Primus, J. Manuel d'impédance acoustique multicouche - user's manual, 2017.

[47] Primus, J., Piot, E., and Simon, F. An adjoint-based method for liner impedance eduction: Validation and numerical investigation. *Journal of Sound and Vibration 332*, 1 (2013), 58–75.

[48] Ramdani, S., Yamasaki, N., Inokuchi, Y., and Ishii, T. Large eddy simulation of conventional and bias flow acoustic liners. In *ASME Turbo Expo 2017: Turbomachinery Technical Conference and Exposition* (2017), American Society of Mechanical Engineers, pp. V02CT43A007–V02CT43A007.

[49] Rienstra, S. W. Fundamentals of duct acoustics. *Von Karman Institute Lecture Notes* (2015).

[50] Robinson, J., and Watson, W. Performance of a checkerboard liner with uncertain impedances. In *11th AIAA/CEAS Aeroacoustics Conference* (2005), p. 2850.

[51] Roche, J.-M., Leylekian, L., Delattre, G., and Vuillot, F. Aircraft fan noise absorption: Dns of the acoustic dissipation of resonant liners. In *15th AIAA/CEAS Aeroacoustics Conference (30th AIAA Aeroacoustics Conference)* (2009), p. 3146.

[52] Rubinstein, R. Y., and Kroese, D. P. *Simulation and the Monte Carlo method*, vol. 10. John Wiley & Sons, 2016.

[53] Shannon, C. E. A mathematical theory of communication. *Bell system technical journal 27*, 3 (1948), 379–423.

[54] Soize, C. A nonparametric model of random uncertainties for reduced matrix models in structural dynamics. *Probabilistic engineering mechanics 15*, 3 (2000), 277–294.

[55] Soize, C. Random matrix theory and non-parametric model of random uncertainties in vibration analysis. *Journal of sound and vibration 263*, 4 (2003), 893–916.

[56] Soize, C. A comprehensive overview of a non-parametric probabilistic approach of model uncertainties for predictive models in structural dynamics. *Journal of sound and vibration 288*, 3 (2005), 623–652.

[57] Soize, C. Random matrix theory for modeling uncertainties in computational mechanics. *Computer methods in applied mechanics and engineering 194*, 12-16 (2005), 1333–1366.

[58] Soize, C. Random matrices in structural acoustics. *New Directions in Linear Acoustics and Vibration: Quantum Chaos, Random Matrix Theory and Complexity* (2010), 206.

[59] Soize, C. Random matrix models and nonparametric method for uncertainty quantification, 2017.

[60] Soize, C. *Uncertainty Quantification. An Accelerated Course with Advanced Applications in Computational Engineering*, vol. Interdisciplinary Applied Mathematics. Springer, 2017.

[61] Tam, C. K. Computational aeroacoustics-issues and methods. *AIAA journal 33*, 10 (1995), 1788–1796.

[62] Tam, C. K. Advances in numerical boundary conditions for computational aeroacoustics. *Journal of Computational Acoustics 6*, 04 (1998), 377–402.

[63] Tam, C. K. Computational aeroacoustics: an overview of computational challenges and applications. *International Journal of Computational Fluid Dynamics 18*, 6 (2004), 547–567.

[64] Tam, C. K., and Dong, Z. Radiation and outflow boundary conditions for direct computation of acoustic and flow disturbances in a nonuniform mean flow. *Journal of computational acoustics 4*, 02 (1996), 175–201.

[65] Tam, C. K., Pastouchenko, N., Jones, M. G., and Watson, W. R. Experimental validation of numerical simulation for an acoustic liner in grazing flow. In *19th AIAA/CEAS Aeroacoustics Conference* (2013), p. 2222.

[66] Tyler, J. M., and Sofrin, T. G. Axial flow compressor noise studies. Tech. rep., SAE Technical Paper, 1962.

[67] USAF. Standard atmosphere, 1976, 1976.

[68] Van Den Nieuwenhof, B., Detandt, Y., Lielens, G., Rosseel, E., Soize, C., Dangla, V., Kassem, M., and Mosson, A. Optimal design of the acoustic treatments damping the noise radiated by a turbo-fan engine. In *23rd AIAA/CEAS Aeroacoustics Conference* (2017), p. 4035.

[69] W. Tam, C. K., and Kurbatskii, K. A. Microfluid dynamics and acoustics of resonant liners. *AIAA journal 38*, 8 (2000), 1331–1339.

[70] Wagner, C., Hüttl, T., and Sagaut, P. *Large-eddy simulation for acoustics*, vol. 20. Cambridge University Press, 2007.

[71] Zhang, Q., and Bodony, D. J. Numerical simulation of two-dimensional acoustic liners with high-speed grazing flow. *AIAA journal 49*, 2 (2011), 365–382.

[72] Zhang, Q., and Bodony, D. J. Numerical investigation of a honeycomb liner grazed by laminar and turbulent boundary layers. *Journal of Fluid Mechanics 792* (2016), 936–980.

[73] Zhang, Y., Chen, H., Wang, K., and Wang, M. Aeroacoustic prediction of a multi-element airfoil using wall-modeled large-eddy simulation. *AIAA Journal* (2017), 4219–4233.

[74] Zhao, D., Ang, L., and Ji, C. Numerical and experimental investigation of the acoustic damping effect of single-layer perforated liners with joint bias-grazing flow. *Journal of Sound and Vibration 342* (2015), 152–167.

[75] Zhao, D., Ji, C., Li, J., and Ang, L. Experimental comparison of noise dissipation effects of single-and double-layer acoustic liners. *Applied Acoustics 141* (2018), 281–292.

[76] Zhao, D., Sun, Y., Ni, S., Ji, C., and Sun, D. Experimental and theoretical studies of aeroacoustics damping performance of a bias-flow perforated orifice. *Applied Acoustics 145* (2019), 328–338.

[77] Zhou, L., and Bodén, H. A systematic uncertainty analysis for liner impedance eduction technology. *Journal of sound and vibration 356* (2015), 86–99.

ABSTRACT : In modern turbofan engines, fan noise is one of the main noise sources due to the constant increasing of engines bypass ratio for fuel burn reduction purposes. As fan noise is characterized by broadband and tonal components, acoustic liners are introduced for their effectiveness in mitigating both components through dissipation effects that are tunable by modifying the liner geometry. Simulations issued from prediction numerical tools are thus extensively used for their tuning, since experiments cannot be considered for obvious costs reasons. As the design of liner systems is frozen in early stages of an aircraft development, it exists a non-negligible variability on its operating environment. This variability directly impacts the design of liners by inducing large discrepencies on the quantities used for its numerical design. Moreover, each time these quantities are updated due to the increased maturity of the aircraft program, lined surfaces are to be reoptimized. The updating phase thus represents important costs in terms of computational time, which could be avoided by accounting for such a variability in preliminary phases of the liner design. This is the main problematic of the present work. As this external variability directly impacts the liner environment, the computational modeling of the liner acoustic performance is uncertain. In order to quantify and account for such an uncertain nature, a robust design of the liner is carried out, by quantifying the overall uncertainty that lies within the liner design computational process. The state-of-the-art computational aeroacoustic model of nacelle liners performance is an industrial numerical code, Actran/TM, which therefore has to be extensively studied so as to exhibit the principle components that are subject to the overall uncertainty. A stochastic modeling of uncertainties is then introduced and grafted on the computational model. It allows for simulating the previously mentioned external variability, by accounting for the uncertainty that lies within the model (modeling errors and model parameters errors), through parametric and nonparametric probabilistic approaches of uncertainties. Then, the propagation of uncertainties in the system is analyzed using the computational model and the Monte Carlo stochastic solver. The acoustic response is then random and the quantification of uncertainties consists in estimating statistics, such as confidence regions associated with a certain confidence level of quantities of interest. From these statistical information, the robustness of a given liner design towards a simulated variability on its performance model can be defined, in addition to the state-of-the-art liner acoustic performance. This information then allows for knowing the propensity of a given liner design to maintain its nominal performance when its environment is changing in a predefined range of variation accounted for by the level of uncertainty imposed on the stochastic model. Then, making a compromise between performance and robustness, the best liner design can be chosen.

Keywords : *Robust design; Computational Aeroacoustics; ACTRAN/TM; Nonparametric probabilistic model; Uncertainty quantification; Monte Carlo method*;

RÉSUMÉ : Dans les moteurs d'avions modernes, le bruit de fan est une des principales sources de bruit du fait d'une augmentation constante du taux de dilution des moteurs visant à réduire leur consommation. Le bruit de fan étant caractérisé par des composantes tonale et multi-modale, des traitements acoustiques appelés liners sont utilisés pour leur efficatié à réduire des composantes de bruit, par des effets de dissipation acoustique réglables en modifiant la géométrie du liner. Des modèles de prédictions numériques sont alors utilisés pour leur réglage. Le design du liner étant gelé dans des phases préliminaires du développement d'un avion, il existe une variabilité non négligeable sur son environnement de fonctionnement. Cette variabilité impacte directement le design du liner en induisant une large disparité des données utilisées pour son design. De plus, à mesure que la maturité de l'avion augmente, chaque mise-à-jour de ces données impose une réoptimisation du liner. Cette étape de réoptimisation induit alors d'importants coûts de calcul qui pourraient être évités en prenant en compte cette variabilité durant les phases préliminaires de design. Il s'agit de la principale problématique de ce travail. À mesure que cette variabilité externe impacte l'environnement d'opérabilité du liner, le modèle numérique de performance du liner devient alors incertain. Afin de quantifier et prendre en compte cette nature incertaine, une conception robuste du liner est alors entreprise, par quantifiant l'incertitude globale qui réside dans le modèle numérique de performance acoustique du liner. Le modèle aéroacoustique numérique utilisé est un code industriel, ACTRAN/TM, et nécessite d'être intensivement étudié afin d'en déduire les principaux composants les plus sensibles vis-à-vis de l'incertitude globale. Un modèle stochastique des incertitudes est alors introduit et greffé sur le modèle aéroacoustique. Il permet de simuler l'incertitude globale mentionnée précédemment, en prenant en compte l'incertitude qui réside dans le modèle numérique (erreurs de modèles et erreurs des paramètres du modèle), en utilisant les approches probabilistes paramétriques et non-paramétriques. Ensuite, la propagation des incertitudes dans le système est analysée en utilisant un solveur stochastique tel que la méthode de Monte Carlo. La réponse acoustique du système est alors aléatoire et la quantification des incertitudes consiste en une estimation de données statistiques telles que les intervalles de confiances associés à un certain niveau de confiance sur les quantités d'intérêts. À partir de cette information statistique, la robustesse d'un design spécifique de liner vis-à-vis d'une variabilité simulée sur son modèle de performance peut être définie, en plus de l'information classique de performance acoustique. Cette information permet alors de connaître la propension d'un design à maintenir sa performance nominale lorsque son environnement change dans un intervalle de variation préalablement défini par le niveau d'incertitudes imposé au modèle stochastique. Alors, le meilleur design peut être choisi en faisant un compromis entre performance et robustesse.

Mots clés : *Conception robuste; Modèle aéroacoustique numérique; ACTRAN/TM; Modèle probabiliste non-paramétrique; Quantification d'incertitudes; Méthode de Monte Carlo*;